

CRANFIELD UNIVERSITY

KARSTEN PROPP

ADVANCED STATE OF CHARGE ESTIMATION FOR
LITHIUM-SULFUR BATTERIES

SCHOOL OF AEROSPACE, TRANSPORT AND
MANUFACTURING
Automotive Engineering

PhD Full Time
Academic Year: 2014–2017

Supervisor: Dr D. J. Auger
10 May 2017

CRANFIELD UNIVERSITY

SCHOOL OF AEROSPACE, TRANSPORT AND
MANUFACTURING
Automotive Engineering

PhD Full Time

Academic Year: 2014–2017

KARSTEN PROPP

Advanced State of Charge Estimation for Lithium-Sulfur
Batteries

Supervisor: Dr D. J. Auger
10 May 2017

© Cranfield University 2017. All rights reserved. No part of
this publication may be reproduced without the written
permission of the copyright owner.

“The better is enemy of the good.”

– Orlando Pescetti

Abstract

Lithium-sulfur (Li-S) batteries have a high theoretical energy density, which could outperform classic Li-ion technology in weight, manufacturing costs, safety and environmental impact. The aim of this study is to extend the research around Li-S through practical applications, specifically to develop a Li-S battery state of charge (SoC) estimation in the environment of electrical vehicles.

This thesis is written in paper based form and is organised into three main areas. Part I introduces general topic of vehicle electrification, the framework of the research project REVB, mechanisms of Li-S cells and techniques for SoC estimation.

The major scientific contribution is given in Part II within three studies in paper-based form. In Paper 1, a simple and fast running equivalent circuit network discharge model for Li-S cells over different temperature levels is presented. Paper 2 uses the model as an observer for Kalman filter (KF) based SoC estimation, employing and comparing the extended Kalman filter, the unscented Kalman filter and the Particle filter. Generally, a robust Li-S cell SoC estimator could be realized for realistic scenarios.

To improve the robustness of the SoC estimation with different current densities, in Paper 3 a fast running online parameter identification method is applied, which could be used to improve the battery model as well as the SoC estimation precision.

In Part III, the results are discussed and future directions are given to improve the SoC estimation accuracy for a wider range of applications and conditions. The final conclusion of this work is that a robust Li-S cell SoC estimation can be achieved with Kalman filter types of algorithms. Amongst the approaches of this study, the online parameter identification approach could deliver the best results and also contains most potential for further improvement.

Keywords

Lithium-sulfur batteries, State of charge estimation, Battery modelling, Offline parameter identification, Online parameter identification, Kalman Filter, Extended Kalman filter, Unscented Kalman filter, Particle Filter, Battery-management system

Acknowledgements

At the very first I would like to acknowledge my supervisor Dr. Daniel J. Auger, who was, with his patience, technical advice and attentiveness, the main reason the learning experience was exciting and inspiring, even if the nature of a PhD feels sometimes intimidating. He and the staff of the Cranfield the Advanced Vehicle Engineering Centre, namely Dr. Abbas Fotouhi, Dr. Stefano Longo and my second supervisor Dr. Efstathios Velenis, had always time for questions and founded a warm and professional work atmosphere.

Furthermore, I want to thank the amazing team of researchers and one team manager at the REVB project, that I had the privilege to work with. Here I especially want to mention Dr. Monica Marinescu, who always took a great deal of time for reviewing texts, despite her busy calendar. Furthermore Dr. Rajlakshmi Purkayastha, Dr. Laura O'Neill, Dr. Geraint Minton, Dr. Sylwia Walus and Dr. Gregory Offer shall be named for valuable help with battery chemistry related questions and pleasant conversations besides work.

For the help with practical Li-S cell tests and countless useful discussions, not always in the field of battery related research, I want to thank Vaclav Knap, who was not a part of the REVB team but nevertheless is a great human being and researcher. As a person who influenced my professional development, I also want to mention Prof. Karlheinz H. Bill, who encouraged me greatly to consider a PhD after I graduated from the University of Applied Science in Berlin.

Apart the professional side, I want to thank Ed Smith, Paul Deepak and Stergios Topouris for being funny. Above all, I also want to express my deepest gratitude to my parents, Margit and Hartmut, who always supported me greatly, even if I sometimes tested their patience. Without their advices and secretary work back in Germany, the time aboard would have been a lot more difficult.

Declaration of authorship

This thesis is submitted to Cranfield University in support of my application for the degree of Doctor of Philosophy. It has been composed by myself and has not been submitted in any previous application for a degree. The work presented in this thesis was carried out by myself as the result of my own original work. More details regarding my contributions of the following list of publications can be found in the introduction of this thesis.

Publications: 1st Author

Journal Papers:

Karsten Propp, Monica Marinescu, Daniel J. Auger, Laura O'Neill, Abbas Fotouhi, Karthik Somasundaram, Gregory J. Offer, Geraint Minton, Stefano Longo, Mark Wild, and Vaclav Knap. "Multi-temperature state-dependent equivalent circuit discharge model for lithium-sulfur batteries." *Journal of Power Sources* 328 (2016): 289-299.

Karsten Propp, Daniel J. Auger, Abbas Fotouhi, Stefano Longo, Vaclav Knap. "Kalman-variant estimators for state of charge in lithium-sulfur batteries." *Journal of Power Sources* 343 (2017): 254-267.

Conference Papers:

Propp, Karsten, Abbas Fotouhi, and Daniel J. Auger. "Low-cost programmable battery dischargers and application in battery model identification." *Computer Science and Electronic Engineering Conference (CEEC)*, 2015 7th. IEEE, 2015.

Propp, Karsten, Abbas Fotouhi, Vaclav Knap, and Daniel J. Auger. "Design, Build and Validation of a Low-Cost Programmable Battery Cycler." *ECS Transactions* 74.1 (2016): 101-111.

Conference Poster:

Propp, Karsten, Abbas Fotouhi, Daniel J. Auger, Vaclav Knap, and Stefano Longo. "Test rig for a dynamic cell temperature control based on cycle parameters." *LI-SM 3rd International Conference* (2017)

Publications: Co-author

Fotouhi, Abbas, Daniel J. Auger, Karsten Propp, Stefano Longo, and Mark Wild. "A review on electric vehicle battery modelling: From Lithium-ion toward LithiumSulphur." *Renewable and Sustainable Energy Reviews* 56 (2016): 1008-1021.

Fotouhi, Abbas, Karsten Propp, and Daniel J. Auger. "Electric vehicle battery model identification and state of charge estimation in real world driving cycles." *Computer Science and Electronic Engineering Conference (CEEC)*, 2015 7th. IEEE, 2015.

Fotouhi, Abbas, Daniel J. Auger, Karsten Propp, and Stefano Longo. "A Study on Battery Model Parametrisation Problem-Application-Oriented Trade-offs between Accuracy and Simplicity." *IFAC-PapersOnLine* 49.11 (2016) 48-53.

Fotouhi, Abbas, Neda Shateri, Daniel J. Auger, Stefano Longo, Karsten Propp, Rajlakshmi Purkayastha, and Mark Wild. "A MATLAB graphical user interface for battery design and simulation; from cell test data to real-world automotive simulation." *Synthesis, Modeling, Analysis and Simulation Methods and Applications to Circuit Design (SMACD)*, 2016 13th International Conference on. IEEE, 2016.

Fotouhi, Abbas, Daniel J. Auger, Tom Cleaver, Neda Shateri, Karsten Propp, and Stefano Longo. "Influence of battery capacity on performance of an electric vehicle fleet." (2016).

Fotouhi, Abbas, Daniel J. Auger, Karsten Propp, and Stefano Longo. "Electric vehicle battery parameter identification and SOC observability analysis: NiMH and Li-S case studies." (2016): 6-6.

Fotouhi, Abbas, Daniel J. Auger, Karsten Propp, and Stefano Longo. "Accuracy Versus Simplicity in Online Battery Model Identification." *IEEE Transactions on Systems, Man, and Cybernetics: Systems* (2016).

Knap, Vaclav, Daniel-Ioan Stroe, Maciej Swierczynski, Rajlakshmi Purkayastha, Karsten Propp, Remus Teodorescu, and Erik Scholtz. "A self-discharge model of Lithium-Sulfur batteries based on direct shuttle current measurement." *Journal of Power Sources* 336 (2016): 325-331.

Knap, Vaclav, Teng Zhang, Daniel Ioan Stroe, Erik Scholtz, Remus Teodorescu, and Karsten Propp. "Significance of the Capacity Recovery Effect in Pouch Lithium-Sulfur Battery Cells." *ECS Transactions* 74.1 (2016): 95-100.

Contents

Abstract	vii
Acknowledgements	ix
Declaration of authorship	xi
Contents	xiii
List of figures	xvii
List of tables	xix
List of abbreviations	xxi
I Introduction and context	1
1 Introduction	3
1.1 Batteries for electric cars	6
1.2 REVB project	7
1.3 Research objectives	9
1.4 Thesis outline	10
2 Fundamental battery chemistry from Li-ion to Li-S	13
2.1 Classic Li-ion batteries	13
2.2 Li-S batteries	23
2.3 Discussion	36
2.4 Conclusion	41
3 Battery state of charge estimation	43
3.1 Cell capacity	44
3.2 State of charge	45
3.3 Coulomb counting	46

3.4	Open circuit voltage	47
3.5	Impedance spectroscopy	48
3.6	Soft computing	49
3.7	Model based approaches	50
3.8	Kalman filter and derivatives	55
3.9	Conclusion	74
4	Methods and experiments	77
4.1	Tested Li-S cells	77
4.2	Experimental hardware	79
4.3	Experimental software	79
II	Papers	83
5	Paper 1 – Equivalent circuit battery model	85
5.1	Introduction	87
5.2	From Li-ion to Li-S modelling	89
5.3	Parameter identification	94
5.4	Battery model set	95
5.5	Experimental design	103
5.6	Identification Results	104
5.7	Model derivation	108
5.8	Model validation	111
5.9	Conclusion	115
5.10	Acknowledgement	116
6	Paper 2 – KF based SoC estimation	117
6.1	Introduction	119
6.2	Lithium-sulfur batteries	122
6.3	Applicability of conventional SoC estimation techniques	124
6.4	Implementation of state estimators	126
6.5	Experimental evaluation	136
6.6	Results and discussion	142
6.7	Conclusion	154
6.8	Acknowledgement	155
7	Paper 3 – Online parametrization SoC estimation	157
7.1	Introduction	159
7.2	On-line parameter estimation with EKF	162
7.3	Experimental design	173
7.4	Current - R_0 relationship	176
7.5	Modelling of the dynamic internal resistance	178

7.6	State of charge estimation	181
7.7	Conclusion	192
7.8	Acknowledgement	194
III	Discussion and conclusion	195
8	Contributions and future directions	197
8.1	Battery model for SoC estimation	198
8.2	SoC estimation with derivations of the Kalman filter	202
8.3	SoC estimation with EKF based online parameter identification	205
9	Conclusion	211
	Appendices	215
A	Cell data sheets from Sion and OXIS	217
B	Experimental software code	223
C	Conference Poster Li-SM³ London 2017	229
	References	231

List of figures

1.1	Energy density chart for different cell chemistries	5
1.2	From battery pack to a single cell	6
2.1	Work principle of a lithium cobalt oxide battery	15
2.2	Intercalation steps of lithium ions into graphite	16
2.3	Voltage profile and SEI formation	17
2.4	SEI decomposition	18
2.5	Intercalation in cobalt oxide cathode	20
2.6	Main mechanisms playing a role in Li-S batteries	24
2.7	Simplified cycling of a typical lithium-sulfur cell	26
2.8	Species in electrolyte during discharge/charge	29
2.9	Surface layers lithium anode	31
2.10	Discharge behaviour of Li-S cells with different current rates	33
2.11	OXIS energy cell voltage over capacity and temperature	36
3.1	SoC definitions of a battery	44
3.2	Pulse discharge test of Li-S battery with two different currents	45
3.3	Principle of Coulomb counting	46
3.4	Principle of open circuit method	47
3.5	Principle of impedance spectroscopy	48
3.6	Principle of model based estimation	50
3.7	Principle of electrochemical modelling	52
3.8	Terminal voltage predicted by mechanistic model	53
3.9	Input- output relationship of the ECN model	54
3.10	Properties of Gaussian distribution	58
3.11	Gaussian distribution through state estimation	61
3.12	Conditional, Gaussian probabilities through state estimation	62
3.13	State propagation Kalman filter	63
3.14	State propagation extended Kalman filter	67
3.15	State propagation unscented Kalman filter	70
3.16	Target- and proportional probability density function and particle density .	71
3.17	Particle distributions during the propagations	72
3.18	State propagation particle filter	74

4.1	Prepared test cell in metal chamber	78
4.2	Test layout and connections between cell, BOP, and computer	79
4.3	Velocity and current profile of vehicle simulation	80
4.4	Current demand vectors in Matlab Simulink	81
4.5	Example of cycling tests with Li-S battery	82
5.1	Work principle of Li-S battery	90
5.2	Basic voltage behaviour Li-S battery	93
5.3	Response of a Thevenin/behavioural battery model to current pulse	97
5.4	Mixed pulse discharge and test installation	104
5.5	Identification results for U_{OC} over pulse and SoC	105
5.6	Identification results for R_0 , R_p and C_p for each current pulse respectively	107
5.7	Parameter functions for U_{OC} , R_0 , R_p and C_p over SoC	112
5.8	Battery model and measured terminal voltage for 23 °C	113
6.1	Discharge/charge behaviour of a Li-S battery.	123
6.2	Model and parameter functions for U_{OCV} , R_0 , R_p and C_p over SoC	130
6.3	Mixed pulse and NEDC current profile with test installation.	137
6.4	Estimation results for EKF, UKF, PF; mixed pulse/NEDC profile, $SoC_0 = 1$	144
6.5	Estimation results for EKF, UKF, PF; mixed pulse/NEDC profile, $SoC_0 = 0.6$	146
6.6	Estimation results EKF, UKF, PF for a lower current NEDC drive cycle.	149
6.7	Estimation results EKF, UKF, PF for a higher current NEDC drive cycle.	150
6.8	Simplified OCV curve and related estimation results for the EKF.	153
7.1	Behaviour and SoC estimation principles of Li-S batteries	160
7.2	Online parameter identification results	172
7.3	Experimental set-up and applied discharge currents	175
7.4	EKF online parametrisation results for different current profiles	176
7.5	Parametrizing D_{iff1} and D_{iff2} (A), Results $R_0 + R_{diff}$ (B)	181
7.6	Results of SoC estimation; different profiles and rate densities, $SoC_0 = 1$	187
7.7	Estimation error with an initially fully charged battery	188
7.8	Results of SoC estimation; different profiles and rate densities, $SoC_0 = 0.6$	189
7.9	Results of SoC estimation; three NEDC current profiles; constant charge	192
8.1	NEDC current profiles with different scaling gains	198
8.2	Voltage response to NEDC current profiles over different temperatures	199
8.3	Discharge tests with the NEDC and UDDS cycle over different temperatures	200
8.4	Mixed pulse, mixed temperature discharge test	202
8.5	Consecutive discharges with NEDC and UDDS cycles with varying gains	204
8.6	Consecutive discharges with model improvement R_{dyn}	206
8.7	Online parameter identification with mixed pulses and mixed temperatures	207

List of tables

2.1	Conductivity electrolyte	21
2.2	Lithium-ion battery chemistries and properties	22
2.3	Developments Li-ion chemistry	23
2.4	Carbon materials for Li-S batteries	35
2.5	Available lithium-sulfur cells and future developments	37
2.6	Comparison of effects on usable capacity	38
2.7	Comparison of effects on rate capability	39
2.8	Comparison of effects on capacity fade	40
5.1	Capacities of test cells	105
5.2	Parameter functions	111
6.1	Discharge experiments	138
6.2	RMSE SoC estimation with EKF, UKF and PF with $SoC_0 = 1$	145
6.3	RMSE SoC estimation with EKF, UKF and PF with $SoC_0 = 0.6$	147
6.4	Discharge experiments with NEDC-low and NEDC-high profile	148
6.5	RMSE SoC estimation with NEDC-low and NEDC-high profile	151
6.6	RMSE SoC estimation with simplified OCV curve	152
6.7	Simulation time for the pulse discharge test (128000 s)	153
7.1	Discharge experiments	173
7.2	RMSE SoC estimation with UDDS/NEDC with different gains, $SoC_0 = 0.6$ 190	

List of abbreviations

ANN	Artificial neural network
BMS	Battery management system
BOP	Bipolar linear power supply (Kepco)
CPU	Central processing unit
DME	Dimethoxy ethane
DOL	Dioxolane
ECN	Equivalent circuit network
ECU	Electronic control unit
EIS	Electrochemical impedance spectroscopy
EKF	Extended Kalman filter
EV	Electric vehicle
GPIB	General Purpose Interface Bus
HEV	Hybrid electric vehicle
HMM	Hidden Markov model
IR	Internal resistance
KF	Kalman filter
LiTFSI	Bis(trifluoromethane)sulfonimide lithium salt
NEDC	New European driving cycle
OCV	Open circuit voltage

PAN	Polyacrylonitrile
PDF	Probability density function
PEM	Prediction error minimisation
PF	Particle filter
RC	Resistor-Capacitor (parallel pair)
REVB	Revolutionary electric vehicle battery
RMSE	Root-mean-square error
SEI	solid-electrolyte-interphase
SoC	State of charge
SoH	State of health
SPKF	Sigma-point Kalman filter
TEGDME	tetra(ethylene glycol) dimethyl
THF	Tetrahydrofuran
UDDS	Urban dynamometer driving schedule
US ABC	US Advanced Battery Consortium
UKF	Unscented Kalman filter

Symbol	Equation Parameters
$\alpha_i^{(c)}$	Weight vector covariances unscented Kalman filter
$\alpha_i^{(m)}$	Weight vector measurements unscented Kalman filter
χ	Augmented state vector
χ^-	A priori augmented state vector unscented Kalman filter
χ^+	A posteriori augmented state vector unscented Kalman filter
X	State of charge
ε	Prediction error
η	Normalization factor for Bayes rule

$\eta_{c\ a}$	Concentration polarisations at anode
$\eta_{c\ c}$	Concentration polarisations at cathode
$\eta_{ct\ a}$	Charge transfer overvoltages at anode
$\eta_{ct\ c}$	Charge transfer overvoltages at cathode
γ	Partial sinusoidal function
ψ^i	Measurement prediction for each sigma point
Ω_p	Dynamic bandwidth
ρ_p	Dynamic fraction of the response
σ_v	Measurement noise variance
σ_w	System noise variance
θ	Parameter vector
A	State matrix
\hat{A}	Jacobian of state matrix
B	Input matrix
\hat{B}	Jacobian of input matrix
C	Output matrix
\hat{C}	Jacobian of output matrix
c	Transition point of parameter functions in between both voltage plateaus
C_P	Capacitance of parallel RC circuit
D	Direct transition matrix
\hat{D}	Jacobian of direct transition matrix
E	Electromotive force
E_0	Electromotive force or open circuit voltage
f_{C_p}	Parameter function RC capacitance over SoC
$f_{OCV-simple}$	Simple, one polynomial, parameter function for OCV
$f_{parameter}$	Fitted polynomial function

f_{R_0}	Parameter function internal resistance over SoC
$f_{R_0\text{--high}}$	Parameter function internal resistance high plateau
$f_{R_0\text{--low}}$	Parameter function internal resistance low plateau
f_{R_p}	Parameter function RC resistance over SoC
$f_{U_{OC}}$	Parameter function OCV over SoC
$f_{U_{OC\text{--high}}}$	Parameter function function OCV high plateau
$f_{U_{OC\text{--low}}}$	Parameter function OCV low plateau
$f_{\dot{U}_p}$	State transition function parallel RC circuit
G	Transfer function
H	Disturbance of the system
h_{U_L}	Model output
I	Operating current
I_{batt}	Cell current
I_{loss}	Current losses between charge and discharge
I_{max}	Current amplitude for impedance spectroscopy
I_L	Load current battery
k	Discrete time step
L	Kalman Gain
m	Scaling factor
P	Covariance Matrix for propagation of Kalman filter
P^-	A priori covariance matrix for propagation of Kalman filter
P^+	A posteriori covariance matrix for propagation of Kalman filter
p	Probability
$p_1 - 10$	Polynomial factors
P_0	Initial estimate of covariance Matrix for propagation of Kalman filter
Q	Covariance Matrix for system noise

q	Forward shift operator
Q_n	Nominal Capacity of a cell
Q_{cap}	Cell capacity
Q_{charge}	System noise covariance matrix for charging
Q_{high}	System noise covariance matrix for high voltage plateau
Q_{low}	System noise covariance matrix for low voltage plateau
Q_t	Remaining capacity of the cell during discharge
R	Covariance Matrix for measurement noise
R_{int}	Total steady-state resistance
R_{charge}	Measurement noise covariance matrix for charging
R_{ct}	Charge transfer internal resistance part
R_{diff}	Dynamic internal resistance part
R_{dyn1}	Factor for dynamic internal resistance
R_{dyn2}	Factor for dynamic internal resistance
R_{high}	Measurement noise covariance matrix for high voltage plateau
R_{low}	Measurement noise covariance matrix for low voltage plateau
R_0	Internal resistance
R_P	Resistance of parallel RC circuit
S	Weighting matrix
SoC	State of charge
SoC_{est}	Estimated SoC in operation
SoC_{max}	Maximum allowed SoC in operation
SoC_{min}	Minimum allowed SoC in operation
SoC_0	Initial SoC for the estimation
$SoC_{0 \text{ ref}}$	Initial reference SoC from coulomb counting
t	Continuous time

u	System input
U_{OC}	Open circuit voltage battery
U_L	Terminal voltage battery
U_p	Capacitor voltage
v	Measurement noise
V_{\max}	Maximum allowed operational cell voltage
$V_{\max i}$	Voltage amplitude for impedance spectroscopy
V_{\min}	Minimum allowed operational cell voltage
V_A	Voltage source in ECN model
V_B	Resistance in ECN model
V_C	Transient response in ECN model
V_N	Cost function
V_{OC}	Battery open circuit voltage
w	System noise
w^m	Weight vector for particle set
x	System state
\dot{x}	Derivative of system state
\hat{x}	Estimated system state
\hat{x}^-	A priori system state estimate
\hat{x}^+	A posteriori system state estimate
x_0	Initial estimate system state
x^m	State particle set
y	System Output
\hat{y}	Estimated system Output
Z	Cell impedance

Part I

Introduction and context

1

Introduction

The question about post fossil fuel mobility is one of the most important in the transport sector of this generation. While previous efficiency improvements were mostly focused on the classical combustion engine to improve fuel efficiency, today's concepts are focused on the uptake of electric vehicles (EVs). This leads to new challenges for the energy storage, since there are no electrical storages that could compete with the high energy density and relative simple handling of fossil fuel. To be competitive, the costs and the performance must be sufficient, which means for EVs to provide enough energy for acceptable ranges but also to be able to give sufficient power for the vehicle performance. From today's perspective, batteries or fuel cells could be a solution. Due to their high specific energy (Wh kg^{-1}) and shorter refuel times, fuel cell electric vehicles are seen as preferable solution for long range applications [1]. However, in a well-to-wheel consideration they are seen as less efficient than battery electric vehicles in most scenarios due to energy losses in the water-electrolytic hydrogen production [2]. Batteries can provide a high power output but due to their lower energy density, the range for reasonable battery sizes was limited to about 240 km [1] [3] in 2010, which has not changed dramatically. A further increase of the battery size would not be efficient because other conceptional

areas, like frame structure, brakes or engine, needs to be reinforced to compensate for the increased weight.

For an up take of electric vehicles from a niche product to a mass marked therefore mostly the energy density has to be increased. Common lithium-ion (Li-ion) batteries, further explained in Chapter 2, have energy densities around 150 Wh kg^{-1} [4], which cannot yet grant a satisfactory range for most customers. And while further improvements in the cell design and chemistry are likely, many advancements of the classic Li-ion technology have been made already [5]. But even if the capacity will increase up to 235 Wh kg^{-1} (on system level), a goal set by the US Advanced Battery Consortium (US ABC) [6], battery powered vehicles may not compete with the classical combustion engine. To cite C.E. Thomas while evaluating fuel cells and batteries [1]:

“A major breakthrough in battery technology, well beyond the US ABC goals, would be required before a long-range battery EV could satisfy customer’s needs for conventional passenger cars, particularly with respect to battery recharging times.”

The second largest challenge is to reduce the costs of battery packs. While prices for Li-ion batteries in general are falling, most of the cost savings are achieved mainly through increased and more efficient production capabilities [5]. The current Tesla model S approximately reaches US\$310 per kWh [7]. However, this is still far away from the US\$150 per kWh barrier, also suggested by the US ABC, which is believed to be necessary to move EVs beyond a niche application into the mass market [8]. A potential near future solution for significantly increased specific energies are lithium-sulfur (Li-S) batteries, as lithium air-based technologies are not seen applicable in the near future [9]. The Li-S technology was invented in the 1960s [10] but difficulties to contain the sulfur led to issues so that cells available for practical applications were just introduced recently. However, the future potential of this chemistry Li-S cell is so great that [9]:

“An all-electric vehicle with a range in excess of 300 miles per charge and a low price

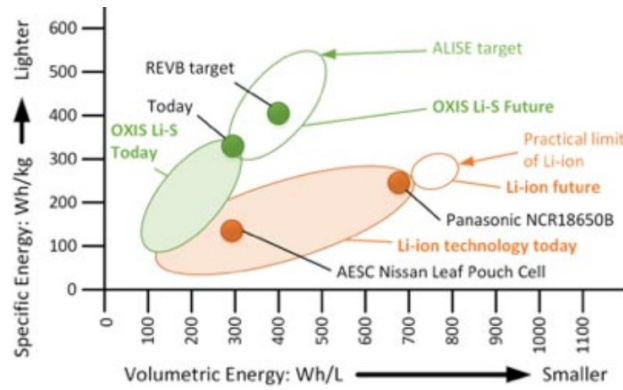


Figure 1.1: Energy density chart for different cell chemistries [12]

could be realized.”

The Revolutionary Electric Vehicle Battery (REVB) project aims to address both, the energy density and cost issues of electric mobility, with its goal to develop a Li-S battery system for automotive applications that will [11]:

1. store more energy with a high density (400 Wh kg^{-1})
2. harnessing significantly more of the theoretically stored energy for applications (90 - 95%).

Even if today’s cell cannot compete with classic Li-ion technology, the energy density of prototype cells already exceeds cells that are used in EVs (Fig. 1.1), which is also interesting for non automotive applications. Next to the improvement of the inner cell reactions, the lack of a Battery Management System (BMS) for Li-S cells is becoming increasingly urgent, since it hinders the use of the cells in larger packs and practical applications. Therefore the aim of this thesis is to develop models and algorithms for a BMS that are capable of optimally operating the cells. In particular this means the SoC estimation for Li-S batteries is explored, which is one fundamental value for a BMS that harnesses a maximum of the cells energy without compromising safety or lifetime. Therefore, the research in this work will contribute to the second major anticipated achievement of the project.

Practical BMS systems are new for Li-S cells and need to accommodate for their unique behaviour. First thoughts about a Li-S compatible BMS system were made by Parfitt [13] with the aim to model Li-S batteries for systems engineers of space applications. The model includes self discharge, charge and discharge hysteresis and degradation. This thesis however, focuses on environment of EVs, which means dynamic loads, temperature variations, sensor noise and tight cost guidelines for the BMS hardware. Therefore the presented work is oriented on a trade-off between accuracy/complexity and uses drive cycle data to test the applicability of the state estimation.

1.1 Batteries for electric cars

In automotive applications, traction batteries have to deliver enough power to overcome the driving resistances of a vehicle, which are acceleration, rolling- and drag resistance in a horizontal plane. The potential-, power- and capacity- demands for EVs are roughly 200 - 400 V, 25-120 kW and 15 - 16 kWh per 100 km [14], which makes an interconnection of many individual cells necessary.

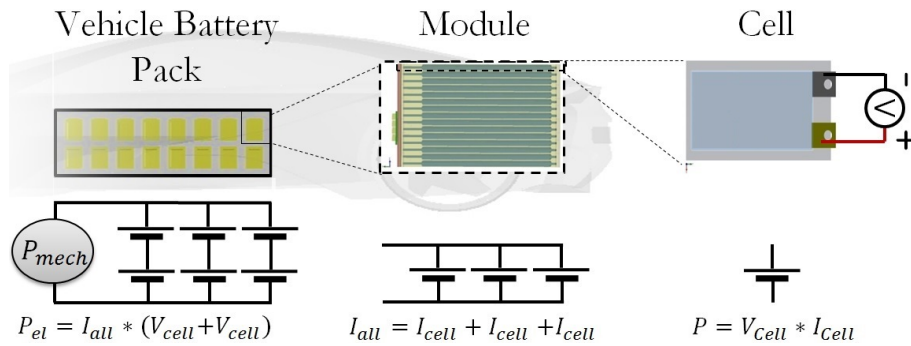


Figure 1.2: From battery pack to a single cell

The overall current of the battery pack must be therefore the sum of the parallel cells and the pack voltage the sum of cells connected in series, defined by Kirchhoff's circuit

laws (Fig. 1.2). The layout of the electric circuit depends on the application. Parallely oriented packs increases the redundancy and will form a more reliable battery pack, but it will also decrease the efficiency due to increased conduction losses at high currents. Serial arrangements will need lower currents to deliver power but the whole serial circuit string could be broken with only one cell defect. Furthermore, each cell in series needs to be controlled for voltage and balanced. An example for a battery pack is given here from the Nissan Leaf. The pack uses cells with 3,75 V and 32,5 Ah nominal voltage and capacity. Four of these cells form a module with two parallel and two serial cells, each module has a voltage of 7,5 V and 65 Ah capacity. The whole pack contains 48 modules which defines the overall voltage of 360 V and a capacity of 24 kWh [15]. Batteries, single cells or whole packs, are usually compared with specific energy (Wh kg^{-1}), volumetric energy density (Wh l^{-1}), specific power (W kg^{-1}) and (vi) power density (W l^{-1}).

For a potential future Li-S battery pack the most significant improvements are specific energy. A comparable Li-S cell pack would contain all cells in series in a module (lower terminal voltage of Li-S batteries but larger capacity), would need twice the control effort (more cells in series that needs voltage measurements and balancing), would be slightly larger (lower volumetric energy density) but also would be significantly lighter. For EVs the lightness can be seen as more significant than the disadvantages because it leads to reduced losses and allows synergy effects with smaller motors and lighter chassis.

1.2 REVB project

One goal of the REVB project was to produce a similar but smaller Li-S battery than the pack used in the Nissan Leaf. Another goal was to get an understanding of the behaviour and necessary control effort to operate Li-S cells in a pack. Under the lead of OXIS energy, three main parties participated in the REVB project. While the Imperial College

London has developed electrochemical models for the complex reaction path of sulfur, Cranfield University has been focussed on controlling the batteries in the environment of EVs. As industry partner Ricardo was responsible for the hardware and building the battery pack. For publications within the project, so as the here presented papers in Chapters 5, 6 and 7, the individual work in each paper can be seen in the authors order. Generally, the first author of published papers in this project performed literature survey, the laboratory tests, formulated the key problem to solve and presented the solution. However, the structure of the project led to multiple interactions and overlaps which are mentioned here to clarify the contributions of the co-authors of the three papers in this thesis. As this thesis is part of the Cranfield contribution to explore the optimal operation for Li-S cells, the team members Daniel Auger, Stefano Longo, Abbas Fotouhi are named in every paper since many discussions, reviews and suggestions for improvements led to the result of each publication. Furthermore team members from OXIS Energy or Imperial college London are named when they contributed.

In the first project phase, OXIS energy was responsible for the practical testing. The company has access to industry standard test facilities and experience with testing Li-S cells so the experimental data was transferred to Cranfield university for further processing. Therefore, the pulse tests, presented in Paper 1 (Chapter 5), were executed by Laura O'Neill. The decision to apply a mixed pulse pattern was made after many discussions with Monica Marinescu and Greg Offer from Imperial College London and Mark Wild together with Karthik Somasundaram from OXIS Energy, since previous tests raised questions about the current dependency of the model parameters. Furthermore Vaclav Knap helped to review the paper as an external advisor since he works in a comparable project at the Aalborg University in Denmark.

With the development of a low-cost test rig and the purchase of a laboratory grade programmable power supply/sink and thermal chamber in the second year of the project,

Cranfield took over the experimental work with cells provided by OXIS for practically oriented experiments in the framework of EVs (Chapter 6, 7). To reproduce a realistic scenario, the applied currents are based on drive cycle data, which provide a velocity over time profile. The current demand over time is calculated by a vehicle model (Nissan Leaf), developed by Abbas Fotouhi (see Chapter 4). For the experiments the resulting current profile was scaled down to a cell level and applied to the cell in different temperatures.

1.3 Research objectives

With the gathered data from the drive cycle tests, the behaviour of Li-S cells in a real world application of EVs could be examined. The measured current and terminal voltage over time contains sufficient information to estimate a reference SoC. Therefore the stored data was used to validate a battery model and experiment with different SoC estimation algorithms to answer the main goals of the thesis:

- **Evaluate potential candidate methods for the SoC estimation:** An evaluation about useful techniques is done based on the main properties of Li-S batteries in the Paper 2 (Chapter 6) [16], after the main SoC estimation techniques are introduced. Since the majority of applied methods are used with classic Li-ion batteries, also both types are introduced to highlight the main similarities and differences for applications.
- **Develop a Li-S cell model for SoC estimation:** Since model based methods are chosen as potential candidate for the unique characteristics of Li-S cells, an observer model is developed in Paper 1 (Chapter 5) [17], capable of running on typical battery management system hardware.

- **Develop robust SoC estimation:** Considering the properties of Li-S batteries, different SoC estimation systems are created and tested in Paper 2 and 3 (Chapter 6 and 7), capable of estimating the SoC in real life scenarios. The estimation accuracy have to be robust even when the conditions are not ideal.
- **Establish accuracy and limitations for the applied algorithms:** Compare the accuracy and robustness of the tested techniques and give recommendations about future improvements.

1.4 Thesis outline

The main content of this thesis contains three research papers on the development of an equivalent circuit model of the tested OXIS cells, a comparison of three model based SoC estimation methods and a combination between online parameter an SoC estimation. Since the applied techniques could only be introduced briefly in a typical journal paper form, the Li-S battery and the background of the SoC estimation are introduced here in greater detail to improve the readability of the thesis. Therefore the thesis has the following structure:

Chapter 2: From Li-ion to Li-S batteries introduces in the chemical reactions and fundamental properties of classic Li-ion and Li-S batteries and concludes with the main differences in the cell behaviour and its meaning for SoC estimation.

Chapter 3: Battery state of charge estimation gives a fundamental introduction of the principles and definitions used for SoC estimation in batteries. Furthermore the theory of probabilistic filters, which could not introduced in the respective publications, is given.

Chapter 4: Methods and experiments describes the details of the test procedures and methods to ensure the tests are reproducible.

Chapter 5: Multi-temperature state-dependent equivalent circuit discharge model for lithium-sulfur batteries defines, parametrizes and validates an equivalent circuit model for Li-S batteries for temperatures from 20 - 50 °C.

Chapter 6: Kalman-variant estimators for state of charge in lithium-sulfur batteries employs the developed model from the previous Chapter for the SoC estimation with probabilistic filters such as the extended Kalman Filter, the unscented Kalman filter and the particle filter.

Chapter 7: Dual extended Kalman filter for online estimation of model parameters and state of charge in lithium-sulfur batteries applies an online parameter identification approach based on the extended Kalman filter to improve the robustness of the SoC estimation for current dependent capacity changes of Li-S cells.

Chapter 8: Contributions and future directions puts the findings of the previous Chapters in perspective and gives suggestions for future improvements for the state of charge estimation.

Chapter 9: Conclusion summarizes the whole thesis and names examples for following projects where the framework of SoC estimation for Li-S batteries from this thesis will be used.

2

Fundamental battery chemistry from Li-ion to Li-S

Common applications of battery powered vehicles are usually based on classical Li-ion batteries, so as the control and estimation methods implemented on their BMS systems for operating the cells optimally and safely. For designing the requirements for the SoC estimation for Li-S batteries, it is therefore useful to understand both reaction principles to find major similarities or differences. This enables the evaluation of the performance of modelling approaches and will improve the evaluation of the SoC estimation requirements. Furthermore, existing techniques, which are used already for Li-ion batteries, can be evaluated for their applicability for Li-S cells. Thus, the main parts of the battery are discussed with the focus of the practical effects for applications.

2.1 Classic Li-ion batteries

The fundamental principle of classic lithium ion batteries is based on intercalation chemistry; inserting a guest atom or molecule into a solid host structure while maintaining the

structural features of the host [18]. Since chemical bonds do not have to be broken, the reaction occurs at mild temperatures and can be highly reversible. Important properties for the capacity is the number of lithium ions that can be stored per mass unit (specific energy) and the speed the ions intercalate into a medium (specific power). Despite its excellent properties, pure lithium is not used as an electrode material for today's batteries due to the growth of dendrites during cycling. These can cause internal short circuits, degradation, and limited coulombic efficiency [19]. The leading cell configuration today uses graphite as an anode (negative electrode), combined with a cathode (positive electrode) of metal oxide compounds (LiCoO_2) [20, 21]. Both electrodes are usually porous materials applied to current collectors, suited in an airtight sealing filled with an electrolyte and are physically separated with a porous separator to prevent contact. In the literature, many graphical examples of the function principles exist. Here a few are combined together to form a new one (Fig. 2.1) from [22, 23, 24, 25]. The lithium cobalt oxide battery is produced discharged and needs to be cycled before use. While charging an external energy source "pumps" electrons to the anode so that lithium ions migrate through the electrolyte and separator to the graphite structure. This process initiates the growth of the solid-electrolyte-interphase (SEI) on the graphite anode due to the instability of the electrolytes with the negative electrode [26]. During the discharge, the lithium ions migrate back from the graphite anode to the cathode. With this configuration a realistic capacity of about 140 mAh g^{-1} is possible on cell level [20].

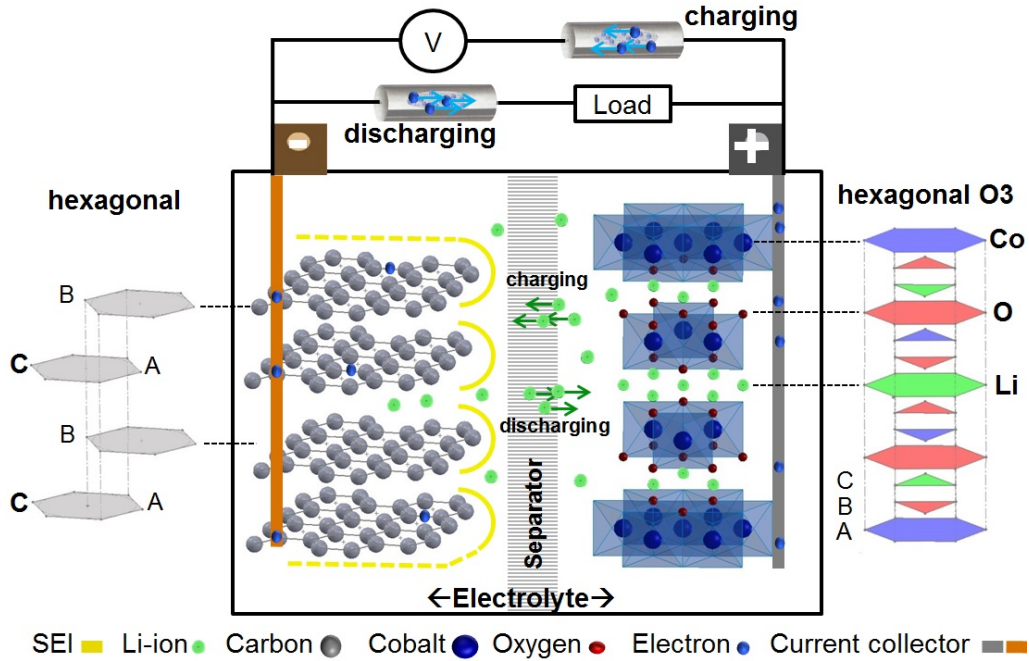


Figure 2.1: Work principle of a lithium cobalt oxide battery

2.1.1 Anode

The most used material for the anode is graphite consisting of physically and chemically robust, layered carbon molecules [18]. The lithium ions intercalate in between the strong layers, which leads to excellent cycling performance and a specific charge of about 372 mAh g^{-1} [27]. However, the exact amount of practical specific charge varies and is dependent on the quality of the structure of the layers. Most lithium intercalates in intact layers of the graphitic structure, without many defects [28]. The diffusion into the layers depends on the direction, parallel or perpendicular to the basal planes of the graphite structure. Lithium ions are strongly absorbed by the edge sites of a particle where they can easily diffuse within the layers (parallel) [29]. This leads to a suggested structure of intact graphite (more storage) with a high ratio of edge-plain sites (higher rates) and is one reason for energy or power emphasised Li-ion batteries. Larger particles can store

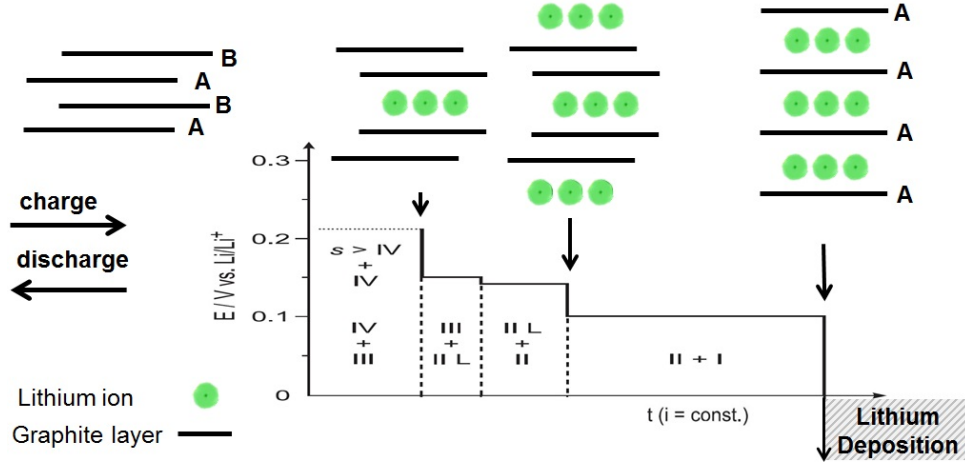


Figure 2.2: Intercalation steps of lithium ions into graphite adapted from [25], [27]

more atoms and smaller ones can store them more quickly. In the normal cycling process, lithium atoms diffuse into the graphite stepwise, filling certain layers before other ones due to lowest energy principles and the repulsive interactions of the guest species [27]. The low step size of under 0.1 V vs Li/Li^+ indicates a relatively constant diffusion rate over the SoC range. Fully packed (Eq. 2.1), a layer widens about 10% and the stacking shifts from ABA to AAA [30] (Fig. 2.2).



The low volumetric changes are one of the reasons for the high lifetime of the anode. When the full capacity of the intercalation is reached and charging is continued, a metallic lithium layer builds over the anode which passives its surface and causes degradation. In the worst case however, metallic lithium can also build dendrites which cause internal short circuits and a thermal run away. The potential difference between the fully packed anode to metallic lithium (Li/Li^+) is just 0.1 V, which requires a precise detection to prevent overcharge. Furthermore, the diffusion coefficient lowers with decreasing temperatures [31], which also can lead to lithium plating at lower charging rates [32].

Therefore, a control system must limit the charging of the cell according to the SoC and temperature if a safe and long operation shall be granted.

2.1.2 SEI anode

The SEI forms due to the difference between the redox potentials of the active metal and the solution species and is dependent on the electrolytes [33]. The rather special nature of the SEI is that it is permeable to lithium cations but impermeable to the components of the electrolyte and electrons [32]. Because there are still doubts concerning the composition of the SEI layer and its mechanism of formation [34], the process is only discussed briefly. It builds during the first charging with loss of 5 - 20% of the active lithium (Fig. 2.3 1st cycle). Therefore after the first charge only 80 - 95% of the theoretical capacity can be recovered. After the second cycle the consumption lowers and charge efficiency rises near 100% while the SEI is stabilized (Fig. 2.3 2nd cycle) [27]. When fully grown, the SEI largely determines performance of graphite anodes, its life time and rate capability.

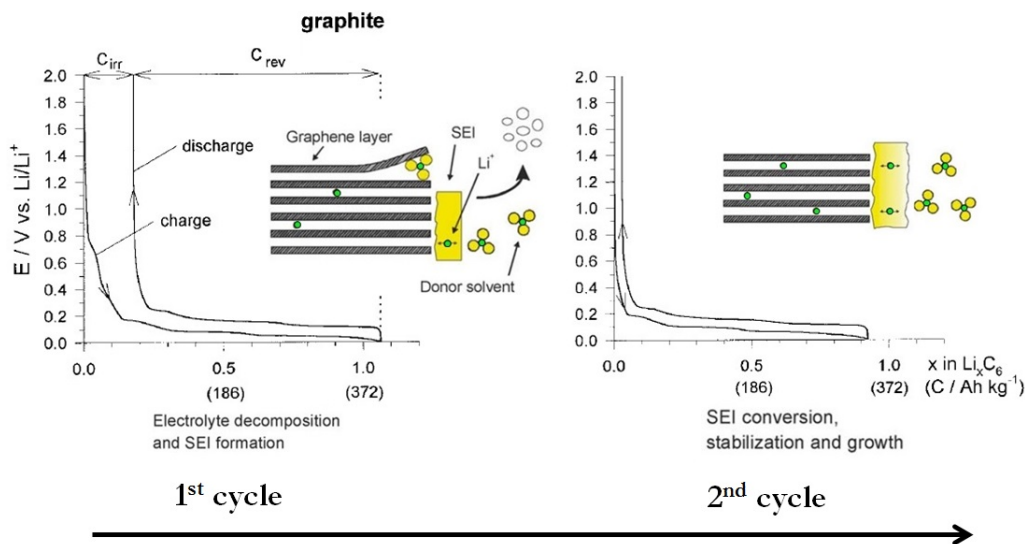


Figure 2.3: Voltage profile and SEI formation adapted from [27], [32]

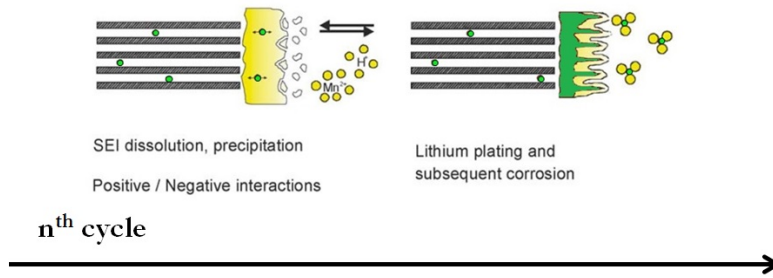


Figure 2.4: SEI decomposition adapted from [32]

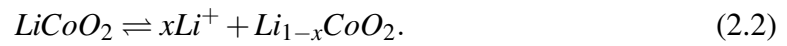
In operation, the SEI faces some decomposition reactions, which are mainly dependent on current density, cell temperature, and electrolyte composition [35]. These reactions are seen as the major source of ageing at the anode. While cycling, the SEI also has to follow the volumetric variations of the anode, leading to a higher impedance and resulting in power fade. Furthermore, small cracks can build which allow other species (electrons, solvents, impurities) to diffuse through the SEI, leading to irreversible capacity loss and self discharge (Fig. 2.4) [32]. These reactions are generally enhanced by high temperatures, which is one reason for the environmental control of large packs. Another limit for the operational temperature is the electrolyte. Depending on the solvent and salt, exothermic reactions can already begin at 58 °C (Salt:LiBF₄, supporting electrolyte: EC/DMC 2:1) [36]. Even if other combinations are more stable, studies indicate that capacity fade can already occur when cells are stored at this temperature [32]. The properties of the SEI are the main reason why the cell temperature of classic Li-ion must be monitored and controlled for large packs with high rates.

2.1.3 Cathode

The lithium cobalt oxide cathode consists of layers of strongly bonded metal complexes of CoO₆ octahedra and lithium ions inserted in between the layers, stacked in ABC sequence (Fig. 2.1). As in graphite, the diffusion occurs mostly along the planes, via tetrahedral

site hops (Fig. 2.5) [37], and the intercalation offers good theoretical capacity and lifetime [23].

The rate capability is mostly dependent on the concentration of vacancy sites (less lithium diffuses faster) and the activation barrier (smaller distance between layers means higher activation energy) [24]. Figure 2.5 also shows the charge/discharge curve of the LiCoO_2 cathode indicating a monotonic rise of the activation barrier when lithium ions are deintercalated during charge



Theoretically this process can continue up to 4.7 V vs Li/Li^+ , removing all the lithium ions from the composite. Practically however the charge stops around 4.2 V vs Li/Li^+ [24], since irreversible structural changes from hexagonal O3 to O1 occur when too many lithium ions are removed. Furthermore, higher voltages can lead to flammable O_2 gas [23], which is why the end of charge is reached when the structure changes to monoclinic O1, using about half of the theoretical capacity of 270 mAh g^{-1} . Hence, a control system, protecting the battery from overcharge, also protects the cathode to avoid capacity fade or, in the worst case, thermal runaways.

2.1.4 Electrolyte

The key role of the electrolyte is to provide high ion conductivity, while being an electronic insulator. Commonly used is the lithium salt LiPF_6 solvated by inorganic alkyl carbonates like ethylene carbonate (EC), dimethyl carbonate (DMC) or ethyl carbonates (DEC) [25]. Through combinations of solvents and their differing properties (EC: high permittivity due to high polarity, DMC and DEC: high mobility due to low viscosity) [34], the electrolyte can be adapted for applications regarding the operational temperature or the

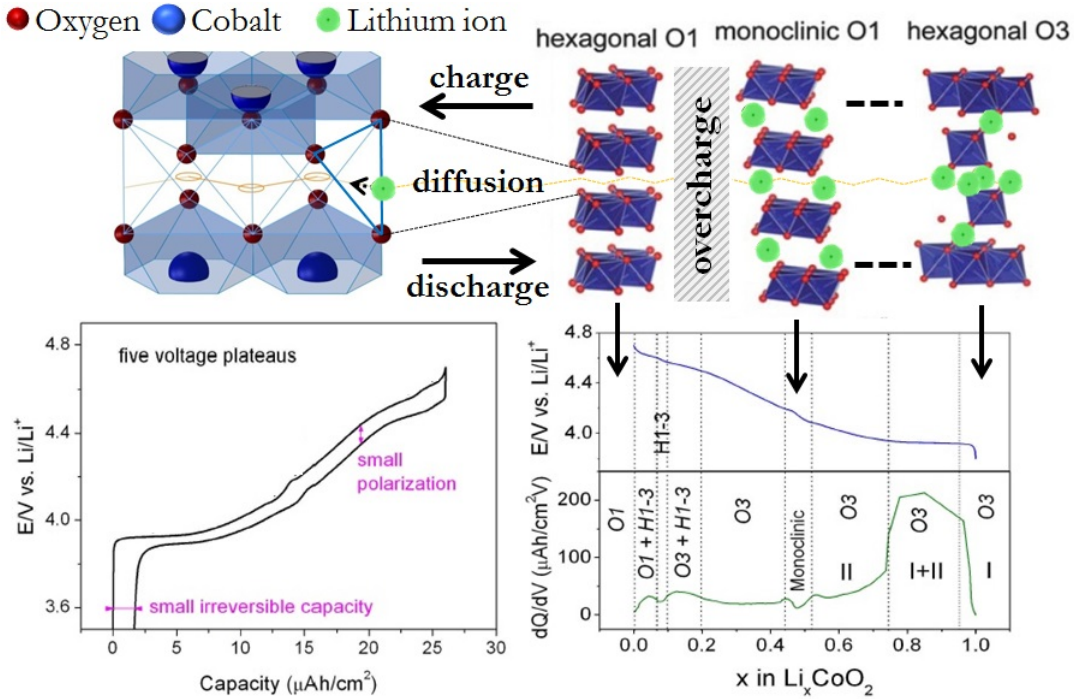
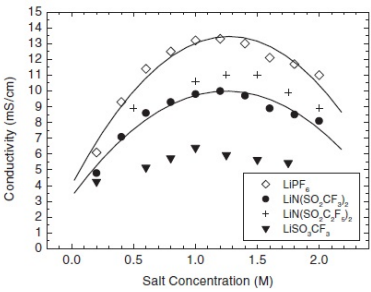
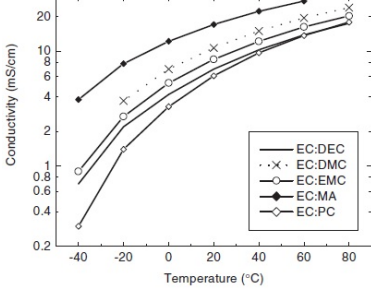


Figure 2.5: Intercalation in cobalt oxide cathode adapted from [24], [38]

optimal conduction [39]. The polar solvent molecules dissolve the lithium salt and form complexes with the positive- and negative ions [40]. The conduction properties in liquid electrolytes are based on (i) diffusion, transport through concentration gradients, and (ii) migration, transport through an electrical field. Important transport factors are the molar ionic conductivity, which represents the mobility of the ions and is influenced by the salt concentration and the viscosity. Optimal transport is a balance of salt ratio, dissolved in electrolyte, and the viscosity. More salt means more charges and increased conductivity. However, high salt ratios also increase the viscosity, which hinders the transport of ions. Best results are archived with equal solution- and salt-quantities [41] (Tab. 2.1). With low temperatures the viscosity rises and the conductivity decreases, increasing the internal resistance. High temperatures (60 - 85 °C) enhance the conductivity, but also encourage decomposition reactions [42]. The behaviour of the electrolyte is another reason for the relatively narrow operational temperature window of classic Li-ion cells.

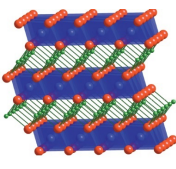
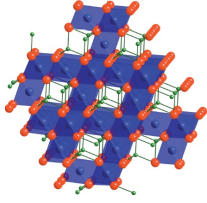
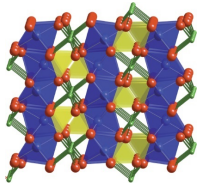
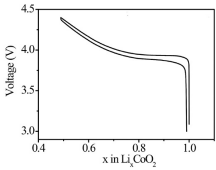
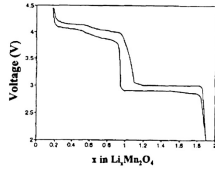
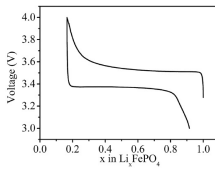
Table 2.1: Conductivity electrolyte [43]

Solution property	Salt concentration ↑	Temperature ↓
		
Conductivity	↑	↓
Viscosity	↑	↑

2.1.5 State of development for classic Li-ion batteries

For high energy automotive applications capacity, cycle life, operational temperature range, materials availability and safety are essential. Today’s leading Li-ion batteries in automotive applications are evolved from the lithium cobalt oxide chemistry, introduced by Sony in the beginning 1990’s. Due to optimisations in cell chemistry, materials and cell design, the capacity doubled during the last decades [44]. Despite their safety issues and the relatively expensive cathode, lithium cobalt oxide cells are the most common cells in consumer electronics due to high capacity and cycle life. However, current developments tend to replace the cobalt oxide cathode with lithium manganese oxide cathodes due to their low production costs or iron phosphates which are also more tolerant against abuse. Table 2.2 summarises different properties of cell chemistries currently used as traction batteries for automotive applications.

Table 2.2: Lithium-ion battery chemistries and properties

	LiCoO ₂	LiMn ₂ O ₄	LiFePO ₄
Image [45]			
Cathode V [45]			
Volt range	4.2 V - 2.5 V [46]	4.2 V - 2.5 V [15]	3.4 V - 2 V [47]
Structure	hexagonal [45]	spinel [45]	olivine [45]
Producer	Panasonic [46]	CPI (LG) [15]	A123 [47]
Sp. power	1200 W kg ⁻¹ [48]	2000 W kg ⁻¹ [48]	3000 W kg ⁻¹ [48]
Sp. energy	175 Wh kg ⁻¹ [48]	80 Wh kg ⁻¹ [48]	108 Wh kg ⁻¹ [48]
E. density	500 Wh l ⁻¹ [20]	-	145 Wh l ⁻¹ [48]
Cycle life	500 cycles [49]	500 cycles [49]	1000 cycles [49]
Charge time	2-4 h [49]	2-4 h [49]	2 h [49]
Self disch.	10% Month ⁻¹ [49]	10% Month ⁻¹ [49]	8% Month ⁻¹ [49]
Security	bad [49]	middle [49]	good [49]
Vehicles	Tesla [50]	Nissan Leaf [15]	E-rockit [51]

Future developments in this field are focused on improving the specific energy and safety. Table 2.3 summarizes the main activities. Despite the continuous improvements of the Li-ion battery technology over the last years, there is a considerable agreement in

Table 2.3: Developments Li-ion chemistry based on [22]

Research area	Advantage	Challenge
$Li - Si$ or $Li - Sn$ -anodes	4000 mAh g ⁻¹ or 990 mAh g ⁻¹	poor cycle life
$Li_4Ti_5O_{12}$ -anodes	no SEI, temp. and cycling stable	low energy density
$LiNi_{0.5}Mn_{1.5}O_4$ -cathode	high, constant voltage (4.5V)	no suitable electrolyte
nano-structure electrodes	power due small diffusion length	increased reactivity
additives for SEI	less degradation, high stability	find material
shut down separators	prevent thermal runaway	find material

the literature that, with the classic cell chemistry, there is no major improvident in energy density to be expected [20]. A step forward for automotive applications is seen generally by the replacement of all battery parts with more efficient and safer components, which are represented by the lithium-air, the lithium-sulfur chemistry or solid state batteries [22].

2.2 Li-S batteries

The most important improvements of lithium-sulfur batteries are seen in the capacity, safety, material availability and temperature range. The chemical reactions are based on a conversion reaction of sulphur instead of intercalation. Sulfur reversibly reacts with lithium ions when reduced from the elemental state S₈ (Fig. 2.6) to lithium sulfide Li₂S, which is the reason for the high theoretical capacity of this reaction (1672 mAh g⁻¹) [52], giving a realistic target for the practical capacity about 550 mAh g⁻¹ on cell level [53]. The basic components of the battery are a metallic lithium anode, an organic electrolyte,

a porous separator and a sulfur composite cathode. During the discharge, the metallic lithium is oxidized and its ions move through the electrolyte to the cathode, where the elemental sulfur is reduced to lithium sulfide. This reaction offers a very high theoretical capacity and very low costs for the cathode materials [54]. However, its use is hindered by the complex properties of the different intermediate species when reducing elemental sulfur S_8 to the discharge product Li_2S which is further explained in the following sections.

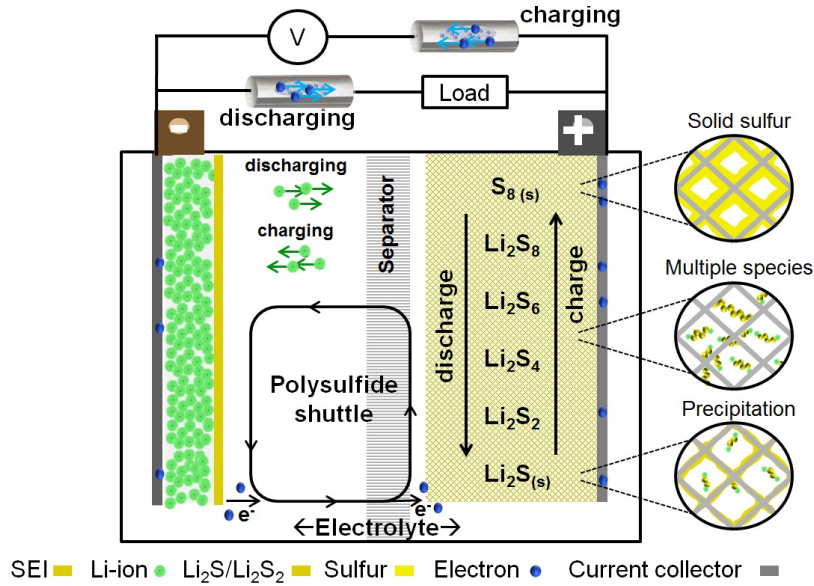


Figure 2.6: Main mechanisms playing a role in Li-S batteries

However, it must be mentioned that a complete understanding of the charge/discharge mechanism is hindered by the difficulty of detecting present species during cycling. The current efforts in the community does not always agree on the subset of detected species. Furthermore, most experiments are done on non-representative cells, such as purpose-built or coin cells, and it has been shown they behave very different from a cell built to be commercially viable (low electrolyte to sulfur ratio, high sulfur to cathode ratio). Therefore, the results presented here are mainly used to introduce the reader into the

complexities of Li-S batteries during cycling and do not always represent what is commonly agreed in this field. For more information the review of Wild et al. [55] is very useful.

2.2.1 Cathode

Although solid elemental sulfur is used as electrode material, it can be classified as a liquid cathode, since only when dissolved sulfur is able to take part in the electrochemical reactions. Compared to a solid intercalation electrode, the chemical behaviour of the dissolved reaction products during the reduction of elemental sulfur (S_8) to (Li_2S) is significantly more complex. During cycling, the sulfur rings are reduced to polysulfides of different lengths and properties. While longer polysulfide chains (LiS_8 , LiS_6) or high order polysulfides are highly soluble and reactive [56], smaller chains or low order polysulfides (Li_2S_2 , Li_2S) become insoluble, insulating and tend to precipitate. These properties, plus the fact that the active species are dissolved in solution, are the main reasons for the low sulfur utilization, poor cycle life and the relatively high self-discharge of lithium-sulfur batteries [53].

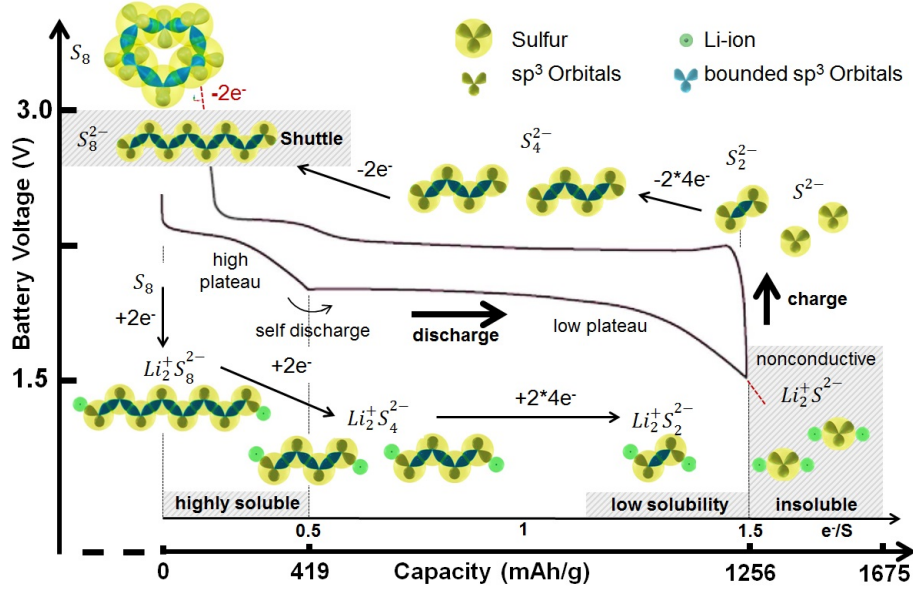
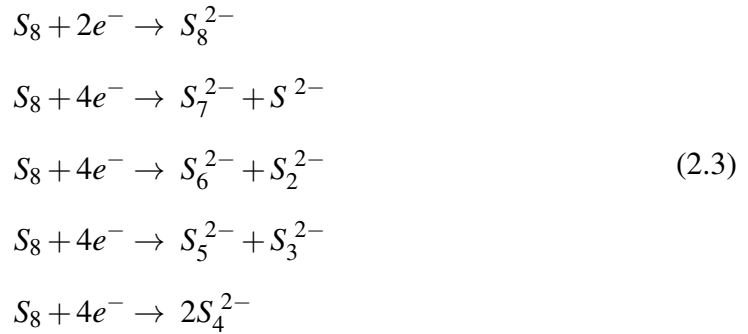


Figure 2.7: Simplified cycling of a typical lithium-sulfur cell

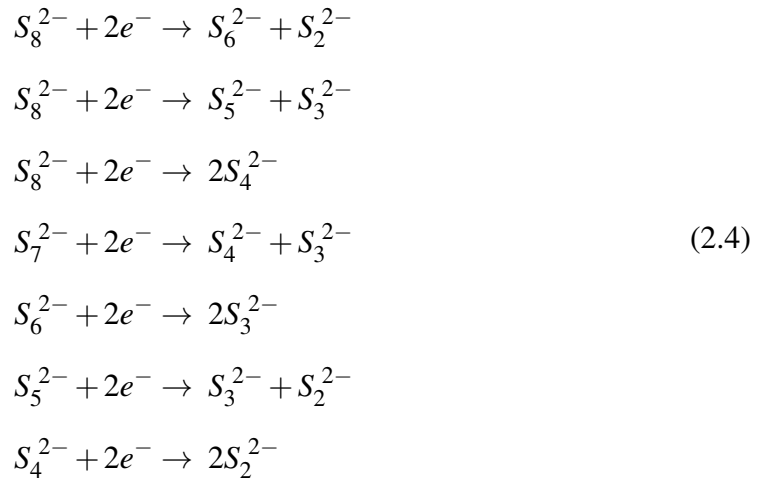
The typical discharge curve, shown in Fig. 2.7, contains two main voltage plateaus. As shown on the right, elemental sulfur dissolves in contribution with lithium ions into liquid form $S_{8(l)}$ [57] and is able to accept electrons. When the lithium migrates through the electrolyte to the cathode, high order lithium polysulfides (Li_2S_8 - Li_2S_6) are formed, which dominate the entire high plateau. However, the reaction path is complex and also a small fraction of low order polysulfides could be found experimentally [55]. As a first part of four suggested stages by Kawase et al. [58], the following species were detected:

Stage 1:



The simultaneous presence of multiple species and occurring precipitation leads to a discharge curve around 2.3 V, with a relatively constant gradient without many smaller plateaus for each of the reduction steps respectively [59]. Since the majority of reaction products are high order polysulfides, which are chemically more active than low order ones [60], the internal resistance of the cell is usually small and high rates can be drawn from the cells. However, the high solubility and mobility of these species also allow them to diffuse directly to the anode and form lower order polysulfides when in contact. The low order polysulfides however, diffuse back again to the cathode to form high order chains until the charging ends. This loop, called the shuttle effect, can lead to infinite recharge, degradation and poor charge efficiency. The transition range between both plateaus is influenced by the second stage of parallel reactions.

Stage 2:



In this area, it is assumed that the amount of dissolved polysulfides in electrolyte reaches a peak, which also causes a peak in the internal resistance due to increases in the electrolyte viscosity. Further discharge causes the majority of polysulfide chains to break further into smaller parts and theoretically the low plateau starts at about 491 mAh g⁻¹ discharged capacity [53]. However, in the practical experiments of Kawase et al. this point is already

reached around 250 mAh g⁻¹ [58] (Fig. 2.8). The main reaction in the low plateau is based on

Stage 3:



Here it is assumed that mostly Li_2S_3 is present and governs the behaviour of the cell in that region. Practically, that region has consistent kinetics and low variations of the internal resistance after the peak in between both plateaus has levelled out. This region is therefore seen as the most useful for practical applications due to its constant terminal voltage and its large contribution to the capacity [58]. Furthermore, the self-discharge is fundamentally reduced here and if the charging stops before the high plateau, the shuttle effect can be avoided. The practical discharge stops theoretically at about 1256 mAh g⁻¹ with the increasing formation of resistive low order polysulfides Li_2S and Li_2S_2 , which insulate and passive the cathode reactions.

Stage 4:



The end of discharge is marked by a dropping cell voltage [61] [62] towards the end of discharge due to rapidly increasing internal resistance of the cell. If discharge further continues, a layer of metallic lithium on the cathode can be formed, which can lead to an unstable electrode [63].

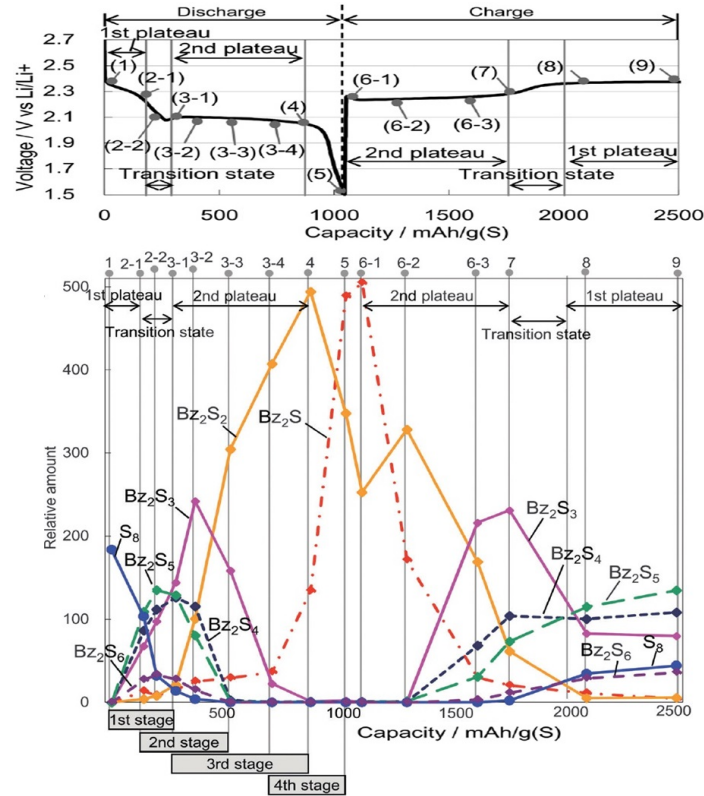


Figure 2.8: Species in electrolyte during discharge/charge [58]

As shown in Fig. 2.8, while charging the reaction reverses until the oxidation process of the polysulfides reaches high order chains. At about 2.35 V, depending on the electrolyte [64], not all of the higher order polysulfides transform back into elemental sulfur. A proportion of them diffuse to the anode where they form lower order chains and shuttle in between both electrodes. While this is generally not desirable, this effect can act as an overcharge protection [52]. The diffusion is dependent on (i) solubility of polysulfides, (ii) the transport properties of the electrolyte, and (iii) dissolution rates and also continues when the battery is resting. While it is agreed that without the charging energy the shuttle effect leads to self-discharge, the exact precesses during charge/discharge and whether it is the same as self-discharge during rest are unclear yet.

2.2.2 Anode

In contrast to classic Li-ion batteries, it is safer to use pure lithium anodes for lithium-sulfur batteries. Here, sulfur especially appeals as a cathode material since some of the reaction species protects the highly reactive lithium, which exceeds the specific capacity of the previously introduced graphite anode with 3860 mAh g^{-1} [65, 66] by a factor of ten. Each lithium can provide one electron so two ions are needed to break the polysulfide chains into smaller pieces (Eq. 2.7).



These insulating and sparingly soluble films are improving the cycling behaviour, leading to less dendrite growth and lower self discharge [67]. Therefore, like classic Li-ion batteries, the properties of the SEI are fundamental for the anode's performance. However, its thickness, morphology, composition and compactness are not only dependent on material properties of salts and electrolytes, but also through the interplay of decomposition- and dissolution-rate while cycling (Fig. 2.9) [63]. Unfortunately, the film cannot eliminate all reactions with the electrolyte, leading to capacity fading mechanisms. For example ROLi and HCO_2Li is produced with 1,3-dioxolane (DOL) and dimethoxy ethane (DME) solvents leading to solvent consumption and the production of oxygen, which is a source of irreversible Li_xSO_y formation [64]. Another reason for loss of active material is the increased dendrite formation rate of metallic lithium with the surface film. Even small amounts of particles on the electrode cause increased dendrite formation, which roughens the surface, increases the anodes contact area and produces more passivation film [59]. However, the passivation also hinders the dendrites to produce inner short circuits like in classic Li-ion cells, which also makes it a safety feature of the cell.

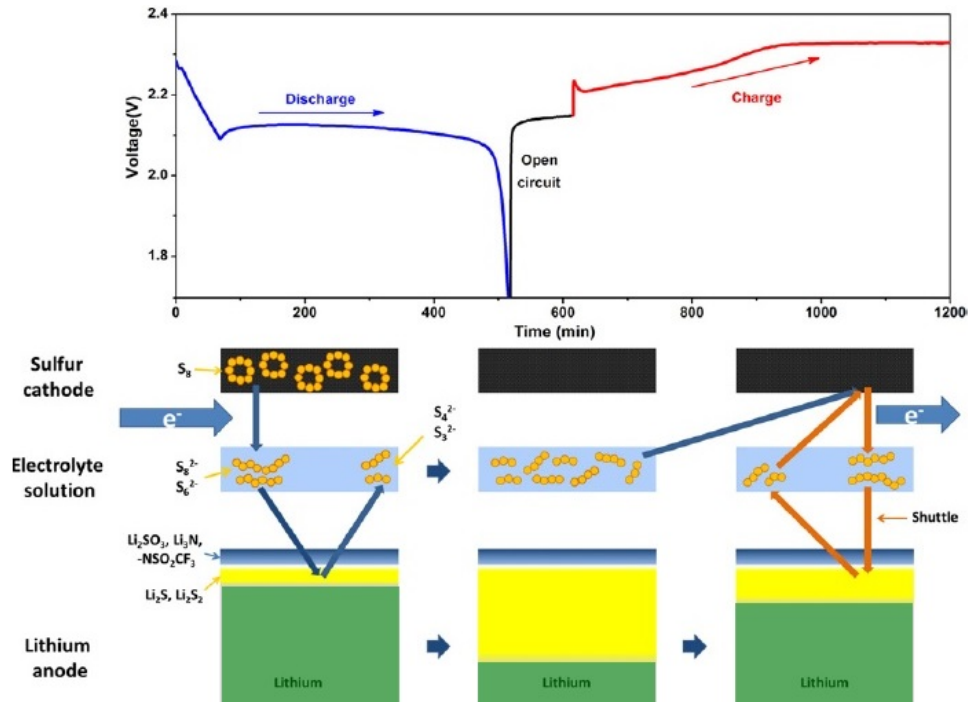


Figure 2.9: Surface layers lithium anode [68]

2.2.3 Electrolyte

The Li-S batteries electrolyte is usually a mixture of tetrahydrofuran (THF), 1,3-dioxolane (DOL), dimethoxy ethane (DME) and tetra(ethylene glycol) dimethyl ether (TEGDME) [69], combined to provide optimal sulfur utilization, rate capability, temperature range and cycle life. Commonly used salts are LiTFSI, LiClO₄, LiNO₃ [64], and their concentration governs the ionic conductivity and viscosity in a similar pattern as in classic Li-ion batteries. However, there is an increased influence of concentration gradients of active species, since the cathode is dissolved. The amount of solved polysulfides changes during cycling, changing the electrolytes viscosity and thus its conductivity. This leads to a unique discharge behaviour. Next to polarisation losses, the capacity provided by the Li-S cell is highly governed by the utilisation of sulfur, which is mainly dependent on the ratio of sulfur/composite material and discharge rate. Usually, higher amounts of carbon

as conductor improve the utilization due to improved conductivity and surface area of the electrode. Fig. 2.10 (frame) shows the specific capacity of a cell manufactured by Sion Power with 47% carbon content together with different other cell chemistries [53]. It can be seen that the overall capacity decreases with higher rates non-linearly. However, more interestingly are the differences between the plateaus. The high plateau, governed by the soluble long chain polysulfides, has a higher reaction rate and therefore a better rate capability. However, it also enhances the shuttle phenomenon resulting in self discharge. Therefore, at very low currents, the shuttle has enough time to reduce the usable discharge capacity of the cell in the high plateau [61]. The low plateau, governed the formation of insulating Li_2S_2 and Li_2S and the viscosity of the electrolyte, is more stable leading to a lower rate capability and self discharge. Here, high currents cause an increased amount of polysulfides, which also increases the viscosity of the electrolyte. This slows diffusion and causes concentration gradients inside the cathode, which can produce solid discharge products in the outer layer of the cathode [69]. This inhomogeneous distribution leads to low discharge efficiencies at higher rates in the low plateau [59]. In other words, the Li_2S precipitation at high currents can hinder the utilisation of the underlying sulfur. The differences (self discharge, utilisation) between the plateaus cause variations in the usable capacity for different rates, as shown Fig. 2.10 with an OXIS Energy cell. The ratio between them rises for this particular cell from about 1.75 (low plateau/high plateau) at 1.5 C to 2.9 (low plateau/high plateau) at 0.2 C.

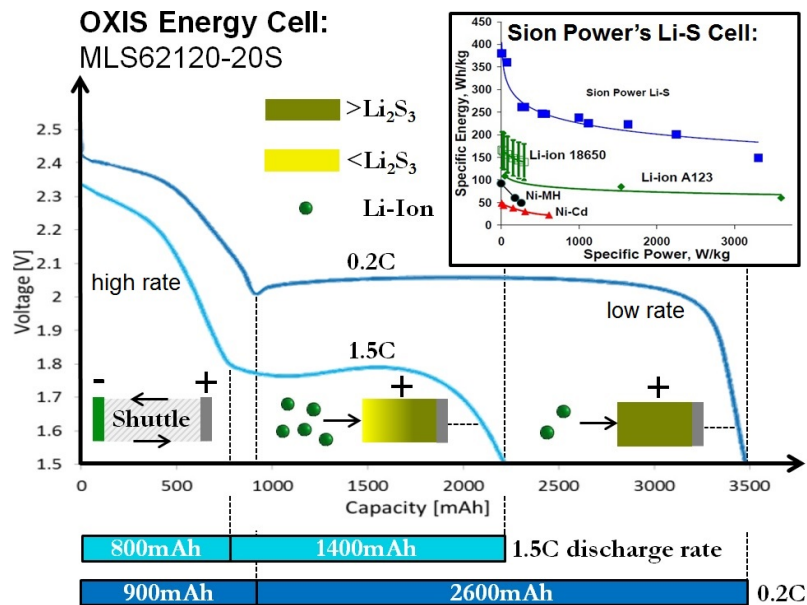


Figure 2.10: Discharge behaviour of Li-S cell with different current rates adapted from [70], [53]

2.2.4 State of development for Li-S batteries

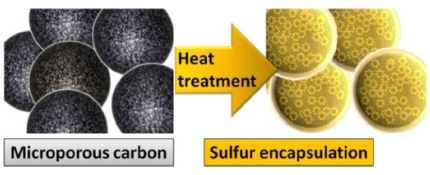
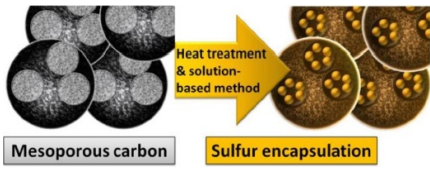
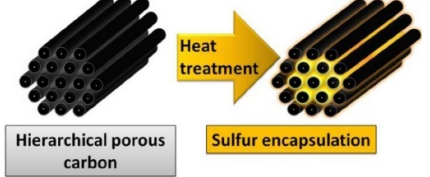
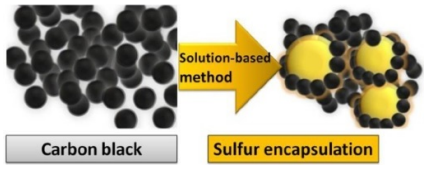
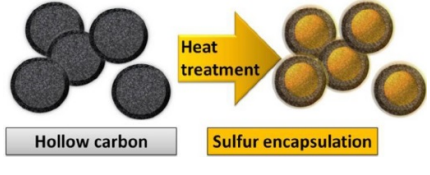
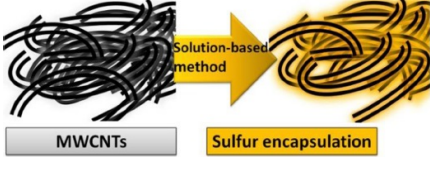
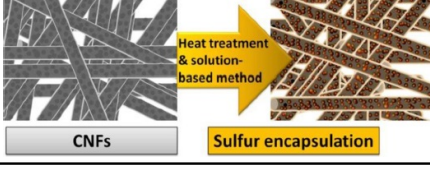
Generally, Li-S batteries are still in their early stage of development with the main focus of improving the capacity, lifetime and rate capability of the cells. Thereby mostly the shuttle has to be reduced or eliminated, the utilisation of sulfur has to be improved and the surface passivation and dendrite formation at the anode have to be addressed. Shuttle preventions can be realized through protective layers on the anode, through cell layout or in the cathode itself. Common approaches cover all involved components of the battery [52], but mainly apply composites to the cathode to enhance the conductivity and also limit the diffusion. Here the difficulty is to find the right material and also the right ratio since a low ratio of active sulfur is not favourable due to the decreasing gravimetric energy density [71]. As a composite material, carbon has an outstanding role due to its various morphologies and high conductivity. To give an overview about the variety of

different forms of containing sulfur, Table 2.4 gives examples with their advantages and disadvantages summarized form [52].

2.2.5 Available Li-S cells

The aims to improve Li-S cells, closer to working cells, use layered graphite as cathode. Similar to conventional lithium batteries, graphite maintains its layered structure when sulfur moves in between and can therefore act as an efficient micro current collector, which also prevents the dissolution [72]. The results suggest a high initial discharge capacity of 1588 mAh g^{-1} when discharged with 25 mA g^{-1} . Most problematic for this approach is the increasing capacity fade with high rates, which is a specific effect of the sulfur-graphite composite. Another approach, introduced by Wang et al. [54], proposed the idea to retard the diffusion of polysulfides in bounding sulfur to polymer matrices. These large molecules not only accommodate the sulfur, but also act as a conductor. The resulting low self discharge, cycling stability, improved rate performance and relatively simple production are promising properties for Li-S cells. However, the vast majority of these approaches are still in laboratory or experimental state. Here, OXIS Energy offers one of the first commercially available Li-S batteries, based on polymer composites. Today's available cells can handle a wide variety of conditions including temperatures, rates and lifetime (Fig. 2.11). However, the provided rate capability and cycle life is not adequate enough to reach automotive demands yet, which is a target for development at OXIS Energy [73].

Table 2.4: Carbon materials for Li-S batteries adapted from [52]

Principle visualisation	Materials and properties
 <p>Microporous carbon</p> <p>Heat treatment</p> <p>Sulfur encapsulation</p>	<p><i>Microporous Carbon:</i></p> <ul style="list-style-type: none"> - constrain sulfur by absorption - no soluble polysulfides, no high plateau - 650 mAh g⁻¹ after 500 cycles
 <p>Mesoporous carbon</p> <p>Heat treatment & solution-based method</p> <p>Sulfur encapsulation</p>	<p><i>Mesoporous Carbon:</i></p> <ul style="list-style-type: none"> - wider pores with higher sulfur loading - best electrical contact with partial loading - initial: 1390 mAh g⁻¹, 840 mAh g⁻¹ after 100 cycles
 <p>Hierarchical porous carbon</p> <p>Heat treatment</p> <p>Sulfur encapsulation</p>	<p><i>Engineered Hierarchical Porous Carbon:</i></p> <ul style="list-style-type: none"> - high S utilisation due to complete redox reaction - MPC's electronic conductor + sulfur stockroom - immobilizing suppress loss of active material
 <p>Carbon black</p> <p>Solution-based method</p> <p>Sulfur encapsulation</p>	<p><i>Carbon Black:</i></p> <ul style="list-style-type: none"> - low cost additive for high electrical conductivity - increased contact area between carbon and sulfur - 777 mAh g⁻¹ after 50 cycles
 <p>Hollow carbon</p> <p>Heat treatment</p> <p>Sulfur encapsulation</p>	<p><i>Hollow Carbon Spheres:</i></p> <ul style="list-style-type: none"> - large interior void space with mesoporous shell - excellent cycling performance - 91% after 100 cycles
 <p>MWCNTs</p> <p>Solution-based method</p> <p>Sulfur encapsulation</p>	<p><i>Carbon Nanotubes:</i></p> <ul style="list-style-type: none"> - interwoven conductive network - high surface area for absorbing polysulfides
 <p>CNFs</p> <p>Heat treatment & solution-based method</p> <p>Sulfur encapsulation</p>	<p><i>Carbon Nanofibers :</i></p> <ul style="list-style-type: none"> - nano-tubes without hollow space in between - high conductivity and structural strength - initial: 1560 mAh g⁻¹, 730 mAh g⁻¹ after 150 cycles

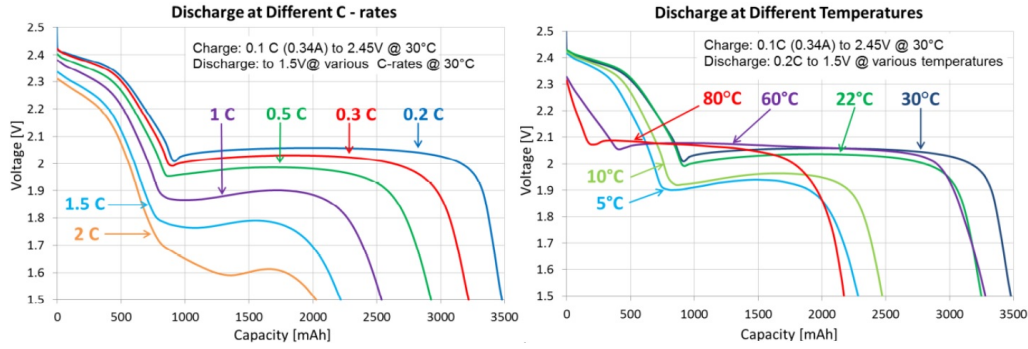





Figure 2.11: OXIS energy cell voltage over capacity and temperature [70]

As mentioned before, the cell development in the REVB project is not exclusively focused on improving the cell properties, but also to create a framework for practical applications. The tested cells need to be characterised and evaluated for compatible SoC estimation. Table 2.5 summarises the cells properties and adds data from a competitor cell (Sion Power) and the future goals for the OXIS cell for comparison.

2.3 Discussion

Li-S batteries behave differently to the standard Li-ion cell in many aspects. From an application oriented point of view (i) the usable capacity, (ii) the rate capability, and (iii) the cycle life are most important. All of them are influenced by internal parameters (SoC, SoH, battery design) and external factors (temperature, current rate, short-term history, long-term history) [76]. The influences of the most important parameters are summarized in Table 2.6 - 2.8, where a single line arrow corresponds to weak dependency and a double line arrow to strong dependency.

Table 2.5: Available lithium-sulfur cells and future developments

	Sion cell	OXIS cell (tested)	OXIS future cell
Image			
Volt range	2.5 V - 1.7 V	2.45 V - 1.5 V	2.45 V - 1.5 V
Nominal volt.	2.15 V	2.05 V	2.05 V
Capacity	2.5 Ah	3.4 Ah	95.2 Ah
Dimensions	55x37x11.5 mm	145x78x5.6 mm	220x110x17.4 mm
Weight	16 g	50.7 g	473 g
Producer	Sion Power	OXIS Energy	OXIS Energy
Sp. power	168* W kg ⁻¹	27.5* W kg ⁻¹	520 W kg ⁻¹
Sp. energy	350 Wh kg ⁻¹	137.5* Wh kg ⁻¹	400 Wh kg ⁻¹
E. density	320 Wh l ⁻¹	110.6* Wh l ⁻¹	450 Wh l ⁻¹
Cycle life	-	>95 cycles	615 cycles
Operating T.	-20 °C to 45 °C	5 °C to 80 °C	-10 °C to +55 °C
Source	[74]	[70]	[75]

* calculated with the nominal capacity, the nominal discharge current for the Sion cell (1.25 A), the recommended discharge current (680 mA) of the OXIS cell and both nominal voltages (2.15 V/2.05 V)

2.3.1 Discharge capacity

In the classical lithium ion chemistry the amount of storable charges depends on the free vacancies in the intercalation compound. Ideally, the amount of them does not change quickly so the capacity fade is slow. Variations are mostly caused by external parameters such as low temperatures, lowering the diffusivity and therefore increasing the internal resistance. Overall however, the capacity changes for different user cases are generally small. Another property of intercalation based batteries is the low self discharge, which means the the SoC does not change significantly if the battery is not in use.

In lithium-sulfur batteries, the capacity is mainly dependent on the utilisation of the sulfur. Due to the complex reaction path, concentration gradients of active species in electrolyte and precipitation the usable capacity varies more. While low temperatures also cause lower diffusion and increased internal resistances, the same effect hinders shuttling and therefore leads to a slightly reduced self discharge in the high plateau. Furthermore there is a sensitivity on the discharge current and its profile. Table 2.6 summarises the main effects, where H stands for usage history.

Table 2.6: Comparison of effects on usable capacity

Lithium-sulfur	-	Parameter	-	cl. Lithium-ion
resistance electrol./ electrodes	⇐	Temp.	⇒	resistance electrol./ electrodes
polysulfide availability	⇐	Current		vacancy sites electrode
Li ₂ S formation in cathode	⇐	Short H.		
active material lost	←	Long H.	→	passivation, decomposition

2.3.2 Rate capability

In classical Li-ion batteries, rates are dependent on the diffusion speed into the electrodes, on their surface reactions and transport properties of the electrolyte. Therefore, they are more dependent on cell design parameters (high energy or high power Li-ion batteries) than cycling parameters.

With lithium-sulfur batteries however, the rate capability depends on availability and reactivity of the dissolved polysulfides, which means that the dynamic cell behaviour is more dependent on concentration gradients. Generally, the rate capability changes in a more complex manner, with a peak of internal resistance in between both plateaus. Here, the concentrated electrolyte with its viscosity hinders high rates. This can cause the cell voltage to drop under the limit before the cell entered the low plateau, which means that the discharge stops prematurely. Towards the end of the low plateau, the rates are limited by increasing amounts of precipitate, reducing the active surface area of the cathode. Generally, it can be concluded that the ability of Li-S cells to deliver high currents changes more significantly, which must be accommodated by the management system of the cells. Table 2.7 summarises the main effects.

Table 2.7: Comparison of effects on rate capability

Lithium-sulfur	-	Parameter	-	cl. Lithium-ion
transport properties el.	⇐	Temp.	⇒	transport properties el., intercal.
polysulfide availability	⇐	Current	→	intercalation distance
Li ₂ S formation in cathode	⇐	Short H.		
active material lost	←	Long H.	→	passivation, decomposition

2.3.3 Capacity fade

Capacity fade over the lifetime of a battery manifests in degrading of the usable capacity and rate capability. The cyclability of classical Li-ion batteries depends mainly on the stability of the host material and the SEI. These batteries need to be protected from overcharge (lithium plating, defects in cathode), high temperatures (SEI-degradation) and high charging currents with low temperatures (lithium plating). However, as long as they are used within safe margins, Li-ion cells degrade only marginally from cycle to cycle.

The processes for Li-S cells are less well understood. Irreversible degradation is assigned to the shuttle effect in the high plateau, which occurs with every full charge. The degradation happens therefore mostly while cycling. Towards depletion, active material is lost due to the reversible precipitation/dissolution of sulfur, when Li_2S_2 and Li_2S form on electrical inactive areas where they cannot oxidise again. Furthermore, high rates can increase the dendrite formation at the anode, which can effect the surface layer and the decomposition of electrolyte. Table 2.8 summarises the main effects.

Table 2.8: Comparison of effects on capacity fade

Lithium-sulfur	-	Parameter	-	cl. Lithium-ion
viscosity el. -shuttle	←	Temperature	⇒	high temp. -ageing of SEI
dendrites anode	←	Current	→	high currents rates
		Short H.		
shuttling, cycling	←	Long H.	→	overcharge, temperature

2.4 Conclusion

From the discussion in this chapter it is shown that the lithium-sulfur chemistry has promising properties for automotive applications. Despite difficulties, intense research led to available cells that can archive $160 - 350 \text{ Wh kg}^{-1}$ on cell level [55], which is a significant increase compared to Li-ion technology. It is therefore wise to initiate thoughts towards the application of Li-S cells. However, due to their entirely different reaction principle and cycling properties, Li-S batteries need a specifically designed battery management system. For each of the important cycling parameters, new methods have to be developed to ensure optimal usage and lifetime of the cells. Despite the different cell reactions and varying complexities, there are similarities. Both cell types react negatively to exceeding the recommended voltage range, which is one major reason for the need of a precise SoC estimation for the dynamic currents in electric vehicles. However, while for Li-ion batteries overcharge can lead to lithium plating and in the worst case a thermal runaway, for Li-S it is more related to degradation. Nevertheless, overcharge with Li-S cells can also lead to self heating effects, which can be critical. Overdischarge however, causes degradation with Li-ion batteries and can cause an unstable electrode cathode with Li-S cell. The clear boundaries are one reason for the urge of precise state estimation for the classical batteries. And despite these boundaries are less well understood for Li-S batteries, it can be concluded:

- **For safety and reliability considerations, control mechanisms of both presented battery types have to have the same quality in determining the end of charge/discharge and therefore the SoC.** Common estimation accuracies of Li-ion batteries in electric vehicles vary from 6% to less than one 1% [77], which is therefore also desirable for this thesis.
- **The estimation task for the more complex and less understood Li-S cells is**

more difficult. In this topic it is an open question how much of the existing techniques, established for a wide range of used battery types, can be used or adapted for Li-S cells.

- **The estimation will focus on the discharge process,** since the charging reaction differs and is generally less understood than the discharge process on a fundamental level [55]. Furthermore, the manufacturer of the tested cells recommends constant current charging with low rates.

3

Battery state of charge estimation

Naturally for all kinds of storage systems, the information of capacity and how much of the storage is still available is vital. For cars with combustion engine with classic tanks this is relatively easy since the amount of petrol in the tank is measurable at any given moment and the capacity of the tank itself is constant. For electrochemical storages however, the relations are more complex. Firstly, for modern batteries there is no possibility to directly measure the remaining energy during the usage and secondly, as introduced in the previous section, the capacity of batteries depends on many parameters. To solve these difficulties, an intense research field with a general goal to predict the performance of different battery types has grown [77]. However, the field of SoC estimation is novel for Li-S batteries and it is unclear yet how to get optimal performance without the risk of sacrificing safety, lifetime or reliability. The SoC estimation is one fundamental part of this, since less uncertainty in the SoC estimation also means less conservatism in operation (Fig. 3.1). In other words, the user can operate the battery closer to its limits when the states of the cell are known. In the following, the definitions of cell capacity and SoC are introduced.

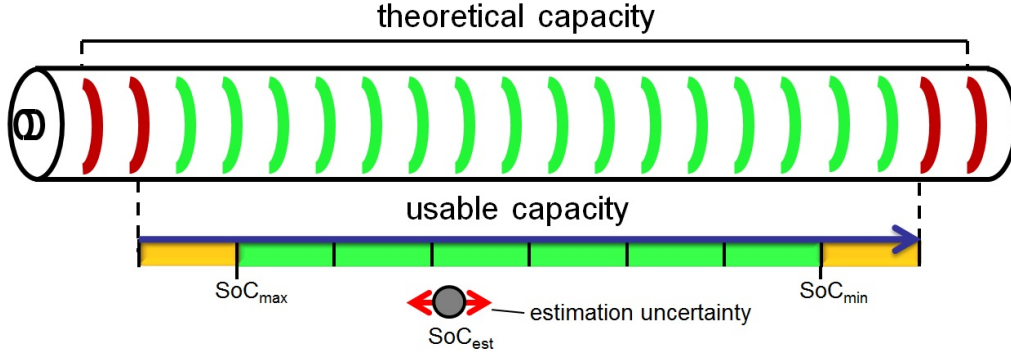


Figure 3.1: SoC definitions of a battery

3.1 Cell capacity

The maximum and minimum operation voltage for the OXIS Energy cells are 2.45 V and 1.5 V respectively [70]. For any application the current that can be drawn within this window for safe operation is a key factor. The definition for the cell capacity is therefore simply

$$Q_n = \int_{t_v}^{t_v} Id(t), \quad (3.1)$$

where t_v stands for the maximum and minimum cell voltage at the beginning and end of the discharge test. To account for the variations of the cell performance with respect to temperature, current and age, common techniques use a slow discharge of 10 hours (C/10) [78], controlled environments and only fresh cells for the experimental tests. Therefore, it is a common practice to name the capacity under these conditions nominal or rated capacity, here called Q_n . Experimental tests for Li-S batteries follow the same pattern in the data sheet for the tested cell (see Appendix A). However, due to significant capacity changes with the OXIS cells (Fig. 3.2), based on the applied current, in this thesis a mixed pulse current experiment, explained in Chapter 5, is used to define a more practical capacity value. Furthermore tests with various realistic drive cycle currents in section 6 and 7 are performed to give a realistic view of the cells in operation.

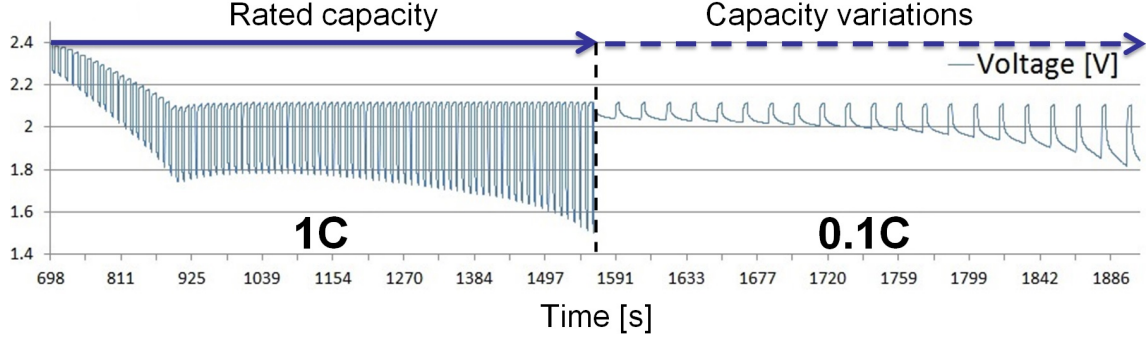


Figure 3.2: Pulse discharge test of Li-S battery with two different currents

3.2 State of charge

The SoC of a cell is defined as a fraction of the nominal capacity, which is still available for the discharge process. While 1 (100%) indicates a fully charged battery, 0 (0%) represents a fully discharged one. The mathematical definition is

$$SoC = \frac{Q_t}{Q_n}, \quad (3.2)$$

where Q_t is the remaining capacity of the cell. While for common Li-ion batteries the full SoC is defined when the charging current does not change within 2 hours at a constant voltage and temperature charge (DIN 43539), the process for Li-S batteries varies due to the shuttle effect. As defined by OXIS Energy, the cell is fully charged when it reaches 2.45 V with a constant current charge of C/10 Amperes. The introduced standard definitions for cell capacity and SoC work well in practice and efficient methods have been developed to handle variations. Nevertheless, the complex reactions affect and weaken even the very basic definitions, which makes a precise SoC estimation, based on amount of chemical reactants, difficult to obtain. Therefore the SoC is estimated mainly on practical thoughts as explained in the next sections. Thereby only the principles of commonly used methods are introduced. For more details the reader is guided to [79, 80] for general

SoC estimation and to Chapter 6 for their applicability to the Li-S chemistry.

3.3 Coulomb counting

As a simple and reliable method, Coulomb counting is used for most of the practical tests, defining the capacity as described before. Its main idea is to integrate the current measurement over time to calculate the amount of energy flowing in or out of the battery (see Fig. 3.3 for simplified visualization). The mathematical description is given in [79] as

$$SoC = SoC_0 + \frac{1}{Q_n} \int_{t_0}^t (I_{batt} - I_{loss}) dt, \quad (3.3)$$

where I_{batt} the measured current and I_{loss} a lost factor for the charge and discharge efficiency. While this method is generally precise, the integration leads to difficulties when the battery is not tested in a laboratory environment. Most problematic is the adding up of small measurement errors to significant values over time. For laboratory tests, using full cycles, a controlled environment and high precision current sensors this error is usually small. However, in real applications without full cycles, less accurate sensors and sensor noise, the drift can lead to strong estimation errors. Furthermore this method by definition needs a precisely known starting point SoC_0 . The accuracy of Coulomb counting increases if points for recalibration can be identified, for example regular complete recharges [81], which is why it is used widely in consumer electronics and is applicable to all battery systems [79].

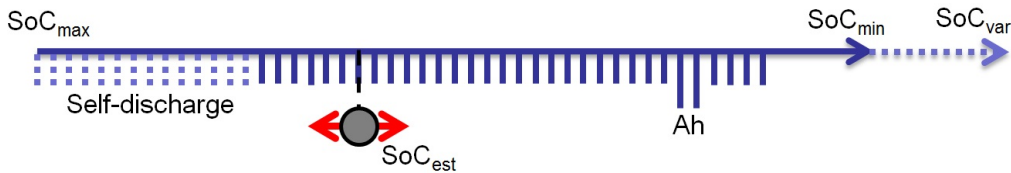


Figure 3.3: Principle of Coulomb counting

3.4 Open circuit voltage

The open circuit voltage method uses the relation between equilibrium potential of both cell electrodes and the SoC and is a relatively simple method that does not require long measurements or precisely known initial conditions. For Li-S batteries, as well as for most other cell chemistries, the open circuit voltage is higher for the charged than the discharge state. This leads to a non-linear relationship of OCV and SoC [81]. Therefore, a functional fit or lookup table can be used, which is in a simple case

$$V_{OC}(t) = f_1 SoC(t) + f_0. \quad (3.4)$$

The limitation of this method is the time needed for reaching equilibrium, which varies in between the used materials and chemical reactions. For the $LiFePO_4$ chemistry for example duration to the OCV can be up to 3 hours and can be influenced by hysteresis effects [82], which makes this method only accurate in applications with long breaks or small and constant currents [79]. The requirements for the voltage measurement depends on the slope of the OCV curve. The steeper the OCV curve over SoC, the smaller the effect of sensor noise. The flat OCV curve of Li-S batteries in the low plateau makes this method particular unattractive for this chemistry (Fig. 3.4), which is examined on more detail in Chapter 6.

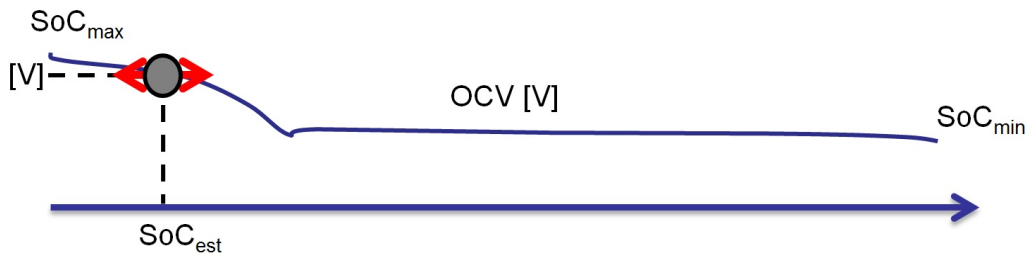


Figure 3.4: Principle of open circuit method

3.5 Impedance spectroscopy

The main thought of using the cell impedance is to quantify the variations in cell behaviour over the discharge range and assign it to the SoC. While in [83] is given a full overview of the technique, here only the basic principles are mentioned. The principle to manifest the cell properties are inspired by thoughts from control engineering, where a systems output to a sinusoidal input contains a lot of information about the system itself (Fig. 3.5).

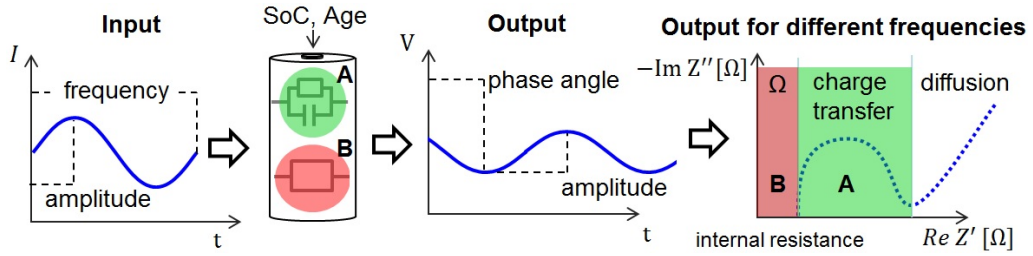


Figure 3.5: Principle of impedance spectroscopy

Here the difference in amplitude and phase angle between the input and output over different frequencies are of interest, summarized as complex number characterized either by its real and imaginary parts [83]

$$Z(f) = \frac{V_{\max i}}{I_{\max}} e^{j\phi}. \quad (3.5)$$

The results of a number of tests are plotted in the Nyquist plane (For batteries the negative side of the imaginary part is usually flipped over to the positive side to create a capacitive behaviour.). It can quantify different effects of a electrochemical reaction so as resistances of the charge transfer or contact inter-phases, the capacitance of double layers or mass transport phenomena [76]. Therefore, it is usually used in the prototype stage of cells to investigate details of the cell reactions. Published studies for Li-S batteries

use this method to gain insight into the reaction path [84], the conductivity of the electrolyte [85], surface layers of the electrodes [86] and the degradation process [87]. For the SoC estimation however, it has not been used yet. The high hardware requirements, i.e. a frequency response analyser, and the high effort and time needed to measure multiple frequencies makes this method seldom implemented [79]. Nevertheless, the idea of interpreting the dynamic cell voltage response to current is picked up in the time domain to parametrize equivalent circuit models, explained in Sec. 3.7.

3.6 Soft computing

As a method that can combine multiple source of information, artificial neural networks (ANN) are used to determine the SoC due to their ability of nonlinear mapping, self-organisation and self-learning [80]. Their principle is based on many relative simple functions with one or more inputs to a single output, the neurons, which are able to reproduce complex input - output relationships when combined together. The parametrisation of the functions is possible with training data where weights and biases of the neurons are iteratively adjusted to minimise the error between predicted and observed outputs [88]. One major advantage of this process is that patterns and relationships between inputs and outputs of a system can be established, without a comprehensive understanding of the inner processes [89]. Therefore, this technique can be used for all types of batteries if enough training data can be supplied [79]. With other words, the 'black box' models of neural networks have no physical meaning to the individual neurons and their connections in between. This is the main reason why model based methods are favoured in this thesis. Despite it is not an explicitly mentioned goal of this study, the understanding of physical processes in Li-S cells in practical applications should also be enhanced. Furthermore, the experimental tests, needed for the training, were developed and gathered during the

project which made model based methods a better starting point.

3.7 Model based approaches

So far each of the basic methods for SoC estimation faces difficulties when applied independently. While the Coulomb counting is accurate for short periods, it needs initial conditions and drifts with time. In contrast, the OCV method can estimate the SoC without prior information, but is not applicable in a wide range of the discharge process for Li-S batteries. As a method to combine both advantages, the idea of an observer is introduced from control engineering. A mathematical model runs parallel to the real system, predicting the output i.e. the terminal voltage of the battery. By using the error between the prediction and the real measurements, the estimation of the hidden states of a system can be improved. Here also the fact that the reaction parameters like electrolyte conductivity or surface layer capacity change over the discharge range, also used with impedance spectroscopy, is exploited. However, the changes are identified in the time domain rather than tested for a range of frequencies. The simple example in Fig. 3.6 shows that the voltage prediction of the observer is above the measurements.

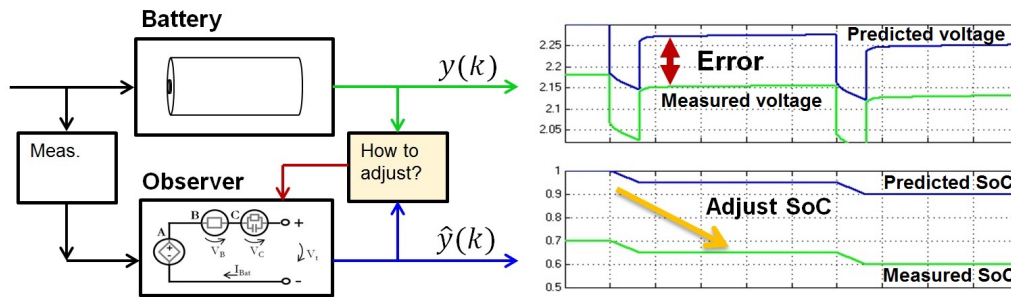


Figure 3.6: Principle of model based estimation

To correct this, now the SoC is shifted to fit the prediction to the observations. Generally, this method works best when the parameter variations over the SoC are more pro-

nounced, which would be for example a steep OCV curve. However, a battery model capable of reasonably accurately predicting the output voltage over the discharge range is usually sufficient. The range of available models reaches from the complex reproduction of the inner cell reactions to the simpler imitation of the voltage curve for current flow [90] and generally is a trade-off between accuracy and simplicity. The following sections introduce two main modelling ideas and summarises approaches for Li-S batteries.

3.7.1 Electrochemical models

The principle of electrochemical models is to reproduce the behaviour and performance of the battery by the inner cell reactions. While the cell potential in resting conditions can be described by the sum of the equilibrium potentials of the electrodes (standard potential), the behaviour with a load current is described by the amount and concentrations of active material for reduction and oxidation [91]. Thereby, the voltage drop is attributed to resistances in the cell components (IR -loss), over-potentials at the electrode-electrolyte inter-phase (activation-polarisation) and limitations of the ion transport in electrolyte (mostly concentration polarisation) [43]

$$E = E_0 - [(\eta_{ct})_a + (\eta_c)_a] - [(\eta_{ct})_c + (\eta_c)_c] - IR_i. \quad (3.6)$$

Where E_0 is the electromotive force or open circuit voltage of the battery, $(\eta_{ct})_a, (\eta_{ct})_c$ are the charge transfer overvoltages at anode/cathode, $(\eta_c)_a, (\eta_c)_c$ are the concentration polarisations at anode/cathode, I the operating current (Fig. 3.7). The internal resistance R_i is the sum of the electrolyte resistance, the resistance of the current collector, the active mass and the transitions resistance between the current collector and active mass [76]. Since the models are based on chemical reactions, they are seen as most accurate of the various modelling methods and due to their high depth, they are particularly useful to

enhance the understanding of the cell [92].

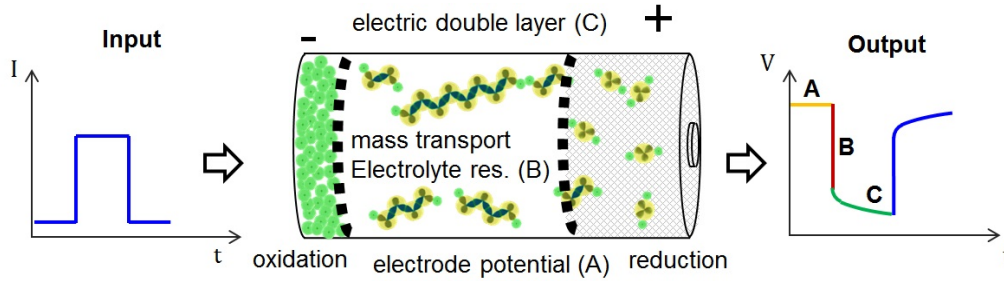


Figure 3.7: Principle of electrochemical modelling

The detail in which chemical reactions are described usually varies, depending on which aspect of a cell is modelled. For Li-S batteries, Mikhaylik et al. [61] initially reproduced the shuttle and self heating effect during charge with a zero dimensional model with a simple two step reduction of sulfur. While Moy et al. [93] added more intermediate sequential steps in the reduction chain, Kumaresan et al. developed a one-dimensional model including multi component transport phenomena in porous electrodes and separator and charge transfer kinetics [57]. While one-dimensional models are most promising to reproduce the features of Li-S cells, no model is currently able to reproduce all features and the research to explore new details is still ongoing [55]. The most important drawback of more precise models is that they require many physical and chemical parameters, which are usually difficult to obtain, and a large amount of computational power to run [94]. Therefore, for the SoC estimation reduced mechanistic models, focused on the runtime performance, are favourable. Here Marinescu et al. [95] presented a model that can predict the evolution of species for charge and discharge. Based on two dominant reaction steps the simulation of both plateaus, the dynamic response of the cell voltage to loads, power limitations and information on the amount of stored energy throughout operation is possible. Figure 3.8 shows the development of the species and cell voltage with the example of a constant discharge current of 1.7 A.

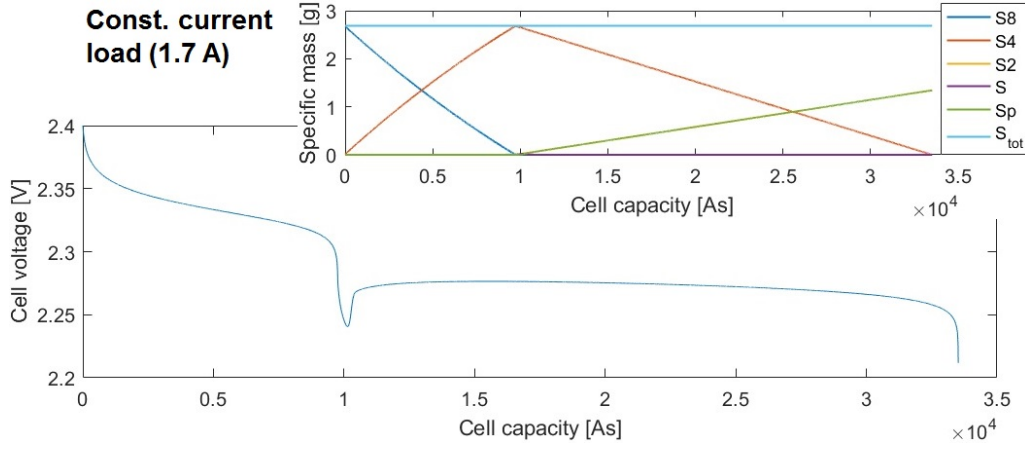


Figure 3.8: Terminal voltage predicted by mechanistic model

However, the following studies in this thesis are based on an even more simplified model approach, the equivalent circuit models.

3.7.2 Equivalent circuit model

Instead of reproducing the chemical reactions of the battery, equivalent circuit models only represent the input-output (input: current, output: terminal voltage) relationship of the cell with basic electrical components like resistors, capacitors and voltage sources. They are mostly used for SoC and SoH estimation, since they are computational inexpensive and relatively simple to parametrize with current pulses (shown in Figure 3.9). The idea behind this is that the systems answer to a step input contains similar information about the system in the time domain to the impedance spectroscopy delivers in the frequency domain.

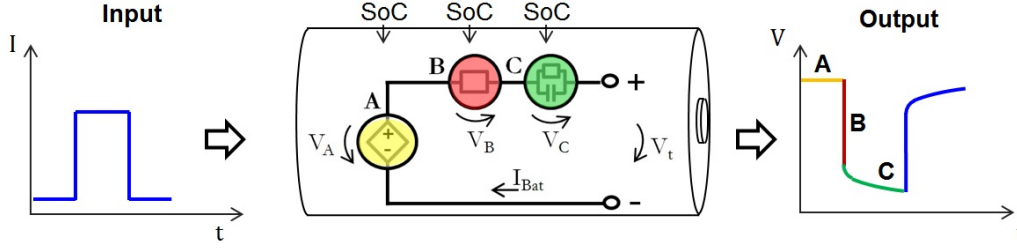


Figure 3.9: Input- output relationship of the ECN model

Therefore, the test procedure is significantly more simple. While the voltage before the pulse is seen as the OCV, the immediate response to current is assigned to be internal resistance. The slow voltage drop afterwards is defined by the double layer capacitance of the electrodes and mass transport effects within the electrolyte, which can be represented by one or more parallel RC circuits [76]. While this approach makes it harder to distinguish the particular cause of the transient response, it is relatively simple and intuitive to handle. The model and computational effort to run or parametrize fits most BMS system requirements and even online methods are used to identify the model parameters while operation. Furthermore the model can be adjusted flexibly since a wide range of electronic components are available to model rate capacity effects [96], self discharge [97] and differences between charge and discharge behaviour [98]. An approach to model Li-S in this practical manner was only done by Knap et al. [99] for equivalent circuit models of different complexity for the discharge range. While he concluded that a two RC model is best suitable to represent the cell behaviour over the discharge range, Chapter 5 of this thesis follows a different approach. Since the main application of the model is the SoC estimation, here the computational effort is evaluated as more important, which led to the usage of the commonly used Thevenin model structure [100] with only one parallel RC circuit. Furthermore, the presented model is characterised with a novel mixed pulse pattern to unveil current related changes and is parametrized over a temperature range of

20 - 50 °C. The model can be described in continuous standard state space form as

$$\begin{aligned}\dot{x}(t) &= Ax(t) + Bu(t) \\ y(t) &= Cx(t) + Du(t)\end{aligned}\tag{3.7}$$

and as

$$\begin{aligned}x_k &= Ax_{k-1} + Bu_{k-1} \\ y(k) &= Cx_k + Du_k.\end{aligned}\tag{3.8}$$

in discrete-time for the recursive state estimation. For the sake of completeness, the following chapter introduces the combination of this model and with probabilistic methods, before they are applied for SoC estimation.

3.8 Kalman filter and derivatives

As introduced before, batteries are complex systems with variations occurring even for their simple definitions for capacity and SoC. Furthermore, the model itself, no matter if high or low fidelity, always contains some level of abstraction and simplification. Methods, found to be robust against these uncertainties, assign a stochastic variable to the observations y and states x respectively and can not only improve the accuracy, they also can handle measurement noise, model inaccuracies and eliminate the need to store past measurements for an expected value. All these advantages, combined with the need for aggressive but reliable battery usage in EVs and HEVs [101], make this field of research growing quickly [102]. The SoC estimation for Li-S batteries in this thesis is heavily based on the Kalman filter theory. Therefore, its principles and derivations are introduced. But since Chapter 6 and 7 already contain the equations and brief introductions

for the applied algorithms, the introduction here follows a graphical pattern. This is contrary to most text books and aims to present an alternative introduction to the complex field of optimal state estimation.

3.8.1 Main Principles

The Kalman filter minimizes the error variance between unknown true and estimated state for assumed Gaussian distributions. In the following, the principles leading to this result are introduced stepwise, from simple assumptions to the final algorithm. The argument is based on chapter four of Gelb's text [103].

Least squares

One widely used paradigm, the least squared error method, relies on deterministic arguments to minimize the sum of the squared error between between the state dependent predicted model output $C\hat{x}_k$ and measurement y_k . Mathematically, the state is transformed to the output through the already introduced linear operator C from the measurement equation

$$y = Cx. \quad (3.9)$$

The minimization occurs through comparing the estimated model output \hat{y}_i with the measurements and sum up the squared values of the difference $y_i - \hat{y}_i$

$$J = (y - C\hat{x})^T (y - C\hat{x}). \quad (3.10)$$

To find the \hat{x} that minimises the result J , the first derivative is taken, set to zero and \hat{x} is brought on one side of the equation

$$\hat{x} = (C^T C)^{-1} C^T y. \quad (3.11)$$

For states with different uncertainties, it can be useful to weight the sum of squares through a positive definite weighting matrix R^{-1}

$$\hat{x} = (C^T R^{-1} C)^{-1} C^T R^{-1} y. \quad (3.12)$$

Now our estimation of \hat{x} is optimal for the least squares criterion and it improves with the amount of observations. However, this problem is a very simple one due, since measured output and prediction are known.

Assumption of uncertain measurements

When statistical assumptions about the measurement are added, \hat{x} can be estimated by maximizing its probability. The maximum likelihood paradigm applies the least squares method to the zero mean Gaussian probability assumption with covariance matrix R .

$$p(y|x) = \frac{1}{(2\pi)^{\ell/2} |R|^{1/2}} * \exp \left[-\frac{1}{2} (y - C\hat{x})^T R^{-1} (y - C\hat{x}) \right] \quad (3.13)$$

In this simple case, the conditional probability density for y , conditioned on a given value for x , is just the density for y centred around $C\hat{x}$. Therefore, by minimizing the quadratic exponent (similar to Eq. 3.12), the probability density $p(y|x)$ reaches its maximum (Fig. 3.10). In other words, for Gaussian distribution the maximum likelihood is equal to the least squares estimation.

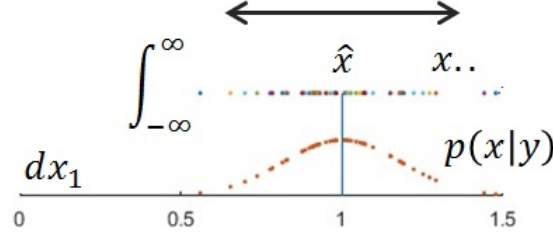


Figure 3.10: Properties of Gaussian distribution.

Assumption of uncertain states and measurements

So far we concentrated on getting an optimal idea of the state x by employing statistical assumptions with observations. Now the Bayesian approach adds the prediction of the observer model as a new information, also containing a degree of uncertainty. It is based on the idea that everything unknown is treated as a stochastic variable with an associated probability density function [104]. The statistical assumptions are given by the framework a hidden Markov model (HMM) of sequential data [105], where the observations $p(y_k|x_k)$ are dependent on the predictable state $p(x_k|x_{k-1})$ and unpredictable measurement $p(y)$. The resulting probability density for, x given the observations y , formulated by Bayes' theorem is

$$p(x|y) = \frac{p(y|x)p(x)}{p(y)}. \quad (3.14)$$

Where $p(x)$ and $p(y)$ are the probability density functions of x and y . The estimate \hat{x} can be drawn from the conditional probability $p(x|y)$ depending on the criterion of optimality.

When the maximum likelihood $p(x|y)$ over x is wanted, the previously introduced thoughts can be joined together. Since the denominator of Eq. 3.14 does not depend on x , it is ignored for the optimization so the conditional likelihood of the measurement times the prior state is maximised.

$$p(x|y) \propto p(y|x)p(x) = \text{likelihood} \times \text{prior} \quad (3.15)$$

With the previously introduced assumption of Gaussian sensor noise

$$p(y|x) \propto \exp \left[-\frac{1}{2} (y - C\hat{x})^T R^{-1} (y - C\hat{x}) \right] \quad (3.16)$$

and Gaussian distribution of the prior state

$$p(x) \propto \exp \left[-\frac{1}{2} (x - x_0)^T P_0^{-1} (x - x_0) \right] \quad (3.17)$$

the function to be maximized is

$$p(x|y) = \exp \left[-\frac{1}{2} (y - C\hat{x})^T R^{-1} (y - C\hat{x}) \right] \times \exp \left[-\frac{1}{2} (x - x_0)^T P_0^{-1} (x - x_0) \right]. \quad (3.18)$$

Where the prior on x is normal distributed with mean x_0 and covariance P_0 . As well as before, this function can be maximized by setting the first derivation to 0.

$$\frac{\delta}{\delta x} \left[-\frac{1}{2} (y - C\hat{x})^T R^{-1} (y - C\hat{x}) - \frac{1}{2} (x - x_0)^T P_0^{-1} (x - x_0) \right] = 0 \quad (3.19)$$

Which leads to

$$\hat{x} = (P_0^{-1} + C^T R^{-1} C)^{-1} (P_0^{-1} x_0 + C^T R^{-1} y) \quad (3.20)$$

When there is little or no a priori information, P_0^{-1} is small compared to $C^T R^{-1} C$, Eq. 3.20 becomes Eq. 3.12. If we further assume that all measurement errors are uncorrelated with the same variance, Eq. 3.12 reduces to 3.11. It is therefore worth to mention, that for Gaussian random variables optimal estimation refers to the result for \hat{x} that minimizes the mean squared estimation error or maximizes its probability.

Practical implementation in state estimator

The implementation of the Bayes rule in practical applications is done in two steps [106, 107].

Prediction:

$$p(x_t|y_{1:t-1}, u_{1:t}) = \int p(x_t|x_{t-1}, u_t) p(x_{t-1}|y_{1:t-1}, u_{1:t-1}) dx_{t-1}$$

Where the actual probability density is calculated from past measurements, the system model and the control input u_t . Thereafter, the posterior probability density $p(x_t|y_{1:t}, u_{1:t})$ is calculated by employing the actual observation.

Update:

$$p(x_t|y_{1:t}, u_{1:t}) = \eta^{-1} p(y_t|x_t) p(x_t|y_{1:t-1}, u_{1:t})$$

Where η is a normalisation factor $p(y_t|y_{1:t}, u_{1:t})$, standing for certainty of all observations. This result leads to filters with the goal of getting a consistent estimate of the states which converges to the true value as the number of measurements increases [103].

Gaussian distribution

To emphasise the principle of recursive estimation and visualise the conditional probabilities with Gaussian assumptions, a simple example is given here with a linear state space representation with additive noise (w_{k-1}, v_k) for states and measurements. The posterior state estimate is calculated through one step of prediction and time update with assumed values for a one dimensional, linear system ($A = 1$, $x_0 = 1$, $C = 2$, $u = 0$, $\sigma_w = 0.18$, $\sigma_v = 0.1$). While the diagrams give correct quantitative information, the amplitudes of probability density functions are scaled differently to emphasise the steps.

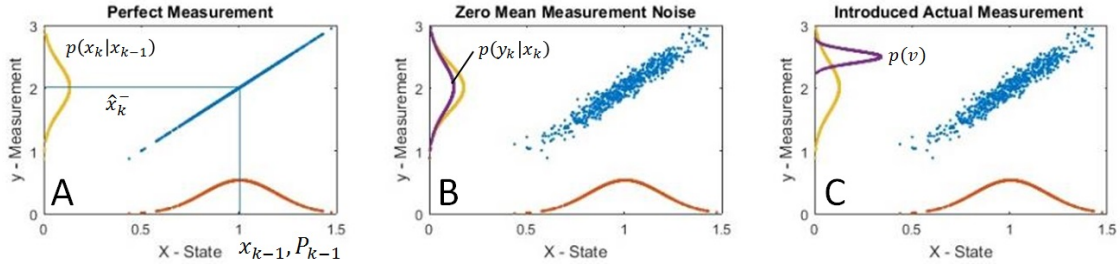


Figure 3.11: Gaussian distribution through state estimation

Figure 3.11-A shows the associated probability of points for x on the x -axis and the propagation of them through A on the y -axis $p(y|x)$. Without any measurement noise the prediction of the state probability can just be obtained with the factor A . However, since each of the predicted points has an uncertainty in the measurement dimension, a vertical random number is added to each of the predicted points (Fig. 3.11-B). Here the numerically simple description and propagation of Gaussian noise is a major advantage, since both independent Gaussian distributions can be added up together by simply summing their variances. In Fig. 3.11-C the measurement with its own distribution $p(v)$ is introduced. Both, the predicted and the measurement probabilities, are multiplied together to build the joint probability (Fig. 3.12-A). With the new knowledge of $p(\hat{y})$ the conditional probability $p(x|y)$ (Fig. 3.12-B) and therefore the posterior state \hat{x} (Fig. 3.12-C) can be derived. With these assumptions, all the calculated distributions stay Gaussian and are therefore describable by their means and variances, stored as states x and covariance matrix P [108]. This simplifies the Bayesian recursion greatly since only these parameters need to be stored and processed through time instead of propagating the whole probability density [106].

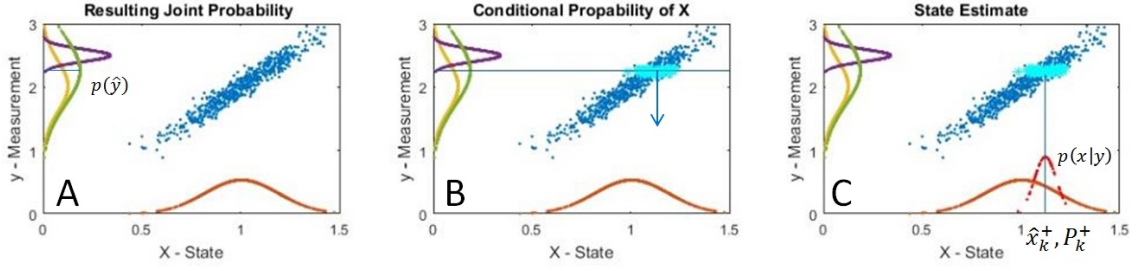


Figure 3.12: Conditional, Gaussian probabilities through state estimation

3.8.2 Kalman filter

An analytical solution of the Bayes filter for linear systems and Gaussian distributions is the Kalman filter (KF), minimizing the error variance between true and estimated state [109]. Through the recursive algorithm all previous information is embedded in the prior estimate at the measurement index k , which eliminates the need for storing the past observations. The minimisation is done by the Kalman gain which dynamically weights the estimation in between the model prediction and the measurements (For a summary of the mathematical background the reader is guided to the textbook [103]). Here the algorithm is introduced without further introduction. However, the Kalman filter is, next to the algorithm, introduced graphically as well to emphasise the principle of the estimation process. For the introduced state space model for a battery, predicting the terminal voltage with a current input, the prediction step uses the input and the past states for the estimation of the present state and probabilities in the *Time update step*:

$$\text{State update : } \hat{x}_k^- = A\hat{x}_{k-1}^+ + Bu_{k-1} \quad (3.21)$$

$$\text{Covariance update : } P_k^- = AP_{k-1}^+A^T + Q \quad (3.22)$$

With the state prediction, the estimation of the related terminal voltage can be done. The error between the prediction and measurement is then multiplied by the Kalman gain

to correct the states. Furthermore, the a posteriori estimations for state and covariances are determined in the *Measurement update step*:

$$\text{Kalman Gain : } L_k = P_k^- C^T (C P_k^- C^T + R)^{-1} \quad (3.23)$$

$$\text{State update : } \hat{x}_k^+ = \hat{x}_k^- + L_k (y_k - C \hat{x}_k^-) \quad (3.24)$$

$$\text{Covariance update : } P_k^+ = (I - L_k C) P_k^- \quad (3.25)$$

The graphical interpretation orients on the propagation of the probability distributions in Sec. 3.8.1. Here however, the steps are presented in a more circular fashion to emphasise the recursive nature (Fig. 3.13).

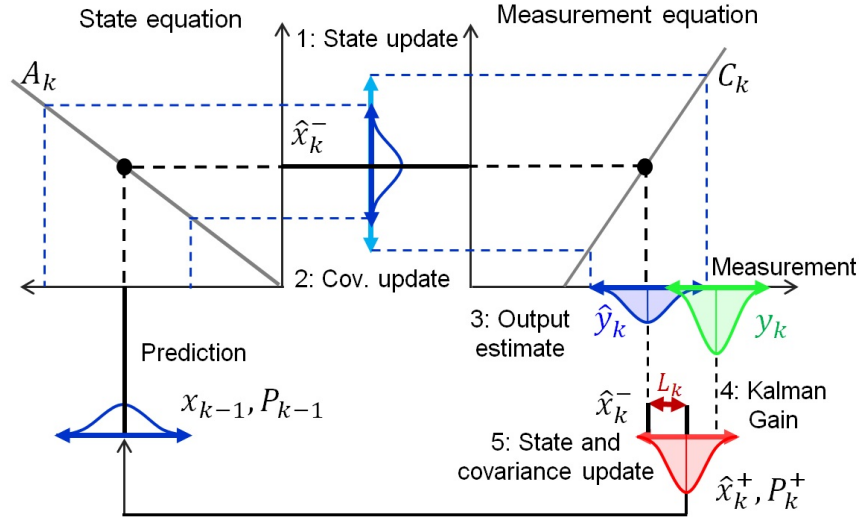


Figure 3.13: State propagation Kalman filter

While the Kalman filter is theoretically the optimal solution, it relies on knowing values for the system and measurement uncertainties. The estimation performance and robustness depends on the user choices for the measurement noise variance R and the system noise variance Q . While R is relatively easy to determine by evaluating sensors or measurements, Q is guessed most of the time. In practice each application has differ-

ences in the system, its observability, model accuracy and measurement quality, which makes a robust filter unique for each application. And while the model based SoC estimation in concept is independent of the battery chemistry ([110] for lead-acid, [111] for LiFePO_4 , [68] LiMnO_2 , [112] [113]), the specific properties of Li-S batteries leads to new challenges. Chapter 6 gives more insight into parametrisation of the system- and measurement-uncertainties for the SoC estimation.

Each method or algorithm has its specific advantages depending on the model, noise behaviour and nonlinearities. Therefore, one important conclusion of this thesis will be how each method compares to each other in the presents of the unique properties of Li-S batteries.

3.8.3 Extended Kalman filter

The assumption of linearity cannot represent most real systems, which leads to the following discrete state space model

$$x_k = f(x_{k-1}, u_{k-1}) + w_{k-1} \quad y_k = Cx_k + v_k. \quad (3.26)$$

However, for a certain range to an operation point the assumption of linearity usually can be utilised. Therefore, the nonlinear extension of the KF, the extended Kalman filter (EKF), is widely used for state estimation with batteries. Every step the system is linearised around the current state mean \hat{x}_{k-1}^+ for the propagation of the probability densities [101] [114]. With the definition of the predicted estimation error

$$\tilde{x}_k^- = x_k - \hat{x}_k^- = f(x_{k-1}, u_{k-1}, w_{k-1}) - f(\hat{x}_{k-1}^+, u_{k-1}, w_{k-1}) \quad (3.27)$$

and the linearised approximation for \hat{x}_k^- with a first order Taylor series around the current mean,

$$\hat{x}_k^- \approx \underbrace{f(x_{k-1}, u_{k-1}, w_{k-1})}_{\mathbf{x}_k} - \frac{\partial f(x_{k-1}, u_{k-1}, w_{k-1})}{\partial x_{k-1}} \bigg|_{x_{k-1}=\hat{x}_{k-1}^+} (x_{k-1} - \hat{x}_{k-1}^+) - \frac{\partial f(x_{k-1}, u_{k-1}, w_{k-1})}{\partial w_{k-1}} \bigg|_{w_{k-1}=\bar{w}_{k-1}} (w_{k-1} - \bar{w}_{k-1}) \quad (3.28)$$

the nonlinearities cancel each other out. With the Jacobians of A and B, \hat{A}_k and \hat{B}_k , defined as

$$\hat{A}_k = \frac{\partial f(x_k, u_k, w_k, k)}{\partial x_k} \bigg|_{x_k=\hat{x}_k^+}, \quad \hat{B}_k = \frac{\partial f(x_k, u_k, w_k, k)}{\partial w_k} \bigg|_{w_k=\bar{w}_k}, \quad (3.29)$$

this leads to

$$\tilde{x}_k^- \approx f(x_{k-1}, u_{k-1}, w_{k-1}) - f(x_{k-1}, u_{k-1}, w_{k-1}) + \hat{A}_{k-1} \tilde{x}_{k-1}^+ + \hat{B}_{k-1} \tilde{w}_{k-1} \quad (3.30)$$

Using this, it is possible to find the covariance the propagation through time with the current mean, the gradient for the system function \hat{A}_{k-1} and the previous estimation error \tilde{x}_k^- , as long there is a starting point, i.e. an initial condition. The definition for the variance $\mathbb{E}[(\tilde{x}_k^-)(\tilde{x}_k^-)^T]$ leads to the equation for the linearly approximated covariance prediction

$$P_k^- \approx \hat{A}_{k-1} P_{k-1}^+ \hat{A}_{k-1}^T + \hat{B}_{k-1} Q \hat{B}_{k-1}^T. \quad (3.31)$$

The same principle applies to the calculation of the Kalman gain. With the definition for the output prediction error

$$\tilde{y}_k = y_k - \hat{y}_k = h(x_k, u_k, v_k) - h(\hat{x}_k^-, u_k, v_k) \quad (3.32)$$

and the linear approximation for \hat{y}_k

$$\begin{aligned} \hat{y}_k \approx & h(x_k, u_k, v_k) + \left. \frac{\partial h(x_k, u_k, v_k)}{\partial x_k} \right|_{x_k = \hat{x}_k^-} (\hat{x}_k^- - x_k) \\ & + \left. \frac{\partial h(x_k, u_k, v_k)}{\partial v_k} \right|_{v_k = \bar{v}_k} (\bar{v}_k - v_k), \end{aligned} \quad (3.33)$$

the nonlinear measurement prediction of the current mean y_k disappears. Again the Jacobians of C and D, \hat{C}_k and \hat{D}_k , are defined as

$$\hat{C}_k = \left. \frac{\partial h(x_k, u_k, w_k, k)}{\partial x_k} \right|_{x_k = \hat{x}_k^-}, \hat{D}_k = \left. \frac{\partial h(x_k, u_k, w_k, k)}{\partial v_k} \right|_{v_k = \bar{v}_k}. \quad (3.34)$$

This leads to the linear factors of \hat{C}_k , multiplied by the previous state error $\hat{x}_k^- - x_k$. With the definition for the covariance $\mathbb{E}[(\tilde{x}_k^-)(\hat{C}_k \tilde{x}_k^- + \hat{D}_k \tilde{v}_k^T)]$, which is equal to $P_k^- \hat{C}_k^T$, the Kalman Gain can be calculated as

$$L_k = P_k^- \hat{C}_k^T \left[\hat{C}_k P_k^- \hat{C}_k^T + \hat{D}_k R \hat{D}_k^T \right]^{-1}. \quad (3.35)$$

As well as the Kalman Gain, the posterior covariance is calculated through the linear Jacobian matrix \hat{C}_k with

$$P_k^+ = (I - L_k \hat{C}_k) P_k^-. \quad (3.36)$$

One of the drawbacks of the filter is the need for the partial derivations of the system model, usually \hat{A}_{k-1} and \hat{C}_k , which can be difficult to obtain. Furthermore, the linearisation of the system to approximate the nonlinear dynamics at every time step is not necessarily optimal. Nevertheless, the EKF often works well [114], even when the simplifications made while propagating the nonlinear states and measurements with Gaussian noise, $(\mathbb{E}f(x) = f(\mathbb{E}[x]))$, are not true in general and the dropped nonlinear terms in the covariance prediction and estimator gain matrix calculation lead to a lower accuracy [101].

The quality of the estimation with these generalisations therefore depends on the nonlinearity of the system function f and varies between applications. While Fig. 3.14 shows the propagation of the EKF in principle, the whole algorithm is presented in Chapter 6.

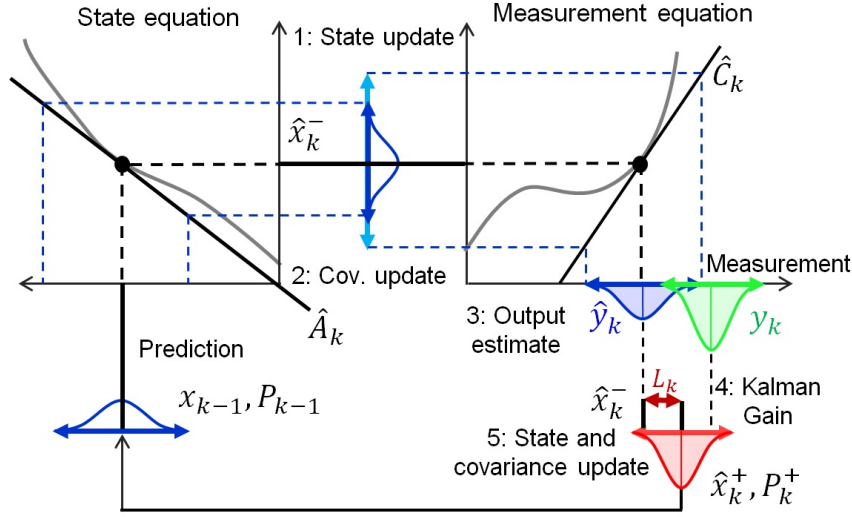


Figure 3.14: State propagation extended Kalman filter

3.8.4 Unscented Kalman filter

Another way of handling nonlinearities is to estimate them with a set of data points. The principle is based on chosen points with mean and covariance of the random variable, being processed through the system function to get the posterior distribution. Therefore the state vector of the unscented Kalman filter (UKF) is augmented to form

$$\chi_{k-1} = \left[\hat{x}_{k-1}^+, \hat{x}_{k-1}^+ + \gamma \sqrt{P_{k-1}^+}, \hat{x}_{k-1}^+ - \gamma \sqrt{P_{k-1}^+} \right]. \quad (3.37)$$

Where the sum of the state vector and the covariance matrix P is not strictly bounded to the matrix notations. It is defined by adding a vector to each column of the matrix [115],

as Eq. 3.38 indicates:

$$x_k + \sqrt{P_k} = \begin{bmatrix} x_1 \\ x_2 \end{bmatrix} + \begin{bmatrix} \sqrt{P_1} & 0 \\ 0 & \sqrt{P_2} \end{bmatrix} = \begin{bmatrix} x_1 + \sqrt{P_1} & x_1 \\ x_2 & x_2 + \sqrt{P_2} \end{bmatrix} \quad (3.38)$$

With the initial conditions \hat{x}_0 and P_0 , this leads to the column-wise update of each states through the system model

$$\chi_k^{i,-} = f(\chi_{k-1}^{i,+}, u_{k-1}), \quad (3.39)$$

the line-wise estimation of the mean

$$\hat{x}_k^- = \sum_{i=0}^{2L} \alpha_i^{(m)} \chi_k^{i,-} \quad (3.40)$$

and covariance from the transformed sigma points

$$P_k^- = \sum_{i=0}^{2L} \alpha_i^{(c)} (\chi_k^{i,-} - \hat{x}_k^-)(\chi_k^{i,-} - \hat{x}_k^-)^T. \quad (3.41)$$

The weights $\alpha_i^{(m)}$ and $\alpha_i^{(c)}$ are vectors containing real constant scalars with the conditions that $\sum_{i=0}^p \alpha_i^{(m)}$ and $\sum_{i=0}^p \alpha_i^{(c)}$ are equal to one [101]. With the scaling value $\lambda = \alpha^2(L + \kappa) - L$ the weights can be calculated with

$$\gamma = \sqrt{L + \lambda}, \quad \alpha_0^{(m)} = \frac{\lambda}{L + \lambda}, \quad \alpha_0^{(c)} = \frac{\lambda}{L + \lambda} + (1 - \alpha^2 + \beta), \quad \alpha_i^{(m)} = \alpha_i^{(c)} = \frac{1}{2(L + \lambda)}.$$

Where parameters γ ($0.01 \leq \alpha \leq 1$), κ (0 or $3 - L$) and β (2) define width of the sigma points[115]. Since the parameters are constant they can be defined once prior executing the filter. For further processing, the a priori points are also processed through the measurement equation column-wise, with a line-wise calculation of the new mean and

variance

$$\gamma_k^j = h(\chi_k^{i,-}, u_k) \quad (3.42)$$

$$\hat{y}_k = \sum_{i=0}^{2L} \alpha_i^{(m)} \gamma_k^i. \quad (3.43)$$

With the consequential covariance matrices P_k^{yy} and P_k^{xy}

$$P_k^{yy} = \sum_{i=0}^{2L} \alpha_i^{(c)} (\gamma_k^i - \hat{y}_k)(\gamma_k^i - \hat{y}_k)^T \quad (3.44)$$

$$P_k^{xy} = \sum_{i=0}^{2L} \alpha_i^{(c)} (\chi_k^{i,-} - \hat{x}_k^-)(\gamma_k^i - \hat{y}_k)^T \quad (3.45)$$

the Kalman Gain is computed simply by divide both values ($L_k = P_k^{xy}(P_k^{yy})^{-1}$). The error covariance measurement update follows as the last step of the filter

$$P_k^+ = P_k^- - L_k P_k^{yy} L_k^T. \quad (3.46)$$

The increased effort for the propagation of the UKF is counterbalanced by better covariance approximations. Furthermore, no derivatives are needed, which also eliminates the need for differentiable system functions. While the algorithm is presented in Chapter 6, Figure 3.15 shows the principles behind the propagation of states and covariances.

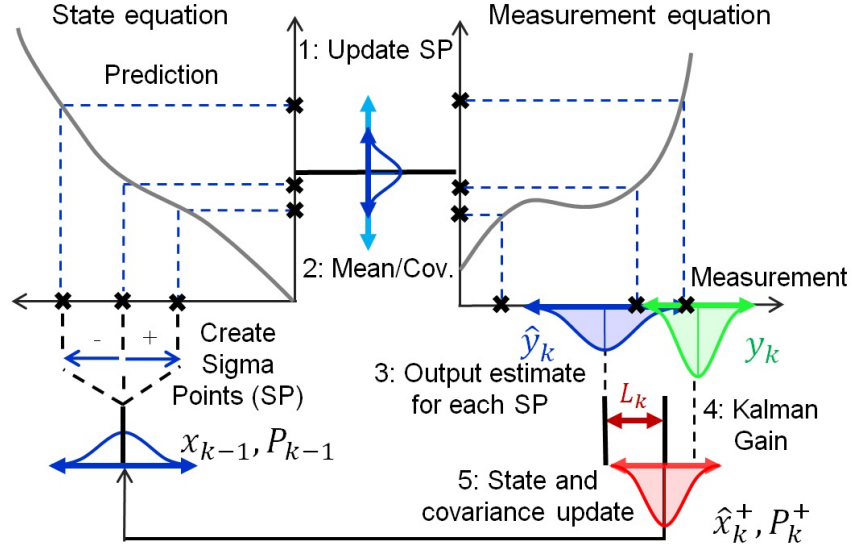


Figure 3.15: State propagation unscented Kalman filter

3.8.5 Particle filter

The introduced Kalman filter methods are only able to process Gaussian distributions. To solve the recursive estimation problem for arbitrary distributions, the Particle filter (PF) generates possible positions for the states, the particles, and weight these to decide how well these explain the observations. Unlike the UKF, where just the means and covariances are transferred to the next step, the PF recursively estimates the whole particle set χ_t between the iterations, which means that the actual hypothetical states are based on the estimation of the previous one χ_{t-1}

$$\chi = \{ \langle x^m, w^m \rangle \}_{m=1, \dots, N}. \quad (3.47)$$

Where x^m is the state hypothesis and w^m the associated importance weight vector. The derivation of the equations orient on Chapter 4.2 of the textbook [116], where the samples

and weights represent by the posterior density

$$p(x) = \sum_{i=0}^N w^m \delta_{x^m}(x). \quad (3.48)$$

Instead of using the mean and covariance of these particles like before (UKF), the principle of the filter is based on the assumption that the probability density function (PDF) can be approximated by the density of particles (Fig. 3.16).

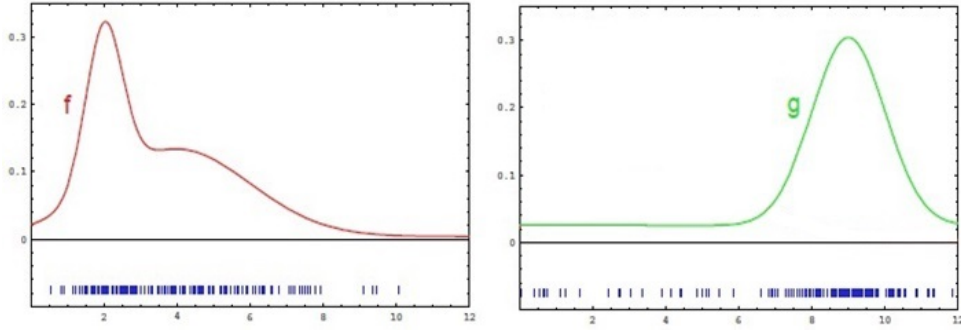


Figure 3.16: Target- and proportional probability density function and corresponding particle density [116].

The more particles fall into an interval or area, the higher is the probability density and therefore the probability that the actual state is in that area as well. With other words, the empirical count of particles in the range A converges to the integral of g under A .

$$\frac{1}{M} \sum_{m=1}^M I(x^m \in A) \rightarrow \int_A g(x) dx \quad (3.49)$$

As before, the filter can be divided in a prediction step, where the particles are randomly generated by a proposal distribution g , and an update step, where the introduced measurement information leads to the weighting of the particles by the target distribution f [117].

Prediction

To add uncertainty and create particles in random locations, the previous particle distribution x_{t-1} is processed through time with the system model with the addition of the proposal distribution

$$x_k^m \approx p(x_k | u_k, x_{k-1}^m). \quad (3.50)$$

The resulting set of particles represents the filter's a priori believe $\overline{bel}(x_t)$.

Update

To determine how well the predicted particles coincides with the observations y_k , the probability of the measurement under each particle is calculated as weight w_t^m using the target distribution f

$$w_k^m = p(y_k | x_k^m) = \frac{f(x_k^m)}{g(x_k^m)}. \quad (3.51)$$

With the normalization factor for all importance weights w^m , the particles converge to the density f

$$\left[\sum_{m=1}^M w^m \right]^{-1} \sum_{m=1}^M I(x^m \in A) w^m \rightarrow \int_A f(x) dx. \quad (3.52)$$

The resulting set of weighted particles approximate the Bayes filter posterior distribution $bel(x_k)$ (Fig. 3.17).

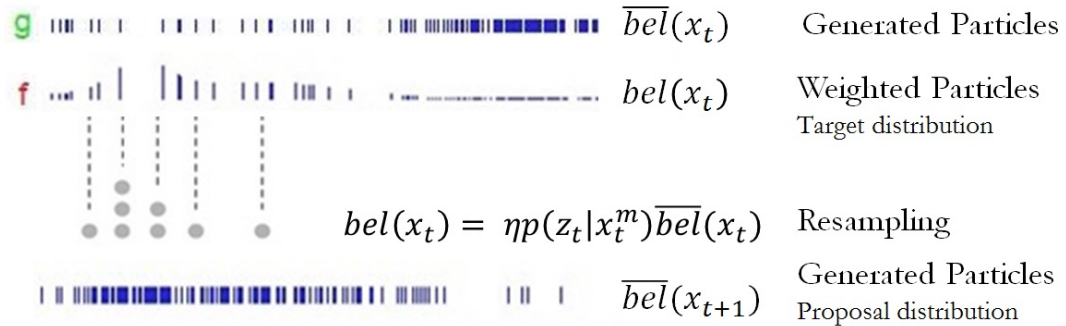


Figure 3.17: Particle distributions during the propagations

Here the option of individually changing the function allows the user to account precisely for the kind of uncertainties with different observations.

Resampling

To account for the new information of the measurement, the resampling of the particles incorporates the weights into the generation of the new set. The algorithm replaces particles from the temporary set $\tilde{\chi}$ based on their probability defined by the weights. Hence, the resampling transforms the particle set M to another set of same size but containing just the most likely particles

$$bel(x_k) = \eta p(y_k | x_k^m) \overline{bel}(x_t). \quad (3.53)$$

Therefore, particles with a high weights are reproduced while low weighted ones die out. Thus, the re-sampled set distributes approximately according to the posterior without the weights in the next iteration. The particle filter is the only one of the presented ones that is able to handle non-gaussian noise assumptions. However, its accuracy depends on users considerations. Firstly, the number of particles are vital. With fewer ones, a systematic bias is induced in the posterior due to the normalisation. A large particle set however, increases the computational expense. Furthermore, the resampling causes a loss of diversity in the particle population reducing the variance of the particles set, which can lead to only a single particle surviving the resampling, decreasing the estimation robustness. Usually the particle filter works well with low dimensional systems which makes it a promising alternative for the state of charge estimation for the Li-S batteries. In the following the algorithm is summarized visually in Fig. 3.18 and mathematically in Chapter 6.

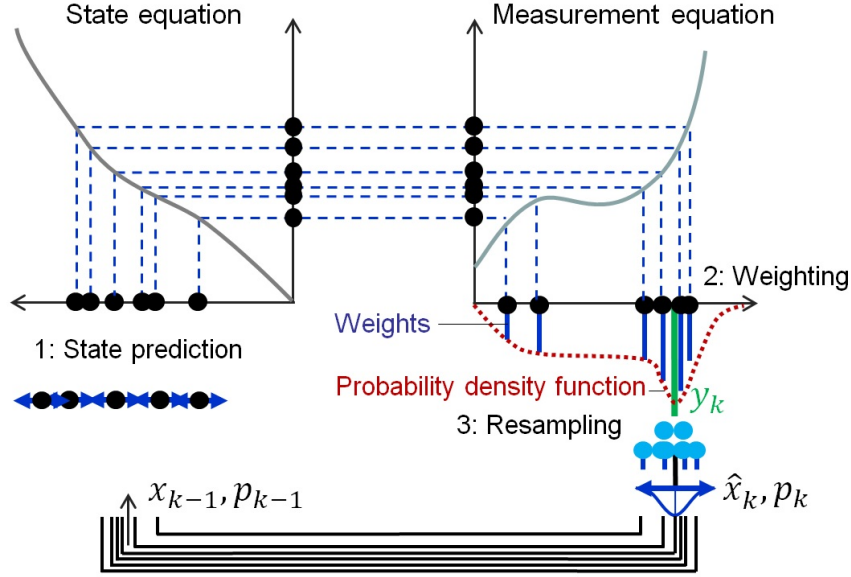


Figure 3.18: State propagation particle filter

3.9 Conclusion

This chapter introduced basic definitions and paradigms in the field of battery SoC estimation and methods to get optimal results in the presence of model and measurement uncertainties. The introduced algorithms use different approaches for handling nonlinearities in a dynamic state space model, which lead to different properties. While the extended Kalman filter, which linearises through a first order Taylor series, has the lowest computational effort of the proposed methods, it needs the partial derivatives of the model and is usually used for systems containing mild nonlinearities. The unscented Kalman filter estimates the mean and covariances through a number of chosen sigma points. This increases the computational expense slightly, but also reduces the effort for setting up the filter. Without the assumption of Gaussian noise the Particle filter is expected to deliver the precise results for individual probability distributions with the downside of high computational requirements. Using these three methods this thesis aims to:

- **Develop an equivalent circuit model for the SoC estimation** with a trade-off between accuracy and computational effort or simplicity.
- **Apply the introduced estimation methods** to find out how well they are able to handle the complex behaviour of Li-S cells.
- **Find out the limitations** of the applied algorithms to give practical recommendations which algorithm is suited best for applications with Li-S cells.

4

Methods and experiments

While the used hardware and test procedures for the model parametrization and SoC estimation are briefly explained in the following chapters, this one aims to introduce the experimental assumptions in more detail. Both OXIS Energy and Cranfield University conducted experiments. While the tests made by OXIS included the pulsed discharge current test, in Cranfield a test rig was created to concentrate on realistic scenarios for EVs. The hardware used by OXIS Energy for pulse current discharge tests generally conforms with the industry standard and is not explained further here. More details for this are given in Chapter 5. But since the more realistic drive cycle tests in Chapters 6 and 7 contain a variety of assumptions, which could not be represented in full detail in a publication framework, the test procedures for these experiments are introduced here more thoroughly.

4.1 Tested Li-S cells

Next to the improvement of the practical understanding of the cells, the REVB project also aims to produce high capacity cells with improved properties. However, due to the

ongoing improvement of the cells this work is based on smaller capacity cells that were available for practical experiments from the beginning of the project. Table 2.5 summarises the main parameters of the test cell as well as these of the target cell. The focus of the smaller cells for the experiments is not seen as a drawback since the main patterns of the cell behaviour will not change significantly. Therefore, it is expected that the findings of this work are easily applicable to other Li-S cells with reasonable adjustments, independent of their size or recent development state. The tested 3.4 Ah 'long life' cells were manufactured in low volumes and may be the subject of manufacturing related cell variations. Therefore, the experiments were done with multiple cells which were pre-chosen by OXIS to exclude cells which could not deliver discharge capacities near the nominal one. Since most cells were stored over several months, each tested cell also was pre-cycled with low constant currents (charge: $C/10$, discharge: $C/10$) at 30 °C, to minimise storing effects that reduce the usable capacity. Except this, the tested cells were 'fresh' so that degradation effects could be reduced. For preparation, the cells were put into a small metal box for protection and connected to the wires for the main currents and cell voltage sensing (Fig. 4.1).



Figure 4.1: Prepared test cell in metal chamber

4.2 Experimental hardware

For the drive cycle tests a BOP100 - 10MG (BOP), which is a calibrated 4 quadrant power source/sink, is used. In current mode, the device is able to charge and discharge the cell with the desired rate and measure the cell voltage. To program the device, a computer is connected to the BOP via a GPIB interface with a digital programming accuracy of 0.03 V and 0.01 A. The battery is connected to the BOP with twisted 5 mm² flexible wires and thinner connections to the cell terminals to measure the cell voltage. While Fig. 4.2 shows the general circuit layout, in Chapter 6 the whole test rig is shown as well.

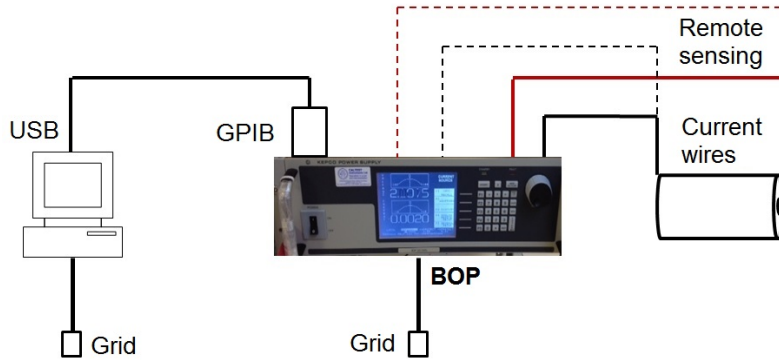


Figure 4.2: Test layout and connections between cell, BOP, and computer

The GPIB communication standard is supported by Matlab [118], which allows to program the BOP directly with Matlab code. Therefore an experimental approach could be developed, based on drive cycle simulation data from Matlab Simulink.

4.3 Experimental software

The goal of the experiments is to simulate the battery in a realistic manner for EVs. Here, standard drive cycles are useful since they combine realistic scenarios with a level of simplification and standardisation. However, the data provided represents only the

velocity over time and leaves information about the power demand open for interpretation and assumptions. To generate a realistic current profile, a vehicle model was simulated, based on the Nissan Leaf [119], and used as a foundation for the experiments on Li-S cells.

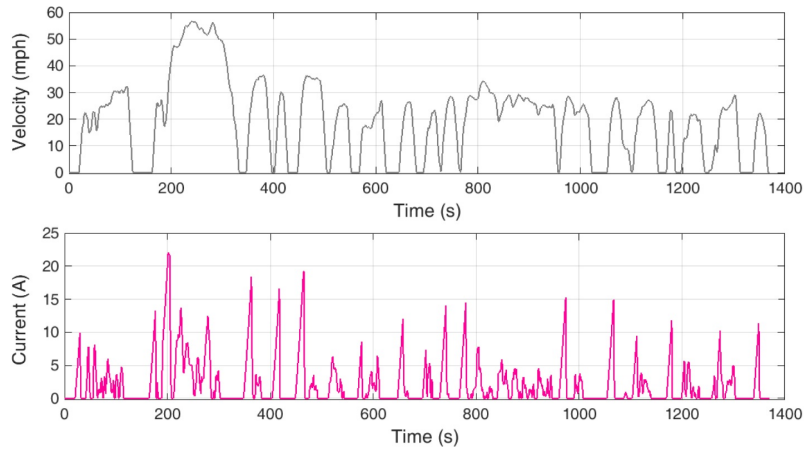


Figure 4.3: Velocity and current profile of vehicle simulation [120]

To scale down the current demand of the whole battery pack, as shown in Fig. 4.3 for the urban dynamometer driving schedule (UDDS), to an individual cell however, further assumptions had to be made. Since a full EV battery pack is considered, it can generally be assumed that the rates of a cell are relatively low, the balancing of the cells is done while charging and they don't necessarily have power or SoH predictions [114]. Together with the power limitations of the prototype cells and the recommended discharge current of the manufacturer of 680 mA, the drive cycles were scaled down so that the peaks of each cycle reached about $C/2$ (Fig. 4.4 right). However, the gains of the applied profile are varied in the course of the experiments to test the robustness of the model and SoC estimation against different current densities. Another assumption for the drive cycle data is to focus on the discharge process, ignoring energy recovery while driving.

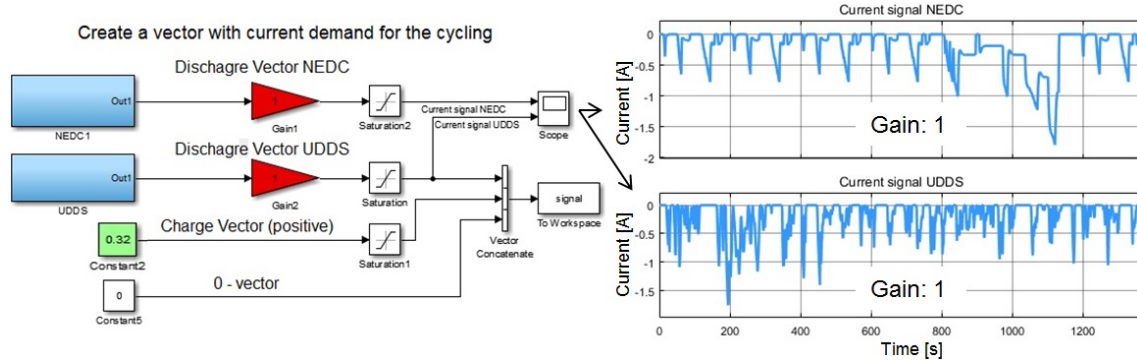


Figure 4.4: Current demand vectors in Matlab Simulink

Since the physical discharge device can be controlled with commands from the Matlab environment, the test procedures could be developed individually. After the cells were put in the thermal chamber with the demanded temperature and were connected to the BOP, a simple Matlab Simulink model was used to create the current demand over time with a charge and discharge vector respectively (Fig. 4.4 left). The cycling was executed by running a script, which was developed and improved in the course of the project. The main principle of the test program is to send a demanded current to the BOP and receive the measurements for the terminal voltage and actual current once per second. While the program code can be found in [121] and in Appendix B, a general list of the executed tasks in the loop is given here after the Matlab time counter is started:

- Send current demand to BOP (negative: discharge, positive: charge)
- Ask for actual current and voltage measurement
- If cell voltage over V_{max} - change to discharge vector
- If cell voltage under V_{min} - change to charge vector
- If cell charging time is over 11 h - change to discharge vector (safety)
- Wait for the next full second to repeat the script

The pattern of switching between the discharge and charge with a minimum and maximum voltage applies also to the SoC definitions. According to the script, the definition of a fully charged cell and a depleted cell is when V_{max} and V_{min} is reached respectively (Fig. 4.5). In between the dynamic discharges with the drive cycles, the cells were charged with slightly less than the recommended charging current of $C/10$ (320 mA) to reduce cell history related effects.

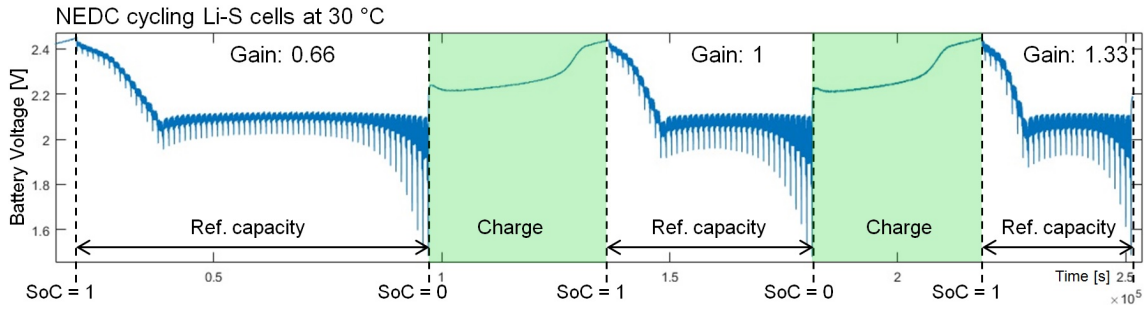


Figure 4.5: Example of cycling tests with Li-S battery

The derived current integral from these experiments, together with the definitions for maximum and minimum SoC, were taken for the reference SoC estimation for each discharge process respectively.

Part II

Papers

5

Paper 1 – Equivalent circuit battery model

Multi-temperature state-dependent equivalent circuit discharge model for lithium-sulfur batteries

Authors:

Karsten Propp, Monica Marinescu, Daniel J. Auger, Laura O'Neill,
Abbas Fotouhi, Karthik Somasundaram, Gregory J. Offer, Geraint Minton,
Stefano Longo, Mark Wild, Vaclav Knap

The paper has been published in the
Journal of Power Sources Vol. 328, pp. 289-299, 2016

Abstract

Lithium-sulfur (Li-S) batteries are described extensively in the literature, but existing computational models aimed at scientific understanding are too complex for use in applications such as battery management. Computationally simple models are vital for exploitation. This paper proposes a non-linear state-of-charge dependent Li-S equivalent circuit network (ECN) model for a Li-S cell under discharge. Li-S batteries are fundamentally different to Li-ion batteries, and require chemistry-specific models. A new Li-S model is obtained using a ‘behavioural’ interpretation of the ECN model; as Li-S exhibits a ‘steep’ open-circuit voltage (OCV) profile at high states-of-charge, identification methods are designed to take into account OCV changes during current pulses. The prediction-error minimization technique is used. The model is parameterised from laboratory experiments using a mixed-size current pulse profile at four temperatures from 10 °C to 50 °C, giving linearised ECN parameters for a range of states-of-charge, currents and temperatures. These are used to create a nonlinear polynomial-based battery model suitable for use in a battery management system. When the model is used to predict the behaviour of a validation data set representing an automotive NEDC driving cycle, the terminal voltage predictions are judged accurate with a root mean square error of 32 mV.

5.1 Introduction

To increase an acceptance and a demand of electric vehicles (EVs) among the public, there is a need to overcome range anxiety [1]. Since the range of EVs is strongly connected to their energy storage, there is a request for a low cost and safe operating battery with high specific energy. Potentially fulfilling these requirements, the lithium-sulfur (Li-S) chemistry is a prospective replacement of the current lithium-ion (Li-ion) battery technology [122] [123]. However, Li-S batteries still suffer from fast degradation and high self discharge [53], which leads the modelling community to be focused on elucidating the complex inner mechanisms governing the cell behaviour. Despite being essential for Li-S technology uptake, operational models and on-line diagnostic tools, capable of predicting and controlling the batteries performance in operation are lacking in the literature. Recently, commercial Li-S cells have become available (e.g. those supplied by OXIS Energy [70], Sion Power, Polyplus), offering the opportunity for application oriented research. In the framework of electric mobility this translates into investigating the cells' performance under the power and temperature demands of an EV [114]. For established battery chemistries, models have been developed, providing varying levels of insight into the cells' internal processes, at varying computational cost [124]. Since the computational power of a typical electronic control unit (ECU) or battery management system (BMS) is limited, simple low-complexity battery models are often needed for application oriented purposes. Examples of such simplified models are equivalent electrical circuit networks (ECN), which reproduce the transient behaviour of a battery with a circuit of electrical components, including resistors, capacitors and a voltage source [100]. The structure of these models is often independent of the cell chemistry, and as such they are not able to give insight into the cell's physical, chemical and electrochemical processes [92]. However, for Li-ion batteries, they have been successfully used for estimating the

internal states, such as state of charge (SoC) and measures of battery health such as increase in resistance and decrease in effective capacity [81] (In this paper, only SoC will be considered in detail). Usually they have relatively low computational effort and use easily available measurements like current and terminal voltage. For Li-S batteries, ECN models of varying accuracy and complexity have been developed in [71] [87] [125] [126]. These models have been developed for the purpose of analyzing impedance spectroscopy data, such that they describe the cell at a fixed SoC. Because of this, they are unsuited to describe performance during cycling. For an OXIS Li-S cell a first operational model including two parallel resistor-capacitor (RC) pairs, has been developed recently with good prediction of the charging process [127]. Furthermore, a comparison of ECN topologies for Li-S batteries in terms of accuracy, and a parameter identification for a three RC model for the same kind of cell were presented in [99]. In this paper, we introduce the complete framework for developing a Li-S battery model with one RC element, suitable for BMS use, and evaluate its accuracy. Thereby, our approach follows the development of a standard ECN model for Li-ion batteries; parametrizing the circuit by fitting pulse discharge data. In order to investigate the temperature dependence of the various circuit parameters for the OXIS Li-S cell, here the parametrization is done for four different temperatures. Also, some of the open questions regarding the suitability of this approach to parametrize the unique properties of Li-S cells are discussed. Therefore we, after a brief introduction into the general requirements for a Li-S battery model (Sec. 5.2), (i) use a robust parameter estimation technique developed for Li-S cells, accounting for OCV differences before and after a current pulse (Sec. 5.3 - Sec. 5.4), (ii) apply a novel mixed current pulse test procedure to explore current-dependencies of the model parameters (Sec. 5.5), and (iii) identify the cell parameters at four different temperatures Sec. 5.6. The validation of a simplified model (Sec. 5.7) is done in Sec. 5.8.

5.1.1 Contributions

1. Evaluation of modelling approaches for Li-S batteries
2. The introduction of a behavioural model to improve the parameter identification and simplify the definition of sensible ranges
3. ECN model identification with mixed pulse current pattern
4. ECN model with joined polynomial functions to represent the behaviour of Li-S cells over the discharge range with temperatures from 20 °C to 50 °C

5.2 From Li-ion to Li-S modelling

In the literature, there are many examples of established Li-ion battery models [92] [128]. The purpose of one kind, the ECN models, is to predict the output voltage, the available capacity and the degradation at relatively low computational cost [100]. These models are successful enough to be widely used in applications. The main reason for their success is that the intercalation-based chemistry of the Li-ion battery offers a relatively consistent and predictable performance when operated within its limits of charge, temperature and current rates [81]. This is not the case for the Li-S batteries, because they are based on conversion reactions rather than on intercalation. Sulfur reacts with lithium ions when reduced from elemental state S_8 , via the intermediates Li_2S_8 , Li_2S_4 , Li_2S_2 , to lithium sulfide Li_2S [129] (Fig. 5.1), offering theoretically a capacity of 1672 mAh g^{-1} [130].

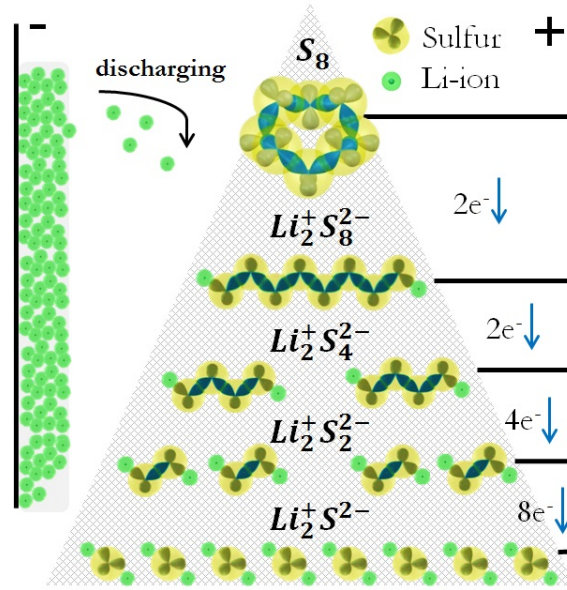


Figure 5.1: Work principle of Li-S battery

However, the practical capacities currently achieved are significantly lower [92] [130], mainly due to poor sulfur utilisation and fast degradation [59]. High order polysulfides are highly soluble and reactive [131] in organic electrolytes, while low order polysulfides tend to be insoluble and form an electrically insulating precipitate [53]. The details of the reduction path during discharge are still a matter of ongoing research and are probably more complex [55]. The discharge curve exhibits two regions [132] (Fig. 5.2): a high plateau at about 2.35 V open circuit voltage (OCV), characterized by the presence of a majority of high order polysulfides in solution (Li_2S_8 , Li_2S_6), and a low plateau at around 2.1 V OCV, where lower order chains have been identified (Li_2S_4 , Li_2S_3 , Li_2S_2), including Li_2S which can precipitate out [133]. With the growing amount of insulating Li_2S_2 and Li_2S , the practical discharge stops at about 1256 mAh g^{-1} , indicated by the increasing cell resistance [134] [135]. While charging, the oxidation of low order polysulfides forms high order chains. However, they do not all become elemental sulfur. Highly soluble, high order polysulfides diffuse to the anode and, in contact with its surface, are reduced

to lower order chains. These can diffuse back to the cathode, where they are oxidised back to longer chains. This phenomenon, called the polysulfide shuttle [61], can act as overcharge protection [130], but is also responsible for self discharge and poor coulombic efficiency, and associated with capacity fade [61] [136].

To identify requirements and challenges towards a fully operational low order Li-S battery model, some Li-ion approaches are listed and examined for their suitability for the Li-S chemistry.

Voltage Curve: The OCV of Li-ion batteries can be measured after some rest time and is sensitive to the SoC [81] and weakly influenced by temperature [97]. Therefore, it is usually represented by a variable voltage source with a function or lookup table over SoC, which simplifies the SoC estimation for those batteries [137]. Li-ion has a known predictable and reproducible temperature dependence on OCV. However, Li-S due to the presence of multiple species and multiple reactions between those species has a highly variable and state dependent temperature dependence on OCV, where the state dependence can be a function of the history of the cell going back many cycles. Attempts to model the OCV [95] have been made, but are yet to include the full temperature dependence, which would be necessary to accurately reproduce this effect. Furthermore, in the low plateau, the OCV is not an indication for the SoC since it will always return to about 2.15 V, when given enough time after current is removed (The time required will depend on the final voltage, but is typically no longer than two hours.). Additionally, the presence of self-discharge and precipitation further complicate the dependence of the rest voltage on the SoC, meaning that it is unclear how one would reliably obtain experimental data for the OCV as a function of the SoC [95]. The transient voltage behaviour of Li-ion batteries are represented by RC circuits, supplemented by parameter-functions for SoC, temperature, current and cycle number. Since the variations of the model parameters for cycle number and currents are usually small [96], they tend to be neglected or simpli-

fied [138]. For Li-S batteries the opportunities for these simplifications are unknown for practical BMS applications.

Capacity: To handle variations of the usable capacity in Li-ion cells, a rate factor can be applied [97]. But since the variations of the usable capacity are usually small, they are also handled with the internal resistance, causing the voltage drops to increase with higher rates and therefore cause different SoC's for the same end-of-discharge voltage [138]. For the Li-S batteries however, the amount of sulfur that can be reversibly utilised during a discharge is strongly affected by the current profile, cycling and temperature [139]. Generally high discharge capacity is only obtained at very low rates. High currents can produce a resistive layer on the cathode, hindering the utilisation of the underlying sulfur [132], leading to strong changes in the usable capacity. Cell operation for optimal utilisation of sulfur remains a challenge and is still a matter of ongoing research [71] [130] [140].

Power Capability: For Li-ion batteries, the power limitations are governed by the diffusion of ions into and out of the electrodes, which is mainly defined by the battery design [141] and therefore not considered to vary rapidly with normal usage. For Li-S batteries, the specific factors limiting rate capability during operation are unknown. Slow diffusion of species through the electrolyte, bottlenecks in the electrochemical reaction pathway, and reduced availability of active surfaces are some of the possible reasons for power limitation. Generally, the polysulfide kinetics in the high plateau region are fast, leading to good rate capabilities and low cell resistance. However, the high voltage plateau usually accounts for merely 10 – 30% of a cycled cell's capacity [142]. At the boundary between the two plateaus a peak in cell resistance is observed, possibly caused by an increase in electrolyte viscosity, due to a high concentration of dissolved polysulfides. A further increase in the resistance at the end of the discharge is associated with precipitation of lower order polysulfides, leading to a decrease in the availability of both active species

and active surface area. The operating temperature does impact power capability, for Li-S as well as for Li-ion cells, as lower temperatures lead to slower diffusion and lower reaction rates. However, the potential for Li-S batteries to work in cold environments is seen as greater [142].

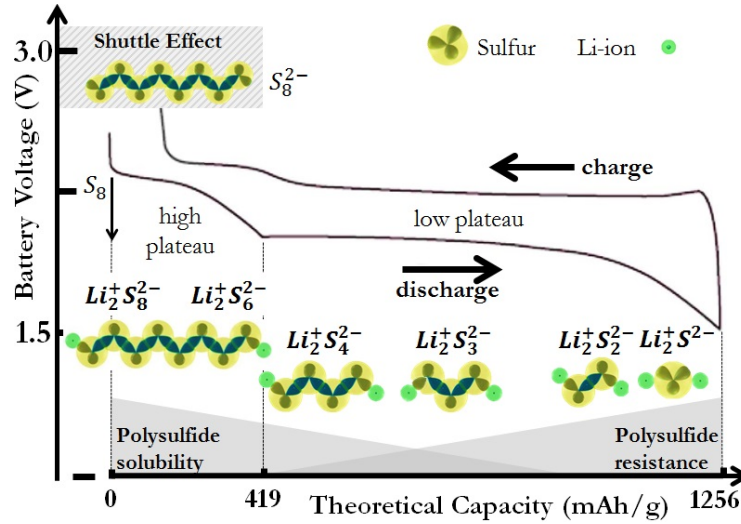


Figure 5.2: Basic voltage behaviour Li-S battery

Degradation For Li-ion the major degradation modes in ECN models are the decreasing rate capability and capacity fade, caused by parasitic reactions at the anode, leading to a growth of the solid-electrolyte interphase (SEI) [143], and the consumption of active material [144]. For Li-S batteries, the degradation modes are not well known [55], and it is unclear which lead to reversible and which to irreversible degradation. Probable causes include the irreversible growth of insulating layers on the anode [145] and possibly cathode, and the associated loss in active material [146]. Much of the degradation is believed to be related to the polysulfide shuttle. In order to prevent it, overcharging is generally avoided, despite not being a safety issue in comparison to Li-ion chemistries.

The comparison shows that the Li-S chemistry is more complex in its reactions as well as the electrical behaviour than current Li-ion batteries. The unique Li-S features,

(i) two regions with different properties, (ii) a flat voltage profile, (iii) self discharge mechanism during charging, (iv) high sensitivity of the usable capacity and power to cycling parameters such as current profile or temperatures, indicate a higher effort towards an application oriented model. It is not clear yet, how accurately these effects have to be represented for future Li-S BMS systems.

5.3 Parameter identification

There are many techniques for system identification, but a good ‘industry standard’ is prediction-error minimization (PEM), a full description of which can be found in Ljung’s seminal work on system identification [147]. The key concept behind PEM is that of the ‘prediction error’, which is estimated based on recorded observations, describing the model

$$y(t) = G(q, \theta)u(t) + H(q, \theta)e(t) \quad (5.1)$$

as a predictor of the next output. Where G represents the transfer function, q the forward shift operator, $H(q, \theta)e(t)$ the disturbance of the system and θ is a parameter vector. The parameter vector consists of the unknown model parameters: for an ECN model, for example, it might be electrical component values. In system identification, a metric is defined, usually as a mathematical norm, such as the ‘prediction error’ $\varepsilon(t, \theta)$ between the measured data $y(t)$ and the model prediction $\hat{y}(t)$ is used; an identification algorithm seeks to minimize this norm, and the minimizing parameter vector, denoted θ_N , gives the best fit

$$\varepsilon(t, \theta) = y(t) - \hat{y}(t|\theta). \quad (5.2)$$

The prediction error minimization algorithm uses numerical optimization to minimize the cost function $V_N(\theta, Z^N)$, a weighted norm of the prediction error, defined as follows for

scalar inputs

$$V_N(\theta, Z^N) = \frac{1}{N} \sum_{t=1}^N (y(t) - \phi^T(t)\theta)^2. \quad (5.3)$$

Usually the cost function includes the number of the data samples

$$Z^N = [y(1), u(1), y(2), u(2), \dots, y(N), u(N)], \quad (5.4)$$

and becomes more accurate for larger data set. PEM system identification is applied to each current pulse individually. To get an accurate result, the estimation window was set to 300 seconds before and after each pulse.

5.4 Battery model set

The quality of the identification strongly depends on the model set. In this section, a new linearized version of a nonlinear SoC-dependent ECN model is presented. First, a Thevenin model [148] [149] (Fig. 5.3) is expressed in terms of its parameter dependence on SoC. The model is then reparameterized in terms of ‘behaviour’, rather than component values. The model is then linearized in a way that captures the dependence of the model behaviour on changing state of charge. This parameterization provides a number of benefits over a standard ECN model:

(i) The application of constraints to behaviours is possible, which makes it possible to relate constraints to observed behaviours; without a behavioral parameterization, such parameterizations are less straightforward. (Dynamic bandwidth, for example, is a function of two equivalent circuit parameters in an RC pair; in the new parameterization, it is a single behavioral parameter.)

(ii) The linearized form of the model explicitly captures terms relating to short-term changes in dynamic behavior due to changes in ECN parameters caused by changing SoC.

(In conventional ECN models, parameters are usually assumed constant over a short time period, but this can cause problems when the SoC has a significant short-term effect, e.g. a noticeable change in OCV during a system identification experiment.

These benefits make the model suitable for system identification tests such as those conducted in this study.

This work differs from the ‘cyclic resistometry’ analytical parameter technique [150] in that where cyclic resistometry attempts to measure a single physical parameter – the electrode resistance – with a series of high-frequency pulses, the techniques of this paper simultaneously identifies all ECN parameters with a ‘behavioural’ rather than physical interpretation.

5.4.1 State-of-charge–dependent ‘Thevenin’ model

Basic model equations

Consider a generic Thevenin model with ECN parameter dependence on SoC X —this is a capital ‘ χ ’ not a capital ‘ x ’. Following common practice, the current \bar{I} is treated as the input and the load voltage is taken as the output. Using the symbolic notation of Fig. 5.3, the output equation is

$$U_L = h_{U_L}(X, U_p, I_L) \quad (5.5)$$

where

$$h_{U_L}(X, U_p, I_L) = U_{oc}(X) - U_p - R_o(X)I_L. \quad (5.6)$$

The system has two dynamic states: state-of-charge, X , and ‘capacitor’ voltage U_p . The state derivatives are given by

$$\dot{X} = f_X(I_L) = -\frac{1}{Q_{cap}}I_L \quad (5.7)$$

where Q_{cap} is the capacity (in Coulombs) of the battery or cell under consideration, and

$$\dot{U}_p = f_{\dot{U}_p}(X, U_p, I_L) \quad (5.8)$$

where

$$f_{\dot{U}_p}(X, U_p, I_L) = -\frac{1}{R_p(X)C_p(X)}U_p + \frac{1}{C_p(X)}I_L \quad (5.9)$$

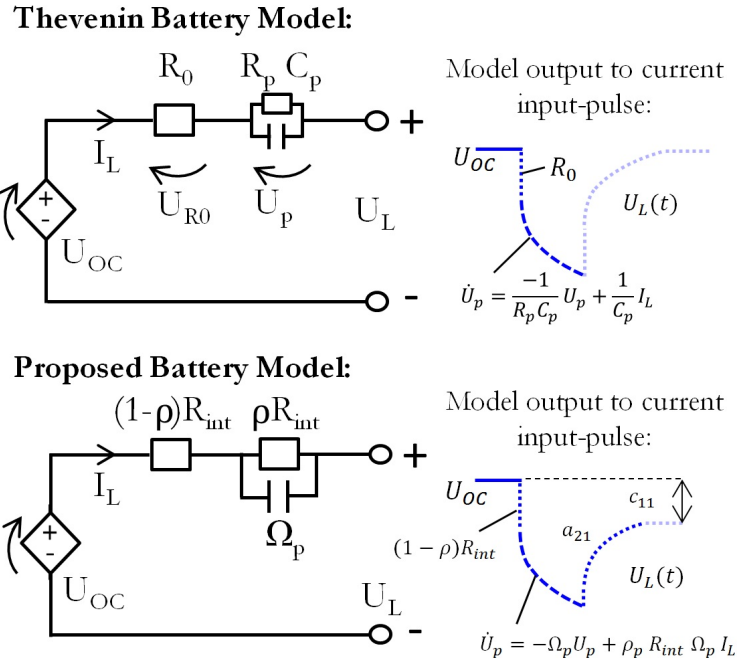


Figure 5.3: Response of the Thevenin and behavioural battery model to a current pulse (Details of the pulses used are given in Sec. 5.5).

Behavioural reparameterization

The ECN model expressed above is perhaps a little cumbersome. During system identification, it is often desirable to constrain parameter searches to sensible ranges. In battery identification, the operator will be particularly concerned to see how well steady-state model behaviour matches reality, what the bandwidth (or time constant) of the model

is, and how much of the response is (as far as can be observed) instantaneous and how much lags. It is important not to lose sight of the fact that ECN models were chosen because their *behaviour* represents observed cell behaviour, not because there is a particular physical significance to the circuit elements employed.

Our circuit can be made more intuitive by working in terms of some new ‘behavioural’ variables:

$$\Omega_p(X) = \frac{1}{R_p(X)C_p(X)} \quad (5.10)$$

$$R_{\text{int}}(X) = R_o(X) + R_p(X) \quad (5.11)$$

$$\rho_p(X) = \frac{R_p(X)}{R_{\text{int}}(X)} \quad (5.12)$$

Here, Ω_p represents the dynamic bandwidth described by R_p and C_p . R_{int} is the total steady-state resistance, and effectively governs the ‘settled’ voltage drop due to a constant current. ρ_p represents the ‘dynamic fraction’ of the response: when ρ_p is zero, the voltage response is wholly instantaneous, and when ρ_p is one, the response is wholly dynamic. Using this parameterization, it is relatively easy to write down behavioural constraints, e.g.

$$\begin{aligned} \Omega_p(X) &\in [\Omega_{\min}, \Omega_{\max}] \\ R_{\text{int}}(X) &> 0 \\ \rho_p(X) &\in [0, 1] \end{aligned} \quad (5.13)$$

The output function and state derivative functions can be re-written in terms of the new parameterization:

$$h_{U_L} = U_{\text{oc}}(X) - U_p - (1 - \rho_p(X))R_{\text{int}}(X)I_L \quad (5.14)$$

$$f_X = -\frac{1}{Q_{\text{cap}}}I_L \quad (5.15)$$

$$f_{\dot{U}_p} = -\Omega_p(X)U_p + \rho_p(X)R_{\text{int}}(X)\Omega_p(X)I_L \quad (5.16)$$

This parameterization of the model is numerically identical to the original ECN model, but there are no longer any ‘reciprocal’ parameters and the application of parameter constraints is straightforward and intuitive. Giving a set behavioural parameters it is of course straightforward to map these back to ‘conventional’ ECN parameters noting that

$$R_p(X) = \rho_p(X)R_{\text{int}}(X), \quad (5.17)$$

$$R_o(X) = R_{\text{int}}(X) - R_p(X) \quad (5.18)$$

and

$$C_p(X) = \frac{1}{R_p(X)\Omega_p(X)} \quad (5.19)$$

5.4.2 Linearised cell model

Motivations for linearisation

For system identification, it is common to use linearised models. In many practical approaches, it is assumed that state-dependent parameters vary sufficiently slowly to be treated as constants, and the nonlinear ECN model is effectively used as a linear model with ‘frozen’ SoC. Unfortunately, this does not always work. When a battery or cell is subject to a high-current discharge pulse, the change in SoC can be sufficient to cause a drop in the OCV between the start and the end of the pulse (as depicted in Fig. 5.3 and 5.4). This does not fit well with the linear model. One way to get round this in practice is subtract a voltage term representing the drop on U_{OC} caused by a change in SoC. More formally, a full linearisation of the nonlinear model can be performed. When this is done, it will be seen that the nonlinear model contains all the expected ‘ECN terms’ but also two

additional terms that we might perhaps not have expected. This is shown in the following sections.

Definition of operating point

The first step in the linearization process is to define an operating point. In this case, the dynamic state pair (\bar{X}, \bar{U}_L) will be assumed. The nominal input is current, chosen such that $\dot{U}_L = 0$:

$$\bar{I}_L = \frac{\bar{U}_p}{\rho_p(\bar{X})R_{\text{int}}(\bar{X})} \quad (5.20)$$

and the nominal output is

$$\bar{U}_L = U_{\text{oc}}(\bar{X}) - \bar{U}_p - (1 - \rho_p(\bar{X}))R_{\text{int}}(\bar{X})\bar{I}_L. \quad (5.21)$$

(Usually, operating points are chosen to represent equilibria. The operating point that has been chosen here is not strictly-speaking an equilibrium unless $\bar{I}_L = 0$ since in general $\dot{X} \neq 0$. But that does not matter: the mathematics holds regardless.)

As a next step, variables describing perturbations from nominal values are defined:

$$\begin{aligned} \hat{u}_L &= U_L - \bar{U}_L, \\ \hat{i}_L &= I_L - \bar{I}_L, \\ \hat{\chi} &= X - \bar{X}, \\ \hat{u}_p &= U_p - \bar{U}_p. \end{aligned} \quad (5.22)$$

This allows us to express what is essentially a ‘small-signal’ model, though such terms are rarely used in the formal language of control theory.

Linear state-space representation

We can define a state vector

$$\hat{\mathbf{x}} = \begin{bmatrix} \hat{\chi} & \hat{u}_p \end{bmatrix}^T \quad (5.23)$$

and form a linearised model:

$$\hat{u}_L \approx \underbrace{\begin{bmatrix} \frac{\partial h_{U_L}}{\partial X} & \frac{\partial h_{U_L}}{\partial U_p} \end{bmatrix}}_{\mathbf{c}^T} \hat{\mathbf{x}} + \underbrace{\frac{\partial h_{U_p}}{\partial I_L}}_D \hat{i}_L \quad (5.24)$$

$$\dot{\hat{\mathbf{x}}} \approx \underbrace{\begin{bmatrix} \frac{\partial f_X}{\partial X} & \frac{\partial f_X}{\partial U_p} \\ \frac{\partial f_{U_p}}{\partial X} & \frac{\partial f_{U_p}}{\partial U_p} \end{bmatrix}}_{\mathbf{A}} \hat{\mathbf{x}} + \underbrace{\begin{bmatrix} \frac{\partial f_X}{\partial I_L} \\ \frac{\partial f_{U_p}}{\partial I_L} \end{bmatrix}}_{\mathbf{b}} \hat{i}_L \quad (5.25)$$

The terms of \mathbf{c}^T are

$$\frac{\partial h_{U_L}}{\partial X} = \frac{\partial U_{oc}}{\partial X} + R_{int} I_L \frac{\partial \rho_p}{\partial X} - (1 - \rho_p) I_L \frac{\partial R_{int}}{\partial X} \quad (5.26)$$

$$\frac{\partial h_{U_L}}{\partial U_p} = -1, \quad (5.27)$$

the term of \mathbf{D} is

$$\frac{\partial h_{U_L}}{\partial I_L} = -(1 - \rho_p) R_{int}, \quad (5.28)$$

the terms of \mathbf{A} are

$$\frac{\partial f_X}{\partial X} = 0, \quad (5.29)$$

$$\frac{\partial f_X}{\partial U_p} = 0, \quad (5.30)$$

$$\begin{aligned} \frac{\partial f_{U_p}}{\partial X} = & (\rho_p R_{\text{int}} I_L - U_p) \frac{\partial \Omega_p}{\partial X} + R_{\text{int}} \Omega_p I_L \frac{\partial \rho_p}{\partial X} \\ & + \rho_p \Omega_p I_L \frac{\partial R_{\text{int}}}{\partial X}, \end{aligned} \quad (5.31)$$

$$\frac{\partial f_{U_p}}{\partial U_p} = -\Omega_p, \quad (5.32)$$

and the terms of \mathbf{b}^T are

$$\frac{\partial f_X}{\partial I_p} = -\frac{1}{Q_{\text{cap}}}, \quad (5.33)$$

$$\frac{\partial U_p}{\partial I_p} = \rho_p R_{\text{int}} \Omega_p. \quad (5.34)$$

We can therefore write:

$$\hat{u}_L \approx \underbrace{\begin{bmatrix} c_{11} & -1 \end{bmatrix}}_{\mathbf{c}^T} \hat{\mathbf{x}} + \underbrace{(1 - \rho_p) R_{\text{int}}}_{D} \hat{i}_L \quad (5.35)$$

$$\dot{\hat{\mathbf{x}}} \approx \underbrace{\begin{bmatrix} 0 & 0 \\ a_{21} & -\Omega_p \end{bmatrix}}_{\mathbf{A}} \hat{\mathbf{x}} + \underbrace{\begin{bmatrix} -\frac{1}{Q_{\text{cap}}} \\ \rho_p R_{\text{int}} \Omega_p \end{bmatrix}}_{\mathbf{b}} \hat{i}_L. \quad (5.36)$$

An important thing to note here is that there are two terms in these matrices that we might not intuitively expect if we were simply writing down the equations for an ECN circuit: c_{11} which relates changes in SoC to the open circuit voltage, and a_{21} which relates changes in SoC to the capacitor voltage.

As a final step, we can apply a state transformation:

$$\hat{\mathbf{x}} = \underbrace{\begin{bmatrix} Q_{\text{cap}}^{-1} & 0 \\ 0 & 1 \end{bmatrix}}_{\mathbf{T}^{-1}} \hat{\mathbf{z}} \quad \text{i.e.} \quad \hat{\mathbf{z}} = \begin{bmatrix} Q_{\text{cap}} \hat{\chi} \\ \hat{u}_p \end{bmatrix}$$

This yields

$$\hat{u}_L = \underbrace{\begin{bmatrix} c'_{11} & -1 \end{bmatrix}}_{\mathbf{c}_z^T = \mathbf{c}^T \mathbf{T}^{-1}} \hat{\mathbf{z}} + \underbrace{(1 - \rho_p) R_{\text{int}}}_{D} \hat{i}_L \quad (5.37)$$

$$\dot{\hat{\mathbf{z}}} \approx \underbrace{\begin{bmatrix} 0 & 0 \\ a'_{21} & -\Omega_p \end{bmatrix}}_{\mathbf{A}_z = \mathbf{T} \mathbf{A} \mathbf{T}^{-1}} \hat{\mathbf{z}} + \underbrace{\begin{bmatrix} -1 \\ \rho_p R_{\text{int}} \Omega_p \end{bmatrix}}_{\mathbf{b}_z = \mathbf{T} \mathbf{b}} \hat{i}_L. \quad (5.38)$$

In this form, the model lends itself well to system identification. As well as the core behavioural equivalent circuit parameters U_{oc} , R_{int} , ρ_p and Ω_p —which also give R_o , R_p and C_p —there are two ‘free’ parameters c'_{11} and a'_{21} that can accommodate parameter changes within a system identification data set caused by c'_{11} . For the purposes of this study, it has been assumed that the effect of SoC on OCV is the dominant distorting effect, as it can be seen from the data that U_{oc} changes between the start and end of a pulse (Fig. 5.4). Accordingly, a'_{21} has been assumed small, but c'_{11} has been accommodated in system identification.

5.5 Experimental design

The battery model parameters are identified through discharge tests within temperatures from 10 - 50 °C. To identify the current dependencies of the model parameters without potential ageing effects, the cells were tested with current pulses of 290 mA, 1450 mA and 2900 mA with a 10 minute resting time in between (Fig. 5.4). The measurement procedure contained pre-cycled (C/10 charge, C/5 discharge, 30 °C) 3.4 Ah long-life chemistry pouch cells from OXIS Energy, following their recommended voltage range between 2.45 V, when the battery is fully charged (SoC = 100%), and 1.5 V, when the

battery is fully discharged (SoC = 0%). We have taken a practical definition of state-of-charge, essentially 'remaining capacity', and we have defined the end point of the test as the first instant at which the terminal voltage reaches 1.5 V, in line with the manufacturer's recommendation.

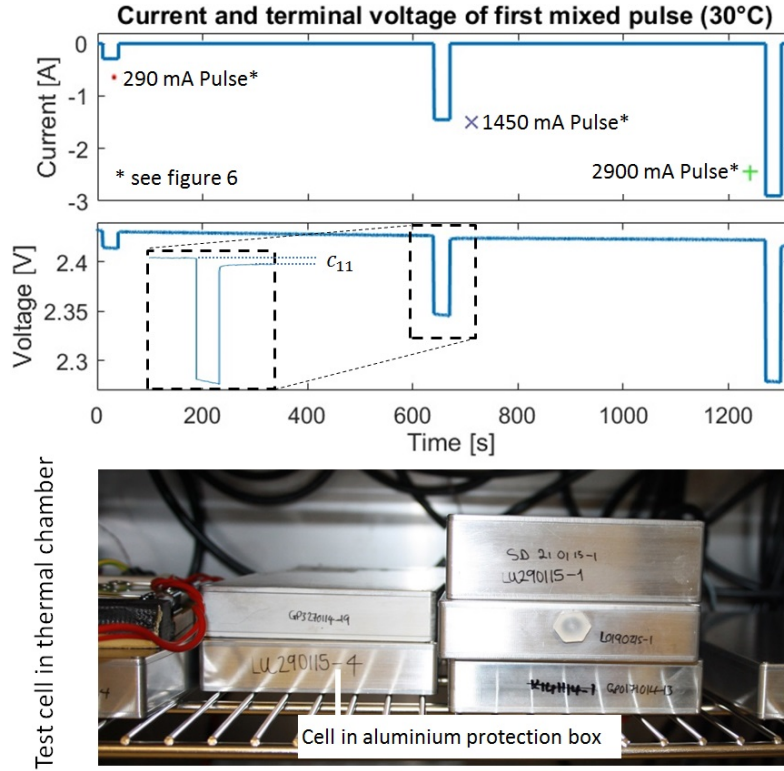


Figure 5.4: Mixed pulse discharge and test installation

The test hardware included a Maccor 4000 battery tester with cells constantly held at temperature in sealed aluminium boxes with a Binder KB53 thermal chamber, also shown in Fig. 5.4.

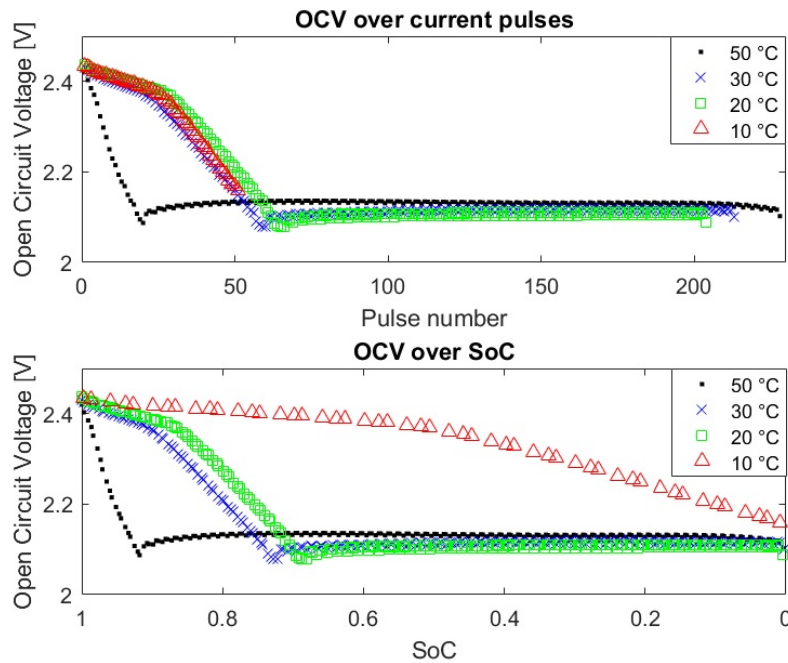
5.6 Identification Results

Since the tested cells are not mass produced, deviations in their discharge capacity or parameters are possible (see Table 5.1).

Table 5.1: Capacities of test cells

Temperature	Test Cell 1	Test Cell 2
10 °C	0.67 Ah	0.68 Ah
20 °C	2.72 Ah	2.79 Ah
30 °C	2.83 Ah	2.79 Ah
50 °C	3.02 Ah	3.03 Ah

Therefore, the identification has been done with two cells respectively. But since the identified parameters follow the same pattern, only the results for cell one are presented.

Figure 5.5: Identification results for U_{OC} over pulse and SoC

The identification results for the model parameters are repeated over the whole discharge range for each current pulse individually, by calculating the SoC from the inte-

grated current, the discharge capacity of the cycle, and the assumption of an initially fully charged battery (Fig. 5.5). (In this work SoC is a dimensionless variable, with 0 representing fully discharged and 1 representing fully charged, following the pattern in [81].)

$$X = X_{(0)} - \frac{1}{3600Q_{\text{cap}}} \int_0^t I(\tau) d\tau. \quad (5.39)$$

The average SoC is assigned for each pulse respectively by using its the start- and end-value of the SoC estimation

$$X_{\text{pulse}} = 0.5(X_{\text{start}} + X_{\text{end}}). \quad (5.40)$$

Figure 5.6 shows the identification results for each pulse over SoC, emphasising the current dependencies of the parameters. Generally the results corresponds well with previous studies. The peak of R_0 between both voltage plateaus, also reported in [55], is associated with the increased viscosity and therefore resistance of the electrolyte, due to the maximum of dissolved polysulfides in the electrolyte at this point [151]. Also due to the electrolytes conductivity, a slight increase of the internal resistance with lower temperatures is reported for a fully charged cell [87]. Additionally shown here is the less pronounced peak for the internal resistance with higher temperatures, presumable caused by the lower electrolyte viscosity. While the internal resistance and double layer capacitance vary only weakly with different rates, the charge transfer resistance R_p differs noticeably. R_p with its similar appearance than R_0 for low currents, is mostly assigned to the thickness of the Li_2S film on the anode, which depends, since high order lithium polysulfides are involved into the re-dissolution of the film, on the amount of dissolved polysulfides. Furthermore, the films conductivity, depending on its surface morphology and the viscosity of electrolyte, matters [85]. The latter is likely due to the also occurring less pronounced peak

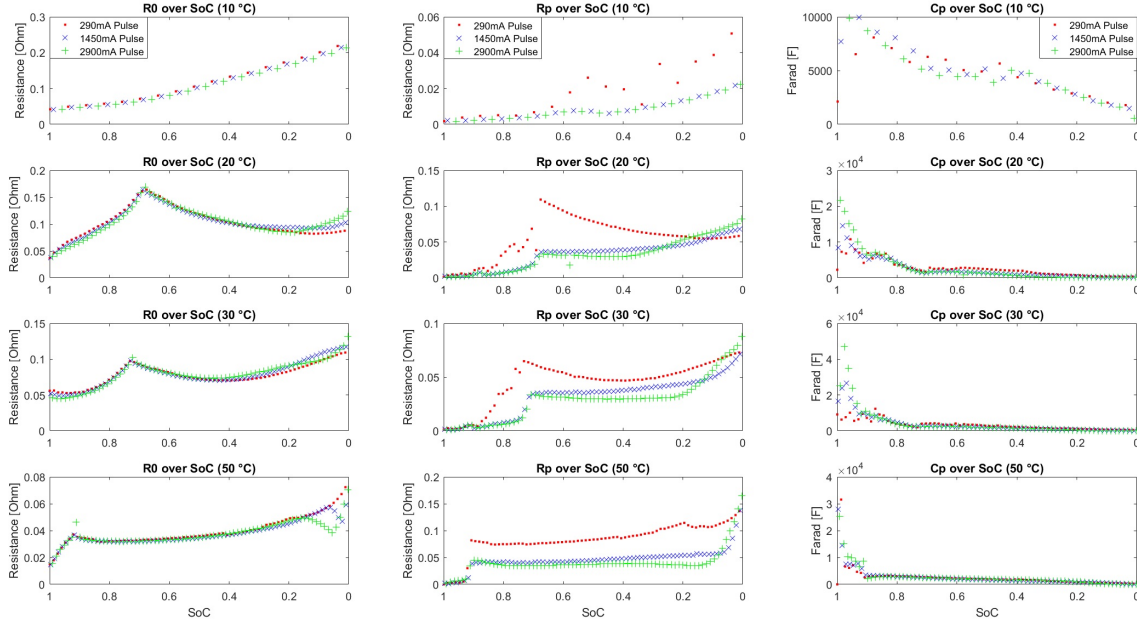


Figure 5.6: Identification results for R_0 , R_p and C_p for each current pulse respectively

with higher temperatures. However, it has to be mentioned that a precise analysis of these effects is difficult since the lagging part of the voltage response contains also diffusion effects. A clear distinction between double layer and diffusion effects is not possible due to the simplified model with just one representing RC circuit. With lower temperatures the usable capacity decreases (see Table 5.1), even when the high plateau can deliver slightly more energy due to a less pronounced shuttle effect. When the temperature gets too low, the increased internal resistance of the cell causes a deeper voltage drop. In our case, by applying discharge currents as 2900 mA, the discharging cut-off voltage of 1.5 V is reached before the beginning of the low voltage plateau. Therefore the usable capacity drops more significantly than reported in [142] and [62], which is mainly due to our test pattern and the higher current pulses we use.

5.7 Model derivation

The derived Li-S cell model excludes the identified parameters for 10 °C due to their large differences to the values of higher temperatures. Therefore, it was skipped for now and is going to be explored more in detail in the future research. It should be noted that temperature is to be used as a constant parameter in this model. Using it as a dynamic fast-varying input may produce unexpected results. (A full electrochemical model would be needed to address this.) The model from 20 °C to 50 °C uses the general state-space representation

$$\begin{aligned}\dot{x}(t) &= \mathbf{A}(t)x(t) + \mathbf{B}(t)u(t) \\ y(t) &= \mathbf{C}(t)x(t) + \mathbf{D}(t)u(t)\end{aligned}\tag{5.41}$$

with added functions for the parameter-variations over the SoC. The usage of functions instead of lookup tables is due to one intended model purpose, the state estimation. The first state in $x = [x_1 x_2]^T$ represents the SoC (X), while the second state represents the transient voltage over the RC circuit (U_p).

$$\begin{aligned}\mathbf{A} &= \begin{bmatrix} 0 & 0 \\ 0 & \frac{-1}{f_{R_p}(X) * f_{C_p}(X)} \end{bmatrix} & \mathbf{B} &= \begin{bmatrix} \frac{-1}{3600Q_{cap}} \\ \frac{1}{f_{C_p}(X)} \end{bmatrix} \\ \mathbf{C} &= \begin{bmatrix} f_{U_{OC}}(X) & -1 \end{bmatrix} & \mathbf{D} &= \begin{bmatrix} f_{R_0}(X) \end{bmatrix}\end{aligned}\tag{5.42}$$

The relationships between the model parameters and the SoC are handled with fitted polynomials,

$$\begin{aligned}f_{\text{parameter}}(X) &= p_{10}x_1^9 + p_9x_1^8 + p_8x_1^7 + p_7x_1^6 + p_6x_1^5 \\ &\quad + p_5x_1^4 + p_4x_1^3 + p_3x_1^2 + p_2x_1 + p_1\end{aligned}\tag{5.43}$$

shown in the matrices A to D, with parameters p_1 to p_{10} . The parameter values are identified by minimizing the squared error between function and identification results with MATLAB [118] for each temperature respectively, summarized in Table 5.2. As shown in Sec. 5.2 and Sec. 5.6, the parameters of Li-S chemistry vary in their patterns between the high- and low plateau. While it is theoretically possible to represent this behaviour with a single polynomial function, the needed degree for a good quality fit would be high. To avoid this without neglecting accuracy, polynomial functions for U_{OC} and R_0 are determined for each plateau separately and combined smoothly and differentiable via a partial sinusoidal function γ .

$$\gamma_{m,c}(X) := \begin{cases} 0, & \text{if a} \\ \frac{1}{2} + \frac{1}{2} \sin(2m(X-c)), & \text{if b} \\ 1, & \text{if c} \end{cases} \quad (5.44)$$

Where the conditions a,b,c stands for the different ranges of the function,

$$\begin{aligned} \text{a : } & 2m(X-c) < -\frac{1}{2}\pi, \\ \text{b : } & -\frac{1}{2}\pi \leq 2m(X-c) < \frac{1}{2}\pi, \\ \text{c : } & 2m(X-c) > \frac{1}{2}\pi, \end{aligned} \quad (5.45)$$

and m is a scaling factor, determining the transition range between both polynomials. The transition point between both functions is determined by c , which leads to the combined function for both polynomials:

$$\begin{aligned} f_{U_{OC}}(X) = & (1 - \gamma_{m,c}(X)) f_{U_{OC-low}}(X) \\ & + \gamma_{m,c}(X) f_{U_{OC-high}}(X) \end{aligned} \quad (5.46)$$

Equally the combined function for R_0 is determined, also using the same γ and c values.

$$\begin{aligned} f_{R0}(X) = & (1 - \gamma_{m,c}(X)) f_{R0-low}(X) \\ & + \gamma_{m,c}(X) f_{R0-high}(X). \end{aligned} \quad (5.47)$$

Since the variations between both plateaus are less pronounced for C_p and less consistent for R_p , the functions for these parameters are only determined with a single polynomial respectively. This decision also simplifies the estimation of the Jacobian matrix of A with foresight to a Kalman filter type state estimation. A further simplification is fitting the polynomial to all pulses, ignoring the discharge current induced fluctuations of R_p . Therefore, the effects of different discharge currents have not been properly represented yet. Figure 5.7 shows the resulting model parameters calculated from the polynomial functions, together with the transition points ($c_{20} = 0.68$, $c_{30} = 0.73$, $c_{50} = 0.92$) for 20 °C, 30 °C and 50 °C. It is easy to spot that the variations between the temperatures changes the battery behaviour significantly. The data suggest that for an interpolation between different temperatures not only the cell capacity Q_{Cap} and the transition points c must be accounted for, but also the shape of the of the polynomial functions itself. Instead of using a two dimensional lookup table to cover for these variations, here the polynomial factors itself are the subject of interpolation.

Each factor is interpolated linearly between 20 °C, 30 °C and 50 °C, leading to a 3×3 one dimensional lookup table for each factor of the polynomial. The values of the lookup tables are given in Table 5.2.

The intended outcome of this method is to change the shape of the parameter functions without influencing their derivability and avoiding the complexity of a two dimensional surface function. Therefore, the presented model can be used for Kalman filter types of estimation [77]. The dotted lines in Figure 5.7 represent these interpolated functions in

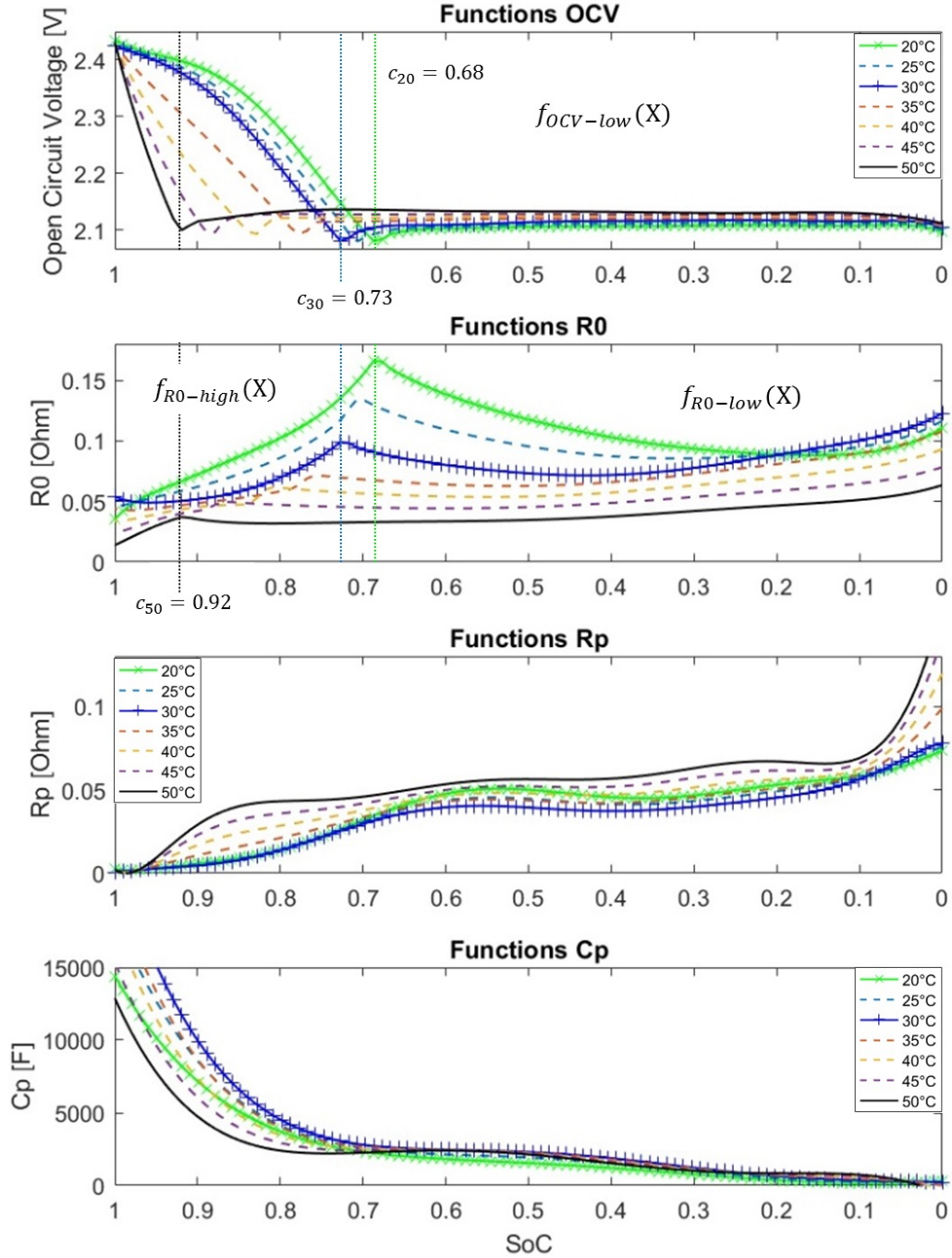
Table 5.2: Parameter functions

Function	T	p_{10}	p_9	p_8	p_7	p_6	p_5	p_4	p_3	p_2	p_1
$f_{U_{OC}-high}$	20					108.1	-361.13	444.73	-238.18	47.03	1.88
	30					100.81	-351.59	452.99	-254.35	52.66	1.92
	50					19.53	-47.78	43.08	-15.5	1	2.1
$f_{U_{OC}-low}$	20	-752.62	2085.66	-2392.87	1466.98	-517.42	105.21	-11.69	0.62	2.1	
	30	-705.23	1997.24	-2329.9	1445.3	-513.3	104.5	-11.55	0.614	2.1	
	50	50.49	-170.36	226.3	-147.74	46.17	-3.8	-1.34	0.32	2.11	
$f_{R0-high}$	20				-1300.2	6470.07	-13362.95	14656.94	-9000.23	2931.67	-395.24
	30				1408.02	-7176.99	15213.74	-17168.84	10880.87	-3673.08	516.32
	50				29.22	-98.6	122.81	-67.96	15.53	-1.06	0.07
f_{R0-low}	20				12.96	-28.54	25.46	-11.65	3.09	-0.42	0.11
	30				14.05	-32.34	28.45	-11.77	2.5	-0.38	0.123
	50				3.597	-9.988	10.631	-5.419	1.393	-0.216	0.063
f_{R_p}	20	140.636	-613.186	1088.525	-1005.911	512.386	-139.174	16.887	-0.011	-0.223	0.074
	30	102.35	-489.63	968.695	-1024.135	624.963	-222.05	43.585	-3.75	-0.11	0.08
	50	270.48	-1110.38	1837.41	-1538.71	643.71	-80.4	-34.99	14.73	-2.02	0.16
f_{C_p}	20					89414.28	-113090.73	25401.28	15392.5	-3017.3	306.23
	30					237957.9	-384453.35	193837.3	-27322.65	2574.15	216.5
	50					373976.04	-799532.2	605077.98	-193678.92	27646.74	-617.5

5 °C intervals, only using the linear interpolation of p_1 to p_{10} and the transition points c . For the sake of completeness however, it must be mentioned that due to the lack of experimental data for 40 °C the polynomials and transition points between 30 °C and 50 °C had been manually tweaked.

5.8 Model validation

To test the model for real life applications another OXIS pouch cell is discharged under different conditions. As main changes to the previous measurements used for the

Figure 5.7: Parameter functions for U_{OC} , R_0 , R_p and C_p over SoC

model identification (i) a more realistic current profile is applied, based on the NEDC drive-cycle, (ii) the temperature controlled environment is neglected, allowing the cell to vary slightly around room temperature (23 °C) and (iii) different discharge hardware (a Kepco BOP 100-10MG) is used. The NEDC drive-cycle is selected because it represents a realistic user scenario but also contains some level of abstraction [152] [153].

NEDC-based current profile:

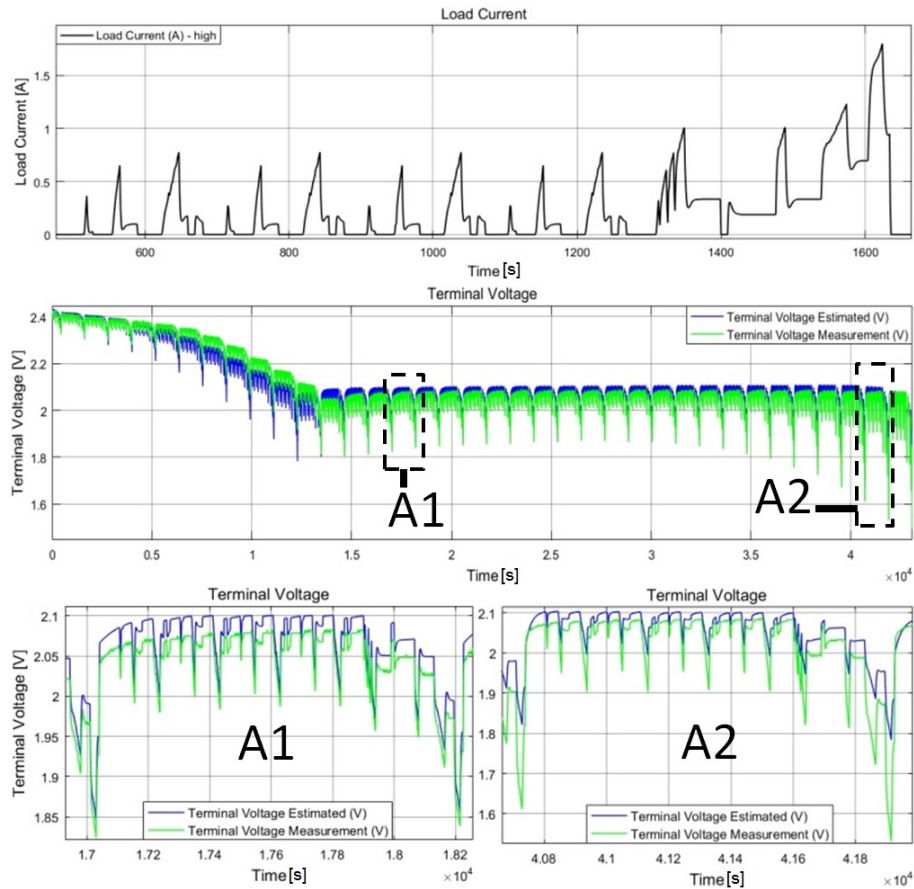


Figure 5.8: Battery model and measured terminal voltage for 23 °C

The results of the Simulink model [154], together with the measured battery terminal voltage is shown in Figure 5.8. As it indicates, there is no energy recovery while braking and the chosen currents are relatively small. Nevertheless the average discharge power is with 0.324 W an order of magnitude larger than the mixed pulse discharge test (0.147 W).

The model accuracy was quantified in terms of the root mean error (RMSE):

$$\text{RMSE} = \frac{1}{\sqrt{n}} \left(\sum_{i=1}^n (V_{t,i} - \hat{V}_{t,i})^2 \right)^{0.5} \quad (5.48)$$

Where n is the number of data points, $V_{t,i}$ is the measured voltage and $\hat{V}_{t,i}$ is the model prediction for the voltage at that point. The model was found to give an RMSE of 32 mV. This is small compared to the overall voltage range. Despite the simplifications of only one RC circuit with neglected current dependencies of R_p , the transient voltage is represented well during the entire discharge range. However, some specific properties of Li-S batteries, as mentioned in Section 2, enhance the model error in certain regions (Fig. 5.8 A1 A2). While the origins of the increasing deviation towards the end of the high plateau, likely due to the self discharge caused the polysulfide shuttle effect, are relatively well understood, the reasons for the deviations in the low plateau are more unclear. There, mostly the decreasing voltage and the increased cell resistance are noticeable. The explanation for the first is difficult due to the difficult-to-define value of the open circuit potential. One observation, noticeable for the tested OXIS cells, is that the voltage in the low plateau, given enough time, always returns to 2.1 V when left in open circuit condition. The behaviour with infinitesimally small (but non-zero) currents should be close or similar but differs towards the voltage profile of Figure 5.2. Since these small discharge currents can cause the voltage to decrease towards the end of discharge, the increased error is presumably caused by the discharge current profile, leaving significantly less relaxation time, and the discharge hardware, allowing a flow of small and unmeasured (5 - 10 mA) leakage currents. Since these are also likely when an electric vehicle is not moving but in the switched on state, a more practical definition of the OCV, considering these small currents, might be a solution. The reason for the increased cell resistance towards the end is likely due to the different current profile as well but also can be in

relation with cell variations. Nevertheless, the proposed battery model, representing the current understanding of Li-S batteries, shows good quality fit with small errors for the simplifying assumptions made and can be potentially used for a Li-S based BMS system.

5.9 Conclusion

After showing the differences of Li-S batteries to the current Li-ion ones, the challenges towards an operational model, capable of predicting the voltage response, capacity, power capability and degradation are presented. As an initial step to address some of them, this study proposes a new robust and easy to tune battery model structure, capable of accounting for differences between the start and end of a discharge pulse. This 'behavioural' model, in combination with the PEM identification method, is used to identify the parameters of a Thevenin equivalent circuit model for different temperatures. Due to a mixed pulse discharge profile, the current dependencies of the parameters could also be revealed. Subsequently, the data is used to create a simplified battery model with polynomial functions for its parameters, which are interpolated for different temperatures. Despite the rather complex nature of the Li-S battery, the validation of the simplified model with a more realistic current profile displays a low estimation error, suggesting that some simplifications in favour for computational- or modelling-effort are possible. Nevertheless, it is also shown that for a precise estimation of the terminal voltage Li-S specific properties like self discharge in the high plateau, the OCV definition in the low plateau and the current profile dependency of the model parameters should be further investigated. Therefore, our further goals towards a usable Li-S compatible BMS system are improvements of the model itself, through implementing self discharge and current effects, and the application of the model as an observer for state of charge and state of health estimation. For a usage of these in a highly demanding environment of an electric vehicle, also the

charge behaviour needs to be investigated.

5.10 Acknowledgement

This research was undertaken as part of the Revolutionary Electric Vehicle Battery (REVB) project, co-funded by Innovate UK under grant TS/L000903/1; university funding is provided by EPSRC under grant number EP/L505286/1 . Enquiries for access to the data referred to in this article should be directed to researchdata@cranfield.ac.uk.

6

Paper 2 – KF based SoC estimation

Kalman-variant estimators for state of charge in lithium-sulfur batteries

Authors:

Karsten Propp, Daniel J. Auger, Abbas Fotouhi, Stefano Longo, Vaclav Knap

The paper has been published in the
Journal of Power Sources Vol. 343, pp. 254-267, 2017

Abstract

Lithium-sulfur batteries are now commercially available, offering high specific energy density, low production costs and high safety. However, there is no commercially-available battery management system for them, and there are no published methods for determining state of charge *in situ*. This paper describes a study to address this gap. The properties and behaviours of lithium-sulfur are briefly introduced, and the applicability of ‘standard’ lithium-ion state-of-charge estimation methods is explored. Open-circuit voltage methods and ‘Coulomb counting’ are found to have a poor fit for lithium-sulfur, and model-based methods, particularly recursive Bayesian filters, are identified as showing strong promise. Three recursive Bayesian filters are implemented: an extended Kalman filter (EKF), an unscented Kalman filter (UKF) and a particle filter (PF). These estimators are tested through practical experimentation, considering both a pulse-discharge test and a test based on the New European Driving Cycle (NEDC). Experimentation is carried out at a constant temperature, mirroring the environment expected in the authors’ target automotive application. It is shown that the estimators, which are based on a relatively simple equivalent-circuit-network model, can deliver useful results. If the three estimators implemented, the unscented Kalman filter gives the most robust and accurate performance, with an acceptable computational effort.

6.1 Introduction

Compared to today's widespread lithium-ion (Li-ion) battery technologies, lithium-sulfur (Li-S) offers increased specific energy storage capability [146]. A greater battery capacity is often advantageous, particularly in applications such as electric vehicles, where it can mitigate consumer concerns about driving range. Li-S batteries also have significant benefits in terms of their wide operational temperature window and safety [140]. The fact that sulfur is abundant and environmentally friendly is also attractive for large-scale cost-driven consumer applications. Commercialization has been hindered by the limitations of early-stage Li-S technologies such as quick degradation and limited sulfur utilization [59]. In recent years, considerable effort has been put into the exploration Li-S's inner cell mechanisms, resulting in enhanced understanding [129]. Commercial cells are now available from suppliers such as OXIS Energy [70] and Sion Power [155]. Although today's cells may not fulfil every aspect of high automotive demands, they do open the opportunity for practical application oriented research.

In order to use a battery in a practical application, it is necessary to have an appropriate battery management system (BMS). A key function of the BMS is determining the remaining usable capacity of the battery, i.e. estimation of the state of charge (SoC). This is important for many reasons: the more accurately SoC is known, the greater the proportion of a battery that can be potentially utilized without fear of overcharging and over-discharging; for consumers, it is often helpful to know how much battery life remains.

In the automotive sector in particular, there has been much research on accurate and robust SoC estimation techniques for Li-ion batteries, aimed at meeting the demanding requirements of the automotive traction battery. Here, the batteries operate in an environment with varying power loads, different operation temperatures, noisy and crude

measurements, and high safety requirements [77]. For systems with limited computational power, the SoC of a Li-ion battery can be estimated through the use of equivalent-circuit-networks (ECNs) [92, 124], which simulate the voltage response of the battery. Due to their simplicity they are not able to give any insight into the inner cell reactions. However, in practice this does not matter: when operated within their specified limits—in terms of state-of-charge, temperature and current rates—performance of intercalation-based lithium-ion batteries is consistent and predictable [81, 96, 138, 143]. This behaviour and the fact that the nonlinear relationship between open-circuit voltage (OCV) and SoC is monotonic means that it is relatively straightforward to determine a Li-ion batteries SoC [137].

For Li-ion batteries, there are many viable techniques for estimating SoC *in situ*. The simplest is to measure the open-circuit voltage and relate it through a nonlinear function or lookup table to the SoC. However, this method needs the battery to be in resting condition which limits the applicability for electric vehicles while driving. For improved robustness, OCV-based estimation is combined with other methods [79]. For a given value of SoC, ECN models can be used to predict terminal voltage output from a known dynamically-changing input current. This can be used to estimate SoC with a good compromise between accuracy, robustness and simplicity. A powerful approach is the use of ‘observers’ or ‘state estimators’ which combine model-based estimation with actual measurements using principles derived from control theory, particularly the Kalman filter and its derivatives. Estimators of this kind are popular (particularly within the automotive environment) due to their ability to handle measurement noise and model inaccuracies [77]. With these estimation methods, a high battery utilization is possible, without compromising battery safety or lifetime [101].

To date, estimation techniques of this kind have not been applied to Li-S batteries. There are big differences between Li-S and the classic Li-ion chemistry. Li-ion has is

an intercalation based process that has a single well-known dominant reaction pathway. Li-S batteries however are more complex with multiple pathways [55], which leads to some unusual and challenging behaviour for the SoC estimation: (i) the OCV-SoC curve has two voltage ‘plateaus’ with different properties; (ii) the OCV-SoC curve has a large flat region, where the OCV does not change with SoC; (iii) the batteries exhibit relatively high self discharge; and (iv) the usable capacity and power exhibit sensitivity to the applied current profile. Until recently, there have been no models of a Li-S cell suitable for use in a battery management algorithm. Recent developments have been made, and there are now published ECN models of Li-S batteries during discharge that are valid for a range of temperatures [17]. However, the use of these for the estimation of SoC, remains unexplored. As initial step towards a full BMS system for Li-S batteries, this study examines SoC estimation techniques for their applicability for Li-S batteries.

In this paper, Sec. 6.2 introduces Li-S batteries and their properties. Sec. 6.3 explores the applicability of state-estimation techniques used for lithium-ion, noting the limitations with OCV measurement and ‘Coulomb counting’ and concluding that a more sophisticated approach is required. Sec. 6.4 describes the filtering techniques that will be used for estimation: Sec. 6.4.1 describes an equivalent circuit model that will be used to implement such filters, and Sec. 6.4.2–6.4.4 introduces three such filters: the extended (nonlinear) Kalman filter (EKF), the ‘unscented’ Kalman filter (UKF) and the particle filter (PF). Sec. 6.5 describes the experimental evaluation of these. The results are presented in Sec. 6.6 where their performance and applicability is discussed.

This work has been conducted as part of an automotive battery project, and the batteries used in this study are kept at a well-maintained constant temperature environment. Accordingly, the work in this paper has been restricted to a constant temperature. (In future work, this could be extended to a varying temperature environment.)

The key contribution of this paper is the development and analysis of these three

recursive Bayesian SoC estimators for Li-S. To the best of the authors' knowledge, no similar work has appeared elsewhere in the literature.

6.1.1 Contributions

1. Evaluation of challenges for SoC estimation for Li-S batteries
2. Implementation of EKF, UKF and PF for SoC estimation
3. Evaluation of different applied SoC estimation techniques

6.2 Lithium-sulfur batteries

A Li-S battery consists of a lithium metal anode and a sulfur-based cathode in electrolyte. Sulfur reversibly reacts with lithium ions when reduced from elemental state S_8 , via the intermediates Li_2S_8 , Li_2S_4 , Li_2S_2 , to lithium sulfide Li_2S , which is the key of the high theoretical capacity of sulfur (1672 mAh g^{-1}) [130]. The large number of different species however, lead to complex inner reactions that are still a matter of ongoing research [55]. As shown in Fig. 6.1, the discharge curve consists of two sections [132]: a high plateau at about 2.35 V OCV, characterized by the presence of a majority of high order polysulfides in solution (Li_2S_8 , Li_2S_6), and a low plateau at around 2.15 V OCV, where lower order chains have been identified (Li_2S_4 , Li_2S_3) [133]. In Li-S batteries the availability of these species in the electrolyte determine the performance. In simple words, the cathode is dissolving and participating in electrolyte [95], which causes two voltage plateaus with different behaviour (usable capacity, internal resistance, self-discharge, transient behaviour) [131, 53]. As an initial step to model these effects, an equivalent circuit model

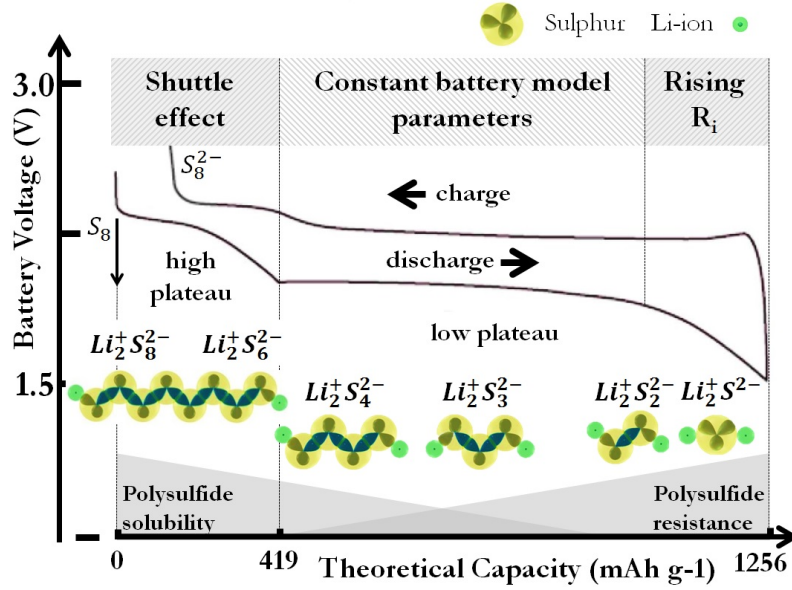


Figure 6.1: Discharge/charge behaviour of a Li-S battery.

was presented recently, employing the Thevenin model structure with a pulse discharge current profile and an off-line prediction error minimisation method for parameter identification [17]. The model does not explicitly consider self-discharge, but is valid for transient behaviour of the kind seen in this study. In practice, lithium-sulfur batteries do experience significant self-discharge during long resting periods. For a shorter-term transient state estimation problem, this can be treated as uncertainty regarding the initial state. For details regarding the model derivation the reader is guided there.

Due to these unique properties of Li-S batteries, a precisely known SoC is helpful to predict the power capabilities of the battery, especially towards the end of discharge where the internal resistance raises quickly. It is not just near depletion that SoC estimation is important. Li-S batteries also need careful monitoring when they are close to fully charged to avoid the problem of ‘shuttle’. While charging, the high solubility of the formed high order polysulfide chains enables them to diffuse to the anode, where they can be reduced to lower order chains directly when in contact. The reaction circle is closed

by the movement of the lower order chains back to the cathode. Here, they form high order polysulfides again when the charging is continued. This redox reaction occurs without electrons passing through the external circuit of the battery and is called polysulfide shuttle [61], which leads, next to self-discharge in the high plateau, to poor coulombic efficiency and is associated with capacity fade [136]. Therefore, overcharging should be avoided despite the fact that the shuttle effect can also protect the battery from being overcharged [130].

6.3 Applicability of conventional SoC estimation techniques

The behaviour of Li-S batteries discussed above leads to difficulties for SoC estimation. Each method faces different challenges: in the following section, these are explained in more detail for the most common SoC estimation techniques. (Impedance spectroscopy is not mentioned further, since it is seldom implemented for practical SoC estimation [79].)

Coulomb counting: Determining the charge flow in and out of the battery is the most common technique since it is easy to implement. With a given starting point SoC_0 and the rated capacity, it is fairly simple to calculate the SoC with

$$SoC = SoC_0 + \frac{1}{C_N} \int_{t_0}^t (I_{\text{batt}} - I_{\text{loss}}) d\tau. \quad (6.1)$$

Where C_N is the rated capacity, I_{batt} the battery current and I_{loss} the current consumed by loss reactions [79]. While this method is seen generally as reliable, it demands high precision current sensors (to reduce the accumulation of measurement errors over time), known values for the charge/discharge efficiency, and a precisely known initial condition [156, 157]. These drawbacks lead to issues with the unique properties of Li-S batteries.

6.3. APPLICABILITY OF CONVENTIONAL SOC ESTIMATION TECHNIQUES 125

Firstly, the polysulfide shuttle effect [61], mainly present in the high plateau, enhances self-discharge, poor coulombic efficiency and capacity fade [136, 61]. This leads to hard to determine values for the I_{loss} or efficiency factors in the calculation and changing initial conditions for an estimator [158]. Secondly, the amount of sulfur that can be reversibly utilised during a discharge is strongly affected by the current profile, age and temperature [139]. Generally high discharge capacity is only obtained at low currents. High currents can produce a resistive layer on the cathode, hindering the utilisation of the underlying sulfur [132]. This effect hampers the determination of the rated capacity, reducing the practicability of the Coulomb counting method itself significantly.

Open circuit voltage: Another common method of SoC estimation is to assign the OCV to the SoC. This is usually used in applications with low and constant currents or long resting periods. This method works well with Li-ion batteries, since they provide generally a monotonic rising relationships between OCV and SoC [137]. For Li-S however, this method is not feasible due to the non-monotonic curve, changing the gradient between the high and low plateau, and the stable OCV within the low plateau (Fig. 6.1). Furthermore, the whole concept of OCV for Li-S batteries is not clear due to self-discharge and precipitation [95].

Soft computing techniques: Avoiding the need for building a mathematical battery model and linearisation, soft computing techniques have the ability to model a highly non-linear system by establishing a relationship between the input and output of a system (a ‘black-box’ model) from training data. This makes these techniques suitable for consideration for battery applications. Particularly for SoC estimation, soft computing techniques have been used in previous studies for NiMH and Li-ion batteries [159, 160]. However, there is no record in the literature where these techniques are used for Li-S batteries. (In [161], the idea is briefly proposed. However, estimation results are not presented.)

Model-based approaches: For the SoC estimation in highly dynamic environments,

model-based solutions with a combination of adaptive algorithms are used. Their principle is based on an off-line established model, predicting the terminal voltage of the cell during operation and an adaptive algorithm, using the error between prediction and measurement to adjust the states. As the computational power of common BMSs are limited, simplified equivalent electrical circuits are often used to reproduce the transient behaviour of a battery [76, 128]. In combination with algorithms such as the extended Kalman filter [162, 163, 164], unscented Kalman filter [165, 166, 167] and particle filter [168, 169, 170] ECN models can help to estimate the batteries internal states with relatively low computational effort and simple measurements of current and terminal voltage. The main advantage of model based methods is that they combine the benefits of direct voltage measurements and 'Coulomb counting' through the use of equivalent-circuit-network models, providing a formal framework for integrating model-based predictions with real-world voltage measurements. This may make them suitable for the properties of the Li-S chemistry. The principle behind these estimation algorithms is described in the following section.

6.4 Implementation of state estimators

As outlined in Sec. 6.2 and Sec. 6.3, Li-S batteries have poorly understood internal dynamics, and state-of-the-art ECN models that cannot represent every aspect of the cell in detail. Methods that have been found to be robust against unmodeled dynamics in the environment are recursive filters [107], that treat the model states x and the observations y as stochastic variables with associated probability density functions [104]. For Gaussian distributions, the Kalman filter (KF), minimizing the error variance between true and estimated state, is heavily applied in battery state estimation. In such estimates, the process state is first estimated from a mathematical representation of the system dynamics; this

is then corrected with feedback from measurements. The continuous model, described in Sec. 6.4.1, is used in its discrete form for propagation of prediction- and update-step.

$$\begin{aligned}x_k &= Ax_{k-1} + Bu_{k-1} + w_{k-1} \\y_k &= Cx_k + v_k\end{aligned}\tag{6.2}$$

The additional terms w_k and v_k are random variables – white, zero mean, with normal distributions—representing process and measurement noise respectively. These describe the uncertainty in each equation. Their values are determined with the process noise covariance matrix Q and measurement noise covariance matrix R , which are usually assumed to be constant and chosen by the user. Simply speaking, the determined values affect whether the Kalman filter emphasises its ‘trust’ on feedback from measurements or the *a priori* estimates from the system model. Larger values indicate higher uncertainty or less trust in general. Referring to [171], the Kalman filter equations are:

Time update equations:

$$\hat{x}_k^- = A\hat{x}_{k-1}^+ + Bu_{k-1}\tag{6.3}$$

$$P_k^- = AP_{k-1}^+A^T + Q\tag{6.4}$$

Measurement update equations:

$$L_k = P_k^- C^T (CP_k^- C^T + R)^{-1}\tag{6.5}$$

$$\hat{x}_k^+ = \hat{x}_k^- + L_k(y_k - C\hat{x}_k^-)\tag{6.6}$$

$$P_k^+ = (I - L_k C)P_k^-\tag{6.7}$$

The beauty of the filter is that it provides an efficient recursive mean, minimizing the mean of the squared error, by supporting past, present and future states, even when the

precise nature of the modelled system is unknown [171]. For the state estimation of Li-S batteries the nonlinear derivatives of the KF [172] (EKF, UKF) and the particle filter (PF) are employed.

The following describes the mathematics of the three recursive filters that were implemented. All three algorithms use the same nonlinear equivalent-circuit-network model (Sec. 6.4.1); the three algorithms are the extended Kalman filter (Sec. 6.4.2), the unscented Kalman filter (Sec. 6.4.3) and the particle filter (Sec. 6.4.4).

6.4.1 Equivalent-circuit-network model

The Li-S battery model, used in this work, is developed and described in detail in [17] and Chapter 5 of this thesis for temperatures from 20 °C to 50 °C. Here however, the temperature is assumed to be constant, assuming a controlled BMS environment at 20 °C. The identification for a Thevenin equivalent circuit model (Fig. 6.2) was done with a similar mixed current pulse discharge as shown in Fig. 6.3-A. The mixed pulse pattern in combination with identification for each pulse individually is used to unveil current-dependent parameter changes in the model. There is self-discharge, defined as current flow (I_{self}) inside the battery, but it is only significant during long resting periods, so I_{self} can be neglected for transient applications. Fig. 6.2 shows the identification results, as well as the chosen simplified parameter functions over the SoC (X) for the modelled parameters. For the observer the identified parameters of all pulses are used to fit polynomial functions over SoC for the open circuit voltage U_{OCV} , the internal resistance R_0 and one parallel RC circuit C_p and R_p with MATLAB [118]. Then the derived functions are included in

the general state-space form

$$\begin{aligned}\dot{x}(t) &= A(t)x(t) + B(t)u(t) \\ y(t) &= C(t)x(t) + D(t)u(t).\end{aligned}\tag{6.8}$$

The dynamic states $x = [x_1 \ x_2]^T$ of the system are the voltage over the RC circuit U_p and the SoC (X), calculated through Coulomb counting. The corresponding state space representation gives

$$\begin{aligned}A &= \begin{bmatrix} \frac{-1}{f_{R_p}(X) f_{C_p}(X)} & 0 \\ 0 & 0 \end{bmatrix} & B &= \begin{bmatrix} \frac{1}{f_{C_p}(X)} \\ \frac{-1}{3600Q_{\text{cap}}} \end{bmatrix} \\ C &= \begin{bmatrix} -1 & f_{\text{OCV}}(X) \end{bmatrix} & D &= \begin{bmatrix} f_{R_0}(X) \end{bmatrix}.\end{aligned}\tag{6.9}$$

In [17] it was shown that the current dependencies of the model parameters mostly influence the transient voltage behaviour, represented by C_p and R_p , and that they can be neglected without compromising the accuracy of the model significantly. But because of the parameter patterns of U_{OCV} and R_0 vary strongly between the high- and low plateau (Fig. 6.2), two separate polynomials were fitted over the SoC for each plateau respectively. (A single polynomial would be impractical, since behaviour changes significantly between the plateaus.) The transition between the polynomials is realized smoothly and differentially via a partial sinusoidal function γ

$$\gamma_{m,c}(X) := \begin{cases} 0, & \text{if a} \\ \frac{1}{2} + \frac{1}{2} \sin(2m(X - c)), & \text{if b} \\ 1, & \text{if c} \end{cases}\tag{6.10}$$

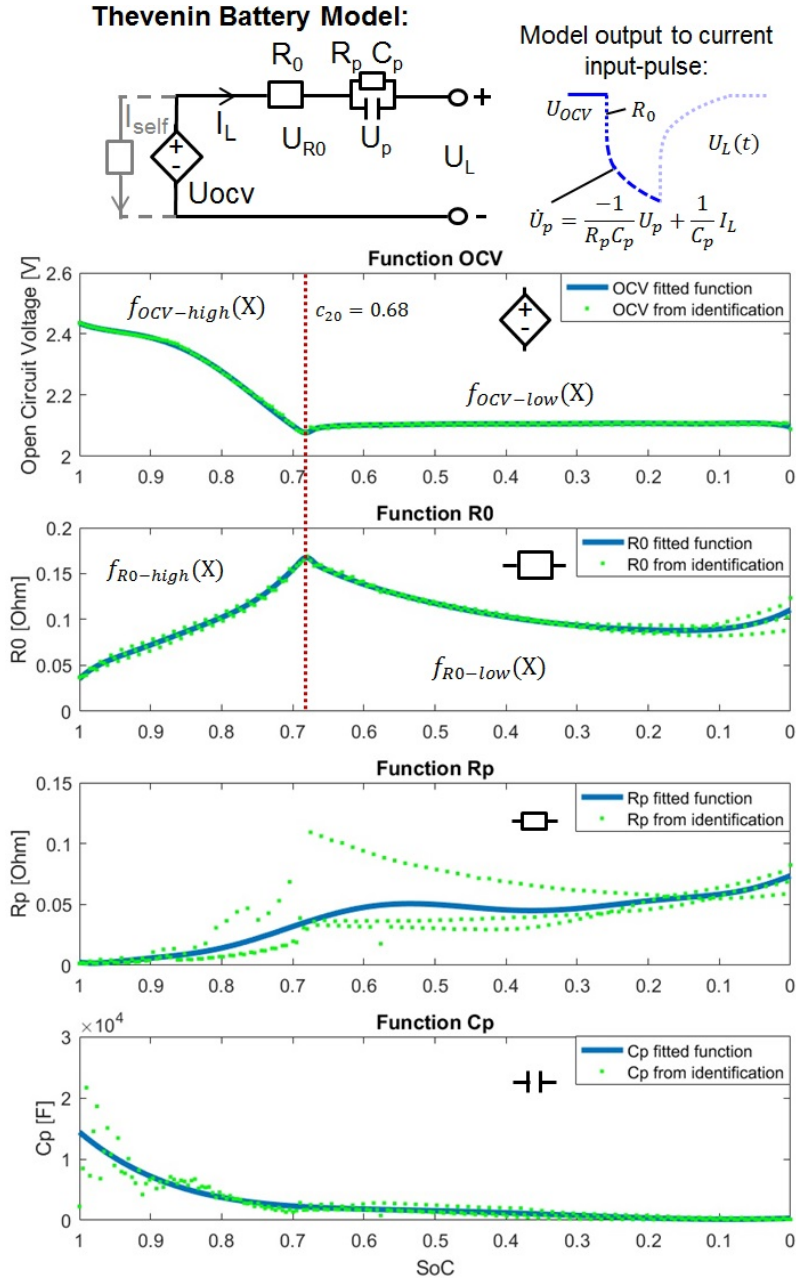


Figure 6.2: Model and parameter functions for U_{OCV} , R_0 , R_p and C_p over SoC for 20 °C.

where the conditions a, b, c stands for the different ranges

$$\begin{aligned}
 \text{a : } & 2m(X - c) < -\frac{1}{2}\pi, \\
 \text{b : } & -\frac{1}{2}\pi \leq 2m(X - c) < \frac{1}{2}\pi, \\
 \text{c : } & 2m(X - c) > \frac{1}{2}\pi,
 \end{aligned} \tag{6.11}$$

and m is a scaling factor for the maximal gradient of the sinusoidal function, determining the transition range between both polynomials. c represents the point where both functions are equally represented. The combined equations of both polynomials and factor γ are

$$\begin{aligned}
 f_{\text{OCV}}(X) = & (1 - \gamma_{m,c}(X)) f_{\text{OCV-low}}(X) \\
 & + \gamma_{m,c}(X) f_{\text{OCV-high}}(X)
 \end{aligned} \tag{6.12}$$

for the open circuit voltage U_{OCV} and

$$\begin{aligned}
 f_{R0}(X) = & (1 - \gamma_{m,c}(X)) f_{R0-low}(X) \\
 & + \gamma_{m,c}(X) f_{R0-high}(X),
 \end{aligned} \tag{6.13}$$

for the internal resistance R_0 over SoC. Since the variations between both plateaus are less pronounced for C_p and R_p , the functions for these parameters are only determined with a single polynomial respectively. This decision also simplifies the estimation of the Jacobian matrix of A for the extended Kalman filter.

For a fuller discussion of this ECN model, the reader is referred to the original source [17].

6.4.2 Extended Kalman filter

The basic Kalman filter algorithm, described in Sec. 6.4, applies to linear systems, not nonlinear systems. The Li-S equivalent-circuit-network is *nonlinear*. This means that the basic algorithm needs adaptation before it can be applied. There are several ways of doing this, which will be explored in the following sections. The simplest is the ‘extended Kalman filter’ (EKF).

The basic idea of the EKF is to linearise the system around the current mean of the state \hat{x}_{k-1}^+ with a first order Taylor series for the propagation of the probability densities [114]. Hence, the EKF predicts the states and measurements with a nonlinear system model f and the covariances and Kalman gain with the Jacobians of A and C , \hat{A} and \hat{C} . Generally this linearisation works well with models containing slight non-linearities as it is the case for most classic Li-ion batteries.

Determining the Jacobians of matrices A and C increases the effort for setting up the filter with the benefit of the lowest computational effort of the proposed methods.

Summary of EKF algorithm

In the following, the algorithm is summarized from [101]. (Details are omitted here for brevity, but can be found in the reference.)

Nonlinear state space model

$$x_k = f(x_{k-1}, u_{k-1}, w_{k-1}, k-1) \quad y_k = h(x_k, u_k, v_k, k)$$

Definitions

$$\hat{A}_k = \left. \frac{\partial f(x_k, u_k, w_k, k)}{\partial x_k} \right|_{x_k = \hat{x}_k^+}, \hat{B}_k = \left. \frac{\partial f(x_k, u_k, w_k, k)}{\partial w_k} \right|_{w_k = \bar{w}_k},$$

$$\hat{C}_k = \left. \frac{\partial h(x_k, u_k, w_k, k)}{\partial x_k} \right|_{x_k = \hat{x}_k^-}, \hat{D}_k = \left. \frac{\partial h(x_k, u_k, w_k, k)}{\partial v_k} \right|_{v_k = \bar{v}_k}$$

Initialisation for $k = 0$

$$\hat{x}_0^+ = \mathbb{E}[x_0], \quad P_0^+ = \mathbb{E}[(x_0 - \hat{x}_0^+)(x_0 - \hat{x}_0^+)^T]$$

Computation EKF for $k = 1, 2, \dots$

$$\text{State estimate update: } \hat{x}_k^- = f(\hat{x}_{k-1}^+, u_{k-1}, \bar{w}_{k-1}, k-1)$$

$$\text{Error covariance update: } P_k^- = \hat{A}_{k-1} P_{k-1}^+ \hat{A}_{k-1}^T + \hat{B}_{k-1} Q \hat{B}_{k-1}^T$$

$$\text{Output estimate: } \hat{y}_k = h(\hat{x}_k^-, u_k, v_k, k)$$

$$\text{Kalman Gain matrix: } L_k = P_k^- \hat{C}_k^T [\hat{C}_k P_k^- \hat{C}_k^T + \hat{D}_k R_k \hat{D}_k^T]^{-1}$$

$$\text{State estimate measurement update: } \hat{x}_k^+ = \hat{x}_k^- + L_k [y_k - \hat{y}_k]$$

$$\text{Error covariance measurement update: } P_k^+ = (I - L_k \hat{C}_k) P_k^-$$

6.4.3 Unscented Kalman filter

To improve the estimation for nonlinear systems, the covariance propagation in the UKF follows the nonlinearities with a set of sigma points, propagated through the main steps of the algorithm. The number of necessary points depends on the state vector's dimension L and leads to $2L + 1$ columns for the resulting vector χ . With the principle of estimating covariances with data rather than a Taylor series, the unscented Kalman filter has the advantage that no derivatives are needed, with only slightly more computational effort. Furthermore, the covariance approximations are usually better than these of the EKF [101]. The differences between both are largely dependent on the nonlinearity of the system. For standard Li-ion batteries for example, the improvements are modest due to their small non-linearities [101].

Summary of UKF algorithm

In the following the algorithm is summarized from [115]. (Again, details are omitted here for brevity, but can be found in the reference.)

Nonlinear state space model

$$x_k = f(x_{k-1}, u_{k-1}) + w_{k-1} \quad y_k = h(x_k, u_k) + v_k$$

Definitions

$$Q_k = \mathbb{E}[w_k w_k^T] \quad R_k = \mathbb{E}[v_k v_k^T]$$

Initialisation

$$\hat{x}_0^+ = \mathbb{E}[x_0]$$

$$P_0^+ = \mathbb{E}[(x_0 - \hat{x}_0^+)(x_0 - \hat{x}_0^+)^T]$$

Computation UKF for k = 1, 2, ...**State estimate time update**

$$\text{Error covariance matrix square root: } \sqrt{P_{k-1}} = \text{chol}(P_{k-1})$$

Create sigma points:

$$\chi_{k-1}^+ = \left[\hat{x}_{k-1}^+, \hat{x}_{k-1}^+ + \gamma \sqrt{P_{k-1}^+}, \hat{x}_{k-1}^+ - \gamma \sqrt{P_{k-1}^+} \right]$$

Update sigma points: $\chi_k^{i,-} = f(\chi_{k-1}^{i,+}, u_{k-1})$ for $i = 0, 1, 2, \dots, 2L$

Mean of updated sigma points: $\hat{x}_k^- = \sum_{i=0}^{2L} \alpha_i^{(m)} \chi_k^{i,-}$

Error Covariance time update

Covariance prediction:

$$P_k^- = Q_{k-1} + \sum_{i=0}^{2L} \alpha_i^{(c)} (\chi_k^{i,-} - \hat{x}_k^-)(\chi_k^{i,-} - \hat{x}_k^-)^T$$

Output estimate

Measurement prediction for each sigma point:

$$\psi_k^i = h(\chi_k^{i,-}, u_k) \text{ for } i = 0, 1, 2, \dots, 2L$$

Mean of the measurement prediction: $\hat{y}_k = \sum_{i=0}^{2L} \alpha_i^{(m)} \psi_k^i$

Estimator gain matrix

Estimate the covariance of measurement:

$$P_k^{yy} = R_k + \sum_{i=0}^{2L} \alpha_i^{(c)} (\psi_k^i - \hat{y}_k)(\psi_k^i - \hat{y}_k)^T$$

Estimate cross covariance state/measurement:

$$P_k^{xy} = \sum_{i=0}^{2L} \alpha_i^{(c)} (\chi_k^{i,-} - \hat{x}_k^-)(\psi_k^i - \hat{y}_k)^T$$

Kalman gain: $L_k = P_k^{yy}(P_k^{xy})^{-1}$

State estimate update: $\hat{x}_k^+ = \hat{x}_k^- + L_k(y_k - \hat{y}_k)$

Error covariance update: $P_k^+ = P_k^- - L_k P_k^{yy} L_k^T$

6.4.4 Particle filter

To solve the recursive estimation problem for arbitrary probability distributions, the PF applies Monte Carlo methods to represent the probability density functions. Unlike the UKF, where just the means and covariances of the sigma points are transferred to the next step, the PF recursively estimates the whole particle set χ_t from the last step χ_{t-1} . Generally three steps are executed [173]. (i) The state transition, where each particle transition is calculated with the input u_{k-1} , after measurement noise is added to the particles of the previous step. Similar to the Kalman filter, the addition of the noise leads to an increasing variance over time. (ii) In the weighting step the observations y_k and a probability density function are used to allocate a weight for each particle, representing the probability state prediction x_k given a certain observation y_k . (iii) During resampling, the variance of the particle set is decreased by sampling a new set of particles according to their weights and allocating new, equal weights. The main advantage of the PF is the independence of the Gaussian noise assumption of the Kalman filter. However, since each particle has to be computed separately, the computational effort exceeds the Kalman filter type algorithms significantly [174].

Summary of PF algorithm

The derivation of the equations orient on Chapter 4.2 of the textbook [116]. (Again, details are omitted here for brevity, but can be found in the reference.) $\bar{\chi}_k = \chi_k = \emptyset$

for $m = 1$ to M do

sample $x_k^m \approx p(x_k | u_k, x_{k-1}^m)$

$w_k^m = p(y_k | x_k^m)$

$\bar{\chi}_k = \bar{\chi}_k + \langle x_k^m, w_k^m \rangle$

endfor

for $m = 1$ to M do

draw i with probability $\propto w_k^i$

add x_k^i to χ_k

endfor

return χ_k

6.5 Experimental evaluation

To investigate the performance of the state estimation algorithms, batteries were discharged with two current profiles and different test rigs. The first, a mixed-current pulse test, is based on the parameter estimation in [17] and represents an abstract test in a controlled environment. Here, a pre-cycled (C/10 charge, C/5 discharge, 30 °C) 3.4 Ah long life chemistry pouch cell from OXIS Energy was tested with current pulses of 290 mA, 1450 mA and 2900 mA at 20 °C (Fig. 6.3-A). The test hardware included a Maccor 4000 battery tester with cells constantly held at temperature in sealed aluminium boxes inside a Binder KB53 thermal chamber, also shown in Fig. 6.3-A.

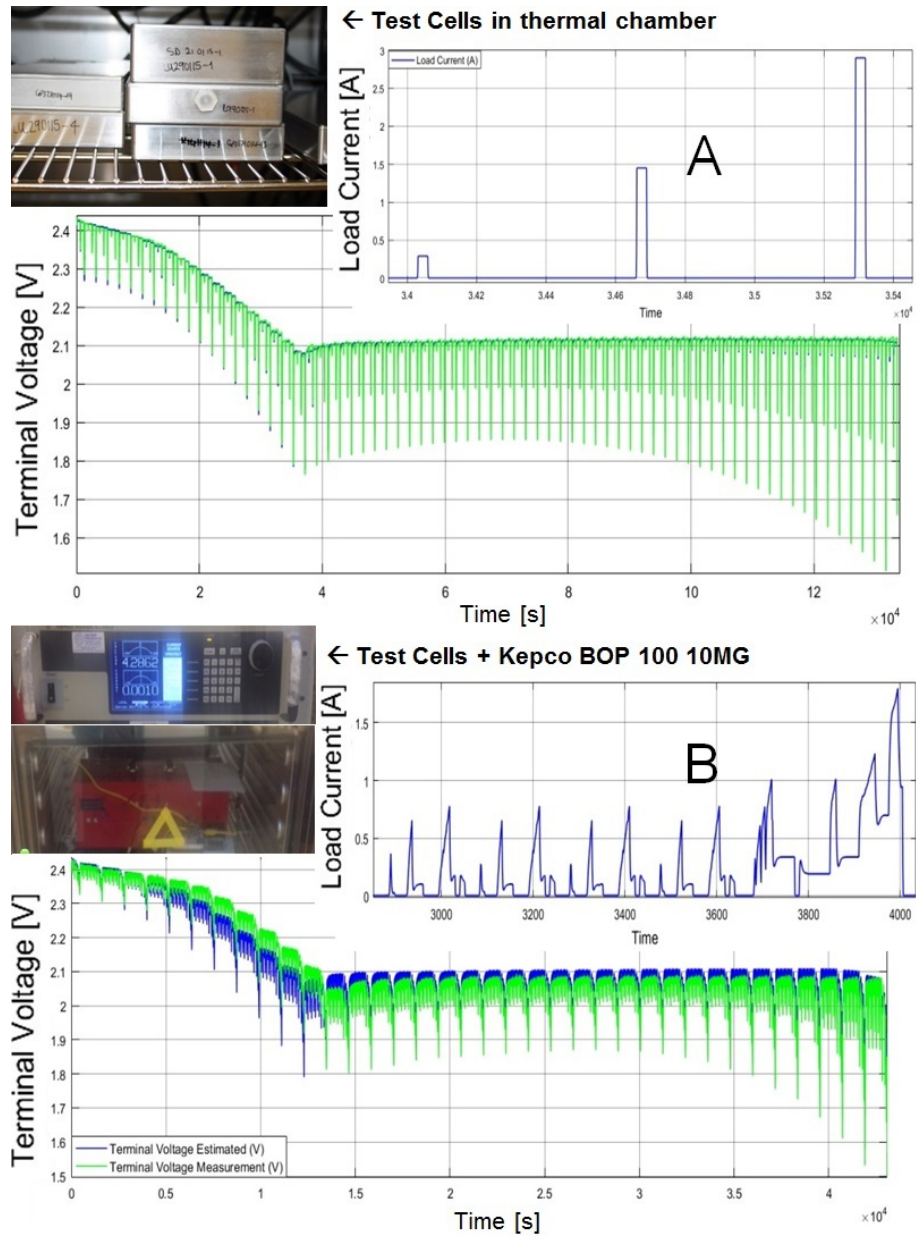


Figure 6.3: Mixed pulse and NEDC current profile with test installation.

To represent a more practical scenario, the same kind of OXIS Energy cell was discharged with a current profile based on the New European Driving Cycle (NEDC) [152]. The related power profile, shown in [153], was chosen due to its compromise of a realistic user scenario, also containing some level of abstraction. The test hardware used in this case is a Kepco BOP100-10MG programmable power source/sink (Fig. 6.3-B) discharging a battery at room temperature (23 °C). The details of the experiments are summarized in Table 6.1.

Table 6.1: Discharge experiments

Discharge	Measured Cap.	Av. Power	Av. Temp.
Pulse	9778 As	0.147 W	20 °C
NEDC	9678 As	0.467 W	23 °C

6.5.1 Reference SoC estimation

The reference SoC for both test benches is calculated with the cumulated current, operating in the cells' recommended voltage range, i.e. between 2.45 V (fully charged, SoC = 1), and 1.5 V (fully discharged, SoC = 0).

$$SoC = SoC_{(0)} - \frac{1}{3600Q_{cap}} \int_0^t I(\tau) d\tau. \quad (6.14)$$

While Coulomb counting is a poor predictor during tests, the discharge capacity for a specified voltage window can be calculated retrospectively, giving a reference SoC that can be used for post-experimental interpretation.

EKF SoC estimation

For the application of the EKF algorithm with the presented Li-S battery model, the Jacobians of the matrices A and C are needed, which are presented here for convenience. With one polynomial function respectively for C_p and R_p dependent on the SoC (here presented as second state of the model x_2), the Jacobian matrix of A is populated as:

$$\hat{A}(1,1) = \frac{-1}{f_{C_p}(x_2) f_{R_p}(x_2)} \quad \hat{A}(2,1) = 0 \quad \hat{A}(2,2) = 0 \quad (6.15)$$

$$\begin{aligned} \hat{A}(1,2) = & \left[\frac{\dot{f}_{C_p}(x_2)}{f_{C_p}(x_2)^2 f_{R_p}(x_2)} + \frac{\dot{f}_{R_p}(x_2)}{f_{C_p}(x_2) f_{R_p}(x_2)^2} \right] x_1 \\ & - \left[\frac{\dot{f}_{C_p}(x_2)}{f_{C_p}(x_2)^2} \right] I_{Bat}, \end{aligned} \quad (6.16)$$

with the same principle for C

$$\hat{C}(1,1) = -1 \quad \hat{C}(1,2) = \dot{f}_{OCV}(x_2) - \dot{f}_{R_0}(x_2) I_{Bat}. \quad (6.17)$$

The derivatives of the combined functions \dot{f}_{OCV} and \dot{f}_{R_0} with respect to x_2 are influenced by the introduced factor γ , here substituted by $f_\gamma(x_2)$.

$$f_{OCV}(x_2) = (1 - f_\gamma(x_2)) f_{OCV-low}(x_2) + f_\gamma(x_2) f_{OCV-high}(x_2) \quad (6.18)$$

Derivation with respect to x_2 leads to

$$\begin{aligned} \dot{f}_{OCV}(x_2) = & \dot{f}_{OCV-low}(x_2) - (\dot{f}_\gamma(x_2) f_{OCV-low}(x_2) + f_\gamma(x_2) \dot{f}_{OCV-low}(x_2)) \\ & + \dot{f}_\gamma(x_2) f_{OCV-high}(x_2) + f_\gamma(x_2) \dot{f}_{OCV-high}(x_2). \end{aligned} \quad (6.19)$$

Where \dot{f}_γ is defined by

$$\dot{\gamma}_{m,c}(x_2) := \begin{cases} 0, & \text{if a} \\ m \cos(2m(x_2 - c)), & \text{if b} \\ 0, & \text{if c} \end{cases} \quad (6.20)$$

with the same conditions for a, b, c as in equation 6.11. The derivation of \dot{f}_{R_0} follows the same pattern. As mentioned before, the unique behaviour of the Li-S battery can vary in a complex manner. Therefore, it is reasonable to assume that the voltage prediction of the observer is, firstly, not necessarily accurate and, secondly, that the predicted voltage is not everywhere an indicator of the SoC. To account for this, the measurement noise value R is with 0.15 relatively high compared to the chosen model noise Q , which assumes uncorrelated states with a low uncertainty for the Coulomb counting state. The specific values for Eq. 6.21 were derived iteratively.

$$P_{0 \text{ EKF}} = \begin{bmatrix} 10 & 0 \\ 0 & 10 \end{bmatrix} \quad Q_{\text{EKF}} = \begin{bmatrix} 0.1 & 0 \\ 0 & 0.0000003 \end{bmatrix} \quad (6.21)$$

The value for the measurement noise R implies a standard deviation for the measurements of 387 mV. This is greater than the values of actual Gaussian noise observed with the measurements. However, since the battery model is not able to predict the terminal voltage for every user case precisely, deviations in this order of magnitude are possible. The values of Q , representing the system noise, were determined iteratively to give good results.

UKF SoC estimation

Within the UKF framework, the weights $\alpha_i^{(m)}$ and $\alpha_i^{(c)}$ are vectors containing real constant scalars with the conditions that $\sum_{i=0}^p \alpha_i^{(m)}$ and $\sum_{i=0}^p \alpha_i^{(c)}$ are equal to 1 [101]. With the scaling value

$$\lambda = \alpha^2(L + \kappa) - L$$

the weights can be calculated with

$$\gamma = \sqrt{L + \lambda}, \quad \alpha_i^{(m)} = \alpha_i^{(c)} = \frac{1}{2(L + \lambda)}$$

$$\alpha_0^{(m)} = \frac{\lambda}{L + \lambda}, \quad \alpha_0^{(c)} = \frac{\lambda}{L + \lambda} + (1 - \alpha^2 + \beta).$$

Here, we chose similar weights as presented in [115], defining the values 1 for α , 2 for β , $L = \dim\{x\} = 2$, and 0 for κ . Since the parameters are constant, they can be defined once prior executing the filter. The values of the measurement and system noise R and Q follow the same pattern of the EKF. However, the values for P_0 are considerably smaller since widely spread, unrestricted sigma points lead to estimation errors when they exceed the defined SoC range of 0-1 in the beginning of the estimation. Furthermore, the UKF was found to be more sensitive to the model prediction errors compared to the EKF, so larger values were used in the measurement noise matrix $R = 0.3$.

$$P_{0 \text{ UKF}} = \begin{bmatrix} 1 & 0 \\ 0 & 0.014 \end{bmatrix} \quad Q_{\text{UKF}} = \begin{bmatrix} 0.0005 & 0 \\ 0 & 0.0000007 \end{bmatrix} \quad (6.22)$$

PF SoC estimation

The chosen probability density function should, on the one hand, accurately determine the most likely observations, but on the other hand hinder the impoverishment of the samples

over time. Examples for non Gaussian probability density functions for SoC estimation are given in [170, 169]. Here however, the Gaussian distribution

$$f(x) = \frac{1}{\sigma\sqrt{2\pi}} e^{-\frac{(x-\mu)^2}{2\sigma^2}} \quad (6.23)$$

is used due to its simplicity and comparably to the EKF and UKF. To account for the uncertainties of the model and Coulomb counting, the standard deviations to sample the states in the prediction step are chosen in the same pattern as the EKF and UKF, allocating larger values to the transient voltage term U_p , to account for the model inaccuracies, and smaller values to the SoC state, to limit the random fluctuations when the battery behaviour does not change.

$$std_{x_1} = 0.004 \quad std_{x_2} = 0.0003 \quad (6.24)$$

The number of particles was chosen iteratively. Tests indicated a decent compromise between computational effort and estimation precision with a constant number of 30 particles.

6.6 Results and discussion

The results of the proposed SoC estimation algorithms are evaluated qualitatively for their convergence time, with imprecise initial states, and quantitatively by their estimation accuracy. As measure for the latter the root mean squared error (RMSE) over the whole discharge range is used

$$RMSE = \frac{1}{\sqrt{n}} \left(\sum_{i=1}^n (SoC_{t,i} - \hat{SoC}_{t,i})^2 \right)^{0.5}. \quad (6.25)$$

Where n is the number of data points, $SoC_{t,i}$ is the reference SoC from the measurement and $\hat{SoC}_{t,i}$ is the estimated SoC by the filters. The accuracy and convergence depend on the quality of the model, the observability of the system itself, the quality of the measurements, their noise pattern and the users choices for the system and measurement uncertainties. In the context of the model accuracy also the discharge profile plays a role. For the pulse test, with its long resting periods, the errors in the OCV are more sensitive to the prediction error, whereas the more realistic NEDC cycle emphasises the internal resistance or transient behaviour. Since Li-S batteries suffer from self-discharge, which can lead to an imprecise initial condition for the SoC estimation, each test is performed with three different initial SoC values. While two of them are located in the high plateau ($SoC_0 = 1, 0.7$), one is chosen after the transition point (0.68) at ($SoC_0 = 0.6$), to test the algorithms ability to converge in between both plateaus. To test their robustness against current profile induced changes, all filters use the predetermined capacity from the mixed pulse discharge profile tests during the model identification (9778 As). The results of the SoC estimation tests are shown in Figure 6.4 and Table 6.2. The following discussion orients on the specific properties of Li-S batteries.

High self-discharge: Self discharge, caused by the shuttle effect, occurs mainly in the high plateau. This can be difficult to handle for the SoC estimators since the state changes when the monitoring system is switched off. However, the high plateau has also a steep OCV gradient which allows the estimator to converge quickly when the state changed. Therefore, the estimation result does not change significantly with an imprecise initial condition as long as both states, the real one and the estimated one, are within the same plateau. Otherwise, the local minimum in the OCV can hinder the convergence. Especially the EKF, with its first order linearisation, and the PF with its particle set far away from the real SoC suffer from this effect (Fig.6.4 EKF: Pulse Test, NEDC PF: Pulse Test, NEDC). Here, the UKF has the best performance. For applications demanding a quick

State estimation with initial reference SoC = 1

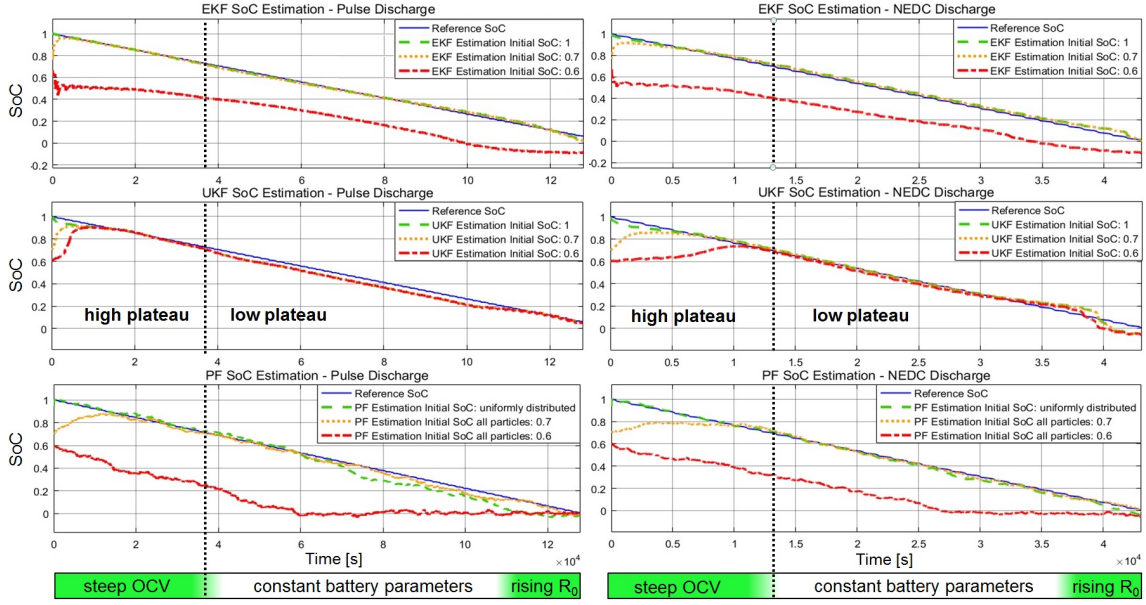


Figure 6.4: Estimation results for EKF, UKF, PF with a mixed pulse- and a NEDC drive cycle current profile, starting with a fully charged battery, i.e. 1 SoC.

conversion without a precise initial condition a self-discharge model is recommended.

Constant OCV: The uncertain region does not contain sufficient information in the battery behaviour to distinguish different SoCs in the low plateau, which leads to a state prediction heavily based on the Coulomb counting. The result of this is a slightly drifting SoC in that region and a slow convergence (Fig.6.4 all filters: Pulse test, NEDC initial $SoC_{0\text{ ref}} = 1$). However, due to the area with increased internal resistance towards the end of discharge, the estimators are able to correct that error mostly before the depletion point. Here, the fact that the constant region is enclosed by the high plateau and an area of increased cell resistance favours the model based estimation. Furthermore, the lower self-discharge within the low plateau allows the Coulomb counting to be accurate and limits the drift.

Conversion with discharged battery: When starting from a partially-discharged

Table 6.2: RMSE SoC estimation with EKF, UKF and PF with initially fully charged battery

Algorithm	SoC_0	Pulse RMSE	NEDC RMSE
EKF	1	0.0114	0.0217
	0.7	0.0160	0.0267
	0.6	0.2986	0.2732
UKF	1	0.0347	0.0280
	0.7	0.0444	0.0537
	0.6	0.0705	0.1199
PF	uni	0.0576	0.0195
	0.7	0.0532	0.0694
	0.6	0.3997	0.3354

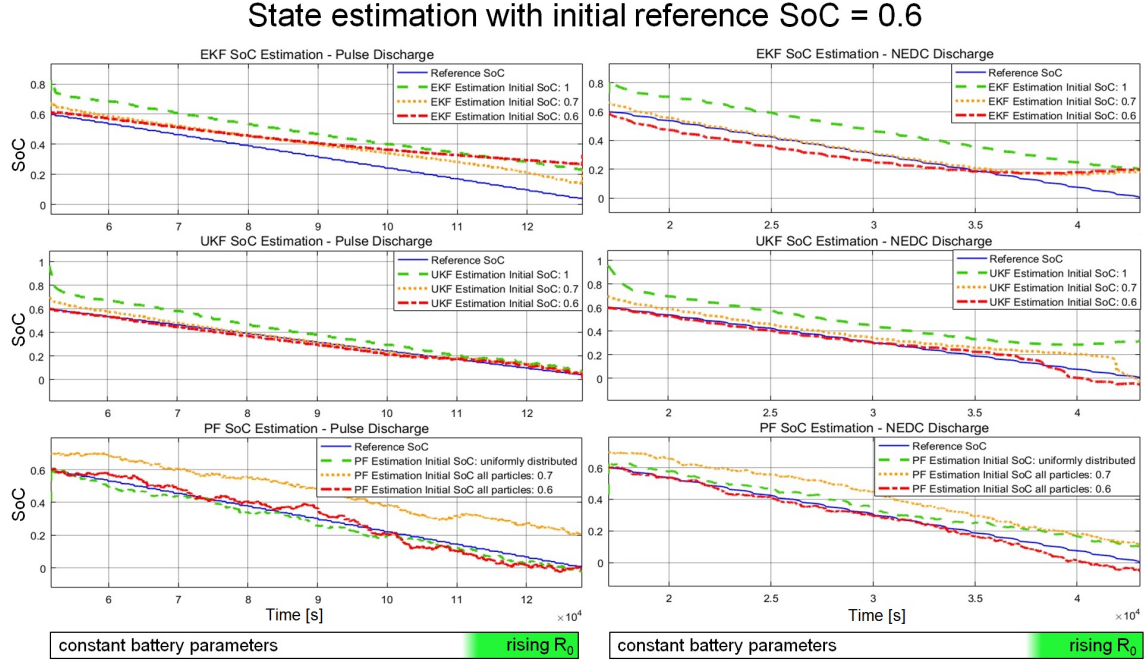


Figure 6.5: Estimation results for EKF, UKF, PF with a mixed pulse- and a NEDC drive cycle current profile with an initially partly discharged battery, i.e. from 0.6 SoC.

state, e.g. where the self-discharge of the battery causes the estimated SoC to be higher than the real one (Fig. 6.5), the differences between the EKF and UKF are more pronounced. Here, the simulation was started at the initial reference SoC of 0.6, with the same initial conditions used in the fully-charged tests for the estimators (SoC_0 estimation = 1, 0.7, 0.6). In these tests, it can be seen that the estimators performance is also depending on the starting point. In general, the UKF works best, though they can fail (Fig. 6.5 UKF NEDC initial SoC_0 ref = 0.6). The EKF tends to converge slowly, requiring more than a full discharge cycle. The particle filter can fail if the particles are poorly distributed at the start, but when the particles are uniformly distributed, it converges to the true state of charge very quickly. The results are summarized in Table 6.3.

Changes of the model parameters: As mentioned before, the smaller parameter variation within the low plateau favours the SoC estimation. However, the dependence of

Table 6.3: RMSE SoC Estimation with EKF, UKF and PF with with partly discharged battery

Algorithm	SoC_0	Pulse RMSE	NEDC RMSE
EKF	1	0.1593	0.1696
	0.7	0.0860	0.0535
	0.6	0.1203	0.0745
UKF	1	0.0887	0.1743
	0.7	0.0240	0.0687
	0.6	0.0189	0.0332
PF	uni	0.0281	0.0561
	0.7	0.1661	0.1176
	0.6	0.0383	0.0320

the battery behaviour on the load profile remains a challenge. Different current rates and profiles cause different utilisations of sulfur and therefore variations in the usable capacity. While these effects are less pronounced in the high plateau, the low plateaus variations are significant. To show their effect to the model accuracy and SoC estimation, further tests were done with a decreased (added gain of 0.66 to current profile) and increased (added gain of 1.33 to current profile) NEDC profile (Table 6.4).

Table 6.4: Discharge experiments with NEDC-low and NEDC-high profile

Discharge	Measured Cap.	Av. Power	Av. Temp.
NEDC-low	10561 As	0.317 W	23 °C
NEDC-high	9072 As	0.610 W	23 °C

Both, Fig. 6.6 and 6.7, show the effects of the current density variations to the model accuracy and SoC estimation. For most of the discharge range the cell behaviour could still be represented well. But the increased capacity, mainly in the low plateau, leads to deviations of model prediction and measured voltage towards the end of discharge (Fig. 6.6), since the model uses the fixed capacity value from the pulse identification process (9778 As).

The rough capacity prediction combined with the constant OCV within the low plateau cause a negative drift of the SoC estimation in this area. Due to the strong divergence between model and measurements towards the end of discharge however, there is some correction towards the reference SoC in the end of the discharge process as well.

With higher rates the ratio of the high plateau of the whole discharge capacity increases which should enable the algorithms to correct the states longer. Nevertheless, the

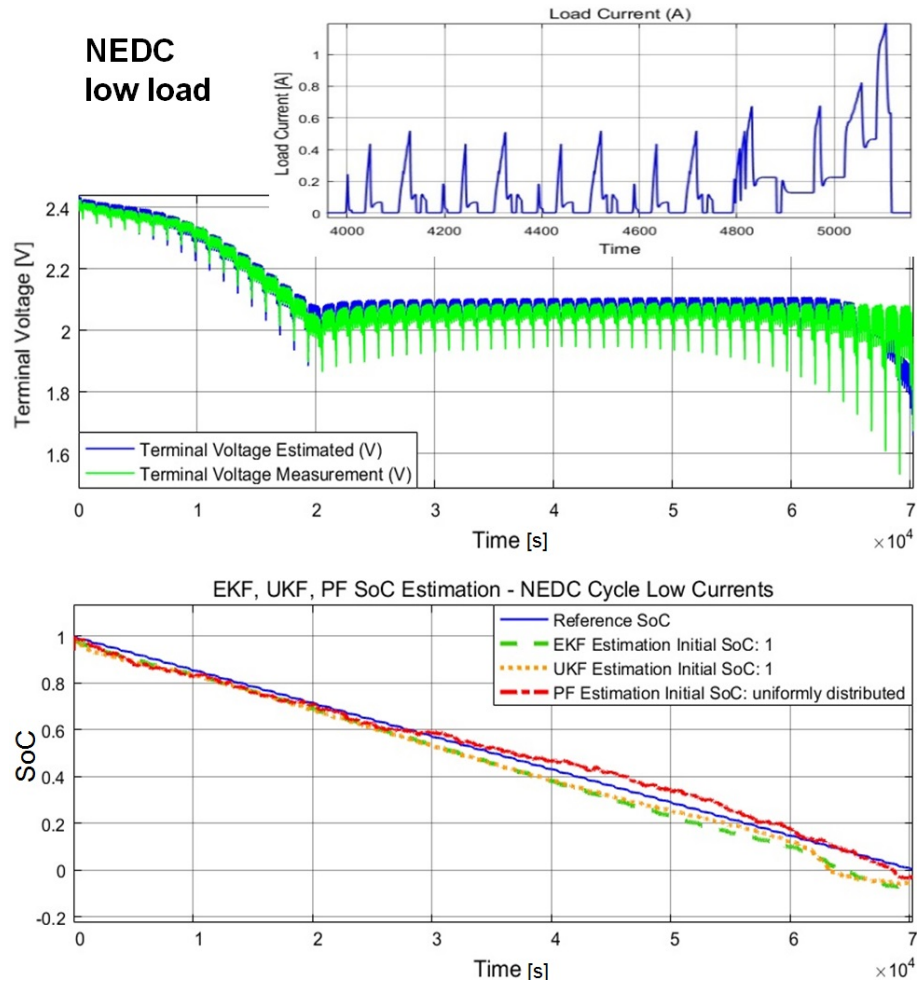


Figure 6.6: Estimation results EKF, UKF, PF for a lower current NEDC drive cycle (Added gain of 0.66 to the reference NEDC drive cycle, described in Sec. 6.5).

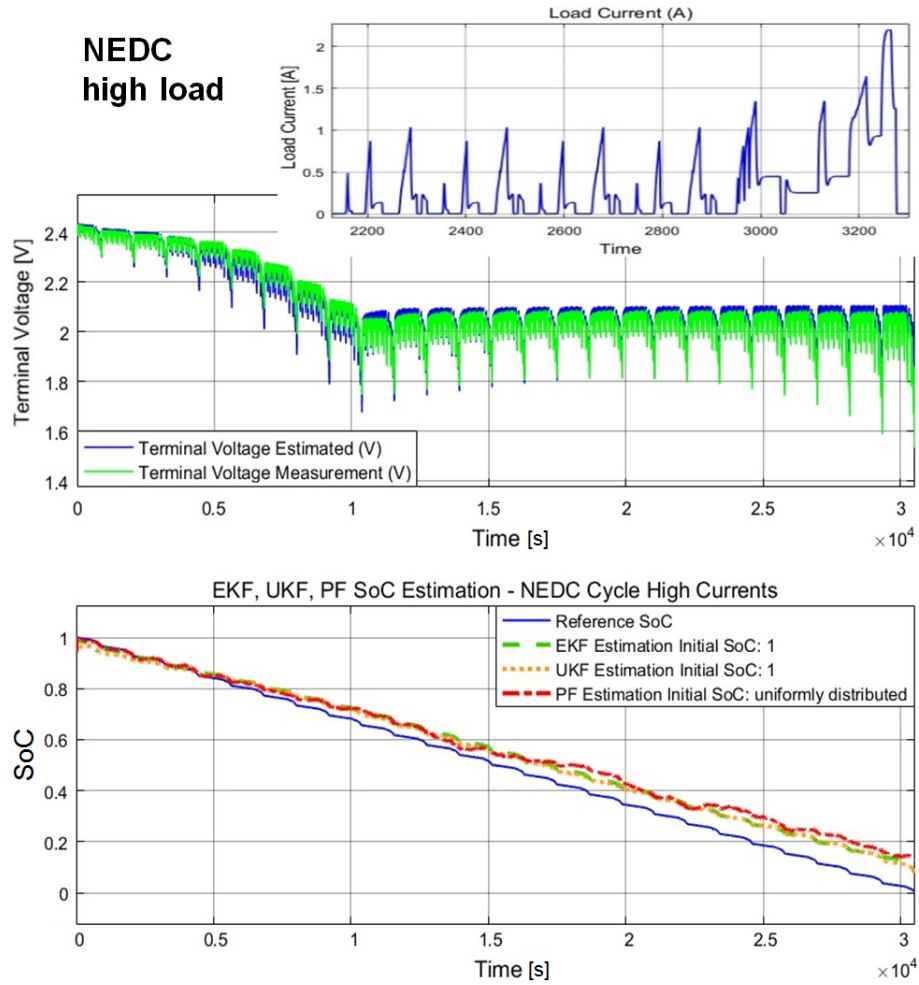


Figure 6.7: Estimation results EKF, UKF, PF for a higher current NEDC drive cycle (Added gain of 1.33 to the reference NEDC drive cycle, described in Sec. 6.5).

estimated SoC drifts towards higher values in this case. Here the differences in between the model and measurements are not significant enough to correct the states sufficiently. The results of the estimation accuracy with different current profile gains are summarized in Table 6.5.

To cover for the uncertainties, an improved observer model, accounting for model changes with current profiles, could be the key for improvement. However, since the inner cell mechanisms are still a matter of ongoing research, on-line parameter estimation could lead to improvements for the SoC estimation easier to obtain.

To achieve optimal results with handling the proposed model and estimation, we suggest the following steps: (i) define a simplified current profile for the intended application; (ii) measure the delivered capacities for this use-case and (iii) apply our presented battery model and estimation method with the derived capacity value.

Table 6.5: RMSE SoC estimation with NEDC-low and NEDC-high profile

Algorithm	SoC_0	NEDC-low	NEDC-high
EKF	1	0.0489	0.0580
UKF	1	0.0625	0.0546
PF	uni	0.0310	0.0694

Two plateaus with transition region: A likely consequence of the local minimum in the identified OCV curve in between the voltage plateaus, the EKF and the PF converge slowly when the initial condition is not located in the high plateau ($SoC_0 = 0.6$). To investigate filter-based solutions to improve the convergence, a simplified OCV curve, neglecting the voltage drop in between the plateaus (Fig. 6.8), was fitted to the OCV

identification data and substituted with the previously used function.

$$\begin{aligned}
 f_{OCV-simple}(x_2) = & 339.78x_2^9 - 1372.71x_2^8 + 2291.23x_2^7 \\
 & - 2066.02x_2^6 + 1107.76x_2^5 - 364.76x_2^4 + 72.94x_2^3 \\
 & - 8.36x_2^2 + 0.48x_2 + 2.1
 \end{aligned} \tag{6.26}$$

The advantage of this single polynomial is an almost monotonic behaviour ignoring highly nonlinear parts in the OCV curve, also simplifying the derivation of the Jacobian matrix. While the estimation results of the PF does not change significantly, the first order linearisation of the EKF leads to the anticipated results if the initial covariance of the SoC is raised ($P_0 = [10 \ 0; 0 \ 21]$). As shown in Figure 6.8, the convergence time for the imprecise initial SoC of 0.6 has improved significantly without losses in the estimation accuracy for the rest of the discharge (Tab. 6.6). Here could be an opportunity for simplification for the EKF.

Table 6.6: RMSE SoC estimation with simplified OCV curve

Algorithm	SoC ₀	OCV Function	NEDC RMSE
EKF	1	one poly	0.0205
	0.6	one poly	0.0272
	0.6	two poly	0.3923

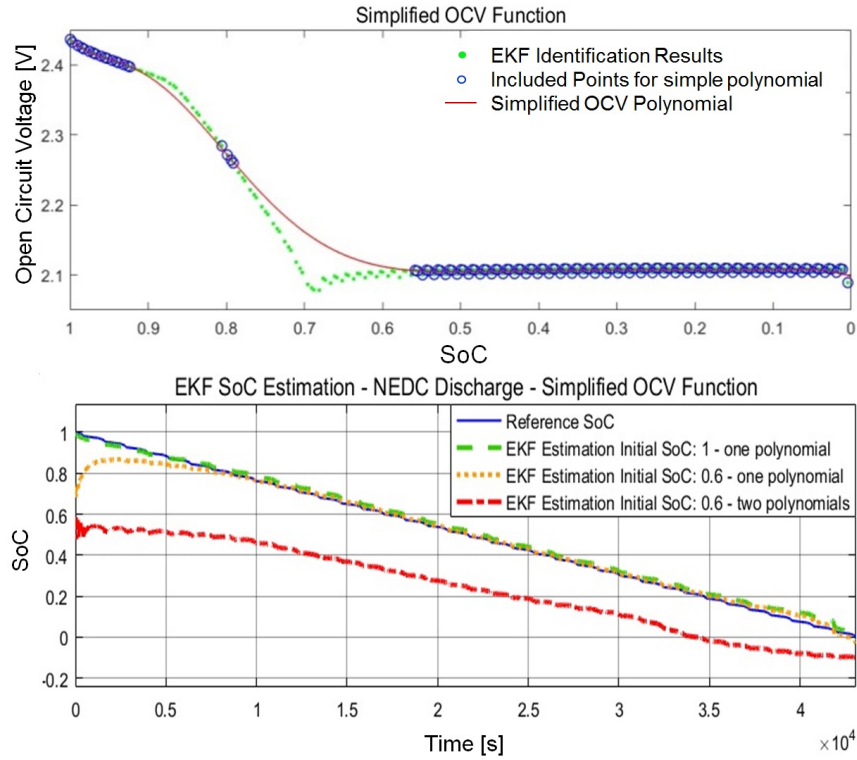


Figure 6.8: Simplified OCV curve and related estimation results for the EKF.

However, all in all we can conclude that the UKF can cope best with the properties of the Li-S battery combined with a reasonable computational effort. Table 6.7 presents the simulation times for the reference battery model and three parallel running estimation algorithms (SoC_0 : 1, 0.7, 0.6) on the same system (Intel(R) Core(TM) i5-5300 CPU @ 2.30 Ghz, 8GB RAM, 64 bit operating system).

Table 6.7: Simulation time for the pulse discharge test (128000 s)

	EKF	UKF	PF
Simulation time	5.25 [s]	7.97 [s]	21.54 [s]

It is shown that the additional computational effort of the particle filter does not lead to significant improvements in this case.

6.7 Conclusion

This paper has introduced the problem of SoC estimation for Li-S batteries, and explored the applicability of ‘standard’ techniques used for lithium-ion batteries. It was noted that Li-S batteries exhibit complex behaviours, some of which prevent the exploitation of ‘standard’ techniques in electric vehicles. Lithium-sulfur’s open-circuit-voltage versus state-of-charge curve has a large flat region, meaning that open-circuit voltage is a poor indicator of SoC. Because there are multiple reaction pathways, the useful capacity of Li-S cells depends on the applied duty cycle. Furthermore, it suffers from high self-discharge, so ‘Coulomb counting’ is unlikely to be effective. As an alternative, this paper has explored three model-based methods of state estimation, all of which were variants of the recursive Bayesian filter: the extended Kalman filter, the unscented Kalman filter and the particle filter. Despite the complexities of Li-S cells, it was demonstrated in experimental tests that the model-based estimators based on an equivalent-circuit-network model were able to perform robustly.

The discussion of the results noted several ways where the complex behaviours of Li-S help to aid the estimation problem. While the high self-discharge within the high plateau hinders the determination of a precise initial SoC, the steep OCV gradient in this region allows a quick convergence. Here, problematic and useful properties for the state estimation cancel each other out. In the low plateau, the flat OCV curve and relative constant battery parameters hinder a precise estimation. In this area also current-related changes in the usable capacity occur mostly, which is the reason why the proposed estimation methods works best within a certain discharge current range. However, due to the

enclosure of the constant region by the high plateau and an area with increased internal resistance, the estimation is mostly able to converge to the correct SoC within one discharge cycle. Therefore a standard model-based estimator, with its multiple sources/states of information, is capable of predicting the SoC of a Li-S cell well enough. Hereby the unscented Kalman filter gives the most robust and accurate performance in combination with a reasonable computational effort.

It was conjectured that improvements to the model to represent self-discharge are likely to benefit the robustness of the estimators. Furthermore, a facility to deal with the current-related parameter changes, is very likely to improve the accuracy. It would also be interesting to consider whether adaptive noise covariance values could be used to improve the model fit whilst accommodating regions of greater uncertainty. The authors also are currently exploring the application of recursive parameter estimation for state estimation. A limitation of the performed tests is the constant-temperature scenario. This mirrors the highly regulated environment of the authors' intended end application, an electric vehicle test environment with a tightly-regulated temperature. However, future work should also explore any challenges associated with state estimation in an environment with significant temperature variations.

6.8 Acknowledgement

This research was undertaken as part of the project 'Revolutionary Electric Vehicle Battery' (REVB), co-funded by Innovate UK under grant TS/L000903/1; university funding is provided by EPSRC under grant number EP/L505286/1 . Enquiries for access to the data referred to in this article should be directed to researchdata@cranfield.ac.uk. (The data used in this article is described at <https://dx.doi.org/10.17862/cranfield.rd.3834057/>; it is subject to an embargo, and will be available from May 2022.)

Paper 3 – Online parametrization SoC estimation

Dual extended Kalman filter for online estimation of model parameters and state of charge in lithium-sulfur batteries

Authors:

Karsten Propp, Daniel J. Auger, Abbas Fotouhi, Monica Marinescu,
Stefano Longo, Vaclav Knap

The paper has been submitted to

Applied Energy

Abstract

Lithium-sulfur (Li-S) is a promising next-generation battery chemistry which is beginning to be used in practical applications. The electrochemical behaviours of Li-S are more complex than those of lithium-ion batteries. For lithium-ion batteries, many state-of-charge estimation techniques exist, but for Li-S, only three methods have been published, using single Kalman-derived estimators for a nonlinear model describing both ‘slow’ parameter changes and ‘fast’ equivalent-circuit-network behaviour. This paper explores an alternative method where the problems of parameter estimation and state estimation are handled separately, using dual extended Kalman filters. The new estimator is demonstrated experimentally with pulse-discharge tests and driving-cycle loads. The underlying equivalent circuit model is then enhanced with a new model of the relationship between current-density and internal resistance terms; estimators based on this are also demonstrated for different load profiles. With appropriate choice of estimator covariance parameters, the proposed dual estimator method gives precise and robust state estimates for a range of current densities and initial conditions. Compared to the previously published estimation technique, accuracy and robustness are improved.

7.1 Introduction

For applications requiring a lightweight, cheap and safe battery, the Lithium-Sulfur (Li-S) chemistry is a promising candidate to replace the current Lithium-ion (Li-ion) technology. However, the large scale adoption of this chemistry still depends on solving performance limitations, such as relatively short cycle life, low charging efficiency and power capabilities [59, 136]. Another reason for the hesitant introduction for practical applications is their complex conversion reaction of elemental sulfur S_8 , via the intermediates $Li_2S_8, Li_2S_4, Li_2S_2$, to lithium sulfide Li_2S [129] during discharge. Within the high plateau (see Fig. 7.1 top) soluble high order polysulfides (Li_2S_8, Li_2S_6) are predominant in electrolyte solution [131], which leads to a small internal resistance but also to self discharge due to the shuttle effect [61]. The low plateau is governed by insoluble species (Li_2S_4, Li_2S_3) [133] that are likely to precipitate (Li_2S_2, Li_2S) [53, 95], which cause a constant battery open circuit voltage (OCV) and a dependence of the sulfur utilisation on the applied current profile [132, 139, 134]. The resulting differences between both discharge patterns of classic Li-ion and Li-S batteries makes it difficult to design a battery management system (BMS) because, on the one hand, it still a matter of ongoing research how to operate Li-S cells optimally and, on the other hand, methods for controlling Li-ion batteries cannot be applied directly.

This is also the case for the state of charge (SoC) estimation. Due to the constant OCV, the self discharge and current related utilisation, leading to variations in the usable capacity, simple techniques like Coulomb-counting and the open-circuit-voltage-method [79] are difficult to apply. Therefore, it was concluded that advanced methods are required for Li-S batteries [16]. One example for that are model based techniques, that are able to match the behaviour of the battery over the discharge range with equivalent circuit network (ECN) models (Fig. 7.1 middle). Although these models are usually not able

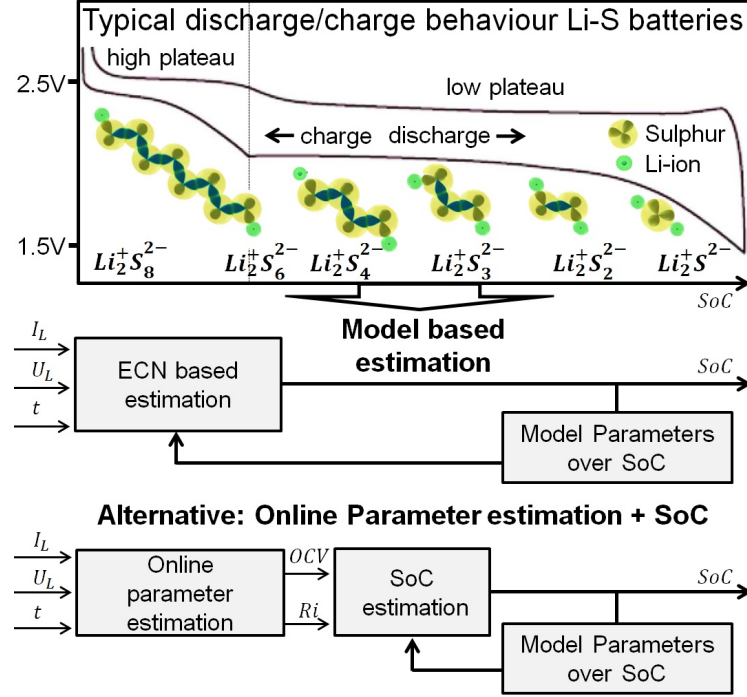


Figure 7.1: Behaviour and SoC estimation principles of Li-S batteries

to give insight into the inner cells reactions, they are relatively simple and accurate [92, 100, 76]. In [99, 17] ECN models for Li-S batteries were presented where the latter was used for Kalman filter based SoC estimation in [16]. And indeed, it could be shown that model based methods can estimate the SoC of Li-S batteries accurately. However, also limitations were found of which mostly the capacity variations in the low plateau with different current rates influenced the estimation accuracy negatively. Here the constant OCV, together with an uncertain battery behaviour lead to inaccuracies in the estimation. To address these and also to test the applicability of another estimation pattern, this study investigates an online identification technique to parametrise an ECN model and use the results for the SoC estimation (Fig. 7.1 bottom). The increased identification speed and the used diverse loads also aim to gain insight into the cell dynamics under more realistic conditions than the commonly used pulse current tests.

A framework for online battery parameter estimation for operational conditions rele-

vant to automotive applications (high current rates, temperature variations and dynamic rate profiles [114]) was proposed by Chiang et al. in [175]. There, an adaptive control method in combination with a Thevenin battery model [148] is used to identify the OCV and internal resistance of lithium-iron-phosphate and lithium polymer cells. The mathematical assumptions made by Chiang (more details in Sec. 7.2) were incorporated by He et al. to apply an adaptive Kalman filter-based online identification for realistic load profiles in electric vehicles [176, 177]. As an adaptation of this approach we implement a behavioural interpretation of the Thevenin model, presented in [17], to simplify the parametrization of the extended Kalman filter (EKF). Furthermore the unique properties of Li-S batteries are considered for the SoC estimation since, oppositely to classic Li-ion batteries [137], the OCV itself is not sufficient for Li-S SoC estimation [161]. Therefore, a dual Kalman filter is proposed, employing the identified values for both, the OCV and the internal resistance. The presented study is to the authors' knowledge the first one to adapt and apply the previously developed online identification technique to Li-S batteries.

The paper is structured in three main parts. The first one, Sec. 7.2, is focused on the Kalman filter based online parameter identification and its validation. The behavioural version of the Thevenin model is introduced briefly and employed for the identification. The applicability of this method for Li-S batteries is proven for two scenarios.

In the second main part, the online parameter estimation is applied to different current profiles with varying amplitudes, described in Sec. 7.3, and the found relationship between the current and the internal resistance is discussed in Sec. 7.4.

As third main part, a reduced order model of the dynamical resistance is then presented in Sec. 7.5, which is used for SoC estimation in Sec. 7.6.

7.1.1 Contributions

1. Implementation of a fast Kalman filter based method to identify the model parameters of the battery online
2. Improving existing ECN models with a current related internal resistance part
3. Improving the robustness and convergence of standard SoC estimation techniques (EKF, UKF and PF) with a dual Kalman filter approach

7.2 On-line parameter estimation with EKF

The model framework for the identification is based on the Thevenin model [148], which has been proven to be a good trade off between computational effort and accuracy for intercalation based Li-ion batteries [128, 178]. For their SoC estimation the identified OCV is of interest [175]. Due to the flat OCV of Li-S batteries however, we must also use the internal resistance. Therefore, both values must be identified and related to the SoC reliably. Here the behavioural interpretation of the Thevenin model, introduced in [17], helps the user to choose the right parameter boundaries, which can simplify the parameterisation of the EKF. For the sake of completeness, this integration is introduced here briefly.

7.2.1 Mathematical cell model

The Thevenin model describes the voltage at the battery terminal as

$$U_L(t) = U_{OC} - U_P(t) - R_0 I_L(t) \quad (7.1)$$

where the voltage over the RC circuit is described as

$$\dot{U}_P(t) = -\frac{1}{R_P C_P} U_P(t) + \frac{1}{C_P} I_L(t), \quad (7.2)$$

which are couched in terms of the components of the electrical equivalent circuit. As shown in [17], recasting the system in terms of the observed behaviours instead can help to separate the circuit parameters into an immediate part and a lagging part after a current pulse. Therefore, we will start by defining the corresponding parameters:

$$\begin{aligned} R_{\text{int}} &= R_0 + R_P, \\ \rho &= \frac{R_P}{R_0 + R_P} \Leftrightarrow (1 - \rho) = \frac{R_0}{R_0 + R_P}, \\ \Omega &= \frac{1}{R_P C_P}. \end{aligned}$$

R_{int} is the steady-state (or quasi-static) internal resistance, ρ is the fraction of the response that is not instantaneous, thus representing a dynamic lag and Ω is the natural frequency of the response. With this new set of parameters, Eq. (7.1) becomes

$$U_L = U_{\text{OC}} - U_P - \underbrace{(1 - \rho) R_{\text{int}}}_{\text{formally } R_0} I_L \quad (7.3)$$

and equation (7.2) becomes

$$\dot{U}_P = -\Omega U_P + \rho R_{\text{int}} \Omega I_L. \quad (7.4)$$

Where the model parameters are U_{OC} for the OCV, U_L for the terminal battery voltage and U_P for the voltage drop over the parallel RC circuit. The main advantage of these transformation is to easily constrain the behavioural parameters to ‘sensible’ ranges since

they are sufficiently decoupled from each other: the dynamic portion of the model can be adjusted without altering the steady-state response.

7.2.2 Battery model equations for EKF

The behavioural model is particularly suitable for the online parameterisation because it can simplify the parametrisation of the covariance matrices of the EKF. Since the model contains more variables than observable states, there is no guarantee for the Kalman filter-based identification to converge towards the anticipated values [114]. In [176] the difficult parameterisation of the EKF covariances is solved with an adaptive algorithm for estimating the covariance matrix for the system noise Q and measurement noise R . Here, we assume that the statistics of measurement noise, and battery parameters are constant. In the following, we adapt the assumptions made by Chiang et al. [175] for Li-S batteries and the behavioural model. We start with the standard Thevenin model's state transition equation for the terminal battery voltage U_L , the derivative of equation 7.1:

$$\dot{U}_L = \dot{U}_{OC} - \dot{U}_p - \dot{I}_L R_0 - I_L \dot{R}_0. \quad (7.5)$$

Generally, the OCV of the battery is dependent on the SoC, the operating temperature (T) and usage history (h). Therefore, the corresponding definition of U_{OC} can be described as a function of SoC, T, h, whose derivation leads to

$$\dot{U}_{OC} = \frac{\delta U_{OC}}{\delta SoC} \frac{\delta SoC}{\delta t} + \frac{\delta U_{OC}}{\delta T} \frac{\delta T}{\delta t} + \frac{\delta U_{OC}}{\delta h} \frac{\delta h}{\delta t}. \quad (7.6)$$

For the representation of the battery in a discrete manner, usually time steps of less than one seconds are used. Due to the naturally slow changing parameters of common Li-ion batteries, the equation can be simplified at each time step by the following assumptions,

made by [175]. However, since here we use Li-S batteries, we evaluate the applicability of these assumptions for this battery chemistry as well.

- $\frac{\delta SoC}{\delta t} \approx 0$ holds for a small change in battery charge

Li-S cell are operated under much lower rates, which makes this assumption more justified than in the case of Li-ion.

- $\frac{\delta U_{OC}}{\delta SoC} \approx 0$ in low plateau

Furthermore, there is no change in OCV over the SoC within the low plateau, which approves the assumption.

- $\frac{\delta T}{\delta t} \approx 0$ when temperature changes slowly

The OCV of Li-S batteries depends more strongly on cell the temperature [17] than the OCV of Li-ion. However, the rate of heat generation is assumed to be lower than that of heat dissipation, which is especially valid at low enough current rates and environmental control.

- $\frac{\delta h}{\delta t} \approx 0$ for long term history

Li-S cells are influenced by the short term discharge history [179, 180], commonly referred as 'history' effect. The precise origins and extent for practical applications are still unexplored. However, it is expected that history effects occur at times longer than a time step. Therefore \dot{U}_{OC} is approximated as 0. Despite the relatively quickly changes of the internal resistance over the SoC between the two plateaus [17], we also assume it to be 0 ($\dot{R}_0 \approx 0$) for small periods. The conversion to the behavioural model can be done from the resulting change of the terminal voltage over time:

$$\dot{U}_L = -\dot{U}_p - R_0 \dot{I}_L. \quad (7.7)$$

The behavioural interpretation is

$$\dot{U}_L = -\dot{U}_p - (1 - \rho)R_{\text{int}}\dot{I}_L, \quad (7.8)$$

for the terminal voltage and

$$\dot{U}_p = -\Omega U_p + \rho R_{\text{int}} \Omega I_L \quad (7.9)$$

for the voltage drop over the RC circuit. By re-write equation 7.3 to bring U_p on one side, substituting it into Eq. 7.9 and including the result for \dot{U}_p in Eq. 7.8, the behavioural state transition equation can be derived as

$$\begin{aligned} \dot{U}_L = \Omega (U_{\text{OC}} - U_L - (1 - \rho)R_{\text{int}}I_L) - \rho R_{\text{int}} \Omega I_L \\ - (1 - \rho)R_{\text{int}}\dot{I}_L. \end{aligned} \quad (7.10)$$

7.2.3 Implementation of the Extended Kalman Filter

The Kalman filter is an efficient algorithm minimizing the error variance between the true and the estimated state. It is often applied for battery state estimation [172, 171] and for online parameter estimation [114]. The EKF is able to predict battery states using a nonlinear system model f . In the following, the algorithm is summarized for a discrete system [101].

Nonlinear state space model

$$x_k = f(x_{k-1}, u_{k-1}, w_{k-1}, k-1) \quad y_k = h(x_k, u_k, v_k, k)$$

Definitions

$$\hat{A}_k = \left. \frac{\partial f(x_k, u_k, w_k, k)}{\partial x_k} \right|_{x_k = \hat{x}_k^+}, \hat{C}_k = \left. \frac{\partial h(x_k, u_k, w_k, k)}{\partial x_k} \right|_{x_k = \hat{x}_k^-},$$

Initialisation for $k = 0$

$$\hat{x}_0^+ = \mathbb{E}[x_0], \quad P_0^+ = \mathbb{E}[(x_0 - \hat{x}_0^+)(x_0 - \hat{x}_0^+)^T]$$

Computation EKF for $k = 1, 2, \dots$

$$\text{State estimate update: } \hat{x}_k^- = f(\hat{x}_{k-1}^+, u_{k-1}, \bar{w}_{k-1}, k-1)$$

$$\text{Error covariance update: } P_k^- = \hat{A}_{k-1} P_{k-1}^+ \hat{A}_{k-1}^T + Q$$

$$\text{Output estimate: } \hat{y}_k = h(\hat{x}_k^-, u_k, v_k, k)$$

$$\text{Kalman Gain matrix: } L_k = P_k^- \hat{C}_k^T [\hat{C}_k P_k^- \hat{C}_k^T + R_k]^{-1}$$

$$\text{State estimate measurement update: } \hat{x}_k^+ = \hat{x}_k^- + L_k [y_k - \hat{y}_k]$$

$$\text{Error covariance measurement update: } P_k^+ = (I - L_k \hat{C}_k) P_k^-$$

The state vector, describing the transition to the next time step for the parameters of the behavioural model is

$$x = \begin{bmatrix} U_{OC} & U_L & U_p & \Omega & \rho & R_{int} \end{bmatrix}^T. \quad (7.11)$$

With the corresponding state transition functions from equations 7.9 and 7.10, the input current $I_L = u$ and the previous considerations ($\dot{U}_{OC} \approx 0, \dot{\Omega} \approx 0, \dot{\rho} \approx 0, \dot{R}_{int} \approx 0$) the state transition functions can be populated in the following form

$$f(x, u) = \begin{bmatrix} f_1 & f_2 & f_3 & f_4 & f_5 & f_6 \end{bmatrix}^T \quad (7.12)$$

where f_1 to f_6 are defined as:

$$f_1 = 0, f_4 = 0, f_5 = 0, f_6 = 0 \quad (7.13)$$

$$f_2 = x_1 x_4 - x_2 x_4 - x_4(1 - x_5)x_6 u - x_6 \\ - x_5 x_6 x_4 u - (1 - x_5)x_6 \dot{u} \quad (7.14)$$

$$f_3 = -x_4 x_3 + x_5 x_6 x_4 u. \quad (7.15)$$

Since the measured terminal voltage of the battery is represented by the second state, the measurement equation is

$$h = x_2. \quad (7.16)$$

The Jacobians of the presented functions f_1 to f_6 , linearising the system around the current mean, are:

$$\hat{A} = \begin{bmatrix} 0 & 0 & 0 & 0 & 0 & 0 \\ x_4 & -x_4 & 0 & x_1 - x_2 - x_6 u & x_6 \dot{u} & a_{2,6} \\ 0 & 0 & -x_4 & -x_3 + x_5 x_6 u & x_6 x_4 u & x_5 x_4 u \\ 0 & 0 & 0 & 0 & 0 & 0 \\ 0 & 0 & 0 & 0 & 0 & 0 \\ 0 & 0 & 0 & 0 & 0 & 0 \end{bmatrix} \quad (7.17)$$

$$a_{2,6} = -x_4 u - \dot{u} + x_5 \dot{u}.$$

\hat{C} can be obtained as

$$\hat{C} = \begin{bmatrix} 0 & 1 & 0 & 0 & 0 & 0 \end{bmatrix}. \quad (7.18)$$

While the presented model has a similar complexity to the parameter based method, the

tuning of the covariance noise matrices $w \sim (0, Q)$ and $v_k \sim (0, R_k)$ is supposed to be easier. Their parameterisation is explained in the following section (Sec. 7.2.4).

7.2.4 Validation

The validation of the proposed method is done by performing two experiments. Firstly, the Li-S battery model presented in [17] generates the voltage input for the EKF parameter estimation and the accuracy of the estimated parameters is evaluated by comparison to the known values from the model (Fig. 7.2 right). Secondly, the pulse test measurements and identification data from the offline parameterisation (Fig. 7.2 left) are compared to the online method. In the following the model parameters are shown in the ‘conventional’ ECN format since as it is customary to map them back with

$$R_p = \rho_p R_{\text{int}}, \quad R_o = R_{\text{int}} - R_p, \quad C_p = \frac{1}{R_p \Omega_p}. \quad (7.19)$$

The online parameterisation uses the measurements error, i.e. the difference between the measured and predicted battery terminal voltage, to correct six parameters or states. While the model determines the separation into the parameters (OCV, R_o , R_p , C_p), the convergence to the right values also depend on the right choices for the system and measurement uncertainties. The values of R and Q determine the relative trust of model prediction and measurement, as these both can generally be ridden with errors. The higher the values in R , the more trusted is the model prediction, such that the predicted states are corrected less, even if a large error between measurement and prediction exists. Large R values thus also mean smaller fluctuations in the system states. Matrix Q determines the trust in each of the states. Here large values, representing more uncertainty, leading to more correction. This rather simple thought mostly determines the parameterisation in this study. The values for Q should be as small as possible, to eliminate fluctuations, but as large

enough to follow the unpredicted changes. One example for such is the change of the OCV within the high plateau. Since the model assumes it as constant, only the correction of the Kalman Gain can follow the changes. Therefore the parametrisation of Q is not only assumed based on the relative trusts, but also on the expected violations of the model assumptions. The presented values for Q and P_0

$$Q = \begin{bmatrix} 0.02 & 0 & 0 & 0 & 0 & 0 \\ 0 & 0.01 & 0 & 0 & 0 & 0 \\ 0 & 0 & 0.01 & 0 & 0 & 0 \\ 0 & 0 & 0 & 0.0002 & 0 & 0 \\ 0 & 0 & 0 & 0 & 0.3 & 0 \\ 0 & 0 & 0 & 0 & 0 & 0.005 \end{bmatrix} \times 10^{-4} \quad (7.20)$$

$$P_0 = \begin{bmatrix} 0.02 & 0 & 0 & 0 & 0 & 0 \\ 0 & 1 & 0 & 0 & 0 & 0 \\ 0 & 0 & 1 & 0 & 0 & 0 \\ 0 & 0 & 0 & 0.00001 & 0 & 0 \\ 0 & 0 & 0 & 0 & 1 & 0 \\ 0 & 0 & 0 & 0 & 0 & 1 \end{bmatrix} \quad (7.21)$$

were derived iteratively in combination with mentioned thoughts. The initial values for the state vector are chosen to be close but not identical to the known values of a fully charged Li-S battery, to account for a level of uncertainty between different batteries.

$$x_0 = \begin{bmatrix} 2.43 \text{ V} & 2.43 \text{ V} & 0 \text{ V} & 0.025 & 0.1 & 0.172 \Omega \end{bmatrix}^T \quad (7.22)$$

Battery model results

For the simulation of the terminal voltage with the known data from the battery model, the realistic but simple NEDC current profile [152, 153] is used (Fig. 7.2 left). As also shown, the identification is able to quickly adjust to the right values, even if the initial conditions for R_0 , R_p and C_p are incorrect. Especially the OCV and R_0 can be estimated precisely and without fluctuations, which makes this algorithm suitable for identifying the battery SoC, as illustrated in Sec. 7.6.

Offline parameterisation results

The offline identification data of the cell parameters over SoC was gathered measuring the response of 3.4 Ah OXIS Energy long life chemistry cells to a mixed current pulse profile (300 mA, 1450 mA and 2900 mA) [17]. In order to identify current-related changes, the identification was done at for each pulse individually with a window of 300 s before and after. The method used is the prediction error minimization (PEM) algorithm, which is described in full detail by Ljung [147].

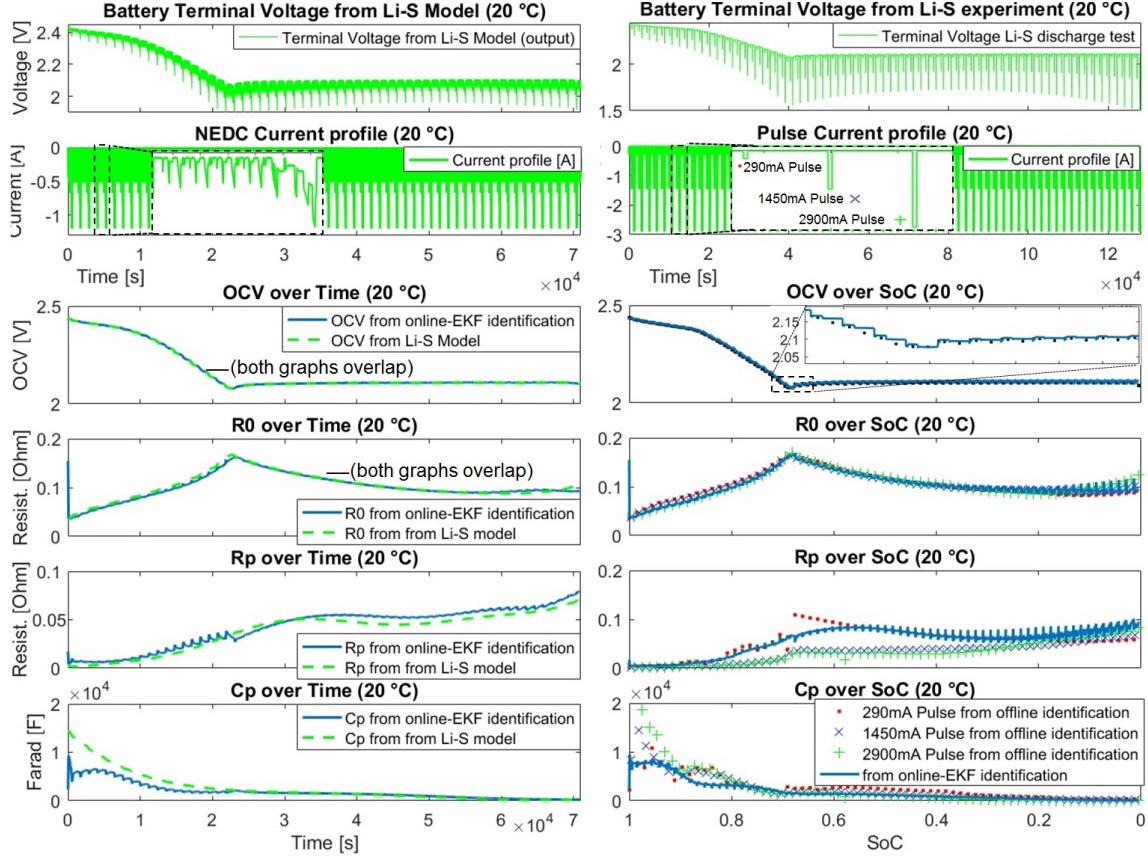


Figure 7.2: Online parameter identification results

The parametrisation results, presented in Fig. 7.2 right, illustrate that, despite a significant reduction in running time, the online estimation with the EKF provides a comparable identification quality to the offline method. Especially for the OCV and R_0 the zoomed-in area demonstrate that the parameter variations can be followed precisely. Therefore, the presented parameter estimation method appears valid for the whole discharge range of Li-S batteries.

7.3 Experimental design

The online parameterisation is applied to two realistic scenarios. Hereby current profiles according to the New European Drive Cycle (NEDC) [152] and the Urban Dynamo-meter Driving Schedule (UDDS) [181] were used in a controlled environment at 20 °C (Thermal Chamber: Memmert ICP260). Two cells were individually tested to reduce the impact of manufacturing variations. The tested cells are pre-cycled (C/10 charge, C/5 discharge, 30 °C) 3.4 Ah Li-S long life chemistry cells, developed by OXIS Energy.

Furthermore, the two different current profiles (NEDC and UDDS) are used with three different gains in order to test the batteries reaction as well as the SoC estimation performance to different power demands (Fig. 7.3). Since both cells follow the same pattern, we only use and present the results of cell 1 in Sec. 7.4 Sec. 7.5 and most of Sec. 7.6. However, to present as many results as possible we also included tests from cell 2 in Sec. 7.6.4. The details of the six tests and the measured usable capacities of both cells are summarised in Table 7.1.

Table 7.1: Discharge experiments

Cycle	Cap. Cell 1	Cap. Cell 2	Av. Current
NEDC 1.2	2.93 Ah	2.98 Ah	0.15 A
NEDC 1.8	2.69 Ah	2.68 Ah	0.22 A
NEDC 2.2	2.52 Ah	2.63 Ah	0.30 A
UDDS 1.2	3.11 Ah	3.13 Ah	0.13 A
UDDS 1.8	2.88 Ah	3.07 Ah	0.19 A
UDDS 2.2	2.58 Ah	2.53 Ah	0.26 A

For all the tests the capacities and reference SoCs are calculated by Coulomb counting for each test separately. This is done by integrating the measured current, following the cell's recommended voltage range between 2.45 V (SoC = 100%) and 1.5 V (SoC = 0%)

$$SoC = SoC_{(0)} - \frac{1}{3600Q_{cap}} \int_0^t I(\tau) d\tau. \quad (7.23)$$

Generally it is difficult to predict the capacity of the cell with Coulomb counting. However, it can be calculated retrospectively for a given voltage window and used as reference SoC in theory. This means that factors like self discharge and precipitation related to capacity changes are included within the reference SoC, which makes it a precise practical value for each scenario respectively.

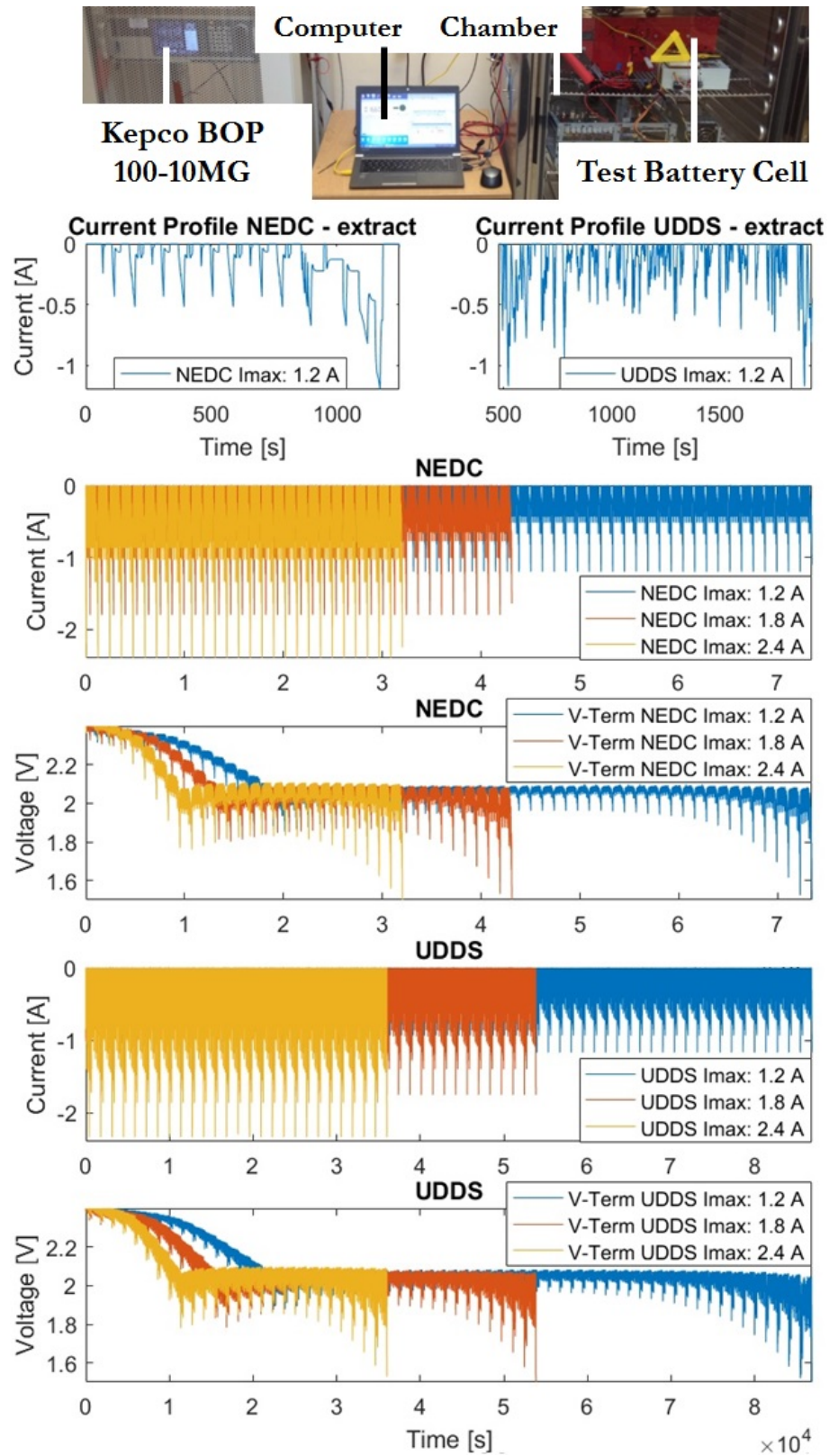


Figure 7.3: Experimental set-up and applied discharge currents

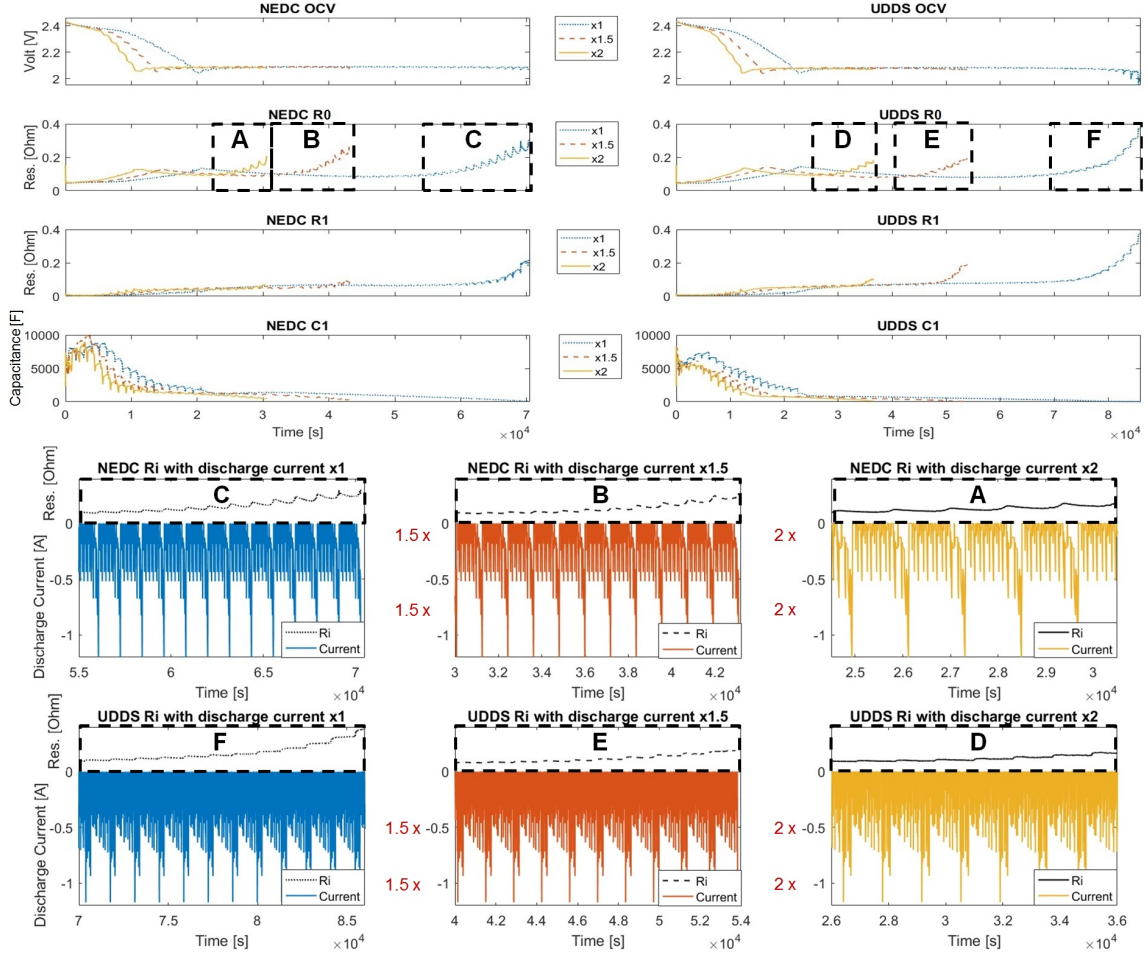


Figure 7.4: EKF online parametrisation results for different current profiles

7.4 Current - R_0 relationship

The results of the parameter estimation over time for all current profiles are shown in Fig. 7.4. Generally, the values of the online identification correspond well to the offline obtained values presented in Fig. 7.2. However, the internal resistance of the cell, R_0 , has a different pattern. Towards the end of discharge R_0 rises more quickly than predicted by the pulse discharge tests [17] and shows a relationship with the applied current density. The zoomed in areas in Fig. 7.4 show the normalised discharge current together with the identified R_0 . While a large current increases the internal resistance, lower currents or

relaxation periods lead to a decrease in resistance. This is particularly visible in the NEDC cycle test. The more uniform currents in the UDDS cycle, containing less relaxation periods, unveil a more persistent growth of R_0 . Furthermore, it is visible that while the internal resistance rises more quickly with higher currents, larger values are reached with smaller rates towards the end of discharge. Here, the high currents cause the battery voltage to drop to the cut-off voltage of 1.5 V before the resistance values can grow further.

The current dependencies in the observed R_0 suggest that it contains, next to the resistance of the electrolyte and current collectors [76], a diffusion part, which has been also reported and modelled in [85, 87] to fit the impedance spectroscopy data. Since we use a different current profile and identification method, also intended to be useful for the SoC estimation, we suggest as a simple solution to separate R_0 into a charge transfer R_{ct} and a diffusion R_{diff} part. While R_{ct} rises generally with lower SoC due to lower availability of cathode active surface area and of reaction species, the dynamic behaviour, R_{diff} , can be explained by the build-up of concentration gradients of species within the cell. High current pulses therefore build up stronger gradients, increasing R_{diff} as well as R_{ct} , due to stronger gradients in the electrolyte and fewer species available at the cathode surface to undergo the reaction.

The building up of internal gradients could also explain why this effect has not been found before. Common techniques, using identification windows [161] with artificial current pulses [99, 17], leave long resting periods in between the pulses. The current pulses, applied after open circuit condition, are therefore not enough to build up the concentration gradients contrary to the way in which a Li-S cell would be used in most applications. Here the continuously running EKF estimation method in combination with realistic current profiles is more suitable to represent real world usage.

7.5 Modelling of the dynamic internal resistance

The existing methods for parameter based SoC estimation for classic Li-ion batteries use the relationship between (online identified) OCV and SoC. As mentioned before, this would not be sufficient for Li-S batteries due to their constant OCV within the low plateau. Therefore, the internal resistance is used as additional information. The results of the EKF method have shown that the internal resistance varies with the discharge current rate. To reduce the fluctuations for the SoC estimation, this relationship should be accounted for by the equivalent circuit model in a preferably simple way. The charge transfer resistance is usually a function of SoC, current and temperature. To model the identified effects, we only assign the SoC and temperature to the charge transfer resistance R_{ct} and assign all current effects to diffusion gradients across the cell R_{diff} .

The dynamic component is calculated via a first order differential equation allowing the rise of R_{diff} when current is applied and a gradual decrease when the battery is left to rest.

This approach allows us to implement the current dynamics through a simple additional state within the existing battery model [17]. The internal resistance is therefore represented by

$$\underbrace{R_0}_{\text{similar to EKF ident.}} = \underbrace{R_{ct}}_{\text{from existing model}} + \underbrace{R_{diff}}_{\text{introduced dynamics}} \quad (7.24)$$

Where R_{diff} is represented by

$$\dot{R}_{diff} = \frac{1}{D_{diff1} D_{diff2}} R_{diff} + \frac{1}{D_{diff2}} I_L. \quad (7.25)$$

D_{diff1} and D_{diff2} are varying parameters over SoC, with no physical meaning. They are chosen to represent the dynamic changes of the internal resistance over time in a similar

manner to the identified values. For their parametrisation we subtract the static R_0 from the model in [17] for 20 °C from the R_0 identified by the EKF.

$$R_{\text{diff}} = R_0 - R_{\text{ct}} \quad (7.26)$$

The result (Fig. 7.5 A) shows the differences between the model parametrised by pulse data and the EKF method. The origins of them can either be due to cell variations, but also are likely to have methodical reasons. However, since the main purpose of the identification is to capture the increase in R_{diff} towards the end of discharge, the parametrisation of the dimensionless factors D_{iff1} and D_{iff2} is only done for the positive values. The methodology is similar to the parameter identification in Sec. 7.2, but simplified. Again we chose a behavioural interpretation of Eq. 7.25 and change the parameters to a steady state value and a time constant

$$\dot{R}_{\text{diff}} = -\Omega_{\text{R}} R_{\text{diff}} + \Omega_{\text{R}} D_{\text{iff1}} I_{\text{L}}, \quad (7.27)$$

where Ω_{R} is

$$\Omega_{\text{R}} = \frac{1}{D_{\text{iff1}} D_{\text{iff2}}}. \quad (7.28)$$

The state vector becomes,

$$x = \begin{bmatrix} R_{\text{diff}} & \Omega_{\text{R}} & D_{\text{iff1}} \end{bmatrix}^T \quad (7.29)$$

and the state transition functions

$$f(x, u) = \begin{bmatrix} f_1 & f_2 & f_3 \end{bmatrix}^T. \quad (7.30)$$

Where f_1 to f_3 are

$$f_1 = -x_2 x_1 + x_2 x_3 u, \quad f_2 = 0, \quad f_3 = 0, \quad (7.31)$$

similar to the R_p and C_p values defined in section Sec. 7.2. The measurement equation is

$$h = x_1. \quad (7.32)$$

The Jacobians are:

$$\hat{A} = \begin{bmatrix} -x_2 & -x_1 + x_3 u & x_2 u \\ 0 & 0 & 0 \\ 0 & 0 & 0 \end{bmatrix} \quad (7.33)$$

$$\hat{C} = \begin{bmatrix} 1 & 0 & 0 \end{bmatrix}. \quad (7.34)$$

The identified values of the parameters of the dynamic part of the internal resistance are also shown in Fig. 7.5 A for the NEDC drive cycle with different gains. To simplify the presented model, all curves are combined to one function (Matlab fitting tool [118]) for D_{iff1} and D_{iff2} respectively to

$$f_{D_{\text{iff1}}}(SoC) = 0.9148 e^{(-10.79SoC)} \quad (7.35)$$

and

$$f_{D_{\text{iff2}}}(SoC) = 3071 e^{(5.036SoC)}. \quad (7.36)$$

The results of the improved model are presented in Fig. 7.5 B, together with the EKF identification results. The dynamic part R_{diff} and the static part R_0 are plotted separately to show each part of the resistance working with different current inputs. Generally the model fits well to the EKF identification. However, for the lowest applied current density the model cannot represent the increasing internal resistance. This is presumably due to the made simplifications and to some factors playing a role at relatively long response times, such as precipitation [182]. For the SoC estimation we accept this error in order to

maintain the model's simplicity.

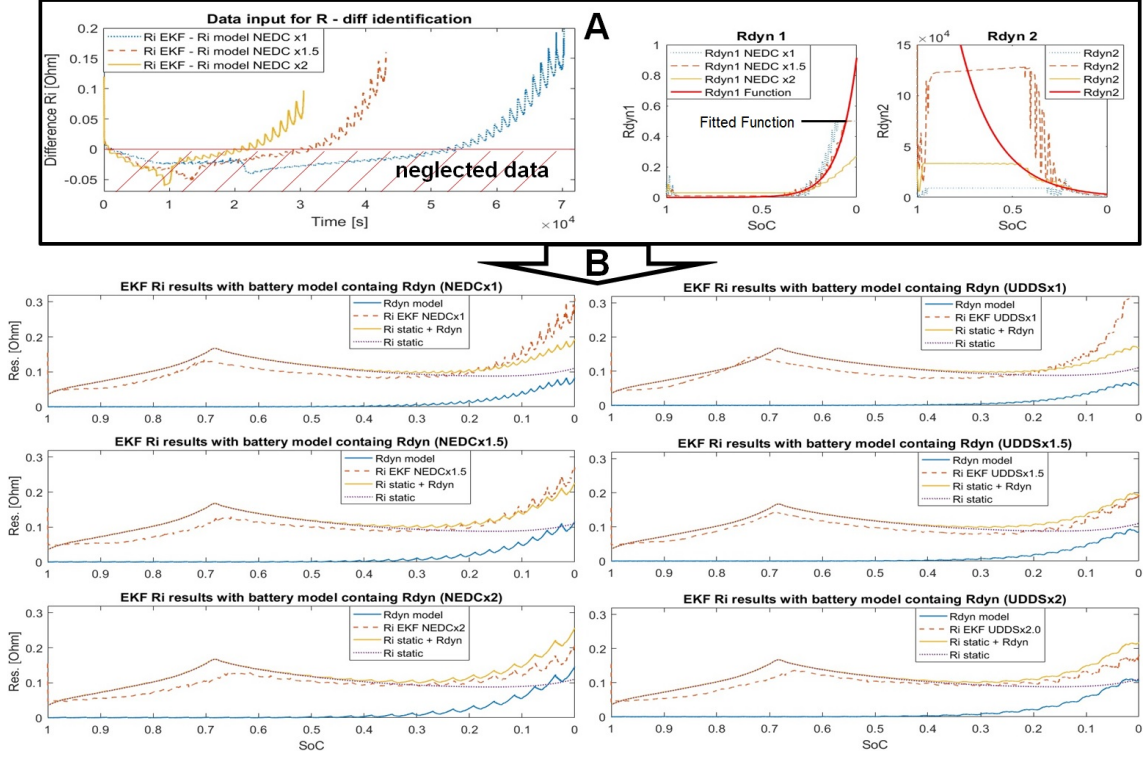


Figure 7.5: Modelling of R_{diff} : Parametrizing D_{iff1} and D_{iff2} (A), Comparison of identification results and dynamic resistance model $R_0 + R_{diff}$ (B)

7.6 State of charge estimation

Since the first EKF is only used to get the battery model parameters, a second one is used to relate them to the SoC. Therefore each Kalman filter works separately, which is chosen to improve the clarity. The battery model presented in [17] uses two polynomial functions for the static resistance R_{ct} and OCV respectively to represent the battery behaviour over

the discharge range. For the sake of completeness they are presented as follows

$$\begin{aligned} f_{OCV}(SoC) = (1 - \gamma_{m,c}(SoC)) f_{OCV-low}(SoC) \\ + \gamma_{m,c}(SoC) f_{OCV-high}(SoC) \end{aligned} \quad (7.37)$$

and R_{ct}

$$\begin{aligned} f_{Rct}(SoC) = (1 - \gamma_{m,c}(SoC)) f_{Rct-low}(SoC) \\ + \gamma_{m,c}(SoC) f_{Rct-high}(SoC). \end{aligned} \quad (7.38)$$

The two polynomial functions are combined smoothly via a partial sinusoidal differentiable function γ :

$$\gamma_{m,c}(SoC) := \begin{cases} 0, & \text{if a} \\ \frac{1}{2} + \frac{1}{2} \sin(2m(SoC - c)) & \text{if b} \\ 1 & \text{if c,} \end{cases} \quad (7.39)$$

where the conditions a, b, c stand for the different ranges,

$$\begin{aligned} \text{a : } 2m(SoC - c) < -\frac{1}{2}\pi, \\ \text{b : } -\frac{1}{2}\pi \leq 2m(SoC - c) < \frac{1}{2}\pi, \\ \text{c : } 2m(SoC - c) > \frac{1}{2}\pi. \end{aligned} \quad (7.40)$$

Here m is a scaling factor for the maximal gradient of the sinusoidal function, determining the transition region between the polynomials and c represents the point where both functions are equally represented. Once the internal resistance and OCV are known over the discharge range, the dynamic internal resistance can be calculated as follows. R_{diff} is included as a state for the SoC estimating EKF, which leads to the following state space

model

$$\begin{aligned}\dot{x}(t) &= A(t)x(t) + B(t)u(t) \\ y(t) &= C(t)x(t) + D(t)u(t).\end{aligned}\tag{7.41}$$

The dynamic states $x = [x_1 \ x_2]^T$ of the system are the dynamic internal resistance R_{diff} , as presented in previous section, and the SoC, calculated through Coulomb counting. The corresponding state space representation gives

$$\begin{aligned}A &= \begin{bmatrix} \frac{-1}{f_{D_{\text{iff}1}}(x_2) f_{D_{\text{iff}2}}(x_2)} & 0 \\ 0 & 0 \end{bmatrix} & B &= \begin{bmatrix} \frac{1}{f_{D_{\text{iff}2}}(x_2)} \\ \frac{-1}{3600Q_{\text{cap}}} \end{bmatrix} \\ C &= \begin{bmatrix} 1 & f_{R_{\text{ct}}}(x_2) \\ 0 & f_{OCV}(x_2) \end{bmatrix}\end{aligned}\tag{7.42}$$

with the current I_L as an input.

7.6.1 State of charge estimation with dual EKF

For the application of the EKF algorithm with the presented Li-S battery model, the Jacobians of the matrices A and C are needed. With the relating functions over SoC, denoted as x_2 , we therefore need the derivatives of $f_{OCV}(x_2)$, $f_{R_{\text{ct}}}(x_2)$, $f_{D_{\text{iff}1}}(x_2)$ and $f_{D_{\text{iff}2}}(x_2)$. Using one exponential function for each $D_{\text{iff}1}$ and $D_{\text{iff}2}$ the Jacobian matrix of A is obtained as follows:

$$\hat{A}(1,1) = \frac{-1}{f_{D_{\text{iff}2}}(x_2) f_{D_{\text{iff}1}}(x_2)} \quad \hat{A}(2,1) = 0 \quad \hat{A}(2,2) = 0\tag{7.43}$$

$$\begin{aligned}\hat{A}(1,2) = & \left[\frac{\dot{f}_{D_{\text{iff}2}}(x_2)}{f_{D_{\text{iff}2}}(x_2)^2 f_{D_{\text{iff}1}}(x_2)} \right. \\ & \left. + \frac{\dot{f}_{D_{\text{iff}1}}(x_2)}{f_{D_{\text{iff}2}}(x_2) f_{D_{\text{iff}1}}(x_2)^2} \right] x_1 \\ & - \left[\frac{\dot{f}_{D_{\text{iff}2}}(x_2)}{f_{D_{\text{iff}2}}(x_2)^2} \right] I_{Bat},\end{aligned}\quad (7.44)$$

where the derivatives of $f_{D_{\text{iff}1}}(x_2)$ and $f_{D_{\text{iff}2}}(x_2)$ are defined as

$$\dot{f}_{D_{\text{iff}1}}(x_2) = -9.875008 e^{(-10.79x_2)} \quad (7.45)$$

$$\dot{f}_{D_{\text{iff}2}}(x_2) = 15465.556 e^{(5.036x_2)}. \quad (7.46)$$

Following the same principle for C its Jacobian matrix is obtained as

$$\begin{aligned}\hat{C}(1,1) &= 1 & \hat{C}(1,2) &= \dot{f}_{R_{ct}}(x_2) \\ \hat{C}(2,1) &= 0 & \hat{C}(2,2) &= \dot{f}_{OCV}(x_2).\end{aligned}\quad (7.47)$$

The derivatives of the combined functions \dot{f}_{OCV} and $\dot{f}_{R_{ct}}$ with respect to x_2 are influenced by the introduced factor γ , here substituted by $f_\gamma(x_2)$.

$$\begin{aligned}f_{OCV}(x_2) &= (1 - f_\gamma(x_2))f_{OCV-low}(x_2) \\ &+ f_\gamma(x_2)f_{OCV-high}(x_2)\end{aligned}\quad (7.48)$$

Derivation with respect to x_2 leads to

$$\begin{aligned}\dot{f}_{OCV}(x_2) &= \dot{f}_{OCV-low}(x_2) - (\dot{f}_\gamma(x_2)f_{OCV-low}(x_2) \\ &+ f_\gamma(x_2)\dot{f}_{OCV-low}(x_2)) \\ &+ \dot{f}_\gamma(x_2)f_{OCV-high}(x_2) \\ &+ f_\gamma(x_2)\dot{f}_{OCV-high}(x_2).\end{aligned}\quad (7.49)$$

Where \dot{f}_γ is defined by

$$\dot{\gamma}_{m,c}(x_2) := \begin{cases} 0, & \text{if a} \\ m \cos(2m(x_2 - c)), & \text{if b} \\ 0, & \text{if c} \end{cases} \quad (7.50)$$

with same conditions for a, b, c as in Eq. 7.40. The derivation of the static internal resistance R_{ct} , given by the Eq. 7.38, follows the same pattern and is not presented. Instead, the derivation of the covariance matrices R and Q is examined thoroughly. In the process of finding the covariances, values capable of improving the convergence with wrong initial conditions within the high plateau and values enhancing the correct estimation towards the low plateau were found. As one advantage, the dual filter offers the opportunity to distinguish between the high and low plateau, simply by evaluating the identified OCV. Therefore, R and Q are varied between the plateaus, using an 'if' function included in the second EKF. If the identified OCV is larger than 2.15 V, Q and R are emphasised on the OCV identification and if the identified OCV is lower than 2.15 V Q and R rely on the results for Coulomb counting and the internal resistance. The resulting the parameterisation of the covariance matrices for the two main discharge regions of Li-S batteries are

$$R_{\text{high}} = \begin{bmatrix} 0.15 & 0 \\ 0 & 0.00054 \end{bmatrix}, Q_{\text{high}} = \begin{bmatrix} 0.1 & 0 \\ 0 & 0.01 \end{bmatrix} \quad (7.51)$$

for the high plateau and

$$R_{\text{low}} = \begin{bmatrix} 0.00015 & 0 \\ 0 & 0.549 \end{bmatrix}, Q_{\text{low}} = \begin{bmatrix} 0.1 & 0 \\ 0 & 0.0000001 \end{bmatrix} \quad (7.52)$$

within the low plateau. In both cases the initial condition for the probabilities P is

$$P_0 = \begin{bmatrix} 10 & 0 \\ 0 & 10 \end{bmatrix}. \quad (7.53)$$

7.6.2 SoC estimation with an initially fully charged battery

The results of the proposed SoC estimation algorithms are evaluated qualitatively for their convergence time, with imprecise initial values for the SoC state, and quantitatively by their estimation accuracy. As a measure for the accuracy, the root mean squared error (RMSE) over the whole discharge range is used

$$\text{RMSE} = \frac{1}{\sqrt{n}} \left(\sum_{i=1}^n (\text{SoC}_{t,i} - \hat{\text{SoC}}_{t,i})^2 \right)^{0.5}. \quad (7.54)$$

Where n is the number of data points, $\text{SoC}_{t,i}$ is the reference SoC from the measurement and $\hat{\text{SoC}}_{t,i}$ is the estimated SoC by the proposed technique.

Since the model does not include a current rate dependency for the discharge capacity of Li-S cells, the SoC estimator (Fig. 7.6) uses the identified capacity of 9778 As (2.72 Ah) for all applied currents. This value has been obtained from a pulse current test at 20 °C in [17] and used for SoC estimation in [16], and therefore allows the comparability to other SoC estimation methods. The initial conditions for the parameter identification are the same as in Eq. 7.22.

The results of the drive cycle tests show measured capacities from 2.52 Ah (for NEDC) to 3.11 Ah (for UDDS), which is a variation of 21% compared to the rated capacity of the cell model. The large difference between measured cell capacity in practical applications indicate again that Coulomb counting on its own is not sufficient for SoC estimation.

However, the estimation results of the dual EKF estimator are promising. As shown in

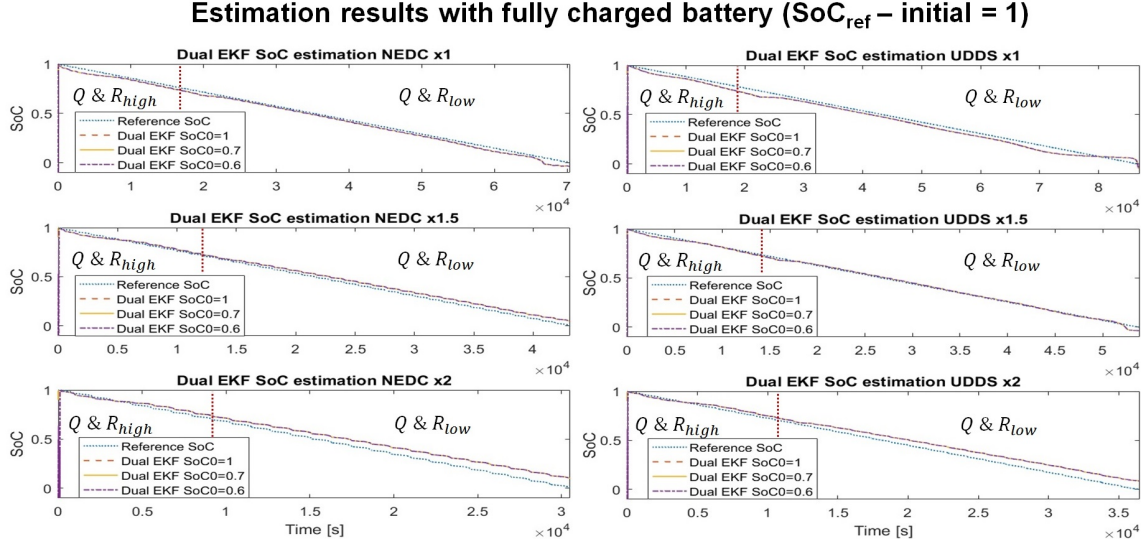


Figure 7.6: Results of the SoC estimation with different current profiles and rates

Fig. 7.6, the over all estimation results vary within 6.8% for all the test cases as illustrated in Fig. 7.7. In addition to the accuracy, the convergence time with the wrong initial SoC ($\text{SoC}_0 = 1, 0, 7, 0, 6$) could also be improved compared to the estimation results presented in [16]. Here the assignment of different covariance values to the plateaus improved the convergence significantly, which is possible due to the simple distinction of the two voltage plateaus of Li-S cells. The best results are archived for the two middle current densities due to the close match between model and measured capacity. However, the variations of the errors are small for all currents which is a sign for the robustness of the estimation.

Surprisingly, the largest estimation error is not reached in lower current density cases where the model is most inaccurate and the usable capacity is about 14% more than the rated one, it is the case of higher rates. Here the SoC estimation slowly drifts to 9.5% percent error towards the end of discharge (NEDC x2). This is presumably caused by the emphasis on the Coulomb counting within the low plateau and could be improved by better use of the behaviour of the internal resistance. However, with an average error of

Estimation error with fully charged battery ($\text{SoC}_{\text{ref}} - \text{initial} = 1$)

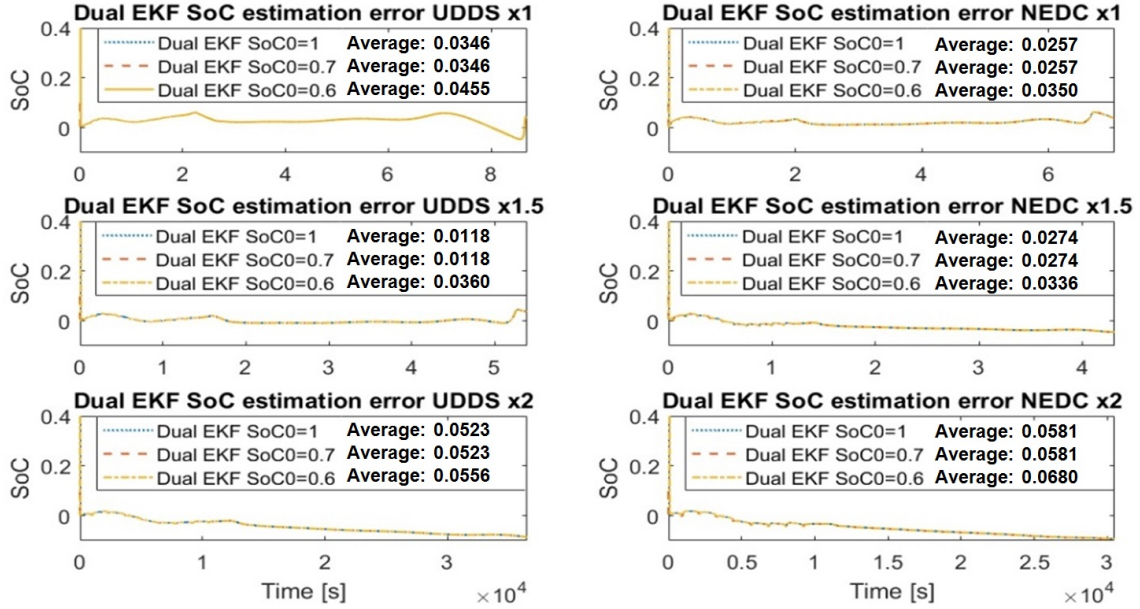


Figure 7.7: Estimation error with an initially fully charged battery

about 6.8% in the worst case of all six SoC estimation evaluation tests, the approach is considered as sufficiently robust (see Fig. 7.7).

7.6.3 SoC estimation with an initially partly discharged battery

Promising results could also be reached by testing the filters ability to handle imprecise initial conditions with a partly discharged battery. Here we started the simulation at the SoC of 0.6, which is roughly 10% lower than the transition point in between both voltage plateaus. This scenario is more realistic since the Li-S battery is likely to self discharge when the SoC estimation system is switched off. For the simulation the initial conditions of the online parametrisation EKF stays the same than before (Eq. 7.22), but is highly imprecise now, and the initial SoC of the second EKF is set to 1. The first output of the test is that the online parametrisation is robust against imprecise initial conditions. The OCV and internal resistance converge in all six cases to steady values within 50 s to 100 s

simulation time, which is particular useful for the SoC estimation since it relies on precise parameters. And indeed, the results presented in Fig. 7.8 and Table 7.2 show that the SoC also converges within the same period. However, the convergence towards the reference SoC stops at the transition point of the voltage plateaus.

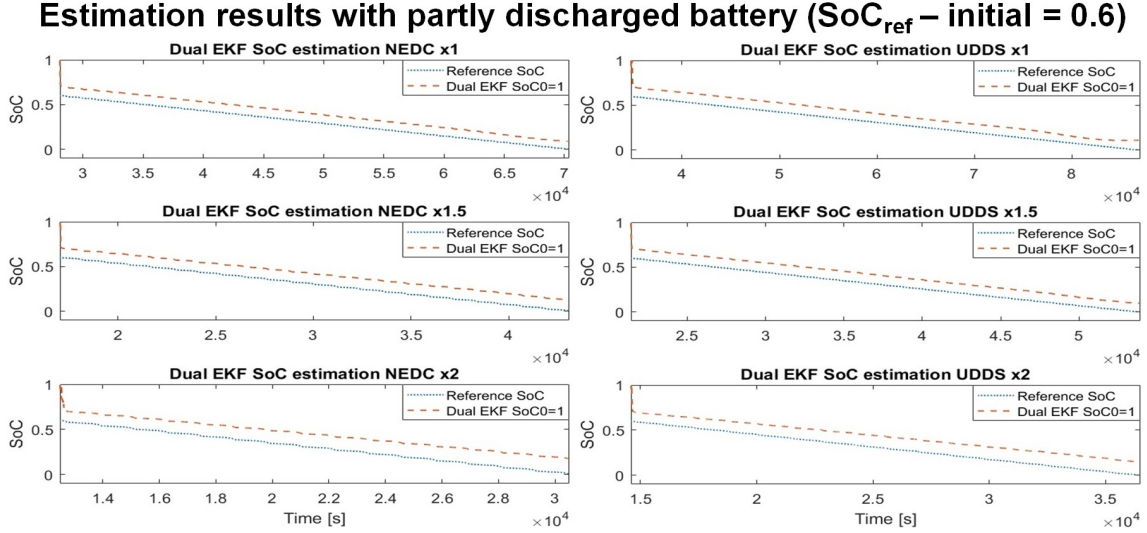


Figure 7.8: Results of the SoC estimation with different current profiles and rate densities with partly discharged battery

After the identified OCV falls under 2.15 V the estimation changes its pattern to place emphasis on Coulomb counting. This means that the correction of the state is slowly and can only be seen for the lower currents ($\text{UDDS} \times 1$, $\text{NEDC} \times 1$). Since the starting point of the simulation was chosen about 10% SoC beneath the transition point, also the estimation errors for this case are in that region. The slow convergence of the SoC estimation within the low plateau is one disadvantage of the presented method and can likely be improved by a better understanding and modelling of the internal resistance towards the end of discharge. Though the properties of Li-S cells help here to keep the estimation error reasonable. The self discharge is expected be present only in the high plateau [158], which founds the assumption that a self discharged Li-S battery is likely to

Table 7.2: RMSE SoC Estimation with UDDS and NEDC current profile with different gains for initially partly discharged battery

Current	SoC_0	UDDS RMSE	NEDC RMSE
$\times 1$	1	0.1061	0.1030
$\times 1.5$	1	0.1100	0.1214
$\times 2$	1	0.1422	0.1538

be near the transition point between both plateaus for a long time. Therefore the presented limitation is expected to be small in most of applications.

7.6.4 SoC estimation with multiple cycles

Although we focused our studies exclusively on the discharge process, we also present one of our experiments with three subsequent NEDC cycles with a constant charge of 0.32 A in between. Here we get good results with small additions to the presented SoC estimation, despite the lack of a charging model or a deep understanding of the charging process.

The additions to the estimator are a linear decay of the internal resistance, a coulombic efficiency of 0.9 and heavily emphasised Coulomb counting during charging

$$R_{\text{charge}} = \begin{bmatrix} 0.00015 & 0 \\ 0 & 55 \end{bmatrix}, Q_{\text{charge}} = \begin{bmatrix} 0.1 & 0 \\ 0 & 0.0000000001 \end{bmatrix}. \quad (7.55)$$

The slow descent of the R_{int} is mostly assumed because the constant charge current does not allow the parameter estimation to adjust automatically. In tests in Fig. 7.9 revealed a

variation in the discharge capacity, variances in the charging efficiency and an unknown (not modelled) charge curve. Here it is visible how useful the uncertainty is for the state estimation. During charge the SoC estimator can roughly estimate the SoC through Coulomb counting, while the uncertainties adjust for inaccuracies of the model or differences in the battery behaviour. Especially in the high plateau the correction works well and the drift from the crude charging assumptions is corrected within seconds after the discharge starts again. Here is one most significant improvements of the dual EKF method against a single EKF version, presented in [16] (Fig. 7.9 extracts). After the second charge the single EKF method roughly has the same error than the dual EKF, but needs considerable more time to converge back to the reference SoC in the subsequent discharge. The overall accuracy of the dual EKF for the entire test period is 0.0450 and can be seen as accurate enough for most applications. However, it has to be invested more effort to understand the charging process to ensure the results are robust for more diverse user cases. Furthermore the robustness has to be proven with drive cycles that assume a recuperation of kinetic energy during the drive cycle.

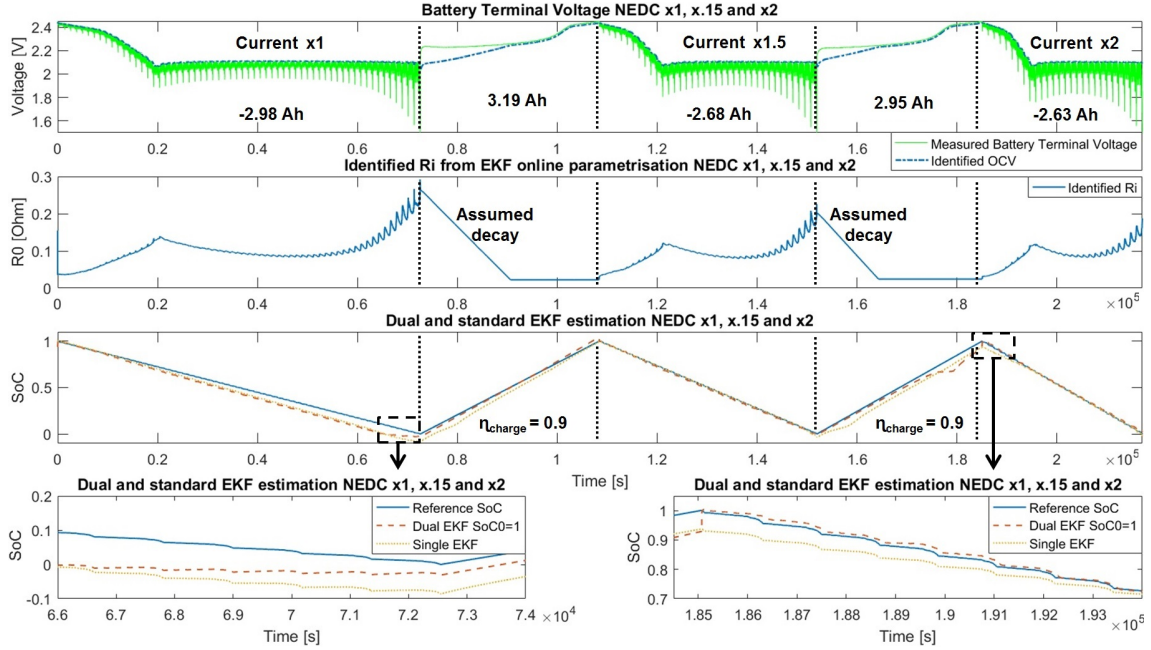


Figure 7.9: Results of the SoC estimation with three NEDC current profiles with constant charge

7.7 Conclusion

This study introduces and discusses three major aspects of the SoC estimation for Li-S batteries. Firstly, it is shown that an online parameter estimation with an extended Kalman filter can identify the parameters of a behavioural interpretation of a Thevenin equivalent circuit reliably. While this method is considerably faster than offline methods, it can identify the model parameters continuously and therefore is able to be used with practical current profiles, as long as they contain some dynamic changes.

In the second main part the proposed online identification method is used with two different drive cycle current profiles, each applied with three varying gains for the power demand. In all of our experiments, a relationship was found between the discharge current rate and the identified internal resistance. Since this behaviour fits the current understand-

ing of the inner cell reactions in the literature, a dynamic internal resistance term is defined and represented in a reduced order model to improve the prediction of the terminal battery voltage with diverse currents.

In the third part, a dual extended Kalman filter is designed for robust SoC estimation. Using the identified values of the OCV and internal resistance, the estimation accuracy can be improved by adjusting the algorithm to the specific properties of Li-S batteries. While in the low plateau, the OCV itself is a poor SoC indicator, it is reliable and precise within the high plateau. Therefore, the estimation in the high plateau trusts the identified OCV from the online parameter identification, while in the low plateau the Coulomb counting and internal resistance are the dominant factors.

The accuracy of the estimation results demonstrates the effectiveness of employing multiple sources of information for SoC estimation for Li-S batteries. With the emphasis on the OCV, the convergence from imprecise initial conditions can be improved. However, it also leads to a Coulomb counting emphasised estimation within the low plateau. Here the fact that the majority of the self discharge happens only in the high plateau of Li-S cells helps. To improve the estimation accuracy in the low plateau, a mechanism should be designed to count for the battery capacity changes with different rates and current profiles, which will be done in our future studies.

Another direction is to employ high fidelity electrochemical cell models for the SoC estimation. Having these, we aim not only to improve the current weaknesses of Li-S battery control models (capacity prediction) but also to enhance the understanding of the discharge reaction path.

7.8 Acknowledgement

This research was undertaken as part of the project ‘Revolutionary Electric Vehicle Battery’ (REVB), co-funded by Innovate UK under grant TS/L000903/1; university funding is provided by EPSRC under grant number EP/L505286/1 . Enquiries for access to the data referred to in this article should be directed to researchdata@cranfield.ac.uk. (The data used in this article is described at [10.17862/cranfield.rd.c.3723934](https://doi.org/10.17862/cranfield.rd.c.3723934); it is subject to an embargo, and will be available from May 2022.)

Part III

Discussion and conclusion

8

Contributions and future directions

In the course of this thesis, three main contributions for the practical use of Li-S batteries have been accomplished. Firstly, a low fidelity and fast running battery model was developed, capable of predicting the cell voltage over a discharge and temperature range. Secondly, the model was used for SoC estimation with Kalman filter based algorithms and thirdly, an online parameterization approach has been presented which could also be used for SoC estimation.

Next to the estimation itself, another contribution for this thesis was to increase the general understanding of Li-S cells in realistic applications, which is why the advantages and limitations of the used methodology are discussed here. Due to the dense nature of scientific publications, the discussion is supplemented by additional material, that have not been published yet. The discussion orients directly on the paper based structure of this thesis and is separated in a section for each paper respectively.

8.1 Battery model for SoC estimation

The emphasis on the equivalent circuit model was to reproduce the battery behaviour for a temperature range of 20 – 50 °C. In the course of the project however, it was found that cell operation at elevated temperature lead to increased degradation. This reduces the recommended operation in a controlled environment to 20 – 30 °C. Within this smaller range however, the temperature variation is relatively small. The changes with the current rate for realistic current profiles, shown in Fig. 8.1, are significantly more pronounced.

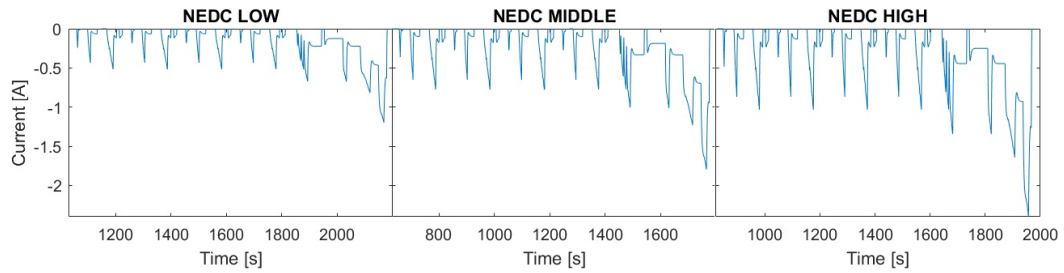


Figure 8.1: NEDC current profiles with different scaling gains

Fig. 8.2 shows the respective voltage responses of one Li-S cell, that is discharged with NEDC current profiles at different temperature levels and current rates. It is clearly visible that the temperature variations within this range are significantly smaller than the larger window of 20 – 50 °C from Chapter 5. However, the variances through the current rate and profile are more pronounced as the capacity values and voltage curves indicate. For practical applications, these variations are significant, since they impede a precise rating of the usable capacity and effect the SoC estimation negatively. This is especially the case for EVs since current rates depends, next to vehicle design parameters like weight, the drive train or battery pack layout, also on the driving style. In the following, the achievements and limitations of the model are summarized and discussed.

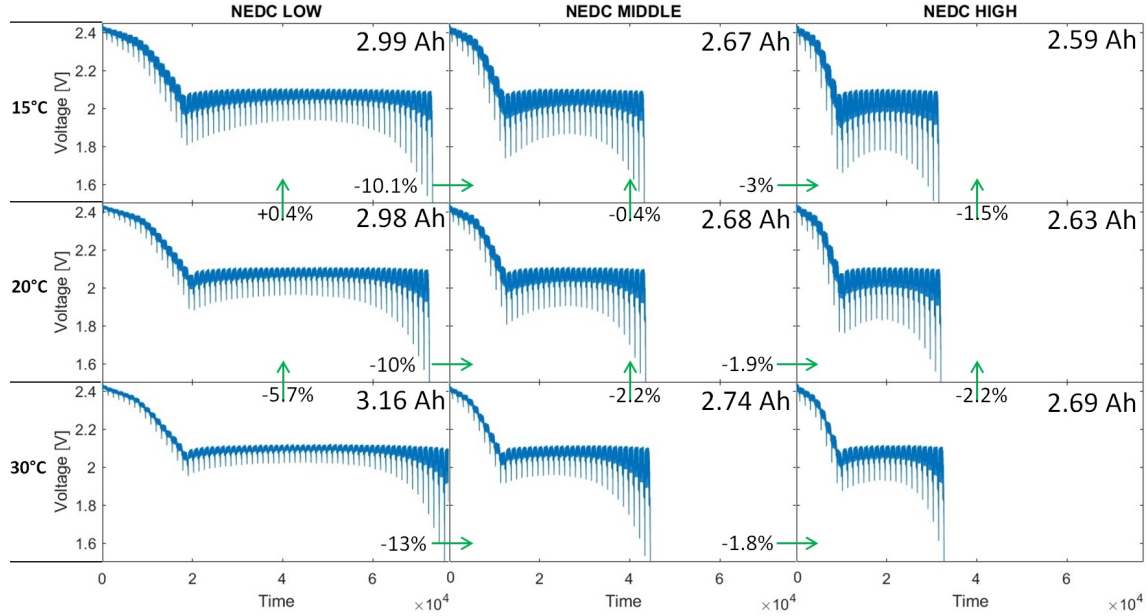


Figure 8.2: Voltage response to NEDC current profiles over different temperatures

8.1.1 Contributions

The model presented in Chapter 5 accounted for the unique behaviour of Li-S cells with three main properties. Firstly, a behavioural interpretation of the Thevenin equivalent circuit have been used in combination with a mixed current pulse, which improved the model fit without enhancing the computational effort for the identification. Secondly, the high and low voltage plateaus were represented by individually fitted polynomial functions that are combined smoothly and derivable with a partial sinusoidal function. Thirdly, the polynomial factors were changed via lookup tables to preserve the derivability over a temperature range of 20 – 50 °C. The resulting model is the simplest in literature, that can accurately predict the voltage behaviour for practical applications for the discharge and varying temperatures. Generally, the model works best for high SoCs as shown in additional experiments (Fig. 8.3) over the temperature range of 15 – 30 °C. Also both plateaus and their transition point could be represented well, which also is the case for different current rates and current profiles. However, the simplifications also led to inaccuracies,

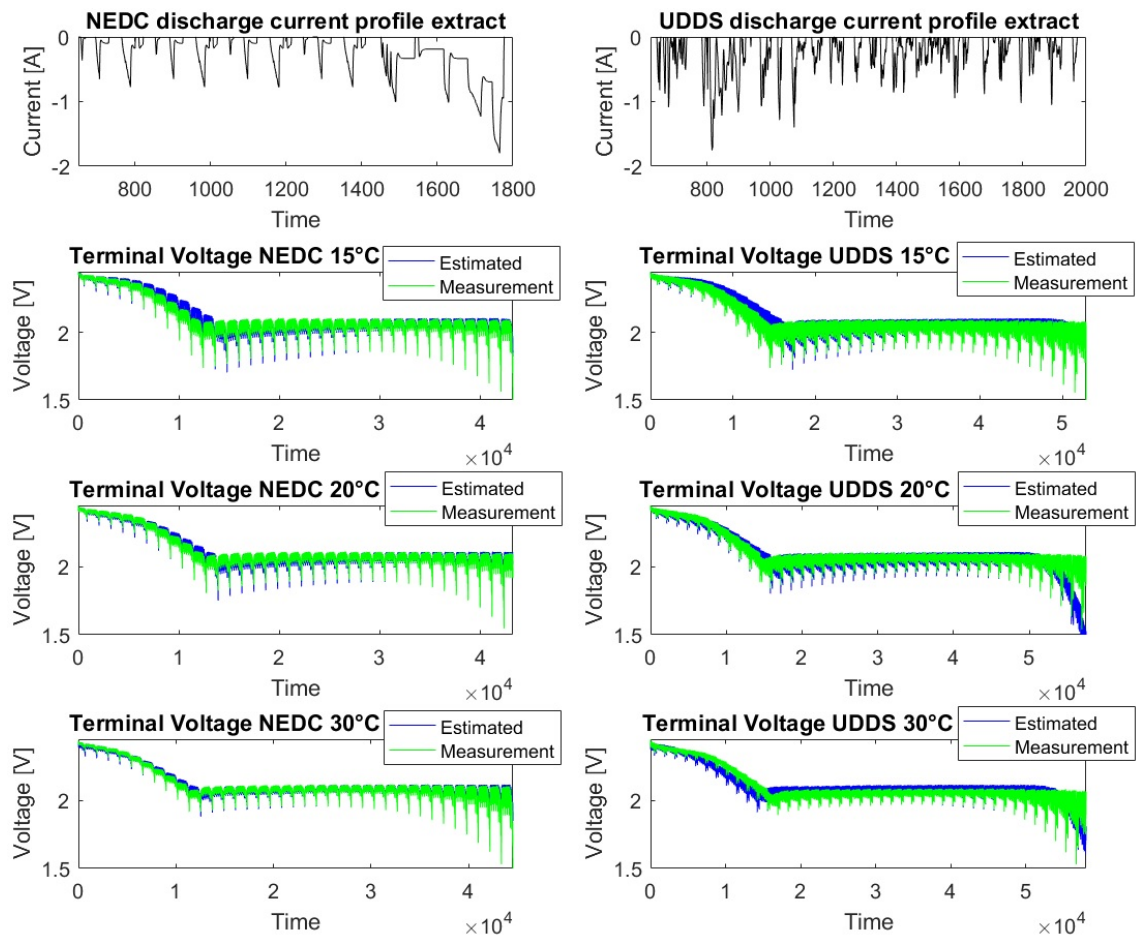


Figure 8.3: Discharge tests with the NEDC and UDDS cycle over different temperatures

which are described in the following section.

8.1.2 Limitations

The most important limitation of the presented model are the unmodeled capacity changes with different rates. As shown before, the capacity variations for temperate changes between 20 and 30 °C are less pronounced than the current density variations. Together with the Coulomb counting based representation of the parameters, this leads to deviations between model and measurements towards the end of discharge, visible for the UDDS cycle in Fig. 8.3. Another limitation of the model is for realistic applications less relevant, but is presented here for the sake of completeness. In the course of the project, a battery cycler was developed to change the temperature of the cell quicker than a thermal chamber [121, 183] (Appendix C). Though the main purpose of the rig was to identify optimal dynamic cycling temperatures, experiments can be used to test the robustness of the thermal model for extreme cases as well. Fig. 8.4 shows a mixed current pulse discharge with mixed temperatures varying between 20 and 45 °C, also following a pulse pattern. In these conditions the modelling of the parameters over the whole discharge range leads to difficulties, especially in the high plateau. The low plateau however, is represented well.

8.1.3 Directions for future work

The model errors with very quickly changed temperatures are negligible for practical applications, since large battery packs either are temperature controlled or change their temperature significantly more slowly than the experiment. Efforts to improve the prediction of the usable cell capacity for different current profiles and rates are more likely to improve the model's accuracy and its applicability for state estimation. Since the Li-S inner cell reactions are not yet fully understood, a zero dimensional reduced-order chemical

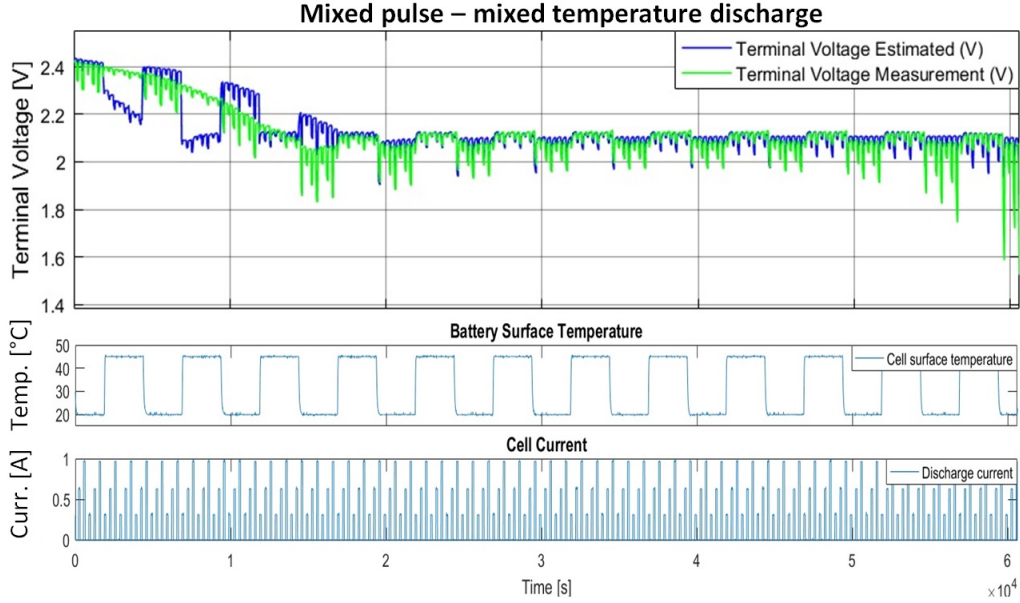


Figure 8.4: Mixed pulse, mixed temperature discharge test

model, based on the amount and concentrations of active material, is a potential solution for this problem. However, simpler techniques based on current and voltage measurements, like average power, might be successful as well. Another major improvement for the capacity prediction of the cell is the implementation of a degradation model, to ensure the SoC estimation is not affected greatly over time. Regarding the experiments conducted in this thesis, effort should also be focused on the evaluation of cell variations, which could hinder the efficient use of a larger pack. Here the existing model together with the mentioned improvements could help to choose cells for a battery pack.

8.2 SoC estimation with derivations of the Kalman filter

Due to the uncertainties of Li-S cells in operation, Bayesian filters have been chosen that use model predictions and measurements for optimal state estimation. As introduced before, the properties of Li-S batteries make a precise state estimation challenging. How-

ever, the applied derivations of the Kalman filter, the EKF, UKF and PF, could estimate the SoC robustly, as long as the predicted usable capacity value of the model corresponds reasonably well to the actual achieved capacity of the cell.

8.2.1 Contributions

The main advantage of the presented filters is their relative simplicity and their ability to include multiple sources of information. While Coulomb counting-oriented estimation can be used in the centre of the low plateau, where the predicted voltage is a weak indicator of the SoC, the correction of accumulated estimation errors can occur in the high plateau and towards the end of discharge. Supplementary to the results in Chapter 6, the SoC estimation for the Kalman filter derivatives are also shown for the experiment with three consecutive discharges with different current gains and profiles, introduced in Chapter 7. Like before, all of the estimators have a fixed usable capacity prediction of 9778 As (2.72 Ah) and a charge efficiency of 0.9, which is only a rough interpretation of the truth (Fig. 8.5). The results suggest a reasonable precise estimation, given the uncertainties of Li-S cells and the relative simple model approach without charging capabilities. Furthermore, the results represent only the pure filters performance which could further improved by calibration points for the fully charged or discharged state. Another presented point in Fig. 8.5 is the measured terminal voltage (green) and the predicted one (blue). Here the model is parameterized retrospectively with the measured values from Coulomb counting for each charge and discharge process respectively. It can be observed that with right capacity values the model stays reasonably accurate for all discharges, which indicates that the voltage prediction for other applications or current rates is not significantly worse, as long the capacity is approximately known. With other words, in reasonable ranges the model is scalable over different capacities.

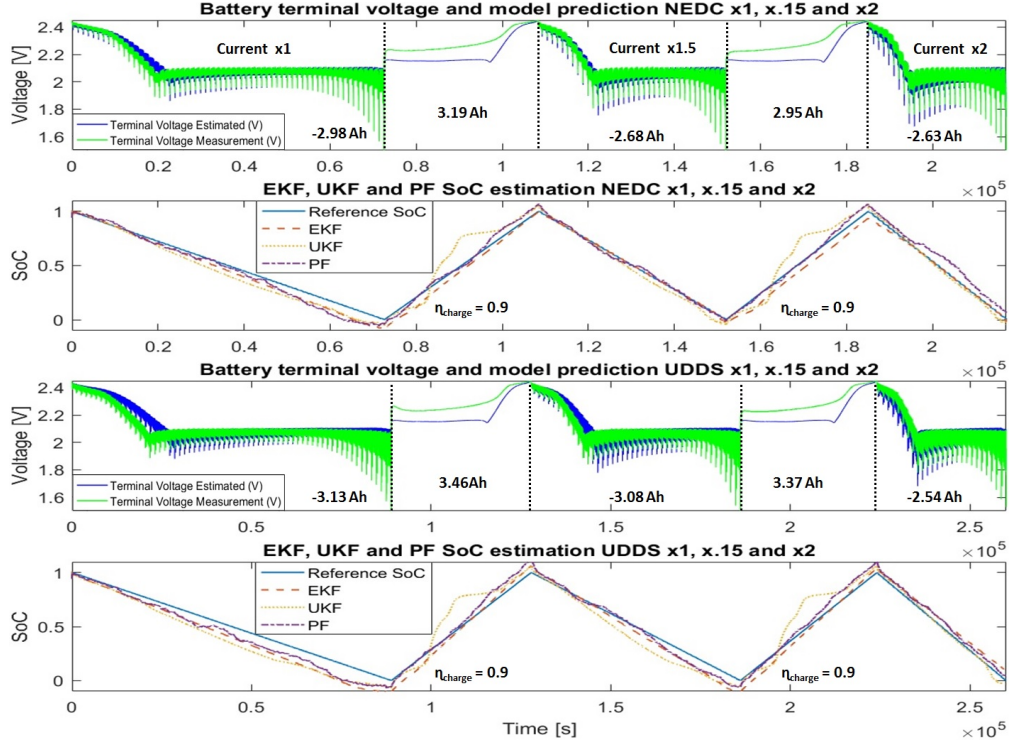


Figure 8.5: Consecutive discharges with NEDC and UDSS cycles with varying gains

8.2.2 Limitations

The imprecisions of the estimation mainly occurred in this experiment for the lower current densities. Due to the relatively small voltage prediction error in the middle of the low plateau, the SoC drifts here and can only be corrected by the increased internal resistance towards the end of discharge. For the presented filters, the correction starts noticeably after the SoC reached 0 due to the drop of the OCV of the model after the SoC leaves the defined range. Here it would be helpful to better employ the internal resistance growth and to reduce the significance of Coulomb counting for the estimation.

8.2.3 Directions for future work

Possible methods for this could be a dynamic, in this thesis as constant assumed, uncertainties depending on the SoC or the discharge current. Furthermore, the already suggested improvements in the model's ability to predict the usable capacity for different user cases would have significant effects on the estimation quality. However, since the introduced uncertainty can correct the states reasonably well, a more simple approach like rate factor might be sufficient as well. In the near future the expansion of the estimation for multiple temperatures is valuable and relatively simple, since the model already delivers changing polynomial functions that can be implemented in the Kalman-filter based algorithms.

8.3 SoC estimation with EKF based online parameter identification

To improve the robustness of the SoC estimation for more diverse current profiles, another approach based on the EKF has been developed and tested. The experiments were extended for two drive cycles with different gains to create more diverse test data. The contributions of this part to the application of Li-S batteries can be separated in two main parts, the online identification itself and the SoC estimation based on the parameters.

8.3.1 Contributions - online parameterization

The parameterization of the ECN model firstly allowed to have a continuously running identification of the model parameters during a realistic discharge, without the limitations of artificial currents pulses or other averaging methods. The results reached the same accuracy as offline methods, despite being significantly faster to run, and also improved

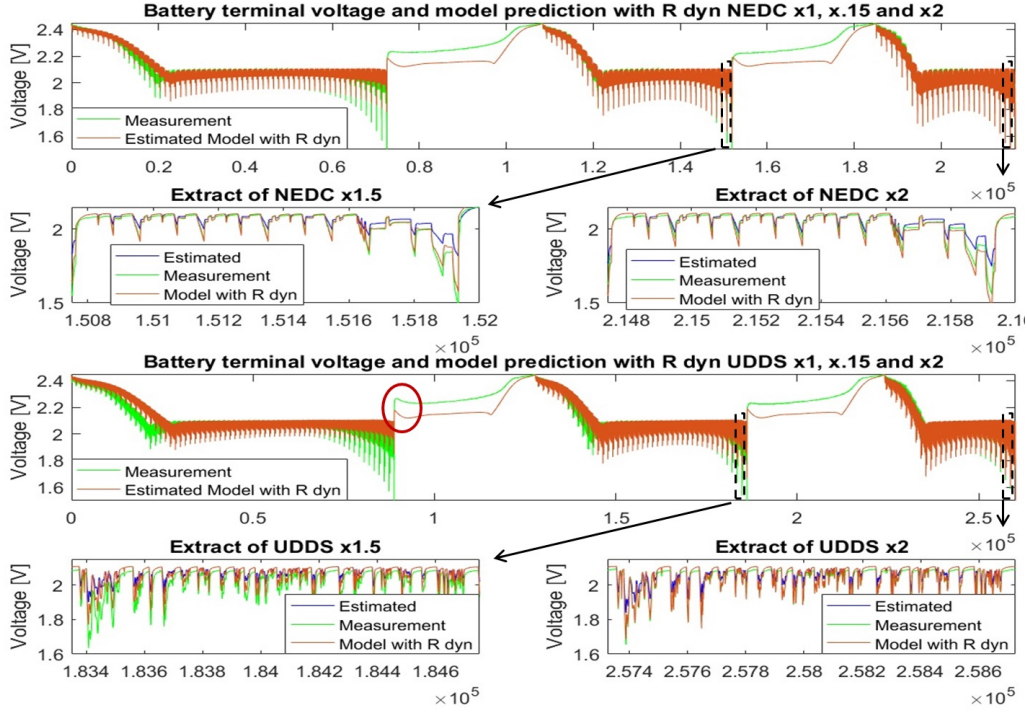


Figure 8.6: Consecutive discharges with model improvement R_{dyn}

insight into the applicability of the Thevenin model framework approach. While the literature identified mostly two parallel RC network models for Li-S cells (Chapter 5), in this thesis a simpler one parallel RC circuit model is used. The online identification revealed limitations of this approach. The smooth results within the first half of the discharge range suggested that the Thevenin model can adequately represent Li-S cell. However, within the second half the current related variations of the internal resistance indicated that a second parallel RC part, representing the concentration gradients of active species in electrolyte, is necessary to represent the behaviour of the cells. And indeed, Fig. 8.6 shows a significant improvement in the model prediction towards the end of discharge with a modelled dynamic internal resistance. Therefore, the relatively poor voltage prediction towards the end of discharge from the offline parameterization in Chapter 5 was already improved. It also should be mentioned that the model of the dynamic internal resistance

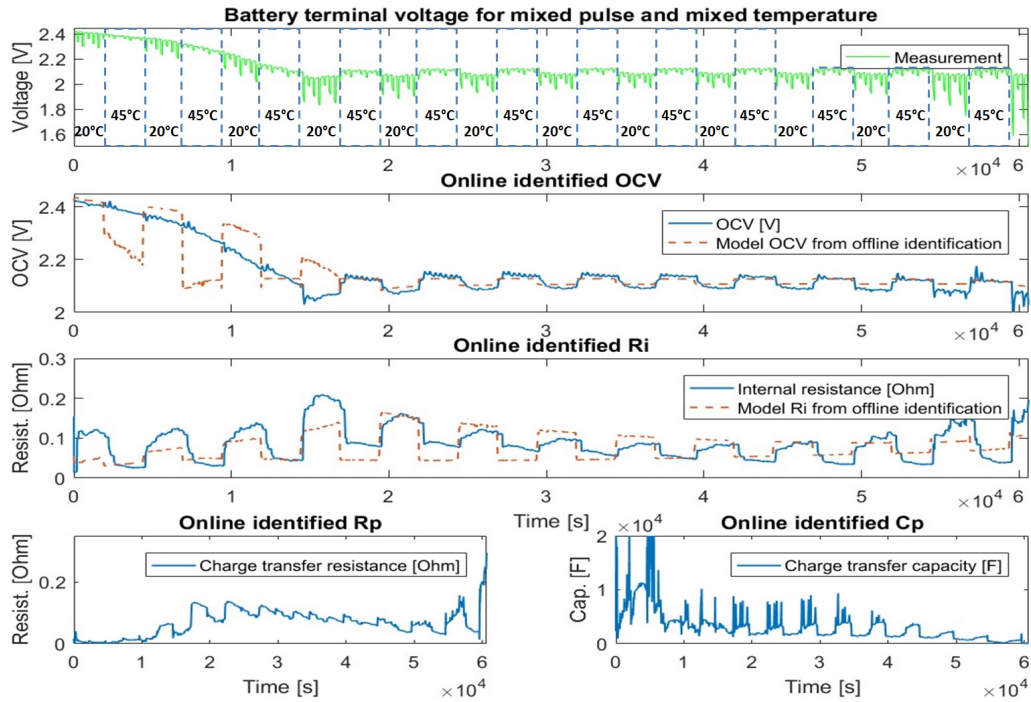


Figure 8.7: Online parameter identification with mixed pulses and mixed temperatures

could be used to model the slight peak of resistance after switching from discharge to charge current (Fig. 8.6 red circle). Another aspect of the online parameterization is its robustness. For a robust SoC estimation especially the OCV and internal resistance have to be identified precisely with only a small margin, even in non optimal conditions. In Chapter 7 the robustness against imprecise initial conditions was presented. To present the robustness under more difficult conditions, the data from the mixed pulse - mixed temperature experiments is used to identify the model parameters (Fig. 8.7). Despite the relative unrealistic scenario and the simple test hardware of the experiments [121], the results represent the current understanding of the cell well. While the identified OCV shows hardly any temperature dependence within the high plateau, the value varies in the lower one. Also the internal resistance gives reasonable values and does not show any numerical instabilities, which indicates a robust identification.

8.3.2 Contributions - SoC estimation

The ability to employ multiple parameters for the estimation is especially useful for Li-S batteries, since the OCV is not sufficient to estimate the SoC. Together with the improvements of the model accuracy, the SoC estimation had been improved in its robustness against varying discharge capacities of different power demands and current profiles. The employment of the internal resistance and the OCV furthermore allowed to robustly define the high and the low plateau, which also allowed more freedom in the parameterization of the process and measurement noises. As presented in Chapter 7, the estimation results and the convergence with wrong initial conditions were improved compared to the single filter solutions of Chapter 6.

8.3.3 Limitations

Generally, the model identification based on input-output relationship of current and terminal voltage needs a certain amount of dynamics in the system, which also accounts for the online EKF parameterization algorithm. With constant discharge current over a long period, the information for the model is not sufficient to parameterize it. Here the separation of the voltage output in OCV, internal resistance and transient behaviour is difficult. Therefore, also the SoC estimation cannot be applied with constant discharge currents. However, such a current profile is extremely unlikely for an electric vehicle. For other applications, the SoC estimation might need to be adjusted. Furthermore, artificial pulses could be added from the BMS internally, to create small dynamics within certain intervals.

8.3.4 Directions for future work

Most promising for the estimation based on the online parameter identification is to reduce the dependence of the Coulomb counting in the SoC prediction step. For every cell and current profile the end of discharge is indicated by a rising cell resistance. By improvements in its modelling, or other techniques to improve the utilisation of this information, the SoC could be predicted more robustly. Another option for the presented Thevenin model would be to utilise the variations of the internal resistance towards the end of discharge. However, more studies have to be made how well the internal resistance is related to the SoC under different conditions.

9

Conclusion

The aim of this thesis is to provide a foundation for the management of Li-S batteries. As a starting point, the SoC estimation in the framework of electric vehicles was chosen, since the high specific energy and the potentially low production costs of Li-S cells would be highly beneficial for a mass produced fully electric vehicle. However, the main findings of this thesis provided the framework for future applications, not only for this field. The key contributions were:

Develop a Li-S cell model for SoC estimation:

In **Paper 1**, a simple yet accurate equivalent circuit model is presented, capable of predicting the Li-S cell voltage from 20 – 50 °C. The unique behaviour of Li-S cells is modelled through two joined polynomial functions for the high and low voltage plateau respectively and lookup tables for the polynomial factors to follow temperature changes. Furthermore, the identification is improved by using a behavioural interpretation of the commonly used Thevenin equivalent circuit model. The presented ECN model gives a simple and computational inexpensive opportunity to simulate Li-S cells for practical applications and can also be used by application engineers to simulate the discharge behaviour for different applications. However,

due to the complex reactions of the Li-S chemistry and the relative simple modelling approach, the model contains inaccuracies. Here, mostly a relative imprecise prediction of the internal resistance towards the end of discharge and a fixed cell capacity assumption affect the prediction negatively.

Develop robust SoC estimation with comparable accuracy to Li-ion approaches:

After evaluating possible SoC estimation methods and choosing model based approaches in **Paper 2**, it has been found that Kalman filter-based algorithms can handle the unique properties of Li-S batteries and the resulting model inaccuracies well. Their ability to converge to the right state with an increasing amount of measurements works particularly well in the high voltage plateau, where there is a strong relationship between the prediction errors and the SoC. Within the low plateau, the SoC estimation is mainly build on Coulomb counting, which is the reason of relatively slow convergence and a slight drift in that region. However, the accumulated error can be reduced towards the end of discharge, which is indicated by a rising internal resistance. Generally, the extended Kalman filter, the unscented Kalman filter and the Particle filter could achieve robust results. Here, the UKF was found to deliver the best compromise between computational effort, accuracy and convergence time with imprecise initial conditions. However, for applications with simpler requirements, the EKF is also an option. The increased computational effort of the Particle filter however, does not lead to improvements in the estimation accuracy for the experiments in this study.

To improve the estimation performance, in **Paper 3** an EKF based online parameter estimation approach was developed. With employing the identified values for the OCV and internal resistance within a second EKF, the SoC estimation accuracy and the robustness against imprecise initial conditions could be improved. Furthermore,

the continuously running online parameter identification helped to gain insight into the cell behaviour with dynamic current profiles. The cell model could be improved with a current related internal resistance, which represents concentration gradients of active species in electrolyte. The online identification was found to be robust against imprecise initial parameters and quick temperature changes, which makes it potentially useful for other fields, since it allows a simple and fast identification of the cell behaviour with dynamic currents.

Establish accuracy, limitations and future directions:

Generally, the presented SoC methods can handle the uncertainties of Li-S cells well. However, when the current rate or the profile changes significantly, the algorithms start to drift. Here a possibility to predict the cell capacity with different discharge currents and current profiles would improve the estimation significantly. For the presented model and methods, the online parameter estimation method delivers the best results. The combined information of OCV and internal resistance allows good precision, even with crude assumptions. One example for this is that the filters also work reasonably well when the battery is charged, even if no charging model exists. The robust identification of model parameters also gives more flexibility for future improvements. The internal resistance, for example, could also be employed for degradation. Furthermore, other definitions for the end of discharge could be introduced. Now the definition of a depleted battery is when it hits the lower cut-off voltage of 1.5 V. Since the power capabilities of the cell are significantly reduced towards the end of discharge, it is also possible to define the end of discharge with a certain internal resistance. However, more studies have to show the feasibility of this approach. Another advantage of the online parametrization is, that it can also give more flexibility for the BMS designer, not strictly related to the

SoC estimation. Here for example a crawling mode for electric vehicles is possible, which reduces the power with a certain internal resistance value.

Generally, the combination of modelling and state estimation is promising and the results presented here, provide a wide base for practically oriented research for Li-S cells. For example, the here developed EKF has been already applied in the framework of the ALISE project [184], which aims to implement a Li-S battery in a plug in hybrid electrical vehicle. Furthermore, the algorithms and findings will be used within the Airbus Zephyr Innovation Programme for high altitude solar powered autonomous air-planes [185]. The special requirements for these planes, emphasising highest efforts on the lightweight energy storage, allows the commercial use of Li-S batteries already in the near future. For electric vehicles however, it will take more time until Li-S batteries could replace the current Li-ion technology. Here the high gravimetric energy density is only one of many factors that have to align with the application and volumetric energy density, power capabilities and lifetime are also important. However, the high interest of this promising technology, measurable in the increasing number of publications per year, has improved the understanding greatly in recent years and it is likely this trend will continue. It is therefore assumed that Li-S batteries will be used for more niche applications and that the commercial value of the cells will increase. This development, and the experience of running the cells in different applications, will also help to refine the introduced methods of this thesis. After all, it will be an exiting path to see if Li-S batteries can supplement today's Li-ion cells as the world's most superior battery type.

Appendices

Appendix A

Cell data sheets from Sion and OXIS



Lithium Sulfur Rechargeable Battery Data Sheet

Lithium sulfur has the highest theoretical specific and volumetric energy densities of any rechargeable battery chemistry (2550 Wh/kg and 2862 Wh/l theoretically). SION Power has learned how to unlock this potential and has created a unique rechargeable battery system. This patented technology is enabling new applications for rechargeable batteries and replacing existing primary and rechargeable batteries in applications where weight is a critical factor.

Typical applications include:

- Unmanned Vehicle Systems
- Weight sensitive electronic applications
- Military communication systems
- Sensors

Electrical Specifications:

Nominal Voltage:	2.15V
Maximum Charge Voltage:	2.5V
Minimum Voltage on Discharge:	1.7V
Nominal Capacity @ 25°C:	2.5 Ah @ C/5
Maximum continuous discharge rate:	2C
Maximum charge rate:	C/5
Specific Energy:	350 Wh/kg
Energy Density:	320 Wh/l
Cell Impedance:	25 mΩ

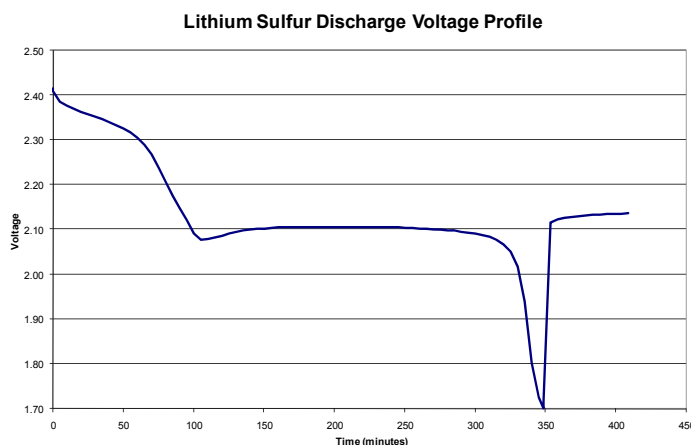


Mechanical Specifications:

Configuration:	Prismatic
Length:	55 mm (top flanged folded)
Width:	37 mm
Thickness:	11.5 mm
Weight:	~16 g

Environmental Specifications:

Discharge Temperature:	-20°C to +45°C
Charge Temperature:	-20°C to +45°C
Storage Temperature:	-40°C to +50°C



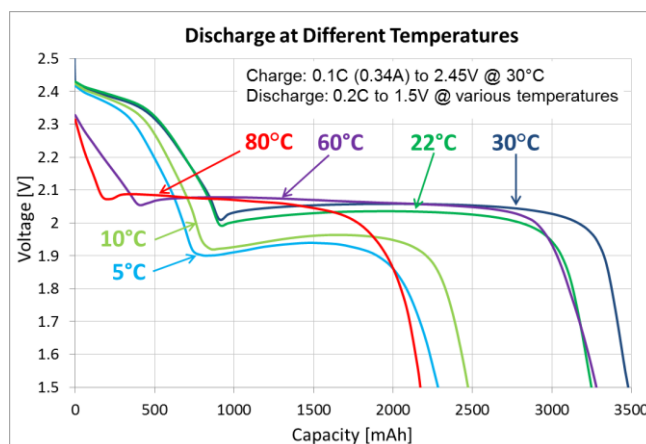
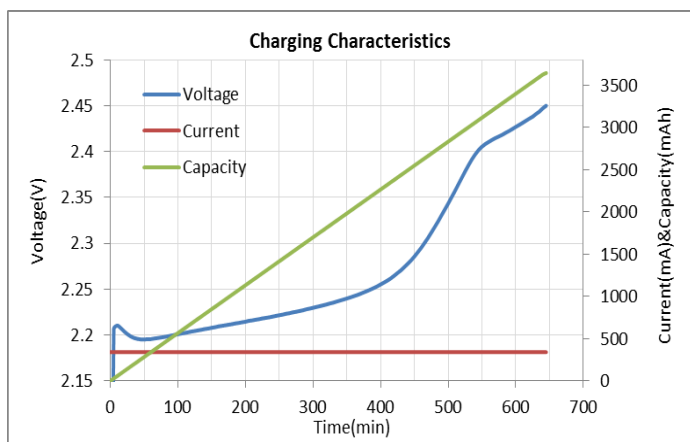
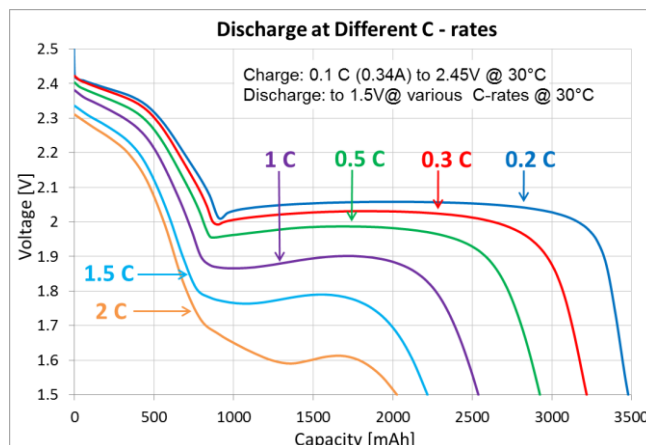
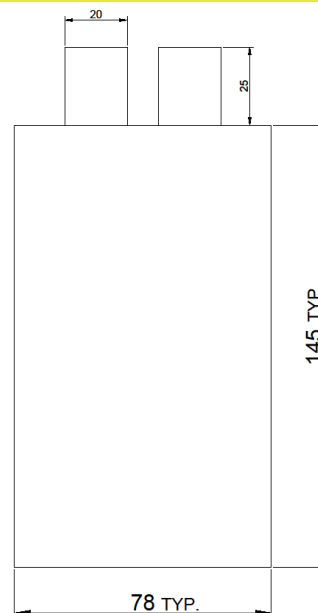
SION Power Inc., 2900E. Elvira Rd., Tucson, AZ 85756 Tel: +1.520.799.7500 Fax: 1.520.799.7501
www.sionpower.com

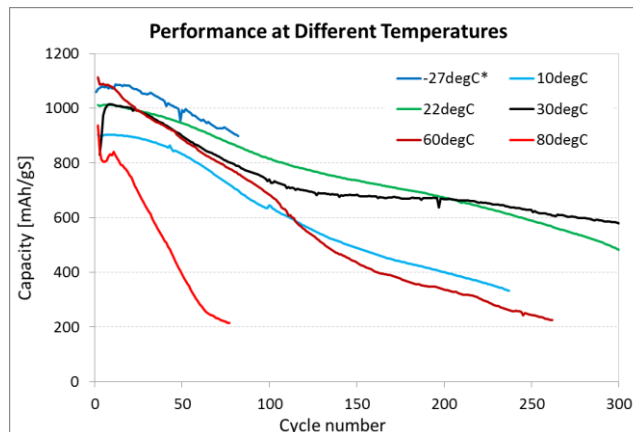
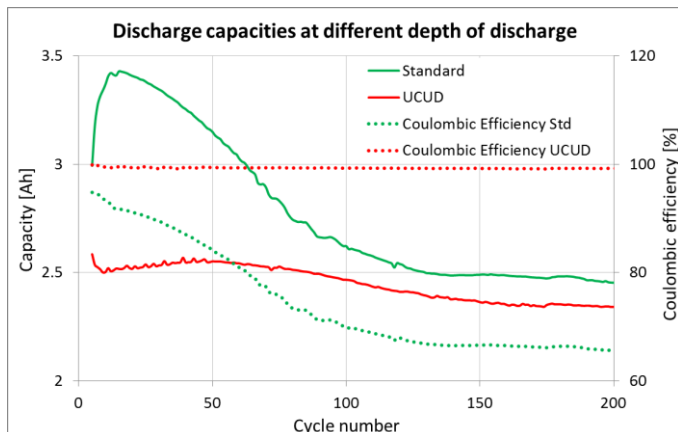
All specifications are subject to change without notice. The information contained here is for reference only and does not constitute a warranty of performance.

Date: 10/3/08 - Supersedes: 09/28/05

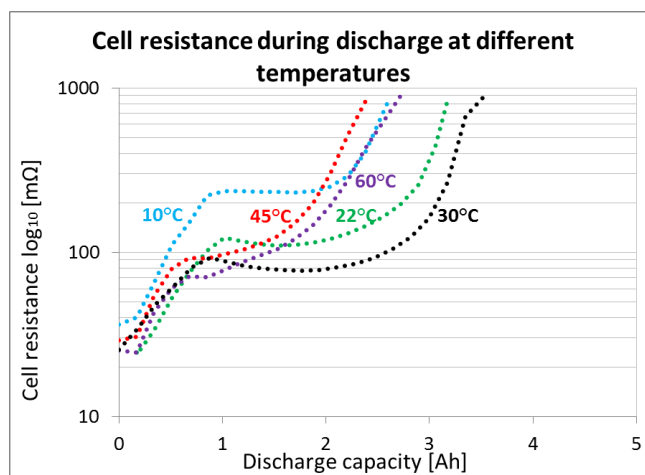
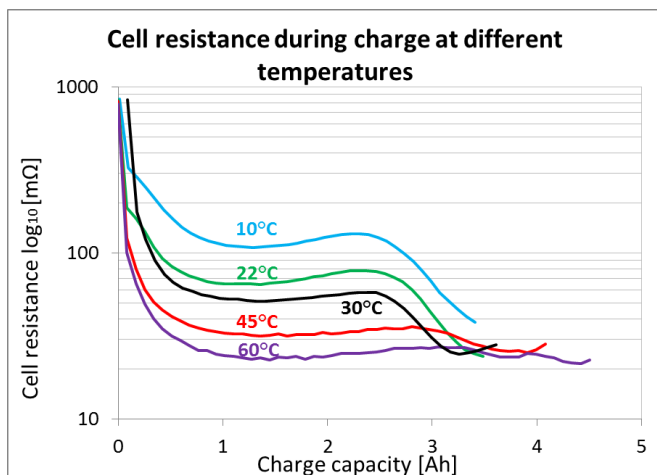
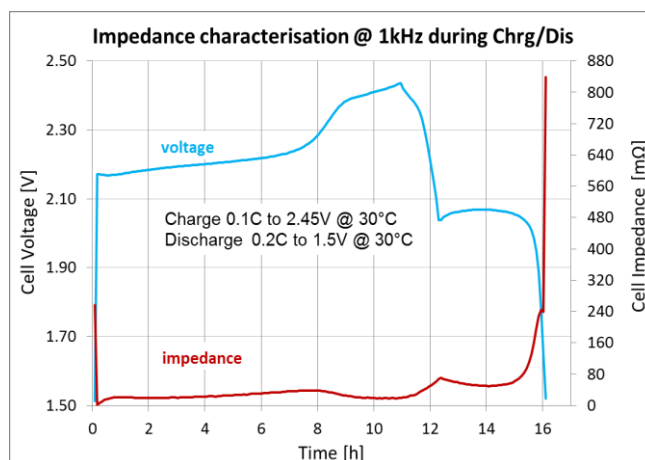
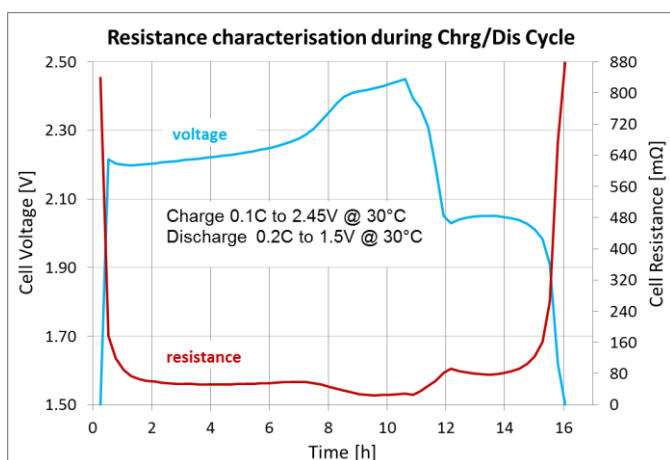
Type	Rechargeable Lithium Sulphur Pouch Cell Remarks: Li Metal Anode
Nominal Dimension (with pouch)	L = 145 mm * W = 78 mm D = 5.6 mm TYP. Tabs size: W = 20 mm, L = 25 mm
Applications	Recommended discharge current 680 mA
Nominal Voltage	2.05V
Capacity	Typical: 3400 mAh Minimum: 3200 mAh When discharged at 680mA to 1.5 V at 30°C
Charging Condition	340 mA to 2.45V at 30°C
Recommended Charging Condition in Applications	340 mA constant current (C/10) Charge termination control recommended: CC stop at 2.45V or 11h max charge time
Clamped Charging Voltage	2.45 V +/- 0.05V
Service Life	>95 cycles (80% of typical capacity)
Weight	Approx. 50.7 g
Internal Resistance	Average Discharge R 159 mΩ End of Discharge R 877 mΩ
Ambient Temperature Range	Charging: 5°C to 80°C Discharging: 5°C to 80°C Storage (1 month): -27°C to 60°C ** Storage (6 month): -27°C to 30°C Storage (1 year): -27°C to 30°C
Note	* without tabs ** ca. 10% irreversible Q loss at 60°C

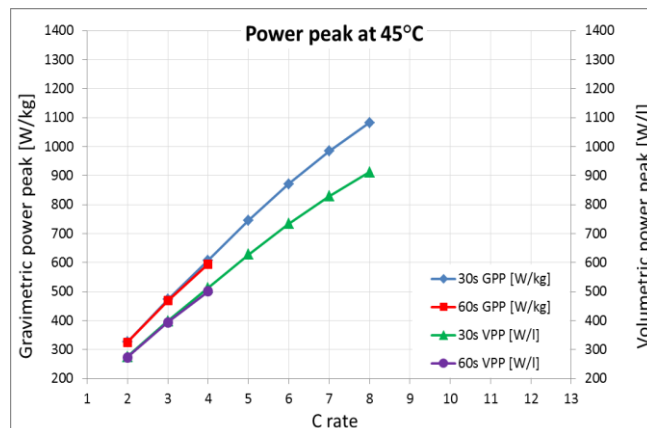
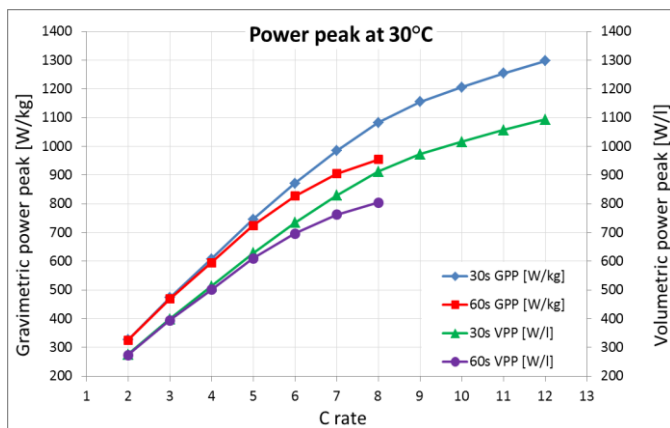
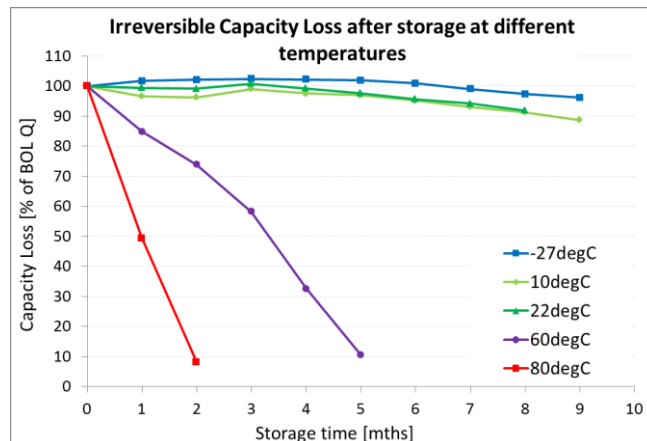
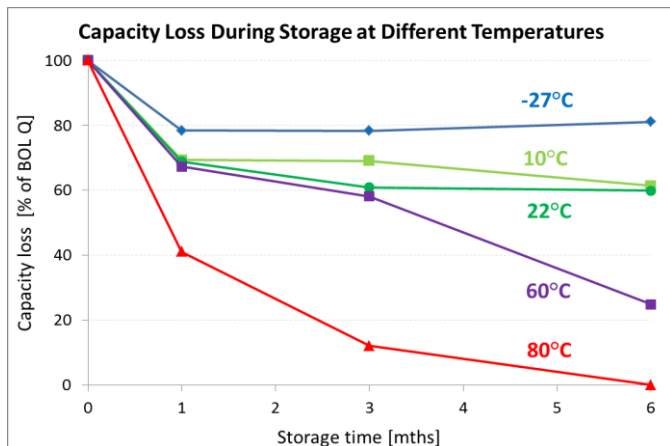
Model: **MLS62120-20S**





* cell kept at -27°C, ten cycles performed every 4 weeks at 30°C





The information (subjected to change without prior notice) contained in this document is for reference only and should not be used as a basis for product guarantee or warranty.

Rev. 03

For detail information, please refer to the relevant product specification.

Revisions:

Rev. 01 (15 Nov 2013) – version 1 released

Rev. 02 (23 Jan 2014) – added new plots: different DoD cycling, performance at different temperatures, resistance and impedance characterisation, capacity fade and aging effect after storage at different temperatures.

Rev. 03 (21.02.14) – cell mass changed from 46.7g to 50.7g

Appendix B

Experimental software code

```
clc;

%Define the Measurement vectors
time = NaN(1,numel(signal(:,1)));
deltaT = NaN(1,numel(signal(:,1)));
Current = NaN(1,numel(signal(:,1)));
Batt_Volt_Pack = NaN(1,numel(signal(:,1)));

% T = NaN(1,numel(signal(:,1)));
% Temp_Meas = NaN(1,numel(signal(:,1)));

%% Initialisation BOP
BOP = visa('ni', 'GPIB0::6::INSTR');
fopen(BOP); %Starts serial communication
fprintf(BOP, 'Func:mode_curr'); %set device to current mode

%set voltage limits for current mode manually
fprintf(BOP, 'Curr:Limit:pos_0.5;neg_5'); %set limitations for
currentn
```

```

LimitsI = query(BOP, 'Curr:Lim?'); %ask for current limitations
LimitsV = query(BOP, 'Volt:prot?'); %ask for volatge limits
fprintf(BOP,'outp_on'); %closes electrical circuit

%% Initial Values for test
%Time
tic; %start timer
fs = 1; %Sampling frequency in Hz
mt = 400000; % max time for measurements in s
i = 1;
ni = 1;

figure(1);

%Set the charging conditions in [s]
chargeTimer = 1;
maxChargeTime = 39600 ; %max charge time in seconds

%Set Min/Max Voltages for the cell
Vmin = 1.5; %1.5 for Li-S
Vmax = 2.45; %2.45 for Li-S

%Set what comes first: Charge or discharge
cd = 2; % 1 for Start with dischagre , 2 for start with charge
cycle = 0;
cycle_max = 4; %defines how many cycles
cycle_factor = 1;

%Temp_max = 45;

```

```

%% Actual cycling code

while toc < mt
%Overall Time + deltaT
time(i) = toc;

%This is to check if the measurements really are taken in the
    demanded time interval
if (i == 1)
deltaT(i) = time(i) - 0;
else
deltaT(i) = time(i) - time(i-1);
end

%Write current demand

%Change the multiplication factor of each cycle
if (cycle == 2 && cd == 1)
cycle_factor = 1.5;
elseif (cycle == 3 && cd == 1)
cycle_factor = 2;
else
cycle_factor = 1;
end

%Take the i-th value from the signal vector and send it to the
    BOP
fprintf(BOP, sprintf('Curr_%.3f', (signal(i,cd)*cycle_factor)))
    ;

%Read the battery current from BOP

```

```

Curr_char = query(BOP, 'Meas:Curr?');
Current(i) = str2double(Curr_char);

%Read the battery terminal voltage from BOP
Volt_char = query(BOP, 'Meas:Volt?');
Batt_Volt_Pack(i) = str2double(Volt_char); %4;

flushinput(BOP);
flushoutput(BOP);

figure(1);
subplot(2,1,1);
plot(time, Current, 'g');
legend('Actual_Current_Load_on_Battery_[A]');
subplot(2,1,2);
plot(time, Batt_Volt_Pack, 'c');
legend('Battery_Terminal_Voltage_Pack_[V]');

%switch between charge and discharge in the range of 1.5 and
2.45V or after the max charge time was reached
if (Batt_Volt_Pack(i) < Vmin)
cd = 2 ; %switch to charge column
end

%count the charging time
if (cd == 2)
chargeTimer = chargeTimer + 1;
end

%
```



```

if (Batt_Volt_Pack(i) > Vmax) || (chargeTimer > maxChargeTime)
cd = 1; %switch to discharge column
chargeTimer = 1;
cycle = cycle + 1;
end

% the third charge/discharge index is filled with zeros to stop
the cycling but not the monitoring of the battery
if (cycle == cycle_max)
cd = 3; %Switches to 0 c
end

drawnow;
display(cycle);
%Makes a measurement with a constant deltaT
%Wait for appropriate time for next measurement
while(ni == i)
ni = floor(toc*fs)+1;
end
i = ni;

%stop after the test time expired
end

fprintf(BOP, 'outp_off ');
fclose(BOP);
fclose(OXIS);

```


Appendix C

Conference Poster Li-SM³ London 2017



Advanced Vehicle
Engineering Centre

Test rig for a dynamic cell temperature control based on duty cycle

Karsten Propp¹, Abbas Fotouhi¹, Daniel Auger¹, Vaclav Knap² Stefano Longo¹

¹School of Aerospace, Transport & Manufacturing, Cranfield University, College Road, Cranfield, Bedfordshire MK43 0AL

²Department of Energy Technology, Aalborg University, Aalborg, 9000, Denmark


Most lithium-sulfur research focuses on improving cells by developing new materials and enhancing inner cell reactions. However, it is also possible to optimize the performance of cells already in existence. One way of doing this is to ensure that temperature management is done effectively and tailored to the duty cycle.

As an example, the shuttle effect, responsible for degradation and self-discharge¹, could be reduced simply by lowering the cell temperature in the high plateau to decrease the transport properties of the electrolyte.

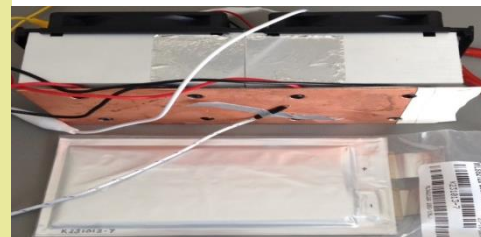
Furthermore cycling tests have indicated that an increased temperature within the low plateau could enhance rate capability and utilisation².

Since most BMS systems are designed to operate the cells at a constant temperature and standard laboratory equipment, like thermal chambers, can only produce slow changes in cell temperature, a specific test rig has been designed and built. The rig is able to change the cell temperatures quickly, yet is simple and inexpensive. The temperature can be controlled and made to follow specified profiles. As well as heating the cells, they can be cooled.

At present, the heating system is powered independently and has not been optimized, but it can inform the design of future temperature management systems.

Parameter	Tested Cell Value
MLS62120-20S lithium sulfur cell	
Dimensions	145 mm x 78 mm x 5.6 mm
Nominal Voltage	2.05 V
Capacity	Typical: 3400 - 3200 mAh
Service Life	> 95 cycles (80% of typical capacity)
Temp. Range	Charge/Discharge: 5°C to 80°C

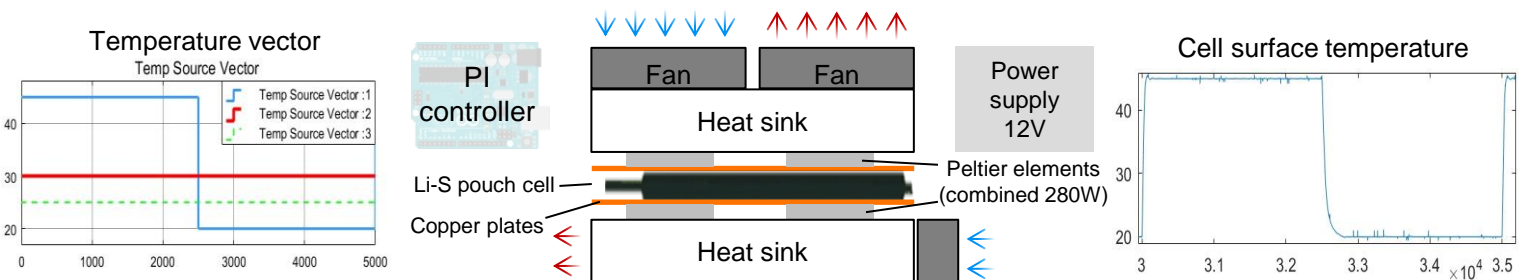
Cell temperature control (top)



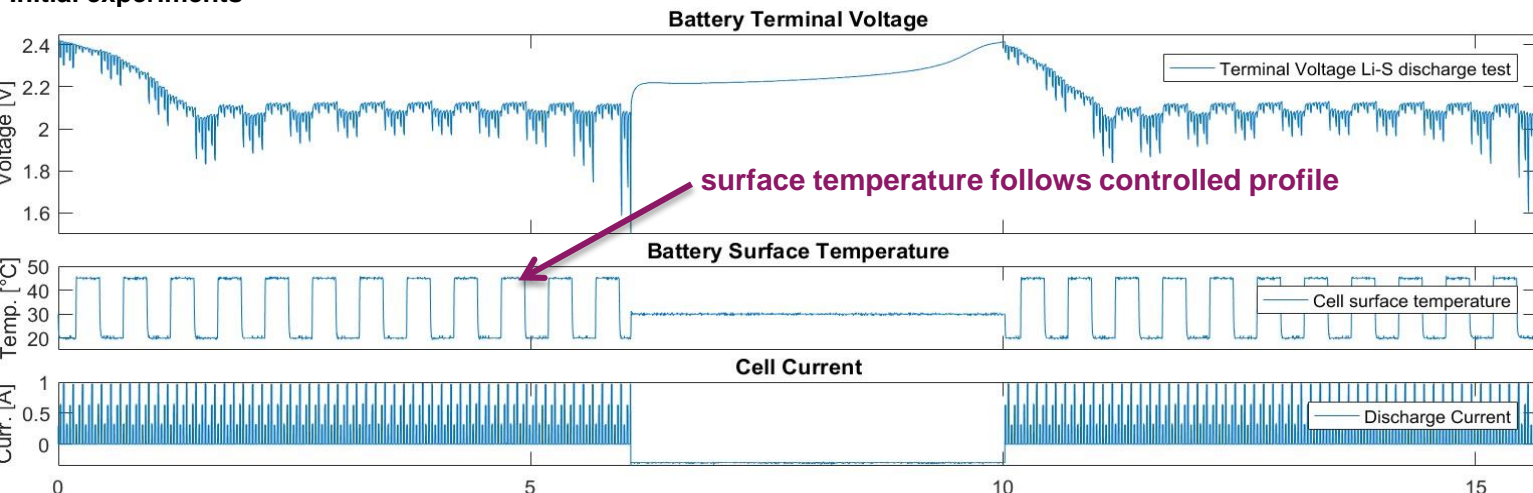
Dynamic temperature control rig

Software: MATLAB and Simulink are used to generate a temperature vector over time

Hardware: an Arduino microcontroller + internal PI controller adjusts the actual cell temperature with four 70 W Peltier elements



Initial experiments



Results and future work

We have introduced a low cost method of controlling battery temperature quickly.

Initial tests with low cost battery cycler suggest that an increased operational temperature could increase the utilization.

Future tests with laboratory power supply and different temperature patterns are planned.

Possible methods are:

- Vary temperatures between voltage plateaus – lower temp in high plateau (self discharge), higher temp in low plateau (utilization)

References

- 1: Mikhaylik, Yuriy V., and James R. Akridge. "Polysulfide shuttle study in the Li/S battery system." *Journal of the Electrochemical Society* 151.11 (2004): A1969-A1976.2
- 2: Propp, Karsten, et al. "Multi-temperature state-dependent equivalent circuit discharge model for lithium-sulfur batteries." *Journal of Power Sources* 328 (2016): 289-299.

References

- [1] C. E. Thomas. Fuel cell and battery electric vehicles compared. *International Journal of Hydrogen Energy*, 34(15):6005–6020, 2009.
- [2] Mengyu Li, Xiongwen Zhang, and Guojun Li. A comparative assessment of battery and fuel cell electric vehicles using a well-to-wheel analysis. *Energy*, 94:693–704, 2016.
- [3] Andrew F. Burke. Batteries and ultracapacitors for electric, hybrid, and fuel cell vehicles. *Proceedings of the IEEE*, 95(4):806–820, 2007.
- [4] Eva Mahnke. *Renews Spezial*. Agentur für Erneuerbare Energien, Berlin, 2012.
- [5] Björn Nykvist and Måns Nilsson. Rapidly falling costs of battery packs for electric vehicles. *Nature Climate Change*, 5(4):329–332, 2015.
- [6] USABC goals for advanced batteries for EVs. <http://www.uscar.org/guest/teams/12/U-S-Advanced-Battery-Consortium-LLC> [Accessed: 12 August 2014].
- [7] K Bullis. How tesla is driving electric car innovation. <https://www.technologyreview.com/s/516961/how-tesla-is-driving-electric-car-innovation> [Accessed: 25 January 2017].

- [8] Linda Gaines and Cuenca Roy. Costs of lithium-ion batteries for vehicles. *Center for Transportation Research, Argonne National Laboratory*, 2000.
- [9] Elton J Cairns and Paul Albertus. Batteries for electric and hybrid-electric vehicles. *Annual Review of Chemical and Biomolecular Engineering*, 1:299–320, 2010.
- [10] Elton J Cairns and H Shimotake. High-temperature batteries. *Science (New York, NY)*, 164(3886):1347–1355, 1969.
- [11] Oxis Energy. Oxis energy teams up with industry leaders to attract technology strategy board funding. <http://www.oxisenergy.com/blog/oxis-energy-teams-up-with-industry-leaders-to-attract-technology-strategy/> [Accessed: 17 August 2014], September 4th 2013.
- [12] Oxis Energy. Energy density diagram. <http://www.oxisenergy.com/technology/> [Accessed: 12 January 2017].
- [13] Claire E Parfitt. Characterisation, modelling and management of lithium-sulphur batteries for spacecraft applications. 2012.
- [14] H. Budde-Meiwes, J. Drillkens, B. Lunz, J. Muennix, S. Rothgang, J. Kowal, and D. U. Sauer. A review of current automotive battery technology and future prospects. *Proceedings of the Institution of Mechanical Engineers, Part D: Journal of Automobile Engineering*, 227(5):761–776, 2013.
- [15] Automotive Energy Supply Corporation. Cell, module, and pack for EV applications. http://www.eco-aesc-lb.com/en/product/liion_ev/ [Accessed: 04 April 2014].

- [16] Karsten Propp, Daniel J Auger, Abbas Fotouhi, Stefano Longo, and Vaclav Knap. Kalman-variant estimators for state of charge in lithium-sulfur batteries. *Journal of Power Sources*, 343:254–267, 2017.
- [17] Karsten Propp, Monica Marinescu, Daniel J Auger, Laura O’Neill, Abbas Fotouhi, Karthik Somasundaram, Gregory J Offer, Geraint Minton, Stefano Longo, Mark Wild, and Vaclav Knap. Multi-temperature state-dependent equivalent circuit discharge model for lithium-sulfur batteries. *Journal of Power Sources*, 328:289–299, 2016.
- [18] M. Stanley Whittingham and Allan J. Jacobson. *Intercalation chemistry*. Materials science and technology. Academic Press, New York, 1982.
- [19] Wu Xu, Jiulin Wang, Fei Ding, Xilin Chen, Eduard Nasybulin, Yaohui Zhang, and Ji-Guang Zhang. Lithium metal anodes for rechargeable batteries. *Energy & Environmental Science*, 7(2):513, 2014.
- [20] Tsutomu Ohzuku and Ralph J. Brodd. An overview of positive-electrode materials for advanced lithium-ion batteries. *Journal of Power Sources*, 174(2):449–456, 2007.
- [21] Vinodkumar Etacheri, Rotem Marom, Ran Elazari, Gregory Salitra, and Doron Aurbach. Challenges in the development of advanced li-ion batteries: a review. *Energy & Environmental Science*, 4(9):3243, 2011.
- [22] Bruno Scrosati and Jürgen Garche. Lithium batteries: Status, prospects and future. *Journal of Power Sources*, 195(9):2419–2430, 2010.

- [23] F Xiong, HJ Yan, Y Chen, B Xu, JX Le, and CY Ouyang. The atomic and electronic structure changes upon delithiation of LiCoO_2 : From first principles calculations. *Int J Electrochem Sci*, 7:9390–9400, 2012.
- [24] H Xia, Shirley Y Meng, Li Lu, and Gerbrand Ceder. Electrochemical behavior and Li diffusion study of LiCoO_2 thin film electrodes prepared by PLD. *Advanced Materials for Micro- and Nano-Systems (AMMNS)*, 2007.
- [25] Doron Aurbach, Yosef Talyosef, Boris Markovsky, Elena Markevich, Ella Zinigrad, Liraz Asraf, Joseph S. Gnanaraj, and Hyeong-Jin Kim. Design of electrolyte solutions for Li and Li-ion batteries: a review. *Electrochimica Acta*, 50(2-3):247–254, 2004.
- [26] M. B. Pinson and M. Z. Bazant. Theory of SEI formation in rechargeable batteries: Capacity fade, accelerated aging and lifetime prediction. *Journal of the Electrochemical Society*, 160(2):A243–A250, 2012.
- [27] Martin Winter, Jürgen O. Besenhard, Michael E. Spahr, Petr Novk. Insertion electrode materials for rechargeable lithium batteries. *Advanced Materials*, 10(10):725–763, 1998.
- [28] J. R. Dahn, A. K. Sleight, Hang Shi, J. N. Reimers, Q. Zhong, and B. M. Way. Dependence of the electrochemical intercalation of lithium in carbons on the crystal structure of the carbon. *Electrochimica Acta*, 38(9):1179–1191, 1993.
- [29] Tri Tran and Kim Kinoshita. Lithium intercalation/deintercalation behavior of basal and edge planes of highly oriented pyrolytic graphite and graphite powder. *Journal of Electroanalytical Chemistry*, 386(1-2):221–224, 1995.

- [30] F. Tuinstra. Raman spectrum of graphite. *The Journal of Chemical Physics*, 53(3):1126, 1970.
- [31] Ping Yu. Determination of the lithium ion diffusion coefficient in graphite. *Journal of The Electrochemical Society*, 146(1):8, 1999.
- [32] J. Vetter, P. Novák, M. R. Wagner, C. Veit, K.-C. Möller, J. O. Besenhard, M. Winter, M. Wohlfahrt-Mehrens, C. Vogler, and A. Hammouche. Ageing mechanisms in lithium-ion batteries. *Journal of Power Sources*, 147(1-2):269–281, 2005.
- [33] Yixuan Wang, Shinichiro Nakamura, Makoto Ue, and Perla B. Balbuena. Theoretical studies to understand surface chemistry on carbon anodes for lithium-ion batteries: Reduction mechanisms of ethylene carbonate. *Journal of the American Chemical Society*, 123(47):11708–11718, 2001.
- [34] Alexandre Chagnes, Jolanta Swiatowska. Electrolyte and solid-electrolyte interphase layer in lithium-ion batteries. *InTech*, 2012.
- [35] Myounggu Park, Xiangchun Zhang, Myoungdo Chung, Gregory B. Less, and Ann Marie Sastry. A review of conduction phenomena in li-ion batteries. *Journal of Power Sources*, 195(24):7904–7929, 2010.
- [36] Anna M. Andersson, Kristina Edström, and John O. Thomas. Characterisation of the ambient and elevated temperature performance of a graphite electrode. *Journal of Power Sources*, 81-82:8–12, 1999.
- [37] Van der Ven, A. and G. Ceder. Lithium diffusion mechanisms in layered intercalation compounds. *Journal of Power Sources*, 97-98:529–531, 2001.
- [38] Toyoki Okumura, Yoichi Yamaguchi, Masahiro Shikano, and Hironori Kobayashi. Correlation of lithium ion distribution and x-ray absorption near-edge structure

- in O3- and O2-lithium cobalt oxides from first-principle calculation. *Journal of Materials Chemistry*, 22(33):17340, 2012.
- [39] M. S. Ding, K. Xu, and T. R. Jow. Phase diagram of EC-DMC binary system and enthalpic determination of its eutectic composition. *Journal of Thermal Analysis and Calorimetry*, 62(1):177–186, 2000.
- [40] Marco Masia, Michael Probst, and Rossend Rey. Ethylene carbonate–Li⁺: A theoretical study of structural and vibrational properties in gas and liquid phases. *The Journal of Physical Chemistry B*, 108(6):2016–2027, 2004.
- [41] D. Aurbach. *Nonaqueous Electrochemistry*. Taylor & Francis, 1999.
- [42] Boris Ravdel, K.M Abraham, Robert Gitzendanner, Joseph DiCarlo, Brett Lucht, and Chris Campion. Thermal stability of lithium-ion battery electrolytes. *Journal of Power Sources*, 119-121:805–810, 2003.
- [43] D. Linden and T. B. Reddy. *Handbook of batteries*. McGraw-Hill, 2002.
- [44] Martin Winter and Ralph J. Brodd. What are batteries, fuel cells, and supercapacitors? *Chemical Reviews*, 104(10):4245–4270, 2004.
- [45] Ying Shirley Meng and Arroyo-de Dompablo, M. Elena. First principles computational materials design for energy storage materials in lithium ion batteries. *Energy & Environmental Science*, 2(6):589, 2009.
- [46] Panasonic Industrial Europe GmbH. LiCoO₂ panasonic NCR-18650A cell datasheet. <http://industrial.panasonic.com/eu> [Accessed: 02 June 2014].
- [47] A123 Systems Inc. ANR26650M1-B technical data. <http://www.a123systems.com/> [Accessed: 02 May 2014].

- [48] Justin Amirault, Joshua Chien, Saurabh Garg, Drew Gibbons. The electric vehicle battery landscape: Opportunities and challenges: CAT technical brief. December 21, 2009.
- [49] A. Chih-Chiang Hua and B. Zong-Wei Syue. Charge and discharge characteristics of lead-acid battery and lifepo4 battery. In *2010 International Power Electronics Conference (IPEC - Sapporo)*, pages 1478–1483.
- [50] Mike Millikin. Panasonic and tesla expand supply agreement for Li-ion cells; nearly 2 billion through 2017, 2013.
- [51] Erockit GmbH. Erockit homepage. <http://www.erokit.net/> [Accessed: 04 April 2014].
- [52] Arumugam Manthiram, Yongzhu Fu, Sheng-Heng Chung, Chenxi Zu, and Yu-Sheng Su. Rechargeable lithium-sulfur batteries. *Chemical Reviews*, 2014.
- [53] Yuriy V Mikhaylik, Igor Kovalev, Riley Schock, Karthikeyan Kumaresan, Jason Xu, and John Affinito. High energy rechargeable Li-S cells for EV application: status, remaining problems and solutions. *Ecs Transactions*, 25(35):23–34, 2010.
- [54] Jiulin Wang, Jun Yang, Jingying Xie, Naixin Xu. A novel conductive polymer-sulfur composite cathode material for rechargeable lithium batteries. *Advanced Materials*, 14(13-14):963–965, 2002.
- [55] M Wild, L ONeill, T Zhang, R Purkayastha, G Minton, M Marinescu, and GJ Offer. Lithium sulfur batteries, a mechanistic review. *Energy & Environmental Science*, 8(12):3477–3494, 2015.
- [56] H. Yamin and E. Peled. Electrochemistry of a nonaqueous lithium/sulfur cell. *Journal of Power Sources*, 9(3):281–287, 1983.

- [57] Karthikeyan Kumaresan, Yuriy Mikhaylik, and Ralph E White. A mathematical model for a lithium–sulfur cell. *Journal of the Electrochemical Society*, 155(8):A576–A582, 2008.
- [58] Ayako Kawase, Soichi Shirai, Yoshinari Yamoto, Ryuichi Arakawa, and Toshikazu Takata. Electrochemical reactions of lithium–sulfur batteries: an analytical study using the organic conversion technique. *Physical Chemistry Chemical Physics*, 16(20):9344–9350, 2014.
- [59] V. S. Kolosnitsyn and E. V. Karaseva. Lithium-sulfur batteries: Problems and solutions. *Russian Journal of Electrochemistry*, 44(5):506–509, 2008.
- [60] VS Kolosnitsyn, EV Karaseva, DY Seung, and MD Cho. Cycling a sulfur electrode in mixed electrolytes based on sulfolane: Effect of ethers. *Russian journal of electrochemistry*, 38(12):1314–1318, 2002.
- [61] Yuriy V Mikhaylik and James R Akridge. Polysulfide shuttle study in the Li/S battery system. *Journal of the Electrochemical Society*, 151(11):A1969–A1976, 2004.
- [62] James R Akridge, Yuriy V Mikhaylik, and Neal White. Li/S fundamental chemistry and application to high-performance rechargeable batteries. *Solid state ionics*, 175(1):243–245, 2004.
- [63] VS Kolosnitsyn, EV Karaseva, and AL Ivanov. Electrochemistry of a lithium electrode in lithium polysulfide solutions. *Russian Journal of Electrochemistry*, 44(5):564–569, 2008.

- [64] Yan Diao, Kai Xie, Shizhao Xiong, and Xiaobin Hong. Shuttle phenomenon – the irreversible oxidation mechanism of sulfur active material in Li–S battery. *Journal of Power Sources*, 235:181–186, 2013.
- [65] Colin A Vincent and Bruno Scrosati. Modern batteries-an introduction to electrochemical power sources . arnold. Technical report, ISBN 0-340-66278-6, 1997.
- [66] Héctor D. Abruña, Yasukuki Kiya, and Jay C. Henderson. Batteries and electrochemical capacitors. *Physics Today*, pages 43–47, 2008.
- [67] M. W. Wagner, C. Liebenow, and J. O. Besenhard. Effect of polysulfide-containing electrolyte on the film formation of the negative electrode. *Journal of Power Sources*, 68(2):328–332, 1997.
- [68] Shizhao Xiong, Kai Xie, Yan Diao, and Xiaobin Hong. On the role of polysulfides for a stable solid electrolyte interphase on the lithium anode cycled in lithium–sulfur batteries. *Journal of Power Sources*, 236:181–187, 2013.
- [69] Duck-Rye Chang, Suck-Hyun Lee, Sun-Wook Kim, and Hee-Tak Kim. Binary electrolyte based on tetra(ethylene glycol) dimethyl ether and 1,3-dioxolane for lithium–sulfur battery. *Journal of Power Sources*, 112(2):452–460, 2002.
- [70] OXIS Energy Ltd. OXIS - MLS62120-20S data sheet-march 2014, 2014.
- [71] Céline Barchasz, Jean-Claude Leprêtre, Fannie Alloin, and Sébastien Patoux. New insights into the limiting parameters of the Li/S rechargeable cell. *Journal of Power Sources*, 199:322–330, 2012.
- [72] Sheng Li, Ming Xie, JingBing Liu, Hao Wang, and Hui Yan. Layer structured sulfur/expanded graphite composite as cathode for lithium battery. *Electrochemical and Solid-State Letters*, 14(7):A105, 2011.

- [73] OXIS Energy Ltd. oxis-brochure-2013, 2013.
- [74] Sion Power. Lithium sulfur rechargeable battery data sheet. <http://www.sionpower.com/> [Accessed: 02 February 2015].
- [75] OXIS Energy Ltd. Electric vehicle lithium sulfur pouch cell: REVB cell development roadmap, 2014.
- [76] Andreas Jossen. Fundamentals of battery dynamics. *Journal of Power Sources*, 154(2):530–538, 2006.
- [77] Mehmet Ugras Cuma and Tahsin Koroglu. A comprehensive review on estimation strategies used in hybrid and battery electric vehicles. *Renewable and Sustainable Energy Reviews*, 42:517–531, 2015.
- [78] Dirk U Sauer, Georg Bopp, Andreas Jossen, Jürgen Garche, Martin Rothert, and Michael Wollny. State of charge—what do we really speak about. In *The 21st international telecommunications energy conference*, pages 6–9, 1999.
- [79] Sabine Piller, Marion Perrin, and Andreas Jossen. Methods for state-of-charge determination and their applications. *Journal of power sources*, 96(1):113–120, 2001.
- [80] Wen-Yeau Chang. The state of charge estimating methods for battery: A review. *ISRN Applied Mathematics*, 2013, 2013.
- [81] Languang Lu, Xuebing Han, Jianqiu Li, Jianfeng Hua, and Minggao Ouyang. A review on the key issues for lithium-ion battery management in electric vehicles. *Journal of Power Sources*, 226:272–288, 2013.

- [82] Languang Lu. Lifepo4 battery performances testing and analyzing for bms. In *2011 US eChina Electric Vehicle and Battery Technology Workshop Presentations*, 2011.
- [83] F Huet. A review of impedance measurements for determination of the state-of-charge or state-of-health of secondary batteries. *Journal of power sources*, 70(1):59–69, 1998.
- [84] Yajuan Li, Hui Zhan, Suqin Liu, Kelong Huang, and Yunhong Zhou. Electrochemical properties of the soluble reduction products in rechargeable Li/S battery. *Journal of Power Sources*, 195(9):2945–2949, 2010.
- [85] VS Kolosnitsyn, EV Kuzmina, EV Karaseva, and SE Mochalov. A study of the electrochemical processes in lithium–sulphur cells by impedance spectroscopy. *Journal of Power Sources*, 196(3):1478–1482, 2011.
- [86] VS Kolosnitsyn, EV Kuzmina, EV Karaseva, and SE Mochalov. Impedance spectroscopy studies of changes in the properties of lithium-sulfur cells in the course of cycling. *Russian Journal of Electrochemistry*, 47(7):793–798, 2011.
- [87] Zhaofeng Deng, Zhian Zhang, Yanqing Lai, Jin Liu, Jie Li, and Yexiang Liu. Electrochemical impedance spectroscopy study of a lithium/sulfur battery modeling and analysis of capacity fading. *Journal of The Electrochemical Society*, 160(4):A553–A558, 2013.
- [88] Ondrej Linda, Edward James William, Matthew Huff, Milos Manic, Vishu Gupta, Jasper Nance, Herbert Hess, Freeman Rufus, Ash Thakker, and Justin Govar. Intelligent neural network implementation for soci development of li/cfx batteries. In *Resilient Control Systems, 2009. ISRCS'09. 2nd International Symposium on*, pages 57–62. IEEE, 2009.

- [89] Thomas Weigert, Q Tian, and K Lian. State-of-charge prediction of batteries and battery–supercapacitor hybrids using artificial neural networks. *Journal of Power Sources*, 196(8):4061–4066, 2011.
- [90] V. Ramadesigan, Northrop, P. W. C., S. De, S. Santhanagopalan, R. D. Braatz, and V. R. Subramanian. Modeling and simulation of lithium-ion batteries from a systems engineering perspective. *Journal of the Electrochemical Society*, 159(3):R31–R45, 2012.
- [91] Alexander Thaler. *Automotive battery technology*. SpringerBriefs in applied sciences and technology. Springer, Cham, 2014.
- [92] Abbas Fotouhi, Daniel J Auger, Karsten Propp, Stefano Longo, and Mark Wild. A review on electric vehicle battery modelling: From lithium-ion toward lithium–sulphur. *Renewable and Sustainable Energy Reviews*, 56:1008–1021, 2016.
- [93] Derek Moy, A Manivannan, and SR Narayanan. Direct measurement of polysulfide shuttle current: A window into understanding the performance of lithium-sulfur cells. *Journal of The Electrochemical Society*, 162(1):A1–A7, 2015.
- [94] Ciprian Antaloae, James Marco, and Francis Assadian. A novel method for the parameterization of a Li-ion cell model for EV/HEV control applications. *IEEE Transactions on Vehicular Technology*, 61(9):3881–3892, 2012.
- [95] Monica Marinescu, Teng Zhang, and Gregory J Offer. A zero dimensional model of lithium–sulfur batteries during charge and discharge. *Physical Chemistry Chemical Physics*, 18(1):584–593, 2016.

- [96] Low Wen Yao, JA Aziz, Pui Yee Kong, and NRN Idris. Modeling of lithium-ion battery using matlab/simulink. In *Industrial Electronics Society, IECON 2013-39th Annual Conference of the IEEE*, pages 1729–1734. IEEE, 2013.
- [97] Ryan C Kroeze and Philip T Krein. Electrical battery model for use in dynamic electric vehicle simulations. In *Power Electronics Specialists Conference, 2008. PESC 2008. IEEE*, pages 1336–1342. IEEE, 2008.
- [98] John Chiasson and Baskar Vairamohan. Estimating the state of charge of a battery. In *American Control Conference, 2003. Proceedings of the 2003*, volume 4, pages 2863–2868. IEEE, 2003.
- [99] Vaclav Knap, Daniel-Ioan Stroe, Remus Teodorescu, Maciej Swierczynski, and Tiberiu Stanciu. Electrical circuit models for performance modeling of lithium-sulfur batteries. In *Energy Conversion Congress and Exposition (ECCE)*, pages 1375–1381. IEEE, 2015.
- [100] Xiaosong Hu, Shengbo Li, and Huei Peng. A comparative study of equivalent circuit models for Li-ion batteries. *Journal of Power Sources*, 198(0):359–367, 2012.
- [101] Gregory L. Plett. Sigma-point kalman filtering for battery management systems of LiPB-based HEV battery packs. *Journal of Power Sources*, 161(2):1356–1368, 2006.
- [102] Mehmet Ugras Cuma and Tahsin Koroglu. A comprehensive review on estimation strategies used in hybrid and battery electric vehicles. *Renewable and Sustainable Energy Reviews*, 42:517–531, 2015.

- [103] Arthur Gelb. *Applied optimal estimation*. M.J.T. Press, Cambridge and Mass. u.a., 8. print edition, 1984.
- [104] Rickard Karlsson. *Particle filtering for positioning and tracking applications*, volume dissertation no. 924 of *Linköping studies in science and technology*. Dept. of Electrical Engineering, Linköping University, Linköping, 2005.
- [105] Yoshua Bengio. Markovian models for sequential data. *Neural computing surveys*, 2(1049):129–162, 1999.
- [106] Rudolph van der Merwe, Eric Wan. Sigma-point kalman filters for probabilistic inference in dynamic state-space models.
- [107] Sebastian Thrun, Wolfram Burgard, and Dieter Fox. *Probabilistic robotics*. MIT press, 2005.
- [108] Ramsey Faragher. Understanding the basis of the kalman filter via a simple and intuitive derivation [lecture notes]. *IEEE Signal Processing Magazine*, 29(5):128–132, 2012.
- [109] Dan Simon. Kalman filtering. *Embedded Systems Programming*, 2001.
- [110] B. S. Bhangu, P. Bentley, D. A. Stone, and C. M. Bingham. Nonlinear observers for predicting state-of-charge and state-of-health of lead-acid batteries for hybrid-electric vehicles. *IEEE Transactions on Vehicular Technology*, 54(3):783–794, 2005.
- [111] Hongwen He, Rui Xiong, Hongqiang Guo, and Shuchun Li. Comparison study on the battery models used for the energy management of batteries in electric vehicles. *Energy Conversion and Management*, 64:113–121, 2012.

- [112] Zheng Chen, Yuhong Fu, and Chunting Chris Mi. State of charge estimation of lithium-ion batteries in electric drive vehicles using extended kalman filtering. *IEEE Transactions on Vehicular Technology*, 62(3):1020–1030, 2013.
- [113] M. Chen and G. A. Rincon-Mora. Accurate electrical battery model capable of predicting runtime and I–V performance. *IEEE Transactions on Energy Conversion*, 21(2):504–511, 2006.
- [114] Gregory L. Plett. Extended kalman filtering for battery management systems of LiPB-based HEV battery packs. *Journal of Power Sources*, 134(2):252–261, 2004.
- [115] Rhudy, M., Y. Gu. Understanding nonlinear kalman filters, part ii: An implementation guide. *Interactive Robotics Letters*, 2013.
- [116] Sebastian Thrun, Wolfram Burgard, and Dieter Fox. *Probabilistic robotics*. Intelligent robotics and autonomous agents. MIT Press, Cambridge and Mass., 2005.
- [117] Orlande, H. R. B. Kalman and particle filters. *METTI V-Thermal Measurements and Inverse Techniques*, 2011.
- [118] The Mathworks, Inc., Natick, Massachusetts. *MATLAB version 8.5.0.197613 (R2015a)*, 2015.
- [119] Abbas Fotouhi, Neda Shateri, Daniel J Auger, Stefano Longo, Karsten Propp, Rajlakshmi Purkayastha, and Mark Wild. A matlab graphical user interface for battery design and simulation; from cell test data to real-world automotive simulation. In *Synthesis, Modeling, Analysis and Simulation Methods and Applications to Circuit Design (SMACD), 2016 13th International Conference on*, pages 1–6. IEEE, 2016.
- [120] Abbas Fotouhi, Karsten Propp, and Daniel J Auger. Electric vehicle battery model identification and state of charge estimation in real world driving cycles. In *Com-*

- puter Science and Electronic Engineering Conference (CEEC), 2015 7th*, pages 243–248. IEEE, 2015.
- [121] Karsten Propp, Abbas Fotouhi, Vaclav Knap, and Daniel J Auger. Design, build and validation of a low-cost programmable battery cyclers. *ECS Transactions*, 74(1):101–111, 2016.
- [122] Heide Budde-Meiwes, Julia Drillkens, Benedikt Lunz, Jens Muennix, Susanne Rothgang, Julia Kowal, and Dirk Uwe Sauer. A review of current automotive battery technology and future prospects. *Proceedings of the Institution of Mechanical Engineers, Part D: Journal of Automobile Engineering*, 227(5):761–776, 2013.
- [123] Bruno Scrosati, Jusef Hassoun, and Yang-Kook Sun. Lithium-ion batteries. a look into the future. *Energy & Environmental Science*, 4(9):3287–3295, 2011.
- [124] Venkatasailanathan Ramadesigan, Paul WC Northrop, Sumitava De, Shriram Santhanagopalan, Richard D Braatz, and Venkat R Subramanian. Modeling and simulation of lithium-ion batteries from a systems engineering perspective. *Journal of The Electrochemical Society*, 159(3):R31–R45, 2012.
- [125] Jun Zhang, Zimin Dong, Xiuli Wang, Xuyang Zhao, Jiangping Tu, Qingmei Su, and Gaohui Du. Sulfur nanocrystals anchored graphene composite with highly improved electrochemical performance for lithium–sulfur batteries. *Journal of Power Sources*, 270:1–8, 2014.
- [126] Natalia A Cañas, Kei Hirose, Brigitta Pascucci, Norbert Wagner, K Andreas Friedrich, and Renate Hiesgen. Investigations of lithium–sulfur batteries using electrochemical impedance spectroscopy. *Electrochimica Acta*, 97:42–51, 2013.

- [127] K Somasundaram, L O'Neill, M Marinescu, T Zhang, G Minton, M Wild, and G J Offer. Towards an operational model for a Li-S battery, 3rd Thomas Young Centre Energy Materials Workshop, poster presentation, 2014.
- [128] Hongwen He, Rui Xiong, Hongqiang Guo, and Shuchun Li. Comparison study on the battery models used for the energy management of batteries in electric vehicles. *Energy Conversion and Management*, 64:113–121, 2012.
- [129] Xiulei Ji and Linda F Nazar. Advances in Li–S batteries. *Journal of Materials Chemistry*, 20(44):9821–9826, 2010.
- [130] Arumugam Manthiram, Yongzhu Fu, Sheng-Heng Chung, Chenxi Zu, and Yu-Sheng Su. Rechargeable lithium–sulfur batteries. *Chemical reviews*, 114(23):11751–11787, 2014.
- [131] H Yamin and E Peled. Electrochemistry of a nonaqueous lithium/sulfur cell. *Journal of Power Sources*, 9(3):281–287, 1983.
- [132] Ho Suk Ryu, Zaiping Guo, Hyo Jun Ahn, Gyu Bong Cho, and Huakun Liu. Investigation of discharge reaction mechanism of lithium— liquid electrolyte— sulfur battery. *Journal of Power Sources*, 189(2):1179–1183, 2009.
- [133] Manu UM Patel, Rezan Demir-Cakan, Mathieu Morcrette, Jean-Marie Tarascon, Miran Gaberscek, and Robert Dominko. Li-s battery analyzed by UV/Vis in operando mode. *ChemSusChem*, 6(7):1177–1181, 2013.
- [134] VS Kolosnitsyn, EV Kuzmina, and EV Karaseva. On the reasons for low sulphur utilization in the lithium–sulphur batteries. *Journal of Power Sources*, 274:203–210, 2015.

- [135] Shizhao Xiong, Kai Xie, Yan Diao, and Xiaobin Hong. Oxidation process of polysulfides in charge process for lithium–sulfur batteries. *Ionics*, 18(9):867–872, 2012.
- [136] Yan Diao, Kai Xie, Shizhao Xiong, and Xiaobin Hong. Shuttle phenomenon—the irreversible oxidation mechanism of sulfur active material in Li–S battery. *Journal of Power Sources*, 235:181–186, 2013.
- [137] Jun Xu, Chunting Chris Mi, Binggang Cao, Junjun Deng, Zheng Chen, and Siqi Li. The state of charge estimation of lithium-ion batteries based on a proportional-integral observer. *Vehicular Technology, IEEE Transactions on*, 63(4):1614–1621, 2014.
- [138] Min Chen and Gabriel A Rincon-Mora. Accurate electrical battery model capable of predicting runtime and IV performance. *Energy conversion*, 21(2):504–511, 2006.
- [139] Martin Rolf Busche, Philipp Adelhelm, Heino Sommer, Holger Schneider, Klaus Leitner, and Jürgen Janek. Systematical electrochemical study on the parasitic shuttle-effect in lithium-sulfur-cells at different temperatures and different rates. *Journal of Power Sources*, 259:289–299, 2014.
- [140] Dominic Bresser, Stefano Passerini, and Bruno Scrosati. Recent progress and remaining challenges in sulfur-based lithium secondary batteries—a review. *Chemical Communications*, 49(90):10545–10562, 2013.
- [141] Tri Tran and Kim Kinoshita. Lithium intercalation/deintercalation behavior of basal and edge planes of highly oriented pyrolytic graphite and graphite powder. *Journal of Electroanalytical Chemistry*, 386(1):221–224, 1995.

- [142] Yuriy V Mikhaylik and James R Akridge. Low temperature performance of Li/S batteries. *Journal of The Electrochemical Society*, 150(3):A306–A311, 2003.
- [143] O Erdinc, B Vural, and M Uzunoglu. A dynamic lithium-ion battery model considering the effects of temperature and capacity fading. In *Clean Electrical Power, 2009 International Conference on*, pages 383–386. IEEE, 2009.
- [144] J Vetter, P Novák, MR Wagner, C Veit, K-C Möller, JO Besenhard, M Winter, M Wohlfahrt-Mehrens, C Vogler, and A Hammouche. Ageing mechanisms in lithium-ion batteries. *Journal of power sources*, 147(1):269–281, 2005.
- [145] Shizhao Xiong, Kai Xie, Yan Diao, and Xiaobin Hong. On the role of polysulfides for a stable solid electrolyte interphase on the lithium anode cycled in lithium–sulfur batteries. *Journal of Power Sources*, 236:181–187, 2013.
- [146] Peter G Bruce, Stefan A Freunberger, Laurence J Hardwick, and Jean-Marie Tarascon. Li-O₂ and Li-S batteries with high energy storage. *Nature materials*, 11(1):19–29, 2012.
- [147] Lennart Ljung. System identification: Theory for the user. *PTR Prentice Hall Information and System Sciences Series*, 198, 1987.
- [148] L Thévenin. Extension de la loi dohm aux circuits électromoteurs complexes [extension of ohms law to complex electromotive circuits]. In *Annales Télégraphiques*, volume 10, pages 222–224, 1883.
- [149] L Thévenin. Sur un nouveau théoreme délectricité dynamique [on a new theorem of dynamic electricity]. *CR des Séances de l’Académie des Sciences*, 97:159–161, 1883.

- [150] Rex Louis Deutscher, Stephen Fletcher, and John Alexander Hamilton. Invention of cyclic resistometry. *Electrochimica acta*, 31(5):585–589, 1986.
- [151] Wook Ahn, Kwang-Bum Kim, Kyu-Nam Jung, Kyoung-Hee Shin, and Chang-Soo Jin. Synthesis and electrochemical properties of a sulfur-multi walled carbon nanotubes composite as a cathode material for lithium sulfur batteries. *Journal of Power Sources*, 202:394–399, 2012.
- [152] S Samuel, L Austin, and D Morrey. Automotive test drive cycles for emission measurement and real-world emission levels-a review. *Proceedings of the Institution of Mechanical Engineers, Part D: Journal of Automobile Engineering*, 216(7):555–564, 2002.
- [153] R Kötz, S Müller, M Bärtschi, B Schnyder, P Dietrich, FN Büchi, A Tsukada, GG Scherer, P Rodatz, O Garcia, et al. Supercapacitors for peak-power demand in fuel-cell-driven cars. In *ECS Electro-Chemical Society, 52nd Meeting,, San Francisco*, 2001.
- [154] The Mathworks, Inc., Natick, Massachusetts. *Simulink version 8.5 (R2015a)*, 2015.
- [155] Sion Power Corporation. Li-sulfur high-energy density lithium-sulfur rechargeable battery. <http://www.sionpower.com> [Accessed: 18 April 2016].
- [156] Bharath Pattipati, Chaitanya Sankavaram, and Krishna R Pattipati. System identification and estimation framework for pivotal automotive battery management system characteristics. *Systems, Man, and Cybernetics, Part C: Applications and Reviews, IEEE Transactions on*, 41(6):869–884, 2011.
- [157] Koray Kutluay, Yigit Cadirci, Yakup S Özkazanç, and Isik Cadirci. A new online state-of-charge estimation and monitoring system for sealed lead-acid batteries in

- telecommunication power supplies. *Industrial Electronics, IEEE Transactions on*, 52(5):1315–1327, 2005.
- [158] Vaclav Knap, D-I Stroe, M Swierczynski, Remus Teodorescu, and Erik Schaltz. Investigation of the self-discharge behavior of lithium-sulfur batteries. *Journal of The Electrochemical Society*, 163(6):A911–A916, 2016.
- [159] Pritpal Singh, Craig Fennie, and David Reisner. Fuzzy logic modelling of state-of-charge and available capacity of nickel/metal hydride batteries. *Journal of Power Sources*, 136(2):322–333, 2004.
- [160] Pritpal Singh, Ramana Vinjamuri, Xiquan Wang, and David Reisner. Design and implementation of a fuzzy logic-based state-of-charge meter for Li-ion batteries used in portable defibrillators. *Journal of Power Sources*, 162(2):829–836, 2006.
- [161] Abbas Fotouhi, Daniel J Auger, Karsten Propp, and Stefano Longo. Electric vehicle battery parameter identification and SOC observability analysis: NiMH and Li-S case studies. *8th IET International Conference on Power Electronics, Machines and Drives (PEMD)*, 2016.
- [162] Jiahao Li, Joaquin Klee Barillas, Clemens Guenther, and Michael A Danzer. A comparative study of state of charge estimation algorithms for LiFePO₄ batteries used in electric vehicles. *Journal of power sources*, 230:244–250, 2013.
- [163] Zheng Chen, Yuhong Fu, and Chunting Chris Mi. State of charge estimation of lithium-ion batteries in electric drive vehicles using extended kalman filtering. *Vehicle Technology, IEEE Transactions on*, 62(3):1020–1030, 2013.
- [164] Daiming Yang, Guoguang Qi, and Xiangjun Li. State-of-charge estimation of lifepo 4/c battery based on extended kalman filter. In *Power and Energy Engi-*

- neering Conference (APPEEC), 2013 IEEE PES Asia-Pacific*, pages 1–5. IEEE, 2013.
- [165] Yong Tian, Bizhong Xia, Wei Sun, Zhihui Xu, and Weiwei Zheng. A modified model based state of charge estimation of power lithium-ion batteries using unscented kalman filter. *Journal of power sources*, 270:619–626, 2014.
- [166] Fengchun Sun, Xiaosong Hu, Yuan Zou, and Siguang Li. Adaptive unscented kalman filtering for state of charge estimation of a lithium-ion battery for electric vehicles. *Energy*, 36(5):3531–3540, 2011.
- [167] Wei He, Nicholas Williard, Chaochao Chen, and Michael Pecht. State of charge estimation for electric vehicle batteries using unscented kalman filtering. *Microelectronics Reliability*, 53(6):840–847, 2013.
- [168] Liang Zhong, Chenbin Zhang, Yao He, and Zonghai Chen. A method for the estimation of the battery pack state of charge based on in-pack cells uniformity analysis. *Applied Energy*, 113:558–564, 2014.
- [169] Xingtao Liu, Zonghai Chen, Chenbin Zhang, and Ji Wu. A novel temperature-compensated model for power Li-ion batteries with dual-particle-filter state of charge estimation. *Applied Energy*, 123:263–272, 2014.
- [170] Simon Schwunk, Nils Armbruster, Sebastian Straub, Johannes Kehl, and Matthias Vetter. Particle filter for state of charge and state of health estimation for lithium-iron phosphate batteries. *Journal of Power Sources*, 239:705–710, 2013.
- [171] Gary Bishop Greg Welch. An introduction to the kalman filter. *Proc. Siggraph Course*, 8, 2006.

- [172] Dan Simon. Kalman filtering. *Embedded systems programming*, 14(6):72–79, 2001.
- [173] M Sanjeev Arulampalam, Simon Maskell, Neil Gordon, and Tim Clapp. A tutorial on particle filters for online nonlinear/non-gaussian bayesian tracking. *Signal Processing, IEEE Transactions on*, 50(2):174–188, 2002.
- [174] Aspasia Papazoglou, Stefano Longo, Daniel Auger, and Francis Assadian. Computational aspects of estimation algorithms for battery-management systems. In *8th Conference on Sustainable Development of Energy, Water and Environment Systems*, 2013.
- [175] Yi-Hsien Chiang, Wu-Yang Sean, and Jia-Cheng Ke. Online estimation of internal resistance and open-circuit voltage of lithium-ion batteries in electric vehicles. *Journal of Power Sources*, 196(8):3921–3932, 2011.
- [176] Hongwen He, Rui Xiong, and Hongqiang Guo. Online estimation of model parameters and state-of-charge of LiFePO₄ batteries in electric vehicles. *Applied Energy*, 89(1):413–420, 2012.
- [177] Rui Xiong, Hongwen He, Fengchun Sun, and Kai Zhao. Evaluation on state of charge estimation of batteries with adaptive extended Kalman filter by experiment approach. *IEEE Transactions on Vehicular Technology*, 62(1):108–117, 2013.
- [178] Abbas Fotouhi, Daniel J Auger, Karsten Propp, and Stefano Longo. Accuracy versus simplicity in online battery model identification. *IEEE Transactions on Systems, Man, and Cybernetics: Systems*, 2016.
- [179] Ariel Rosenman, Ran Elazari, Gregory Salitra, Elena Markevich, Doron Aurbach, and Arnd Garsuch. The effect of interactions and reduction products of LiNO₃, the

- anti-shuttle agent, in Li-S battery systems. *Journal of The Electrochemical Society*, 162(3):A470–A473, 2015.
- [180] Anthony Ferrese and John Newman. Modeling lithium movement over multiple cycles in a lithium-metal battery. *Journal of The Electrochemical Society*, 161(6):A948–A954, 2014.
- [181] Mohammed Fellah, Gurhari Singh, Aymeric Rousseau, Sylvain Pagerit, Edward Nam, and George Hoffman. Impact of real-world drive cycles on PHEV battery requirements. Technical report, SAE Technical Paper, 2009.
- [182] Teng Zhang, Monica Marinescu, Laura O’Neill, Mark Wild, and Gregory Offer. Modeling the voltage loss mechanisms in lithium–sulfur cells: the importance of electrolyte resistance and precipitation kinetics. *Physical Chemistry Chemical Physics*, 17(35):22581–22586, 2015.
- [183] Karsten Propp, Abbas Fotouhi, Daniel J Auger, Vaclav Knap, and Stefano Longo. Test rig for a dynamic cell temperature control based on duty cycle. *Poster, LiSM3 Conference in London*, 2017.
- [184] J Pegueroles Queralt. Battery management controller for Li-S batteries. *Poster, LiSM3 Conference in London*, 2017.
- [185] Airbus Defence and Space. Zephyr, the high altitude pseudo-satellite. <https://airbusdefenceandspace.com/our-portfolio/military-aircraft/uav/zephyr/> [Accessed: 04 April 2017].